Feedback in Galaxies During the Peak Epoch of Cosmic Star Formation Activity and Black Hole Growth

Rebecca Louise Davies

München 2020

Feedback in Galaxies During the Peak Epoch of Cosmic Star Formation Activity and Black Hole Growth

Rebecca Louise Davies

Dissertation
an der Fakultät für Physik
der Ludwig-Maximilians-Universität
München

vorgelegt von
Rebecca Louise Davies
aus Sydney, Australien

München, den 20. August 2020

Erstgutachter: Prof. Dr. Hans Böhringer
Zweitgutachter: Prof. Dr. Andreas Burkert
Tag der mündlichen Prüfung: 7. Oktober 2020

Zusammenfassung

Diese Doktorarbeit behandelt die physikalischen Prozesse von Gasausflüssen auf galaktischen Skalen, hervorgerufen durch Sternentstehung und Akkretion auf supermassive Schwarze Löcher, und deren Auswirkungen auf die Eigenschaften des interstellaren Mediums und der Galaxienentwicklung. Der Fokus liegt dabei auf sternebildenden Galaxien während der Hochzeit der kosmischen Sternentstehung und des Wachstums von Schwarzen Löchern, bei Rotverschiebungen $1 \lesssim z \lesssim 3$, wenn die Feedbackeffizienz erwartungsgemäß maximal ist. Diese Arbeit wurde durch hochmoderne, nahinfrarote integralfeldspektroskopische Beobachtungen ermöglicht, welche entscheidende Emissionslinien bei hoher räumlicher Auflösung und Signalrauschverhältnis und für eine representative Auswahl von Galaxien bei hohen Rotverschiebungen untersuchen.

Um die Initiierung und die treibende Kraft hinter den Gasausflüssen, die durch junge Sternpopulationen hervorgerufen werden, zu studieren, wird das größte Set von $z \sim 2$ Galaxien genutzt, die auf der Größenskala massiver sternebildender Klumpen aufgelöst sind. Es wird untersucht, wie die typische Geschwindigkeit und Feedbackeffizienz von Gasausflüssen mit den lokalen Sternentstehungseigenschaften in galaktischen Scheiben variieren. Die hohe räumliche Auflösung der Beobachtungen ist dabei entscheidend, da intrinsische Korrelationen zwischen Sternentstehung und Gasausflüssen durch die Mittelung über größere Bereiche der Galaxien, die sowohl aktive Sternentstehungsgebiete als auch passive Gebiete enthalten, vermindert werden können. Es stellt sich heraus, dass die Gebiete mit der intensivsten Sternentstehungsaktivität die schnellsten Gasausflüsse mit den höchsten Massenladefaktoren hervorrufen. Durch den Vergleich der beobachteten Zusammenhänge mit Modellvorhersagen wird geschlossen, dass am wahrscheinlichsten die mechanische Energie von Sternwinden, Supernovaexplosionen und Strahlungsdruck von massiven Sternen zusammenwirken, um ionisiertes Gas aus den Galaxienscheiben zu stoßen.

Sehr tiefe Daten mehrerer Wellenlängenbereiche von drei Galaxien mit Gasausflüssen durch aktive Galaxienkerne (AGN) werden genutzt, um die Auswirkungen von AGN-Aktivität auf die Sternentstehungsrate und die Eigenschaften des ionisierten Gases auf zentralen, galaktischen, und zirkumgalaktischen Skalen zu untersuchen. Die Ergebnisse zeigen, dass die Akkretionsenergie von AGN an Gas koppeln kann und dadurch möglicherweise Sternentstehung auf Skalen von wenigen hundert Parsec bis zu $\gtrsim 5$ Kiloparsec unterdrücken kann. Allerdings sind diese Effekte relativ lokalisiert und es gibt keine Hinweise darauf, dass Gasausflüsse irgendeinen signifikanten Einfluss auf die momentane globale Sternentstehungsrate dieser Galaxien haben.

Abschließend wird untersucht, ob Sternentstehungsfeedback direkt für die erhöhten Elektronendichten verantwortlich ist, die in sternebildenden Galaxien bei hohen Rotverschiebungen beobachtet werden. Die integrierten Spektren von mehr als 600 Galaxien werden genutzt, um sowohl die lokale Elektronendichte im linienemittierenden Gas als auch die durchschnittliche Elektronendichte in der sternebildenden Scheibe in vier Rotverschiebungsbereichen von $0 \lesssim z \lesssim 2.6$ zu messen. Die beobachtete Entwicklung der Elektronendichte wird zu quantitativen Vorhersagen für eine Reihe plausibler Szenarien verglichen. Dabei stellt sich heraus, dass die Elektronendichte am wahrscheinlichsten durch die molekulare Gasdichte bestimmt wird. Diese Ergebnisse legen nahe, dass die beobachtete Korrelation zwischen Elektronendichte und Sternentstehungsrate nicht ein Anzeichen von Feedback ist, sondern dadurch entsteht, dass beide Größen im direkten Zusammenhang mit der Menge und Dichte des molekularen Gases in Galaxien stehen.

Abstract

This thesis investigates the physics of galaxy scale gas outflows driven by star formation and accretion onto supermassive black holes, and examines their effects on the properties of the interstellar medium and the evolution of galaxies. The focus is on star-forming galaxies at the peak epoch of cosmic star formation activity and black hole growth, at redshifts $1 \lesssim z \lesssim 3$, where the efficiency of feedback is expected to reach a maximum. This work is enabled by state-of-the-art near infrared integral field spectroscopic observations that probe key diagnostic emission lines at high spatial resolution and signal-to-noise ratio across representative samples of galaxies at high redshift.

The largest sample of $z \sim 2$ galaxies resolved on the scales of massive star-forming clumps is used to study the launching and driving mechanisms of outflows powered by young stellar populations. The typical velocity and feedback efficiency of outflows are measured as a function of local star formation properties across galaxy disks. The high spatial resolution of the observations is crucial because intrinsic correlations between star formation and outflow properties are diluted when averaging over larger sections of galaxies containing both actively star-forming and more quiescent regions. The results show that the regions with the most intense star formation activity drive the fastest outflows with the largest mass loading factors. By comparing the observed relationships with model predictions, it is shown that mechanical energy from stellar winds and supernova explosions and radiation pressure from massive stars most likely work together to push ionized gas out of galaxy disks.

Very deep multi-wavelength data for three galaxies with outflows driven by active galactic nuclei (AGN) are used to examine the impact of AGN activity on the rate of star formation and the properties of ionized gas on nuclear, galactic and circumgalactic scales. The results show that the AGN accretion energy can couple to gas and potentially suppress star formation on spatial scales ranging from a few hundred parsecs to $\gtrsim 5$ kiloparsecs. However, the effects are relatively localized and there is no evidence that the outflows have any significant impact on the current global star formation rates of the AGN host galaxies.

Finally, it is investigated whether star formation feedback is directly responsible for the elevated electron densities observed in star-forming galaxies at high-z. Integrated spectra of more than 600 galaxies are used to measure both the local electron density in the line-emitting gas and the electron density averaged over the volume of the star-forming disk in four redshift slices spanning $0 \lesssim z \lesssim 2.6$. The observed electron density evolution is compared to quantitative predictions for a range of plausible scenarios, and it is found

that the electron density is most likely to be governed by the molecular gas density. These results suggest that the observed correlation between electron density and star formation rate is not a signature of stellar feedback, but instead arises because both quantities are intrinsically linked to the amount and density of molecular gas in galaxies.

Acknowledgements

First and foremost I would like to thank my project supervisor Natascha Förster Schreiber. Thank you for inviting me to work with you on these exciting science projects, and for being an excellent model of thoroughness and rigorousness in research. I very much appreciate the time and care you put into guiding me through my PhD.

Thank you to Reinhard Genzel, Linda Tacconi, Dieter Lutz, Natascha, and the other senior members of the Infrared Group at MPE for giving me the opportunity to be a part of the group, for encouraging the group members to work together and to always strive for excellence in research, and for sharing your vast knowledge of astrophysics with the more junior researchers.

Many thanks go to my kind and supportive mentors. Firstly, to my postdoc mentor at MPE, Taro Shimizu, for always being ready to calmly listen and provide encouragement and advice whether I was stressed, frustrated, or excited. Secondly, to my undergraduate supervisor and mentor at ANU, Lisa Kewley. Your encouragement and support took me further than I ever could have dreamed of during my undergraduate research career, and gave me the energy to continue with my PhD during times when I felt hopeless.

I would like to thank the many other former and current members of the IR Group who supported me during my PhD. Thank you especially to Hannah Übler for helping me to navigate the final stages of the PhD and for assisting me with German language translations, to my office mate Alejandra Jiménez Rosales for providing a friendly working environment, and to Sirio Belli, Rodrigo Herrera-Camus, and Emily Wisnioski for lively research discussions. Thank you to all of the students and postdocs for creating a fun social atmosphere.

Thank you to my family and friends in Australia for supporting me and for travelling half way around the world to visit me, and to my friends in Munich for making me feel at home here.

Last but definitely not least, thank you to my wonderful husband Joshua - for moving to Munich to give me this opportunity, for always being caring, supportive, and encouraging, and for our many fun travel adventures across Europe. I am very grateful for everything you have done for me.

Publications

This cumulative dissertation is based on the following articles:

- Chapter 2: *Kiloparsec Scale Properties of Star Formation Driven Outflows at $z \sim 2.3$ in the SINS/zC-SINF AO Survey.* 2019, ApJ, 873, 122.

  R. L. Davies, N. M. Förster Schreiber, H. Übler, R. Genzel, D. Lutz, A. Renzini, S. Tacchella, L. J. Tacconi, S. Belli, A. Burkert, C. M. Carollo, R. I. Davies, R. Herrera-Camus, S. J. Lilly, C. Mancini, T. Naab, E. J. Nelson, S. H. Price, T. T. Shimizu, A. Sternberg, E. Wisnioski, and S. Wuyts.

- Chapter 3: *From Nuclear to Circumgalactic: Zooming in on AGN-driven Outflows at $z \sim 2.2$ with SINFONI.* 2020, ApJ, 894, 28.

  R. L. Davies, N. M. Förster Schreiber, D. Lutz, R. Genzel, S. Belli, T. T. Shimizu, A. Contursi, R. I. Davies, R. Herrera-Camus, M. M. Lee, T. Naab, S. H. Price, A. Renzini, A. Schruba, A. Sternberg, L. J. Tacconi, H. Übler, E. Wisnioski, and S. Wuyts.

- Chapter 4: *The KMOS^{3D} Survey: Investigating the Origin of the Elevated Electron Densities in Star-forming Galaxies at $1 \lesssim z \lesssim 3$.* Submitted to the Astrophysical Journal (ApJ).

  R. L. Davies, N. M. Förster Schreiber, R. Genzel, T. T. Shimizu, R. I. Davies, A. Schruba, L. J. Tacconi, H. Übler, E. Wisnioski, S. Wuyts, M. Fossati, R. Herrera-Camus, D. Lutz, J. T. Mendel, T. Naab, S. H. Price, A. Renzini, D. Wilman, A. Beifiori, S. Belli, A. Burkert, J. Chan, A. Contursi, M. Fabricius, M. M. Lee, R. P. Saglia, and A. Sternberg.

R. L. Davies performed the data analysis, developed the interpretation, and produced all of the text, figures, and tables presented in these publications, with the exception of the lens modelling and source plane reconstruction for the galaxy J0901+1814 and the associated explanatory material which is presented in Appendix A.1 of the second paper (Section 3.9.1 of this thesis) and was provided by Dieter Lutz.

Contents

List of Figures

List of Tables

Chapter 1

Introduction

This thesis addresses the physics of feedback processes from star formation and accretion onto supermassive black holes, and their impact on the properties of the interstellar medium (ISM) and the evolution of galaxies. The investigation is focused on star-forming galaxies (SFGs) at the peak epoch of star formation and black hole growth (at redshifts $1 \lesssim z \lesssim 3$, ~ 7 – 11 Gyr ago), when the rate of energy injection into the ISM and the rates of mass and energy ejection via outflows are expected to reach a maximum. The highest quality data currently available for individual galaxies are employed to bring unique insights into the driving mechanisms of outflows and how they interact with the surrounding material as they propagate through galaxies and halos. Large statistical samples of galaxies with spatially resolved spectroscopy are used to carry out the most comprehensive study to date of the physical processes driving the evolution of a key property of ionized gas in star-forming (H II) regions over cosmic time.

This introductory chapter describes the broad observational framework within which the present research is conducted, and outlines key physical concepts relevant to the analysis. Section 1.1 introduces the cosmological concordance model and examines the role of feedback processes in regulating the relationship between the masses of dark matter halos and the properties of the galaxies embedded within them. Section 1.2 summarizes how the properties of SFGs have evolved from $1 \lesssim z \lesssim 3$ to the present-day universe. Section 1.3 discusses the driving mechanisms and multi phase structure of outflows, and how they are probed observationally. Section 1.4 explains how emission line ratios can be used to measure the electron density and pressure of gas in H II regions. Section 1.5 describes the unique instrumentation used to obtain the data presented in this work, and Section 1.6 outlines the subsequent chapters of this dissertation.

1.1 The Imprint of Feedback on Galaxy Properties

The ΛCDM Cosmological Concordance Model

ΛCDM is the current cosmological concordance model which describes the formation,

composition, and evolution of structure in the Universe. The cosmological constant Λ represents 'dark energy' – a form of vacuum energy with negative pressure that is postulated to drive the accelerating expansion of the Universe. Cold Dark Matter (CDM) is a non-baryonic, collisionless and dissipationless form of matter that is required to explain, among other things, the unexpectedly large rotation velocities of gas beyond the optical disks of spiral galaxies (e.g. Einasto et al., 1974; Ostriker et al., 1974) and the discrepancy between the observed (luminous) and inferred (dynamical) masses of galaxy clusters (see Massey et al. 2010 and references therein). Comparisons between observations and ΛCDM model predictions suggest that baryonic matter accounts for only $\sim 5\%$ of the present-day energy density of the Universe, while dark matter and dark energy account for $\sim 25\%$ and $\sim 70\%$, respectively (e.g. Planck Collaboration et al., 2018).

Although the nature of dark matter (DM) and the physical origin of dark energy are unknown, the ΛCDM model reproduces many observed properties of the Universe to a very high level of accuracy. The ΛCDM model predicts that directly following the Big Bang and inflation, the matter component of the Universe was comprised of DM and ionized plasma, and that the matter density distribution was uniform except for quantum fluctuations on all spatial scales. Gravitational interactions caused the DM to collapse towards the peaks of the density field, but radiation pressure counteracted the gravitational collapse of the baryons, creating oscillations in the baryon density distribution which propagated outwards like sound waves (known as Baryon Acoustic Oscillations). After $\sim 380{,}000$ years the plasma had cooled enough for electrons and protons to recombine and form hydrogen, decoupling the baryons from the photons. The distance travelled by the baryons between the end of inflation and the time of recombination is known as the sound horizon. After recombination, gravitational interactions caused baryons and DM to congregate and form galaxies, both at the locations of the original density peaks and on the sound horizon scale.

The first important observational verification of this prediction was the discovery of the Cosmic Microwave Background (CMB) radiation (Penzias & Wilson, 1965). Both the observed average temperature of the CMB and the size of the temperature fluctuations are in extremely good agreement with the predicted properties of the black body radiation from the ionized plasma at the time of recombination (Dicke et al., 1965; Planck Collaboration et al., 2018). The predicted peak in the clustering of galaxies on the sound horizon scale was detected 40 years later by Eisenstein et al. (2005), providing further observational evidence to support the existence of Baryon Acoustic Oscillations.

The Relationship Between Dark Matter Halos and Galaxies

The ΛCDM model makes clear predictions for how the clustering and mass function of DM halos evolve over cosmic time. If galaxy growth was primarily governed by gravitational processes, then the stellar masses of galaxies would be expected to scale linearly with the masses of the host DM halos. However, the observed galaxy stellar mass function deviates strongly from the predicted halo mass function (Figure 1.1). Only a small fraction of the baryons in halos are in the form of stars, and the efficiency of galaxy formation is strongly mass-dependent, peaking around the mass scale of the Milky Way and drop-

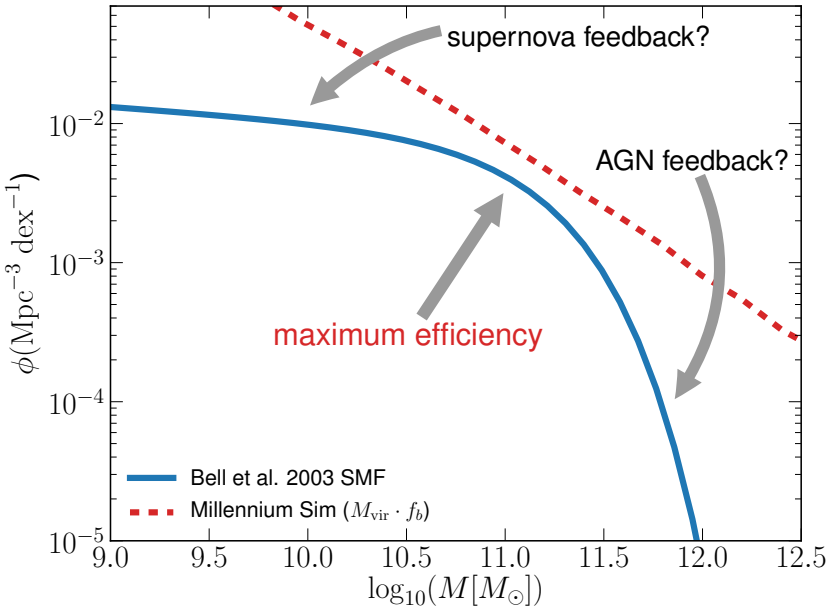

Figure 1.1: Comparison between the predicted halo baryonic mass function from the Millennium ΛCDM cosmological simulation (dashed red line) and the observed galaxy stellar mass function (solid blue curve), both at $z = 0$. Figure taken from Mutch et al. (2013).

ping steeply towards lower and higher masses (e.g. Baldry et al., 2008; Li & White, 2009; Moustakas et al., 2013; Moster et al., 2018; Behroozi et al., 2019). This suggests that star formation is strongly influenced by non-gravitational (hydrodynamic) processes.

Early ΛCDM cosmological simulations were unable to reproduce the strong suppression of star formation in low and high mass halos (e.g. Balogh et al., 2001). It has long been recognized that feedback from supernovae and active galactic nuclei (AGN) are key ingredients for the production of realistic galaxy populations (e.g. White & Frenk, 1991). Supernova feedback is energetic enough to efficiently expel cold gas from low mass galaxies which inhabit shallow potential wells, removing the fuel for future star formation (e.g. Dekel & Silk, 1986; Springel & Hernquist, 2003; Davé et al., 2017). In high mass halos, AGN feedback is thought to be responsible for both ejecting cold gas and injecting large amounts of energy into the circumgalactic medium, compounding the effects of virial shock heating to prevent the halo gas from cooling and replenishing the molecular gas reservoir in the galaxy disk (e.g Springel & Hernquist, 2005; Bower et al., 2006; Croton et al., 2006; Somerville et al., 2008). The recent successes of feedback models in producing realistic populations of simulated galaxies have strengthened the notion that feedback is an important factor leading to the low and mass-dependent efficiency of galaxy formation.

However, it remains unclear whether the feedback prescriptions implemented in cosmological simulations are realistic. Large volume simulations cannot resolve the physical scales required to self-consistently model supernova explosions and black hole accretion disk winds, and instead rely on sub-grid models that inject energy when certain conditions

are met (e.g. Springel & Hernquist, 2005). The strength, type, and frequency of energy injection can have significant effects on the properties of the resulting galaxy populations (e.g. Crain et al., 2009; Puchwein & Springel, 2013), but there is currently no clear observational picture of how the energy produced by supernova explosions and black hole accretion is coupled to the surrounding gas or of how the properties of the resulting outflows vary as a function of redshift and galaxy properties (see e.g. discussion in Nelson et al., 2019). Tighter observational constraints on the physical drivers, incidence, and efficiency of feedback processes are required to more stringently test the current theoretical paradigm of galaxy formation.

1.2 Galaxies from the Peak Epoch of Cosmic Star Formation to Now

In recent years, multi-wavelength surveys of extragalactic deep fields have significantly improved our understanding of how the properties of galaxies have evolved over the history of the Universe. Far infrared (FIR) imaging from *Spitzer* and *Herschel* and ultraviolet (UV) imaging from the *Hubble Space Telescope* (HST) have made it possible to trace the average level of star formation in galaxies back to very early epochs. Near infrared integral field spectrographs such as the *K-band Multi Object Spectrograph* (KMOS) and the *Spectrograph for INtegral Field Observations in the Near Infrared* (SINFONI) have enabled detailed measurements of the kinematic properties of SFGs beyond the local universe. Facilities such as the *NOrthern Extended Millimeter Array* (NOEMA) and the *Atacama Large (sub)Millimeter Array* (ALMA) have provided unique insights into how the molecular gas reservoirs of galaxies influence their star formation rates (SFRs), disk structure, and the amount of turbulence in the ISM. This section summarizes the current observational understanding of how the key properties of SFGs have changed over cosmic time.

Star Formation and Black Hole Growth

The average rate of star formation in galaxies has evolved significantly over the history of the Universe. Compilations of SFR measurements for galaxies spanning $0 \lesssim z \lesssim 8$ indicate that the SFR per unit volume in the Universe (referred to as the cosmic SFR volume density and denoted as ψ) rose steeply ($\psi \propto (1+z)^{-2.9}$) during the first ~ 4 Gyr of cosmic history, reached a peak at $z \sim 2$, and then declined steadily ($\psi \propto (1+z)^{2.7}$), dropping by an order of magnitude over the intervening ~ 10 Gyr until the present-day (Gruppioni et al. 2013; Magnelli et al. 2013; Madau & Dickinson 2014; see panel a) of Figure 1.2). The era of maximum star formation activity spanning $1 \lesssim z \lesssim 3$ is known as the 'peak epoch of cosmic star formation'. Deep X-ray and far-infrared surveys have revealed that the volume-averaged growth rate of supermassive black holes tracks the cosmic SFR volume density (Shankar et al. 2009; Aird et al. 2010; Delvecchio et al. 2014; see panel (b) of Figure 1.2), supporting other observational evidence to suggest that supermassive black holes co-evolve

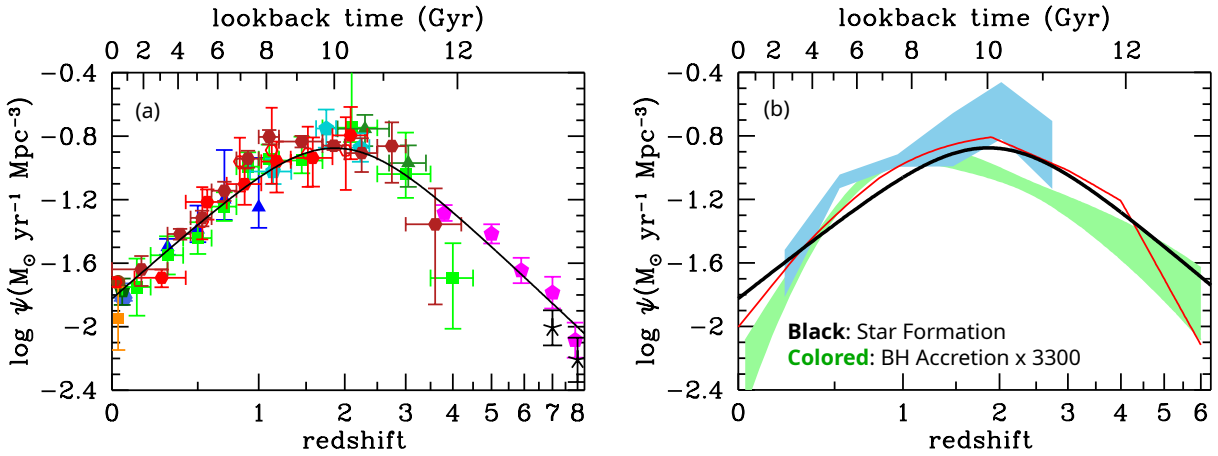

Figure 1.2: The evolution in the average SFR (left) and black hole accretion rate (BHAR; right) per unit volume in the Universe, as a function of both redshift (lower x axes) and lookback time (upper x axes). The BHAR volume density measurements in panel (b) have been scaled up by a factor of 3300 to match the normalization of the SFR volume density. The cosmic SFR and BHAR densities both peaked at $1 \lesssim z \lesssim 3$, the era known as the 'peak epoch of cosmic star formation'. Figure adapted from Madau & Dickinson (2014).

with their host galaxies (see Section 1.3.1 for further discussion). Most of the stellar mass in present-day massive galaxies was formed in SFGs at $1 < z < 3$ (see review by Madau & Dickinson 2014, and references therein), and therefore these systems are important probes of the physical processes that shaped the properties of the local galaxy population.

Main Sequence of Star Forming Galaxies

The majority of SFGs follow a tight redshift-dependent correlation between galaxy stellar mass and SFR known as the star-forming main sequence, which has been observationally verified to exist up to at least $z \sim 5$ (a lookback time of $\gtrsim 12$ Gyr). The normalization of the main sequence evolves strongly over cosmic time such that at fixed stellar mass, the typical SFR increases monotonically towards higher redshifts (e.g. Daddi et al. 2007; Elbaz et al. 2007; Noeske et al. 2007; Whitaker et al. 2014; Speagle et al. 2014; Tomczak et al. 2016; Pearson et al. 2018; Leslie et al. 2020; see Figure 1.3). The shape of the main sequence also changes, particularly in the high stellar mass ($\log_{10}(M_*/M_\odot) \gtrsim 10.2$) regime where the relationship becomes progressively flatter towards $z \sim 0$. As a result, the most massive SFGs at $z \sim 2$ ($\log_{10}(M_*/M_\odot) \gtrsim 11.0$) form stars ~ 60 times faster than SFGs with the same stellar mass at $z \sim 0$, whereas for lower mass ($\log_{10}(M_*/M_\odot) \lesssim 10.0$) galaxies the difference is much smaller (a factor of $\lesssim 35$). The flattening of the main sequence could trace the onset of quenching at high stellar masses, potentially as a result of strong feedback in these systems (e.g. Whitaker et al., 2014; Schreiber et al., 2015). The existence of a tight star-forming main sequence (with a constant scatter of $\sim 0.2 - 0.4$ dex) over the majority of the history of the Universe suggests that galaxies evolve in a quasi-equilibrium

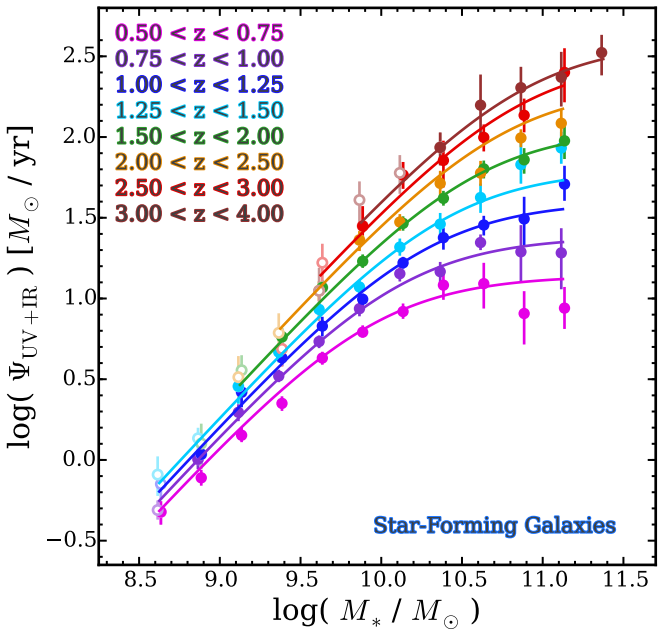

Figure 1.3: Average SFRs of star-forming galaxies as a function of stellar mass, in eight redshift intervals indicated by different colors. Figure adapted from Tomczak et al. (2016).

state regulated by the balance between inflows, outflows, and star formation (e.g. Bouché et al., 2007; Genzel et al., 2010; Davé et al., 2012; Lilly et al., 2013; Tacchella et al., 2016), and that any significant deviations from this equilibrium (due to e.g. major mergers) must be rare and/or short-lived (e.g. Rodighiero et al., 2011).

Molecular Gas Reservoirs

The enhanced star formation activity in SFGs at high-z must be driven by an increase in the mass fraction of the cold molecular gas (H_2) out of which stars form and/or a decrease in the molecular gas depletion time (defined as M_{H_2}/SFR) towards higher redshifts. There is a strong correlation between molecular gas surface density Σ_{H_2} and SFR surface density $\Sigma_{\rm SFR}$ in the local universe, known as the Kennicutt-Schmidt relation (Schmidt, 1959; Kennicutt, 1998). SFGs at $z \sim 2$ follow a similar relationship but have a factor of ~ 3 higher $\Sigma_{\rm SFR}$ at fixed Σ_{H_2} due to the decrease in the molecular gas depletion time (e.g. Genzel et al. 2010; Tacconi et al. 2013; Sargent et al. 2014; Béthermin et al. 2015; see left-hand panel of Figure 1.4). The majority of the SFR evolution is driven by the order of magnitude increase in the typical gas fractions of SFGs from the local universe to the peak epoch of cosmic star formation (e.g. Scoville et al. 2017; Liu et al. 2019; Millard et al. 2020; Tacconi et al. 2020; see right-hand panel of Figure 1.4). The elevated gas fractions in SFGs at high redshift are thought to be the direct result of higher accretion rates onto dark matter halos (e.g. Lilly et al., 2013; Genzel et al., 2015; Tacchella et al., 2018; Tacconi et al., 2020).

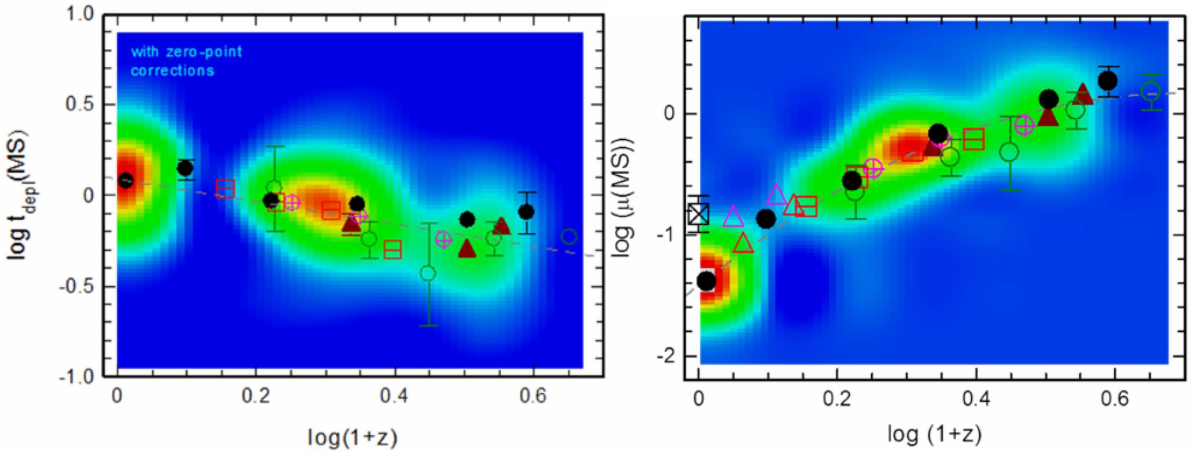

Figure 1.4: Molecular gas depletion time (M_{H_2}/SFR, left) and molecular gas fraction (M_{H_2}/M_*, right) of galaxies on the star-forming main sequence as a function of redshift. The background colors indicate the number of galaxies in each pixel of the plotted parameter space, increasing linearly from blue to red. The symbols show binned average measurements from different molecular gas tracers: CO line emission (filled black circles), dust continuum emission at $\lambda = 1$ mm (maroon triangles), and the far infrared spectral energy distribution (open markers). The grey dashed lines show the best fit to the redshift evolution of each property. Figure adapted from Tacconi et al. (2018).

Structural and Kinematic Properties

The large molecular gas reservoirs of $z \sim 2$ SFGs also appear to have a substantial impact on their structural and kinematic properties. SFGs at high-z often show evidence for large clumps with $\Sigma_{\rm SFR}$ significantly exceeding the median level across the rest of the galaxy (e.g. Elmegreen & Elmegreen, 2005; Förster Schreiber et al., 2011; Genzel et al., 2011; Wisnioski et al., 2012; Guo et al., 2018). These clumps have typical diameters of ~ 1 kiloparsec (kpc), making them $\sim 2-3$ times larger than the most extreme H II regions in the local universe. Clumpy galaxies generally show relatively smooth stellar mass distributions (Wuyts et al., 2012; Guo et al., 2015; Soto et al., 2017) and velocity fields (e.g. Genzel et al., 2011), suggesting that the clumps are transient phenomena with lifetimes of ~ 100 Myr (Genzel et al., 2011; Genel et al., 2012; Hopkins et al., 2012a; Wuyts et al., 2012). The critical size at which a clump becomes unstable to gravitational collapse scales with the molecular gas fraction, and therefore gas-rich galaxies are expected to have larger star-forming complexes than gas-poor galaxies (e.g. Bournaud et al., 2008; Genzel et al., 2008; Dekel et al., 2009).

The clumpy gas disks at $z \sim 2$ are also turbulent. The intrinsic disk velocity dispersions of $\sim 40-50$ km s^{-1} are $\sim 2-3$ times larger than what is observed in the comparatively gas-poor disks at $z \sim 0$ (e.g. Genzel et al., 2006; Wisnioski et al., 2015; Johnson et al., 2018; Übler et al., 2019). Comparisons between observations and models suggest that the increased turbulence at high-z is likely to be driven by the release of gravitational energy

through accretion, clump formation, and radial transport of material within marginally stable Toomre disks. Stellar feedback could plausibly be the primary driver of turbulence in disk galaxies at $z \sim 0$, but seems insufficient to drive the elevated turbulence in SFGs at $z \sim 2$ (e.g. Krumholz et al., 2018; Übler et al., 2019; Varidel et al., 2020).

1.3 Galaxy Scale Outflows

Galaxy scale outflows are thought to play a crucial role in driving the evolution of galaxies: regulating their star formation and chemical enrichment histories (e.g. Davé et al., 2012; Hopkins et al., 2012b; Hirschmann et al., 2013; Vogelsberger et al., 2013; Chisholm et al., 2017), setting the size and angular momentum of galactic disks (e.g. Okamoto et al., 2005; Sales et al., 2010), and coupling the growth of black holes and their host galaxies (e.g. Silk & Rees, 1998; Fabian, 2012; King & Pounds, 2015). Outflows transport both gas and kinetic energy from galaxies to the circumgalactic medium, emptying galaxies of their gas reservoirs and helping to prevent circumgalactic gas from cooling to replenish the fuel for star formation (e.g Di Matteo et al., 2005; Springel & Hernquist, 2005; Croton et al., 2006; Schaye et al., 2015; Weinberger et al., 2017; Davé et al., 2019). Outflows are powered by momentum and energy injection from young stellar populations and/or accretion onto supermassive black holes, and should therefore be the strongest at the peak epoch of star formation and black hole growth. For this reason, galaxies at $z \sim 1 - 3$ are valuable laboratories in which to study the impact of outflows on galaxy evolution.

1.3.1 Driving Mechanisms

Massive Stars: Stellar Winds, Supernovae, and Radiation Pressure

Outflows from star-forming regions can be driven by several different mechanisms, the most commonly considered of which are energy injection from stellar winds and supernovae, and momentum injection from radiation. A single supernova explosion ejects $1 - 10\ M_{\odot}$ of material with a typical kinetic energy of 10^{51} erg (e.g. Abbott, 1982). The expansion of the ejecta into the surrounding ISM drives a strong shock that heats the ejecta to very high temperatures, allowing the gas to expand freely with negligible energy loss (e.g. Taylor, 1950; Sedov, 1959). As the hot bubble expands it sweeps up ionized, neutral, and molecular material, creating a multi phase outflow. Over time the ejecta cools and radiative energy losses become significant, leading to pressure driven and momentum conserving expansion phases (e.g. Cox, 1972; McKee & Ostriker, 1977). Simulations suggest that the swept-up ISM material can increase the momentum rate of the outflow by a factor of ~ 10 (e.g. Kim & Ostriker, 2015). Collisions between stellar winds can produce bubbles of hot gas that evolve in a similar manner, expanding into and sweeping up the surrounding material (e.g. Cantó et al., 2000).

Outflows can also be driven by radiation pressure. Photons transfer momentum to dust grains at a rate of $\dot{p}_{\rm rad} \sim \tau L_{\rm SF}/c$ (where τ is the optical depth of the material, $L_{\rm SF}$ is the

bolometric luminosity of the young stars, and c is the speed of light), and the gas that is coupled to the dust accelerates with it. The resulting wind does not have a hot component and is purely momentum driven. Radiation pressure is likely to be the primary driver of outflows from young H II regions, prior to the explosion of the first supernovae (e.g. Nath & Silk, 2009; Murray et al., 2011). However, it remains unclear which process dominates the outflow energetics at later evolutionary stages.

Active Galactic Nuclei

Outflows driven by Active Galactic Nuclei (AGN) have long been considered a key mechanism to couple the growth of supermassive black holes to the evolution of their host galaxies. There is a tight relationship between the black hole mass $M_{\rm BH}$ and the velocity dispersion of the stellar bulge σ_* (the $M_{\rm BH}-\sigma_*$ relation) over at least 4 orders of magnitude in black hole mass (e.g. Ferrarese & Merritt, 2000; Gebhardt et al., 2000; Kormendy & Ho, 2013), suggesting that black holes grow in lock-step with their host bulges. The sphere of influence of a 10^9 $M_\odot$ black hole is ~ 50 parsecs, and therefore even a very massive black hole cannot gravitationally influence the growth of the bulge on kpc scales. However, the gravitational potential energy released in the process of black hole accretion far exceeds the binding energy of the host bulge. If the accretion energy is able to efficiently couple to gas on kpc scales, it could provide a mechanism to link the growth of black holes and their host galaxies (see review by King & Pounds 2015).

The total amount of gravitational energy released over the lifetime of a black hole is $E_{acc} = \eta M_{\rm BH} c^2$, where the dimensionless parameter η is the efficiency of conversion from accreted mass to energy and is typically assumed to have a value of ~ 0.1 (e.g. King, 2010). For a $10^8 M_\odot$ black hole, $E_{acc} \simeq 10^{61}$ erg. Assuming that the bulge can be approximated as a uniform density sphere with mass M_b and radius R, its gravitational binding energy is given by $E_{bind} = 3GM_b^2/5R$, where G is the gravitational constant. The mass enclosed within a radius R is related to σ_* by $M_b(R) = 2\sigma_*^2 R/G$. Combining the last two equations, the gravitational binding energy can be expressed as $E_{bind} \simeq M_b \sigma_*^2$. Adopting values approximately appropriate for the host bulge of a 10^8 $M_\odot$ black hole ($M_b \simeq 10^{11} M_\odot$, $\sigma_* \simeq 200$ km s^{-1}; e.g. McConnell & Ma 2013) yields $E_{bind} \simeq 10^{59}$ erg. The binding energy of the bulge is $\gtrsim 2$ orders of magnitude smaller than the accretion energy released during the growth of the black hole.

The most efficient way for the accretion energy to couple to the surrounding material is mechanically, through winds. It has been suggested that the $M_{\rm BH} - \sigma_*$ relation may arise as a locus of balance between radiation pressure (which drives winds) and the gravitational potential of the bulge (which resists the propagation of the wind material). The outward force on a shell of ionized hydrogen in the radiation field of a black hole accreting at the Eddington limit (the accretion rate at which the inward gravitational force on material in the accretion disk is balanced by the outward radiation force) is given by:

$$F_{rad} = \frac{L_{edd}}{c} = \frac{4\pi G M_{\rm BH} m_p}{\sigma_T} \tag{1.1}$$

where m_p is the proton mass and σ_T is the Thomson scattering cross-section for electrons. The inward gravitational force on the shell of gas is given by

$$F_{grav} = \frac{GM_{b,gas}M_b}{R^2} = \frac{Gf_{gas}M_b^2}{R^2} = Gf_{gas}\left(\frac{2\sigma_*^2}{G}\right)^2 = \frac{4\sigma_*^4 f_{gas}}{G} \tag{1.2}$$

where $M_{b,gas}$ and f_{gas} are the gas mass and gas mass fraction of the bulge, respectively. If the outward and inward forces are equal (i.e. $F_{rad} = F_{grav}$), Equations 1.1 and 1.2 can be equated to derive the relationship between $M_{\rm BH}$ and σ_*:

$$\begin{aligned} \frac{4\pi G M_{\rm BH} m_p}{\sigma_T} &= \frac{4\sigma_*^4 f_{gas}}{G} \\ M_{\rm BH} &= \frac{f_{gas}\sigma_T}{\pi G^2 m_p}\sigma_*^4 \end{aligned} \tag{1.3}$$

The resulting expression is quantitatively very similar to the observed $M_{\rm BH} - \sigma_*$ relation. Therefore, one possible explanation for the existence of the $M_{\rm BH} - \sigma_*$ relation is that black holes that are under-massive compared to their host bulges do not release enough accretion energy to overcome the local gravitational potential, allowing the black holes to continue growing, whereas over-massive black holes drive winds that expel the surrounding material and prevent further accretion (e.g. King, 2003; Zubovas & King, 2012; Lapi et al., 2014).

There is substantial observational evidence for the presence of winds powered by accretion onto supermassive black holes. A large fraction of AGN show broad, strongly blueshifted, highly ionized metal absorption lines in their X-ray spectra, tracing Ultra-Fast Outflows with velocities of 0.1 – 0.2 c (e.g. Tombesi et al., 2011; Gofford et al., 2013). These velocities are consistent with the prediction of a simple spherical wind model. Assuming that the AGN is accreting at the Eddington limit, and that the photons emitted by the AGN impart $\sim 100\%$ of their momentum to the wind (i.e. $\dot{p}_{\rm wind} \simeq L_{\rm AGN}/c$, where $L_{\rm AGN}$ is the bolometric luminosity of the AGN), the predicted wind velocity is $v_{\rm wind} \simeq \eta\ c$.

Similar to the supernova driven outflow case, the hot wind launched from the black hole accretion disk will eventually collide with the ISM of the host galaxy, become shock heated, and sweep up the surrounding multi phase material. If the cooling timescale in the shocked wind is shorter than the flow time, the majority of the wind kinetic energy will be radiated away and only the momentum will be transferred to the cooler gas phases, resulting in a momentum driven outflow (top row in Figure 1.5). Due to the large energy losses, momentum driven outflows are expected to be confined to relatively small galactocentric radii. If the cooling timescale is long, most of the kinetic energy will be transferred to the ISM, resulting in a galaxy scale energy driven outflow (bottom row in Figure 1.5). In the energy driven case, the swept-up ISM material can boost the momentum rate of the outflow by a factor of ~ 5 – 20 (e.g. Faucher-Giguère & Quataert, 2012). Studies based on numerical simulations have reported that if $\sim 5\%$ of the kinetic energy of the hot wind was able to couple to the ISM, the resulting outflow would be energetic enough to efficiently regulate the growth of black holes and their host stellar bulges (e.g. Di Matteo et al., 2005).

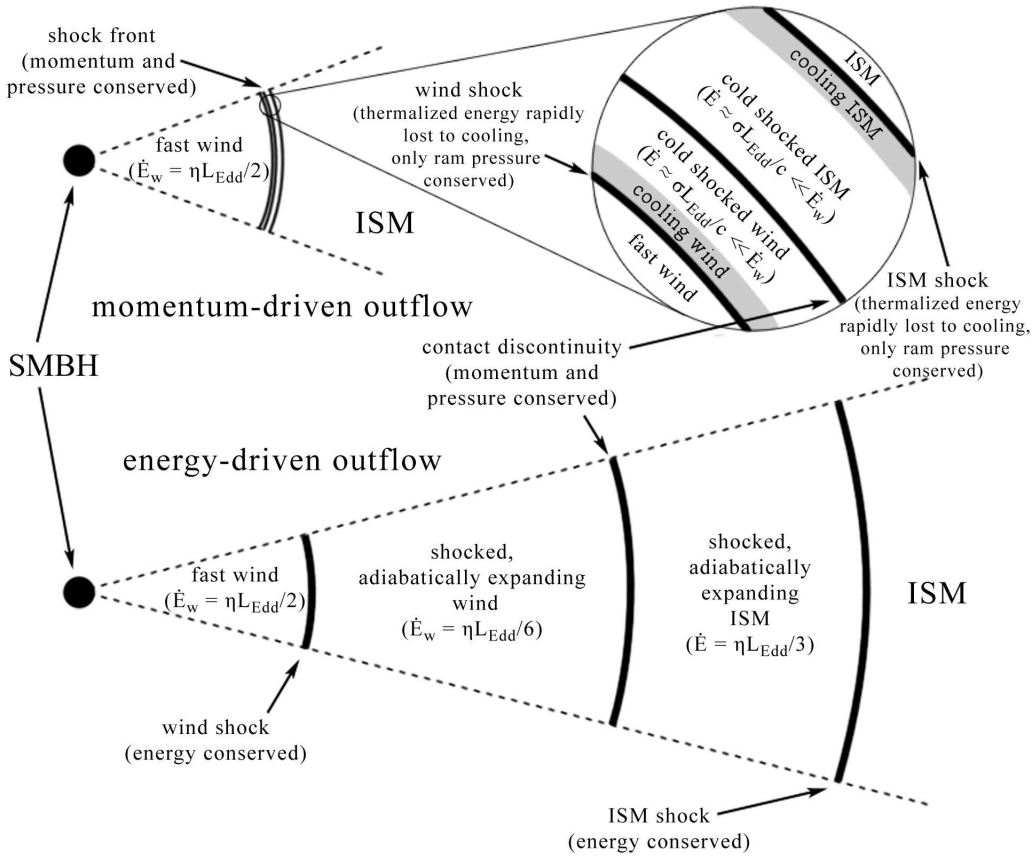

Figure 1.5: Schematic diagram illustrating the expected time evolution of an AGN driven outflow in the momentum conserving (top) and energy conserving (bottom) cases. Figure taken from Zubovas & King (2012).

1.3.2 Observational Characteristics

Multi Phase Structure

Both star formation and AGN driven outflows contain gas at a range of temperatures and densities. The hot ($T \sim 10^7$ K) wind fluid that powers energy driven outflows can be detected in soft X-ray continuum or in X-ray absorption lines of highly ionized species. As the hot wind propagates it compresses and entrains warm ($T \sim 10^4$ K) ionized gas and colder ($T \sim 100$ K) neutral and molecular gas in its path. The ionized gas can be probed through nebular emission lines (hydrogen recombination lines and/or fine structure transitions of heavier elements) at visible wavelengths or through absorption lines in the ultraviolet. The cold phase is most commonly probed using either emission lines associated with rotational transitions of CO (at millimeter wavelengths) or far-infrared absorption lines of molecular species such as OH. The kinematic imprints of outflows on the emission

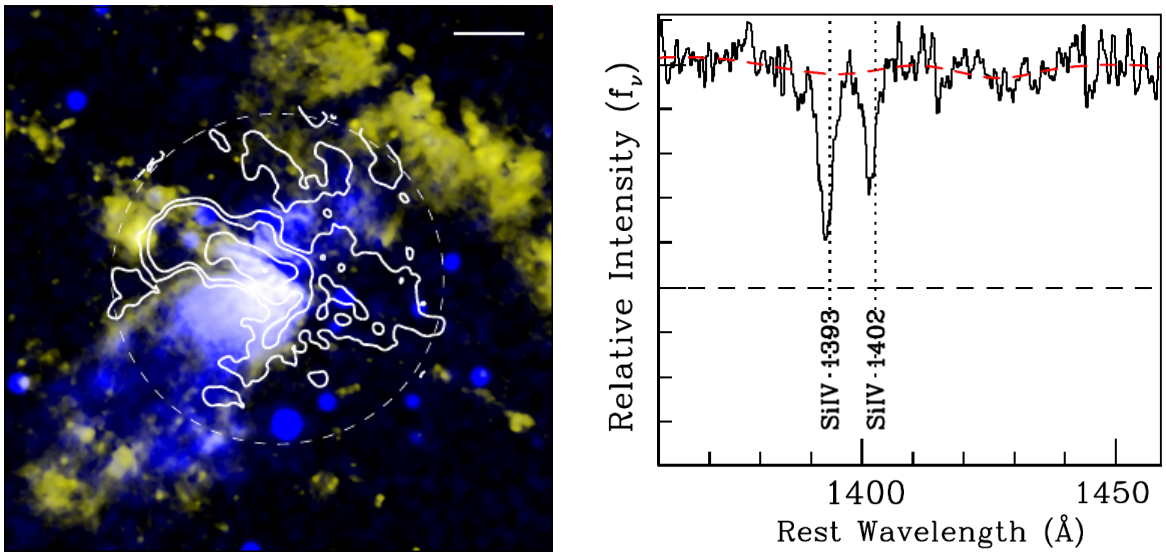

Figure 1.6: Left: The multi phase star formation driven outflow launched from the nuclear region of the local galaxy NGC 253. Colors show the spatial distribution of the soft X-ray (blue), Hα (yellow) and CO (white contours) emission. Figure adapted from Bolatto et al. (2013). Right: Si IV absorption line profiles in a stacked spectrum of SFGs at $z \sim 2 - 3$. The line centroids are blueshifted relative to the expected wavelengths of ISM absorption (marked by the dotted black lines), indicative of outflows. Figure adapted from Steidel et al. (2010).

line and absorption line spectra of galaxies are discussed in more detail at the end of this section.

The left-hand panel of Figure 1.6 shows the multi phase structure of the star formation driven outflow launched from the nuclear region of the nearby galaxy NGC 253. The hot volume-filling wind fluid is shown in blue, and the other colors indicate the spatial distributions of the entrained ionized (yellow), neutral and molecular (white contours) gas. In some outflows (such as this one) the different gas phases are arranged in a stratified density structure, where the hot wind is surrounded by a layer of ionized gas and then a layer of neutral gas (e.g. Shopbell & Bland-Hawthorn, 1998; Bolatto et al., 2013; Leroy et al., 2015). However, there are also examples of galaxies in which the neutral and ionized outflows do not appear to be linked spatially (e.g. Rupke et al., 2017). In general, the relationships between the different outflow phases and their relative contributions to the total kinetic energy and mass budget of outflows remain poorly constrained, in part because any given dataset generally only probes a single gas phase.

The ionized phase is the only outflow phase that is currently observationally accessible for large samples of galaxies at $z \sim 1 - 3$, but there is growing evidence that it is not the dominant outflow component by mass. The molecular and atomic gas outflow rates are typically larger than the ionized gas outflow rate, both at $z \lesssim 0.1$ (e.g. Fiore et al., 2017; Fluetsch et al., 2020; Roberts-Borsani, 2020) and in the few sources with multi phase

observations at higher redshifts (e.g. Vayner et al., 2017; Brusa et al., 2018; Herrera-Camus et al., 2019). The hot wind component is very difficult to observe, but simulations suggest that it may carry the majority of the mass in energy conserving outflows (e.g. Li et al., 2017; Fielding et al., 2018; Kim & Ostriker, 2018; Nelson et al., 2019). Consequently, mass outflow rates measured from warm ionized gas observations are likely to significantly underestimate the total energetics and feedback efficiency of outflows. The primary motivation for studying outflows in ionized gas is to gain insights into their demographics and physical drivers. Statistical studies of hundreds of ionized outflows across the massive galaxy population at $z \sim 1 - 3$ have revealed that star formation driven and AGN driven outflows have different characteristic velocities and follow orthogonal trends in the parameter space of galaxy mass versus star formation properties (e.g. Harrison et al., 2016; Freeman et al., 2019; Leung et al., 2019; Förster Schreiber et al., 2019; Swinbank et al., 2019). Integral field spectroscopy provides the ability to map ionized gas across galaxies, enabling detailed studies of the launching and driving mechanisms of outflows (e.g. Genzel et al., 2011; Newman et al., 2012a) and the impact of outflows on the properties of gas in galaxy disks (e.g. Cano-Díaz et al., 2012; Cresci et al., 2015; Carniani et al., 2016). These latter aspects are primary topics of focus in this thesis.

Kinematic Signatures

Outflows are most commonly identified through their kinematic imprint on emission line and absorption line profiles in galaxy spectra. Emission lines trace relatively dense material close to the launch sites of the outflows, whereas absorption lines probe the total column density of material along the line of sight and can trace lower density gas ejected over multiple outflow episodes. Therefore, combining emission line and absorption line information for matched samples of galaxies provides insights into the duty cycles of outflows.

Gas is often expelled and entrained in an approximately biconical structure perpendicular to the plane of the galaxy. Absorption lines are produced when photons emitted by stars in the host galaxy are absorbed by outflowing material between the galaxy and the observer. Only the approaching side of the outflow can be detected in this way, because stellar continuum photons do not pass through gas on the receding side of the outflow on their way to the Earth. Therefore, outflows produce absorption line profiles that are blueshifted relative to the systemic velocity of the host galaxy (see the right-hand panel of Figure 1.6 and the review by Veilleux et al. 2005).

In this work, outflows are identified through the presence of broad and/or blueshifted components in the emission line spectra. Outflowing material produces many of the same emission lines as the ISM, but has a very different velocity distribution to the gas in the main body of the galaxy which follows gravitational motions (such as disk rotation). Therefore, each emission line in the combined galaxy + outflow spectrum will be a superposition of two (or more) kinematic components. If the emission from the receding side of the outflow (redshifted emission) is strongly attenuated by the host galaxy in the foreground, the outflow component signature will appear blueshifted relative to the systemic velocity of the galaxy.

1.4 Physical Properties of H II Regions: The Electron Density

Understanding how and why the properties of H II regions have changed over cosmic time is a key goal of galaxy evolution studies because H II regions are the birthplaces of stars. The relative intensities of the strongest emission lines in H II region spectra are primarily determined by four properties: the metallicity (typically expressed as the abundance of oxygen relative to hydrogen, where the other elements are assumed to follow standard abundance scalings), the hardness (spectral shape) of the ionizing radiation field, the ionization parameter (the speed at which the radiation field can push an ionization front through the nebula), and the electron density. Variations in these parameters are often inter-dependent and can have degenerate effects on the strong line ratios (see e.g. discussion in Kewley et al., 2013). The only way to robustly determine how the different properties have evolved over cosmic time is to measure each one using tracers that are relatively insensitive to variations in the other key parameters.

This work focuses on the electron density (n_e) which is intrinsically related to the ionization/recombination balance and determines the size of the region that can be ionized by a given radiation source. The electron density can be calculated from the flux ratio of any two transitions of the same ion that have similar excitation energies, such that the ratio of their excitation rates will be approximately independent of temperature. If the two transitions have different radiative decay and/or collisional de-excitation probabilities, the relative number of electrons in each state and therefore the ratio of the line fluxes will vary with n_e. There are many pairs of transitions that satisfy these conditions and can be observed in the spectra of astrophysical nebulae (see e.g. Kewley et al., 2019), including the rest-frame optical [O II]$\lambda\lambda$ 3726, 3729 and [S II]$\lambda\lambda$ 6716, 6731 doublets and the FIR [N II] lines at 122μm and 205μm. A given flux ratio is sensitive to electron densities similar to the critical densities of the individual transitions, where the probabilities of collisional de-excitation and radiative decay are equal.

1.4.1 [S II]λ6716/[S II]λ6731 as an Electron Density Diagnostic

The summaries of atomic physics concepts presented in this section are based on material from Dopita & Sutherland (2003), Osterbrock & Ferland (2006) and Kewley et al. (2019).

In this work, n_e is measured using the [S II]λ6716/[S II]λ6731 ratio (hereafter '$R_{\rm SII}$'). [S II]λ6716 and [S II]λ6731 are two of the strongest lines in the rest-frame optical spectra of H II regions, and they lie relatively close in wavelength to Hα ($\Delta\lambda \simeq 150 - 170$ Å), meaning that they are within the wavelength coverage of many existing spectroscopic observations targeting Hα emission in galaxies at the peak epoch of star formation (described in Section 1.5). The [S II] lines are separated by $\Delta v \simeq 640$ km s^{-1} and are well resolved in the majority of the datasets used in this dissertation which have a typical spectral resolution of $R = \lambda/\Delta\lambda \simeq 3000 - 4000$, corresponding to a line spread function with a full width

at half maximum (FWHM) of ~ 75 – 100 km s^{-1}. This section provides a more detailed description of why $R_{\rm SII}$ is a good tracer of the electron density in H II regions, and discusses difficulties associated with measuring the average electron densities of nebulae with radially varying density and ionization structure.

The ion S+ can be approximated as a three-level atom for which the energy separation between the ground state and the first excited state (E_{12}) is much larger than the energy separation between the first and second excited states (E_{23}); i.e. $E_{12} >> E_{23}$ and $E_{12} \simeq E_{13}$. The flux produced by radiative decay from excited state i to the ground state is given by

$$F_{i1} = N_i A_{i1} E_{1i} \tag{1.4}$$

where N_i is the fraction of electrons in energy level i and A_{ij} is the radiative decay rate which is determined by the quantum mechanical properties of the ion. The [S II]λ6716 and [S II]λ6731 fluxes correspond to F_{31} and F_{21}, respectively, and therefore the line flux ratio is given by

$$R_{\rm SII} = \frac{N_3 A_{31} E_{13}}{N_2 A_{21} E_{12}} \simeq \frac{N_3 A_{31}}{N_2 A_{21}} \tag{1.5}$$

In the low density limit, the timescale for collisional excitation and de-excitation between the excited states is much longer than the timescale for radiative decay. Assuming that the population levels are in equilibrium, collisional excitation from the ground state to the excited states is balanced by radiative decay out of the excited states such that

$$N_1 C_{12} = N_2 A_{21}, \;\; N_1 C_{13} = N_3 A_{31} \tag{1.6}$$

Here C_{ij} is the collisional excitation rate, given by

$$C_{ij} = n_e \beta \frac{\Omega_{ij}}{g_i} T_e^{-1/2} \exp\left(\frac{-E_{ij}}{kT_e}\right) \tag{1.7}$$

where β is a collection of physical constants, g_i is the statistical weight of state i, T_e is the electron temperature, and Ω_{ij} is the collision strength which represents the dimensionless probability of collisional (de)excitation between states i and j. The flux ratio in the low density limit is therefore given by

$$\begin{aligned} R_{\rm SII,low} \simeq \frac{N_1 C_{13}}{N_1 C_{12}} = \frac{C_{13}}{C_{12}} &= \frac{n_e \beta \frac{\Omega_{13}}{g_1} T_e^{-1/2} \exp\left(\frac{-E_{13}}{kT_e}\right)}{n_e \beta \frac{\Omega_{12}}{g_1} T_e^{-1/2} \exp\left(\frac{-E_{12}}{kT_e}\right)} \\ &= \frac{\Omega_{13}}{\Omega_{12}} \exp\left(\frac{-(E_{13}-E_{12})}{kT_e}\right) \simeq \frac{\Omega_{13}}{\Omega_{12}} \end{aligned} \tag{1.8}$$

The collision strengths are approximately independent of electron energy and therefore the line flux ratio does not vary strongly as a function of temperature. For S+, the line flux ratio in the low density limit is $R_{\rm SII,low} \simeq 1.45$.

In the high density limit, every collisional excitation from the first excited state to the second excited state is followed by a collisional de-excitation, so that the excited states will be populated according to the Boltzmann equilibrium:

$$\frac{N_j}{N_i} = \frac{g_j}{g_i} \exp\left(\frac{-E_{ij}}{kT_e}\right) \tag{1.9}$$

The flux ratio in the high density limit is therefore given by

$$R_{\mathrm{SII,high}} \simeq \frac{A_{31}}{A_{21}} \frac{g_3}{g_2} \exp\left(\frac{-E_{23}}{kT_e}\right) \simeq \frac{A_{31}}{A_{21}} \frac{g_3}{g_2} \tag{1.10}$$

The line flux ratio in the high density limit is primarily governed by the quantum mechanical properties of the ion, and for S+ is $R_{\mathrm{SII,high}} \simeq 0.45$.

In the high density limit, F_{31} and F_{21} scale linearly with n_e because $N_i \propto N_1$ and therefore $N_i \propto n_{S+} \propto n_e$. In the low density limit, the population ratios also depend on the collisional excitation rates and therefore the line fluxes scale with n_e^2. As a result, R_{SII} traces a double exponential shaped profile, decreasing from $R_{\mathrm{SII}} \simeq 1.45$ at the low density limit to $R_{\mathrm{SII}} \simeq 0.45$ at the high density limit.

The locations of the high and low density limits are determined by the critical density at which the probability of collisional de-excitation and radiative de-population from the second to the first excited state are equal:

$$\begin{aligned} A_{32} = C_{32} &= n_{e,crit} \frac{\beta\ \Omega_{32}}{g_3} T_e^{-1/2} \\ n_{e,crit} &= T_e^{1/2} \frac{A_{32}\ g_3}{\beta\ \Omega_{32}} \end{aligned} \tag{1.11}$$

The critical density scales with $T_e^{1/2}$, and as a result there is a weak positive correlation between n_e and T_e at fixed R_{SII}.

1.4.2 Using R_{SII} to Measure H II Region Electron Densities

The relationships outlined above can be used to calculate the electron density of a homogeneous slab of gas illuminated by a spatially uniform radiation field. However, H II regions are inhomogeneous and the temperature, density and ionization state of the gas all vary moving from the center to the outer boundary of the ionized region. These spatial variations and their impact on the emergent line ratios can be accounted for self-consistently using photoionization models.

The left-hand panel of Figure 1.7 shows relationships between R_{SII} and n_e that have been calculated by running plane-parallel H II region photoionization models at different (constant) electron densities, metallicities (colors) and ionization parameters (line styles) (described in Kewley et al. 2019). The metallicity is anti-correlated with T_e because metal lines are the primary source of cooling in the 10^4 K ISM. R_{SII} is only weakly dependent on metallicity/temperature (and even less dependent on ionization parameter), but is very

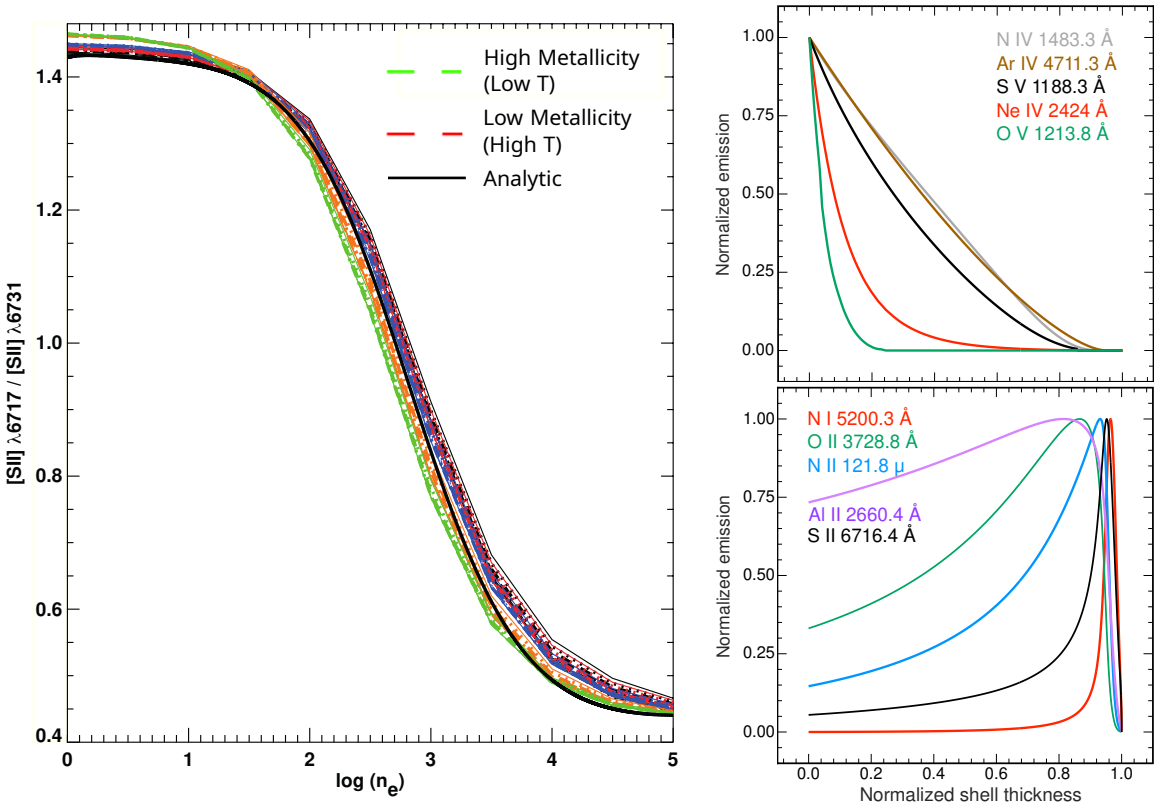

Figure 1.7: Outputs of plane-parallel H II region photoionization models. Left: $R_{\rm SII}$ as a function of n_e, for a range of metallicities (colors) and ionization parameters (line styles). The thick black line was calculated analytically assuming a constant T_e. Right: Normalized emission from high ionization (top) and low ionization (bottom) species as a function of radius from the central ionizing source. Figure adapted from Kewley et al. (2019).

sensitive to n_e in the range $n_e \sim 40$ – 5000 cm^{-3}, and is therefore a good probe of the conditions in H II regions which have typical electron densities of ~ 30 cm^{-3} at $z \sim 0$ and ~ 200 cm^{-3} at $z \sim 2$.

The model shown in Figure 1.7 assumes that n_e is constant throughout the nebula. However, there is observational evidence for strong negative n_e gradients in some H II regions (e.g. Binette et al., 2002; Phillips, 2007). It is therefore important to consider the spatial origin of the [S II]-emitting gas and whether its properties are representative of the average gas properties across the nebula. Sulfur exists as S+ for photon energies in the range 10.4 – 23.3 eV[1]. The lower end of this range is below the 13.6 eV ionization potential of both hydrogen and O+ (the latter of which has an associated doublet ratio that also serves as an n_e diagnostic), and therefore S+ is expected to originate primarily from dense clumps and from the partially ionized zone at the outer edge of the nebula (e.g. Proxauf

[1]NIST Atomic Spectra Database (ver. 5.7.1); https://physics.nist.gov/asd.

et al., 2014). This is illustrated in the right-hand panel of Figure 1.7, which shows the normalized emission from high ionization (top) and low ionization (bottom) species, both as a function of normalized distance from the ionizing source. If n_e decreases with distance from the center of the H II region, then the n_e measured from $R_{\rm SII}$ could under-estimate the true average n_e across the nebula.

A more meaningful description of the gas conditions is the thermal pressure $P_{\rm therm}$, which will not vary radially if the sound crossing time is shorter than the cooling and heating timescales; a condition that is expected to be met in the majority of H II regions (e.g. Field, 1965; Begelman, 1990). $P_{\rm therm}$ is proportional to $n_e T_e$, and as a result the relationship between $R_{\rm SII}$ and $P_{\rm therm}$ is strongly dependent on T_e. However, the need to assume (and measure) a constant T_e can be circumvented if the metallicity is known. Photoionization models account for metal line cooling and therefore naturally reproduce the variation in temperature structure as a function of metallicity. The thermal pressure can be calculated by running a photoionization model at the correct metallicity, computing $P_{\rm therm}$ as a function of $R_{\rm SII}$, and comparing the predicted $R_{\rm SII}$ to the measured $R_{\rm SII}$ (e.g. Kewley et al., 2019). As part of this thesis the redshift evolution of n_e and $P_{\rm therm}$ are compared to verify that possible systematic biases in the n_e measurements do not have a significant impact on the shape of the inferred electron density evolution.

1.5 Near Infrared Integral Field Spectroscopy

Sections 1.1 to 1.4 have outlined various lines of evidence to suggest that the growth and evolution of galaxies are strongly influenced by feedback processes and the gas conditions in H II regions. However, the detailed physics of the aforementioned feedback processes and how they affect the properties of the ISM remain unclear. As highlighted in Section 1.3, feedback is expected to be most efficient during the peak epoch of cosmic star formation and black hole growth ($1 \lesssim z \lesssim 3$), and therefore SFGs at these redshifts are valuable laboratories in which to study the physics of feedback and how it impacts the growth and evolution of galaxies.

The research presented in this thesis is primarily based on near infrared integral field spectroscopic observations of SFGs at $z \sim 2$. Integral field observations yield three dimensional 'datacubes' with two spatial dimensions and one spectral dimension, such that there is a spectrum for every spatial pixel ('spaxel') across the observed object. Spatially resolved spectroscopy is a crucial element of the work presented in this thesis for two main reasons. Firstly, robust measurements of outflow properties rely on the ability to distinguish between emission from outflowing material and emission from gas in the galaxy. This is typically achieved by fitting each emission line as a superposition of two Gaussian components – a narrow component tracing gas in the galaxy and a broader component tracing gas in the outflow. However, when spectra are integrated over large regions of galaxies, the presence of gravitationally driven velocity gradients causes the narrow emission from the galaxy to be smeared out in velocity space, decreasing the contrast between the galaxy and outflow components. With spatially resolved spectroscopy it is possible to measure

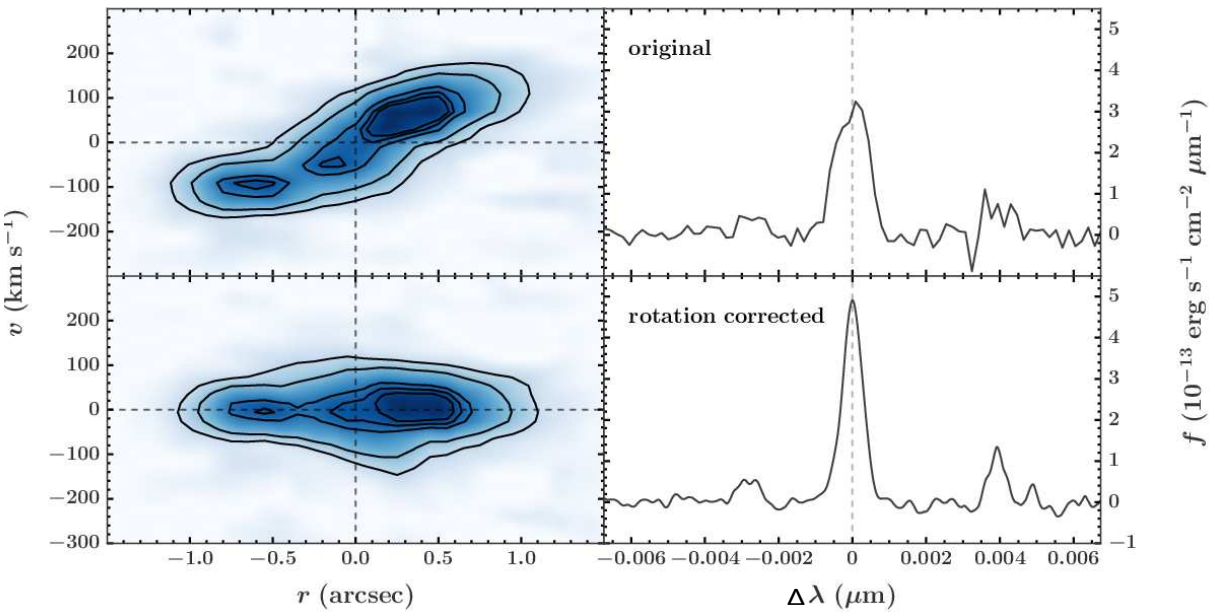

Figure 1.8: Position-velocity diagram (left) and integrated spectrum centered around the Hα emission line (right) of a star-forming galaxy with no outflow, before (top) and after (bottom) removing the disk rotation. Figure adapted from Swinbank et al. (2019).

and subtract the velocity field of the galaxy prior to summing the spectra, resulting in a sharper narrow component with a higher signal-to-noise ratio. This is illustrated in Figure 1.8, which compares the position-velocity diagram (left) and integrated spectrum (right) of a star-forming galaxy with no outflow, before (top) and after (bottom) subtracting the disk rotation. The velocity shifting technique maximizes the outflow detection fraction by pushing the detection limit to lower outflow velocities and luminosities, and is used in all three main chapters of this thesis. The second key benefit of integral field spectroscopy is the ability to map emission line fluxes, ratios, and kinematics across galaxies. Given integral field observations with sufficient depth and spatial resolution, the relationships between star formation, feedback processes, and ISM conditions can be studied on sub-galactic scales.

Typical SFGs at $z \sim 2$ have small angular (apparent) sizes and are relatively faint, meaning that very sensitive, high angular resolution integral field spectrographs are required to obtain resolved observations with a sufficient signal-to-noise ratio per resolution element in a reasonable integration time. As a result, direct empirical constraints on the driving mechanisms of outflows and their impact on the properties of the ISM in high-z SFGs have so far been quite scarce. The latest generation of integral field spectrographs has significantly improved the quality and quantity of the available data, providing both uniquely detailed high spatial resolution observations of modest samples (tens) of galaxies which can be used to study feedback physics, and lower spatial resolution observations of representative samples of hundreds of galaxies which facilitate statistical studies of outflow demographics and ISM properties across the galaxy population. These key new observa-

tional capabilities are at the foundation of the unique and timely research presented in this thesis.

The majority of the data used in this dissertation were obtained using two near infrared integral field spectrographs that have complementary capabilities: KMOS (Sharples et al., 2004, 2013; Davies et al., 2013), which is currently mounted on Unit Telescope 1 (UT1) of the *Very Large Telescope* (VLT) on Cerro Paranal in Chile, and SINFONI (Eisenhauer et al., 2003; Bonnet et al., 2004), which was mounted on VLT UT4 before being decommissioned in June 2019. KMOS and SINFONI operate at near infrared wavelengths of $\lambda \simeq 0.8 - 2.5$ μm. This wavelength range is of particular interest because many of the key emission lines used to probe star formation, ISM conditions and gas excitation (including Hα, [N II], [O III], Hβ, and [S II]) lie at rest frame wavelengths of $\lambda_{\rm rest} \sim 5000 - 7000$ Å. The expansion of the Universe causes the wavelengths of these photons to increase by a factor of $1 + z$ as they propagate from galaxies at $1 \lesssim z \lesssim 3$ to our telescopes, shifting them to the near infrared part of the spectrum.

The key feature of KMOS is the multiplexing capability which makes it an extremely powerful survey instrument. KMOS has 24 arms that each contain an integral field unit (IFU) and can be used to simultaneously observe up to 24 individual targets within the seven arcminute diameter patrol field of the instrument. Each IFU has a 2.8" × 2.8" field of view (FOV) and 0.2" × 0.2" spatial sampling. The instrument operates in seeing limited mode. The KMOS data used in this thesis were obtained as part of the KMOS$^{\rm 3D}$ survey, a 75 night program that targeted 740 galaxies at $0.6 \lesssim z \lesssim 2.6$ and provided the most complete census to date of star formation, gas kinematics and ISM properties across the galaxy population at the peak epoch of cosmic star formation (Wisnioski et al., 2015, 2019).

SINFONI has only a single IFU but can operate in either seeing limited or adaptive optics (AO) mode. The majority of the SINFONI observations used in this thesis were performed using the AO mode. During observations, light from a nearby reference source (either a bright star or a sodium laser) is fed to an optical wavefront sensor that measures distortions introduced by turbulence in the atmosphere. The distortions are removed from the science light beam by changing the shape of a deformable mirror up to 500 times per second. Without the AO correction, the typical FWHM of the point spread function (PSF) at near-infrared wavelengths and on high altitude sites like Cerro Paranal is 0.5". This corresponds to a physical resolution of 4 – 5 kpc at $z \sim 1 - 3$, which is comparable to the typical half light radii of massive galaxies at this epoch (e.g. van der Wel et al., 2014). In contrast, the AO data have a typical PSF FWHM of 0.2" ($\sim 1.5 - 2$ kpc). This is still an order of magnitude larger than the characteristic sizes of star-forming regions, but the factor of ~ 6 increase in the number of resolution elements per galaxy (over the seeing limited observations) enables detailed studies of feedback processes occurring on sub-galactic scales.

A large fraction of the SINFONI AO data used in this thesis were obtained as part of the SINS/zC-SINF AO survey, a survey of 35 SFGs at $1.5 \lesssim z \lesssim 2.5$ that aimed to place strong constraints on the physical processes governing disk structure and dynamics, bulge growth, and galactic winds (Förster Schreiber et al., 2018). The observations were conducted using the SINFONI 3" × 3" FOV with a spatial sampling of 0.05" × 0.05".

1.6 Outline of this Thesis

In this thesis, the state-of-the-art integral field spectroscopic data described in Section 1.5 are used to address several important questions regarding the physics of stellar and AGN feedback processes and their impact on the growth and evolution of galaxies:

1. *How do the velocities and mass loading factors of star formation driven outflows scale with the local properties at their launch sites? What does this reveal about the launching and driving mechanisms of the outflows?*

2. *How do outflows couple AGN accretion energy to gas in the interstellar medium and the circumgalactic medium? How does this coupling affect star formation in the host galaxy?*

3. *How do the electron densities in H II regions vary as a function of cosmic time? What is the role of star formation feedback in driving this evolution?*

Each of the main chapters of this dissertation addresses one of these sets of questions, as outlined below.

1. *How do the velocities and mass loading factors of star formation driven outflows scale with the local properties at their launch sites? What does this reveal about the launching and driving mechanisms of the outflows?*

The broad line emission associated with star formation driven outflows in SFGs at $z \sim 2$ tends to be co-spatial (in projection) with highly star-forming clumps, which are likely to be the launch sites of the outflows (e.g. Genzel et al., 2011; Newman et al., 2012a). This spatial coincidence makes it possible to study the relationships between the properties of the launch sites and the parameters of the resulting outflows. The predicted slope of the relationship between $\Sigma_{\rm SFR}$ and the outflow velocity $v_{\rm out}$ is strongly dependent on whether the outflows are powered by energy injection from stellar winds and supernovae ($v_{\rm out} \propto {\Sigma_{\rm SFR}}^{0.1}$) or by momentum injection through radiation pressure ($v_{\rm out} \propto {\Sigma_{\rm SFR}}^{2}$) (e.g. Strickland et al., 2004; Chen et al., 2010; Murray et al., 2005, 2011; Kornei et al., 2012). Therefore, empirical constraints on the scaling between $\Sigma_{\rm SFR}$ and $v_{\rm out}$ are a crucial element in the development of realistic sub-grid stellar feedback models for cosmological hydrodynamical simulations. Absorption line studies have examined the relationship between the integrated SFRs of galaxies and the average $v_{\rm out}$ of neutral and ionized material along the line of sight (e.g. Weiner et al., 2009; Kornei et al., 2012; Bordoloi et al., 2014; Rubin et al., 2014). However, the velocity of the outflowing material may change as it propagates from the launch site to the galaxy halo, and galaxy-to-galaxy variations in the spatial distribution and/or temporal evolution of both star formation and outflows will induce scatter in the relationship between the characteristic outflow velocity and the integrated SFR.

The SINS/zC-SINF AO survey provides integral field spectroscopy for 28 SFGs with no evidence of AGN activity at $z \sim 2 - 2.5$. The observations have a spatial resolution

of $\sim 1.5 - 2$ kpc, allowing the highly star-forming clumps to be robustly separated from the less active inter-clump regions. Chapter 2 presents the first systematic investigation into how the typical velocities and mass loading factors of star formation driven outflows vary across a large range of the environments found within typical $z \sim 2$ disks, spanning a factor of ~ 50 in $\Sigma_{\rm SFR}$. The most novel aspect of this study is that the star formation and outflow properties are measured from the [N II]+Hα emission line profiles of kpc scale regions that are stacked in bins of their local physical properties, rather than from galaxy-integrated spectra that each include emission from regions with a wide range of properties and may therefore smear out the intrinsic relationships between star formation and outflow properties. The results indicate that regions with higher $\Sigma_{\rm SFR}$ launch faster outflows with larger mass loading factors. By comparing the slope of the measured $\Sigma_{\rm SFR} - v_{\rm out}$ relation to model predictions, it is argued that the outflows are likely to be driven by a combination of mechanical energy from stellar winds and supernovae, and radiation pressure from massive stars.

2. *How do outflows couple AGN accretion energy to gas in the interstellar medium and the circumgalactic medium? How does this coupling affect star formation in the host galaxy?*

There is a growing consensus that AGN feedback is required to explain the low efficiency of star formation in high mass halos, but it remains unclear how the AGN accretion energy couples with gas in the interstellar medium and the circumgalactic medium to quench star formation. There is some evidence to suggest that outflows driven by luminous quasars ($\log_{10}(L_{\rm AGN}/[{\rm erg\ s^{-1}}]) \gtrsim 46$) can eject large fractions of their host galaxy molecular gas reservoirs (e.g. Maiolino et al., 2012; Cicone et al., 2014; Brusa et al., 2015a; Tombesi et al., 2015) and suppress star formation as they propagate through galaxy disks (e.g. Cano-Díaz et al., 2012; Cresci et al., 2015; Carniani et al., 2016). However, quasars are rare and have short duty cycles (e.g. Boyle et al., 2000; Martini, 2004), and it is unclear to what degree they impact the overall properties of the galaxy population over long timescales. Outflows driven by more typical AGN at $z \sim 2$ ($\log_{10}(L_{\rm AGN}/[{\rm erg\ s^{-1}}]) \simeq 45$) have less extreme mass outflow rates, but still eject ionized gas at typical velocities of $\sim 1000 - 2000$ km s^{-1} and therefore deposit significant amounts of momentum and kinetic energy into galaxy halos (e.g. Genzel et al., 2014; Harrison et al., 2016; Leung et al., 2019; Förster Schreiber et al., 2019). These results favor 'preventive mode' AGN feedback as the primary mechanism for star formation quenching (e.g. Bower et al., 2017; Nelson et al., 2018; Pillepich et al., 2018), as opposed to an 'ejective' mode where substantial amounts of gas are removed from the host galaxy via winds. However, more high spatial resolution studies are required to better establish the mechanisms by which AGN driven outflows couple the AGN accretion energy to gas on nuclear, galactic and circumgalactic scales, and to determine how this coupling affects star formation, both in the host galaxy and in nearby companion galaxies.

Chapter 3 presents an in-depth study of the geometry, velocity and mass loading of the outflows and the kinematics and ionization state of the ISM in three AGN host galaxies at $z \sim 2.2$. This investigation is based on a combined total of 80 hours of KMOS and SINFONI

observations of these three targets, including deep [N II]+Hα observations in both seeing limited and AO assisted modes which are used to map the star formation, outflows, and ISM properties, and shallower [O III]+Hβ observations which provide important additional constraints on the outflow kinematics and dust attenuation. The results suggest that AGN driven outflows can couple the AGN accretion energy to the ISM and potentially suppress star formation on scales ranging from a few hundred parsecs to $\gtrsim 5$ kpc. However, all three AGN host galaxies lie on the star-forming main sequence, indicating that any impact of the outflows on the overall instantaneous star formation activity of their host galaxies is likely to be limited.

3. *How do the electron densities in H II regions vary as a function of cosmic time? What is the role of star formation feedback in driving this evolution?*

Measurements of the [S II]λ6716/[S II]λ6731 ratio ($R_{\rm SII}$) suggest that the electron density of the [S II]-emitting gas in SFGs, n_e([S II]), has decreased by a factor of ~ 6 – 8 from $z \sim 2.5$ to $z \sim 0$ (e.g. Steidel et al., 2014; Sanders et al., 2016; Kaasinen et al., 2017; Kashino et al., 2017). There is significant circumstantial evidence to suggest that this evolution is linked to the strong decrease in the average level of star formation in galaxies over the same period of cosmic history (e.g. Shimakawa et al., 2015; Kaasinen et al., 2017; Jiang et al., 2019; Kashino & Inoue, 2019). The electron density could plausibly be set by stellar feedback (e.g. Groves et al., 2008; Krumholz & Matzner, 2009), but there are other possible reasons for n_e to be elevated in galaxies with enhanced star formation activity, such as higher gas densities in the parent molecular clouds, higher pressure in the ambient medium, or a larger fraction of young and over-pressured H II regions. One source of difficulty in determining what drives the observed $R_{\rm SII}$ evolution is that the [S II]-emitting material typically fills ~ 0.1 – 10% of the volume of H II regions (e.g. Osterbrock & Flather, 1959; Kennicutt, 1984; Hunt & Hirashita, 2009). It is unclear whether and how the properties of the small scale [S II]-emitting clumps are linked to the properties of the surrounding ambient medium and ultimately to the global level of star formation in galaxies.

Another complication is that [S II] emission can originate from H II regions, outflows, and/or diffuse ionized gas (DIG). Outflows are much more prevalent at $z \sim 2$ than at $z \sim 0$ (e.g. Steidel et al., 2010; Newman et al., 2012b; Förster Schreiber et al., 2019), and there is observational evidence to suggest that ionized outflows have a higher n_e than the ionized ISM of the galaxies driving the outflows (e.g. Förster Schreiber et al., 2019; Fluetsch et al., 2020). On the other hand, the DIG is much less dense than ionized gas in H II regions and contributes most significantly to the [S II] emission of galaxies at $z \sim 0$. Therefore, the observed $R_{\rm SII}$ evolution could potentially trace a change in the relative contribution of outflows and/or DIG to the observed [S II] emission over cosmic time.

Chapter 4 presents the most comprehensive study to date of the physical processes driving the redshift evolution of n_e([S II]) from $z \sim 2.6$ to $z \sim 0$, using a sample of 140 SFGs drawn primarily from the KMOS$^{\rm 3D}$ and SINS/zC-SINF surveys and distributed across three redshift slices ($z \sim 0.9$, 1.5 and 2.2), and 471 SFGs at $z \sim 0$ from the Sydney AAO Multi-object IFS (SAMI) survey. Galaxies with outflows are identified through visual

inspection of the integrated emission line profiles, which are constructed from velocity shifted datacubes to maximize the outflow detection fraction (as discussed in Section 1.5). The typical n_e([S II]) of H II regions at each redshift is measured by stacking the spectra of galaxies with no evidence of outflows or AGN activity, and the full sample of galaxies is used to examine the potential effects of redshift-dependent contamination from outflows. For the first time, Hα luminosity measurements are used to estimate the average number of electrons per unit volume across star-forming disks at different redshifts, bridging the gap between the small scale n_e([S II]) measurements and the global star formation properties of galaxies. The local and volume-averaged electron densities are found to evolve at similar rates, suggesting that the volume filling factor of the line-emitting gas is approximately constant across $0 \lesssim z \lesssim 2.6$. Finally, the n_e measurements are compared to quantitative predictions for several plausible drivers of the n_e evolution. The results suggest that the elevated electron densities in SFGs at $z \sim 2$ could plausibly be the direct result of higher gas densities in the parent molecular clouds, or could be a consequence of the greater ambient pressure resisting the expansion of the H II regions.

Chapter 2

Kiloparsec Scale Properties of Star Formation Driven Outflows at $z \sim 2.3$ in the SINS/zC-SINF AO Survey

This Chapter is a reprint of the ApJ publication *Kiloparsec Scale Properties of Star Formation Driven Outflows at $z \sim 2.3$ in the SINS/zC-SINF AO Survey* by Davies et al., 2019, ApJ, 873, 122. Published on March 12, 2019.

R. L. Davies performed the data analysis, developed the interpretation, and produced all of the text, figures, and tables presented in the main text and appendices of this publication.

This work is based on observations collected at the European Organisation for Astronomical Research in the Southern Hemisphere under ESO Programme IDs 075.A-0466, 079.A-0341, 080.A-0330, 080.A-0339, 080.A-0635, 081.A-0672, 081.B-0568, 183.A-0781, 087.A-0081, and 088.A-0209.

Abstract - We investigate the relationship between star formation activity and outflow properties on kiloparsec scales in a sample of 28 star forming galaxies at $z \sim 2 - 2.6$, using adaptive optics assisted integral field observations from SINFONI on the VLT. The narrow and broad components of the Hα emission are used to simultaneously determine the local star formation rate surface density ($\Sigma_{\rm SFR}$), and the outflow velocity $v_{\rm out}$ and mass outflow rate $\dot{M}_{\rm out}$, respectively. We find clear evidence for faster outflows with larger mass loading factors at higher $\Sigma_{\rm SFR}$. The outflow velocities scale as $v_{\rm out} \propto {\Sigma_{\rm SFR}}^{0.34\pm0.10}$, which suggests that the outflows may be driven by a combination of mechanical energy released by supernova explosions and stellar winds, as well as radiation pressure acting on dust grains. The majority of the outflowing material does not have sufficient velocity to escape from the galaxy halos, but will likely be re-accreted and contribute to the chemical enrichment of the galaxies. In the highest $\Sigma_{\rm SFR}$ regions the outflow component contains an average of ∼45% of the Hα flux, while in the lower $\Sigma_{\rm SFR}$ regions only ∼10% of the Hα flux is

associated with outflows. The mass loading factor, $\eta = \dot{M}_{\rm out}/{\rm SFR}$, is positively correlated with $\Sigma_{\rm SFR}$ but is relatively low even at the highest $\Sigma_{\rm SFR}$: $\eta \lesssim 0.5 \times (380\ {\rm cm}^{-3}/n_e)$. This may be in tension with the $\eta \gtrsim 1$ required by cosmological simulations, unless a significant fraction of the outflowing mass is in other gas phases and has sufficient velocity to escape the galaxy halos.

2.1 Introduction

Galaxy scale outflows are expected to play a major role in regulating the star formation and chemical enrichment histories of galaxies (e.g. Davé et al., 2012; Hopkins et al., 2012b; Vogelsberger et al., 2013; Hirschmann et al., 2013; Chisholm et al., 2017), mediating the co-evolution of galaxies and their central supermassive black holes (e.g. Silk & Rees, 1998; Fabian, 2012; King & Pounds, 2015), and setting the sizes of galaxy disks (e.g. Okamoto et al., 2005; Sales et al., 2010). Powerful winds driven by star formation and AGN activity transfer large amounts of mass and energy from galaxies to the surrounding circumgalactic medium (e.g. Peeples et al., 2014; Tumlinson et al., 2017), depleting the supply of cold gas available for star formation within galaxies and preventing the circumgalactic gas from cooling and falling back onto galaxies (e.g. Di Matteo et al., 2005; Springel & Hernquist, 2005; Croton et al., 2006; Hopkins et al., 2006; Somerville et al., 2008; Erb, 2015; Beckmann et al., 2017). Outflows are therefore thought to play an important role in driving the low baryon fractions of galactic disks (Dekel & Silk, 1986; Efstathiou, 2000; Sales et al., 2010). The cosmic stellar mass density peaks at ∼20% of the cosmic baryon density for a stellar mass of $\log(M_*/M_\odot) \sim 10.5$, and drops to ∼5-10% towards higher stellar masses (where black hole accretion feedback is most efficient) and lower stellar masses (where star formation feedback is most efficient) (e.g. Baldry et al., 2008; Moster et al., 2013; Moustakas et al., 2013; Behroozi et al., 2013).

Star formation driven outflows are expected to have the biggest impact on galaxies at $z \sim 1 - 3$, during the peak epoch of star formation (see Madau & Dickinson, 2014, and references therein). Blueshifted absorption components are ubiquitous in the rest-frame UV spectra of $z \sim 2$ star forming galaxies, revealing extended (tens of kiloparsec) reservoirs of diffuse outflowing material expelled from galaxies over long periods of time (e.g. Shapley et al., 2003; Weiner et al., 2009; Rubin et al., 2010; Steidel et al., 2010; Erb et al., 2012; Kornei et al., 2012; Bordoloi et al., 2014). Broad high velocity components in the rest-frame optical emission line spectra of star forming galaxies trace denser outflowing material within a few kiloparsecs of the launching points of the outflows. These emission components provide an instantaneous snapshot of the current outflow activity and are seen in ∼ 10-30% of star forming galaxies at $z \sim 2$ (when AGN host galaxies are explicitly excluded; Genzel et al., 2011; Newman et al., 2012b; Freeman et al., 2019; Förster Schreiber et al., 2019). Despite the prevalence of star formation driven outflows at high redshift, there are few quantitative constraints on their physical properties.

Many studies have reported trends between the velocities of star formation driven outflows and the global M_*, SFR and/or $\Sigma_{\rm SFR}$ of their host galaxies (e.g. Rupke et al.,

2005; Martin, 2005; Weiner et al., 2009; Rubin et al., 2010; Steidel et al., 2010; Erb et al., 2012; Kornei et al., 2012; Newman et al., 2012b; Talia et al., 2012; Arribas et al., 2014; Bordoloi et al., 2014; Rubin et al., 2014; Chisholm et al., 2016; Heckman & Borthakur, 2016; Sugahara et al., 2017; Förster Schreiber et al., 2019). Correlations between the outflow velocity $v_{\rm out}$ and star formation properties arise naturally because the level of star formation activity determines the amount of energy injected into the ISM by supernovae, stellar winds and radiation pressure from massive stars (e.g. Chevalier & Clegg, 1985; Strickland et al., 2004; Murray et al., 2011). The stellar feedback combines with the turbulence driven by disk instabilities to counteract the disk gravity and launch outflows (see e.g. Ostriker & Shetty, 2011; Krumholz et al., 2018). The galaxy stellar mass drives the depth of the local potential which decelerates the outflowing material, but is also positively correlated with the SFR (e.g. Brinchmann et al., 2004; Elbaz et al., 2007; Noeske et al., 2007; Peng et al., 2010b; Whitaker et al., 2014) which determines the amount of energy available to accelerate the outflowing material.

It is important to accurately characterise the SFR-$v_{\rm out}$ and $\Sigma_{\rm SFR}$-$v_{\rm out}$ relationships, because their scalings provide constraints on the primary outflow driving mechanism(s). If the outflows are driven by mechanical energy from supernovae and stellar winds, the outflow velocity is predicted to be weakly dependent on the level of star formation activity ($v_{\rm out} \propto {\Sigma_{\rm SFR}}^{0.1}$; Strickland et al. 2004; Chen et al. 2010, $v_{\rm out} \propto {\rm SFR}^{0.2-0.25}$; Ferrara & Ricotti 2006; Heckman et al. 2000). On the other hand, if the outflows are radiatively driven, the outflow velocity is predicted to scale strongly with the level of star formation ($v_{\rm out} \propto {\Sigma_{\rm SFR}}^{2}$; Murray et al. 2011; Kornei et al. 2012, $v_{\rm out} \propto {\rm SFR}$; Sharma & Nath 2012). If the dominant outflow driving mechanism varies within individual galaxies, the power law scaling will be intermediate between the energy and momentum driven cases.

The slopes of the $\Sigma_{\rm SFR}$-$v_{\rm out}$ and SFR-$v_{\rm out}$ relations remain a matter of debate. Some studies report relatively flat power law scalings with indices of 0.1-0.15 (e.g. Chen et al., 2010; Arribas et al., 2014; Chisholm et al., 2016), while other studies report somewhat steeper scalings with power law indices of 0.25-0.35 (e.g. Martin, 2005; Weiner et al., 2009; Heckman & Borthakur, 2016; Sugahara et al., 2017). The discrepancies between different scalings reported in the literature are likely to originate from differences in the observed outflow tracers, adopted definitions of $v_{\rm out}$, and range of probed outflow velocities (see discussions in e.g. Kornei et al. 2012; Heckman & Thompson 2017).

The relationship between the level of star formation activity and the incidence and properties of outflows has, for the most part, only been investigated using galaxy integrated values. However, high spatial resolution observations of high SFR galaxies (both at $z \sim 2$ and in the local universe) indicate that star formation driven outflows are launched from small ($\sim$ 1 kpc) regions coincident with the most intense star formation events (Shopbell & Bland-Hawthorn, 1998; Genzel et al., 2011; Newman et al., 2012a; Bolatto et al., 2013). Therefore, it may not be the global level of star formation which is most relevant for shaping the outflow properties, but the *local* level of star formation. Bordoloi et al. (2016) found that the properties of the outflowing material along different lines of sight to a lensed galaxy at $z \sim 1.7$ are correlated with the properties of the nearest star forming region, suggesting that the outflows are indeed 'locally sourced'. On the other hand, James

et al. (2018) found that the strongest outflow in a lensed galaxy at $z \sim 2.38$ is associated with the most diffuse star forming region, suggesting that the outflow is 'globally sourced'. Systematic studies of larger galaxy samples are required to conclusively determine whether the properties of star formation driven outflows are more strongly dependent on global or local galaxy properties.

In this paper, we investigate the relationship between resolved ∼1-2 kpc scale (0.15-0.25") star formation activity and the incidence and properties of outflows in a sample of 28 star forming galaxies at $z \sim 2.3$ from the SINS/zC-SINF AO Survey (Förster Schreiber et al., 2018). We build on the work of Newman et al. (2012b), who explored the relationship between *global* galaxy properties and the incidence and velocity of outflows in a similar sample of galaxies to the one used in this paper, and the work of Genzel et al. (2011) and Newman et al. (2012a), who performed detailed analyses of the star formation and outflow properties of individual star forming clumps in 5 SINS/zC-SINF AO galaxies, of which 3 are included in our sample. Here we extend these analyses to study outflow properties as a function of resolved physical properties across 28 galaxies, considering not only the highly star forming clump regions but also the less active inter-clump regions.

The outline of the paper is as follows. We probe the star formation and outflow properties on ∼0.17" scales using adaptive optics assisted integral field observations of the Hα emission line (described in Section 2.2). We stack the spectra of individual spaxels of the integral field datacubes to create high signal-to-noise (S/N) spectra in bins of resolved physical properties, and perform single and multi-component emission line fitting to analyse the properties of the outflow component in individual stacks (described in Section 2.3). We explore which physical properties are most closely linked to the presence of outflows in Section 2.4, and present more detailed results on the relationship between the local $\Sigma_{\rm SFR}$ and the incidence and properties of outflows in Section 2.5. The implications of our findings are discussed in Section 2.6 and our conclusions are presented in Section 2.7.

Throughout this work we assume a flat ΛCDM cosmology with $H_0 = 70$ km s^{-1} Mpc^{-1} and $\Omega_0 = 0.3$.

2.2 Data

2.2.1 Sample Overview

In order to investigate the kiloparsec scale properties of star formation and outflows in galaxies at $z \sim 2.3$, we utilise deep adaptive optics assisted near infrared integral field observations from the SINS/zC-SINF AO Survey (Förster Schreiber et al., 2018). All of our targets were observed in the K band (1.95-2.45μm) with the Spectrograph for INtegral Field Observations in the Near Infrared (SINFONI; Eisenhauer et al. 2003; Bonnet et al. 2004) on the Very Large Telescope (VLT). The K band observations span a rest-frame wavelength range of at least 6450-6950Å across the full redshift range of our sample. We use the Hα emission line at 6563Å as a tracer of both star formation and ionized gas outflows (see Sections 2.3.2 and 2.4). In this section we present an overview of the SINS/zC-SINF

AO sample, and refer the reader to the indicated survey papers for further information.

The SINS/zC-SINF AO Survey targeted 36 star forming galaxies at $z \sim 1.5 - 2.5$ with SINFONI. The 36 galaxies were drawn from the Spectroscopic Imaging survey in the Near-infrared with SINFONI (SINS; Förster Schreiber et al., 2009) and the zCOSMOS-SINFONI survey (zC-SINF; Mancini et al., 2011), which together provided seeing limited (0.5-0.6" resolution) Hα observations for 110 star forming galaxies with stellar masses in the range $2\times10^9 - 2\times10^{11} M_\odot$. The SINS and zC-SINF parent samples were selected from spectroscopically confirmed subsets of several imaging surveys, using a range of criteria to probe different star forming populations at high redshift (K band and 4.5μm flux selection, sBzK color selection, and the optical BX/BM criteria). The final targets were required to have a secure optical spectroscopic redshift, with the Hα line falling in a region of the SINFONI H or K band filter relatively free of contamination from OH lines. 17 SINS galaxies and 19 zC-SINF galaxies with suitable AO reference stars were chosen for AO follow up, with some preference given to brighter targets (integrated Hα flux $\gtrsim 10^{-16}$ erg s^{-1} cm^{-2}). The full width at half maximum (FWHM) of the point spread function (PSF) for the AO observations ranges from 0.15-0.25" (median 0.17", or $\sim$1.4 kpc physical size), and the pixel scale in the final datacubes is 0.05". The spectral resolution of the observations, measured from sky lines in the unsubtracted data cubes, is $R = 3530$ (FWHM = 85 km s^{-1}; see Appendix B of Förster Schreiber et al. 2018).

The AO sample is representative of the no-AO SINS + zC/SINF parent sample, and covers well the bulk of the $z \sim 2$ star forming galaxy population in the $M_* - \mathrm{SFR}$ and $M_* - R_e$ planes, over 2 orders of magnitude in M_*. Figure 2.1 shows the $M_* - \mathrm{SFR}$ distribution of the AO sample (circles and squares), compared to the underlying star forming galaxy population at $1.4 < z < 2.6$ (green contours) and the main sequence of star forming galaxies at $z \sim 2.3$ (Whitaker et al. 2014, black solid line). Due to the requirement for a pre-existing spectroscopic redshift, redder galaxies are underrepresented and there is some bias towards higher SFRs at low M_*. There is no particular size bias in the sample. More detailed discussions of the sample properties can be found in Förster Schreiber et al. (2018) and Tacchella et al. (2015a).

In this work, we focus on the K band subset of the SINS/zC-SINF AO Survey (33 galaxies at z = 2-2.5). The high resolution AO observations are key for analysing the relationship between star formation properties and outflow properties on kiloparsec scales. Five galaxies were removed from the sample because of evidence for AGN activity (based on mid infrared, X-ray, radio and/or optical emission line indicators) which could significantly contaminate the Hα SFRs. Our final sample consists of 28 galaxies (indicated by the markers with red centers in Figure 2.1) which span 1.4 dex in stellar mass ($9.4 \leq \log(M_*/M_\odot) \leq 10.8$, median $\log(M_*/M_\odot) = 10.1$) and 1.8 dex in main sequence offset ($-0.8 \leq \log(\mathrm{SFR}/\mathrm{SFR}_{MS}) \leq 1.0$, median $\log(\mathrm{SFR}/\mathrm{SFR}_{MS}) = 0.3$).

2.2.2 Global Galaxy Properties

The global stellar masses, SFRs and visual extinctions (A_V) towards all the galaxies in our sample were calculated using standard Spectral Energy Distribution (SED) fitting

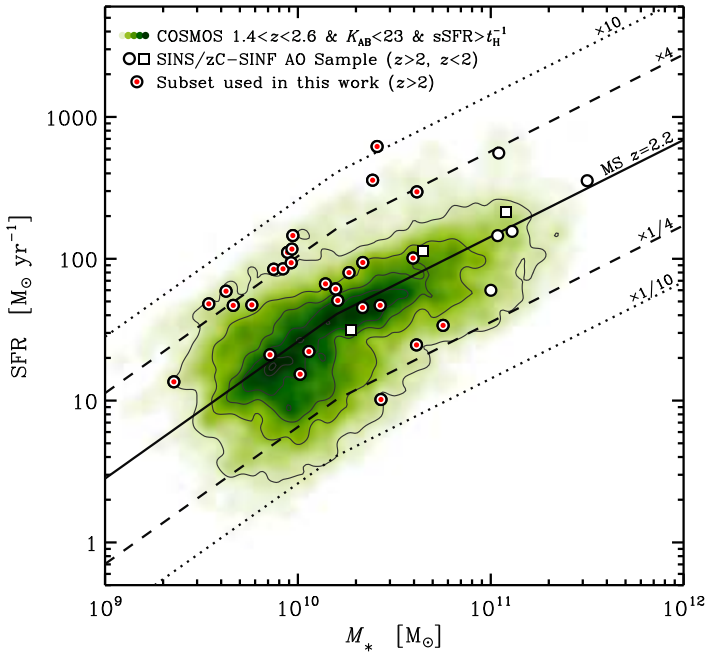

Figure 2.1: Distribution of the SINS/zC-SINF AO sample in the M_*-SFR plane. Galaxies at $z > 2$ and $z < 2$ are indicated by circles and squares, respectively. Markers with red centers indicate the subset of galaxies used in this paper (galaxies at $z > 2$ with no evidence for AGN activity). The green contours trace the density distribution of star forming galaxies in the COSMOS field which lie in the redshift range $1.4 < z < 2.6$ and have $K_{S,AB} < 23$ and inverse specific SFR lower than the Hubble time at the redshift of each object (Ilbert et al., 2009; Wuyts et al., 2011a). The solid line indicates the main sequence of star forming galaxies at $z \sim 2.3$ from Whitaker et al. (2014), and the dashed and dotted lines indicate SFRs offset from the main sequence by factors of 4 and 10, respectively.

procedures, described in Förster Schreiber et al. (2009) and Mancini et al. (2011). In brief, the optical-to-NIR broad-band SEDs (plus the mid-IR 3-8μm photometry when available) were fit with Bruzual & Charlot (2003) stellar population models, assuming the Chabrier (2003) IMF, solar metallicity, the Calzetti et al. (2000) reddening law, and constant or exponentially declining star formation histories. The galaxy ages were restricted to be between 50 Myr and the age of the universe at the redshift of each object.

The SINS/zC-SINF targets were drawn from several fields with varying photometric coverage, ranging from four to ten optical-to-NIR bands, supplemented with four-band IRAC 3-8μm data when available (as summarised by Förster Schreiber et al. 2009, 2011; Mancini et al. 2011). More specifically, the SED modelling for the zCOSMOS targets (16/28 galaxies) was based on 10 band optical-to-NIR photometry from Subaru and CFHT (Capak et al., 2007; McCracken et al., 2010) and IRAC 3-8μm photometry (Ilbert et al., 2009). For the BX targets (7/28 galaxies) we used the ground based $U_n GRJK_S$ photometry presented in Erb et al. (2006b), supplemented with HST H_{160} measurements from Förster Schreiber et al. (2011) for three of these objects. One BX target lacked NIR ground-based

data but was among the sources imaged in H-band with HST. The SED modelling for the GMASS targets (2/28 galaxies) was based on photometry from HST ($BVIZ$), VLT (JHK_S) and IRAC (3-8μm) (Kurk et al., 2013). For the K20 targets (2/28 galaxies) we used the B-8μm photometry from the FIREWORKS catalogue (Wuyts et al., 2008), and for the one GDDS target we used the 7 band B-K_S photometry from the Las Campanas Infrared Survey (Chen et al., 2002; Abraham et al., 2004).

The effective radii, axis ratios and position angles of the galaxies in our sample were derived by fitting a single Sérsic component to either the HST F160W (H band) light distribution (when available; see Tacchella et al. 2015a) or the Hα flux distribution (see Section 2.3.1 and Förster Schreiber et al. 2018). The galaxy inclinations (i) were calculated directly from the axis ratios (q), using $i = \cos^{-1}(q)$.

2.3 Method

The emission line spectra of galaxies are superpositions of emission associated with different gas components. In normal star forming galaxies at $z \sim 2$, the Hα emission primarily traces star formation in the disk of the galaxy. In integral field data, the centroid of the emission line varies spatially, tracing the underlying orbital motions of the ionized gas. If the galaxy has an outflow, a broader (sometimes blue-shifted) Hα emission component will be superimposed on the emission from the star forming disk. The width and velocity offset of the outflow component are tracers of the outflow velocity (e.g. Rupke et al., 2005; Veilleux et al., 2005; Genzel et al., 2011), while the total flux in the outflow component is a tracer of the outflowing mass (e.g. Genzel et al., 2011; Newman et al., 2012a).

A first order estimate of the strength and width of the outflow component can be obtained by fitting a single Gaussian component. If there is no outflow component, the measured σ will be defined by the core of the line profile, but if there is significant flux in the wings of the emission lines, the best fit Gaussian will broaden to include some of this flux (see also Förster Schreiber et al., 2018). Not all of the flux in the wings will be captured by a single Gaussian fit, and therefore the measured σ will provide a lower limit on the velocity dispersion of the outflow component (σ_b). More accurate measurements of the flux and kinematics of the outflow component can be obtained by fitting the Hα line profile as a superposition of two Gaussian components (e.g. Shapiro et al., 2009; Genzel et al., 2011; Newman et al., 2012b,a; Förster Schreiber et al., 2014; Leung et al., 2017; Freeman et al., 2019; Förster Schreiber et al., 2019).

We characterise the variation in outflow properties as a function of local physical properties across the SINS/zC-SINF AO galaxies by shifting the spectra of individual spaxels to remove large scale velocity gradients across the galaxies, splitting the spectra into bins in a range of physical properties (SFR, $\Sigma_{\rm SFR}$, Σ_*, $\Sigma_{\rm SFR}/\Sigma_*$, A_V, and R/R_e), and creating high S/N stacks of the spectra in each bin. We use single component Gaussian fits to investigate the relationships between these six physical quantities and the presence of outflows. We find that the line width is primarily determined by the level of star formation (probed by the SFR and $\Sigma_{\rm SFR}$), but that Σ_* may also play an important role in modu-

lating the presence and properties of outflows. We focus our more detailed investigation on $\Sigma_{\rm SFR}$, because it is directly linked to the star formation processes which provide the energy to drive the outflows, and because it is normalised by area, making it easier to consistently compare with measurements at different spatial scales than the SFR. We use two component Gaussian fitting to quantify the relationships between $\Sigma_{\rm SFR}$ and the incidence, velocity and mass loading factor of outflows.

The assumption that the star formation and outflow components are well represented by Gaussian profiles is justified by the central limit theorem, because the star formation component is an average over many H II region spectra, and the outflow component is an average over many outflow spectra (see also Förster Schreiber et al., 2019). The validity of the assumption is also confirmed empirically - we find that the emission line profiles of stacks with no evidence for broad emission are well fit by a single Gaussian component (see also Genzel et al., 2011), and the line profiles of stacks with clear broad wings are well fit by two Gaussian components, with no evidence for strong asymmetries or blueshifts in the outflow components (see Section 2.5.2).

2.3.1 Mapping Physical Properties Across Galaxies

Hα Flux Maps

Hα flux, velocity and velocity dispersion (σ) maps for all of the galaxies in our sample are presented in Förster Schreiber et al. (2018), and the details of the line fitting are described in that paper. Briefly, the Hα line profiles were fit using the IDL emission line fitting code LINEFIT (Förster Schreiber et al., 2009; Davies et al., 2011). Before fitting, the datacubes were lightly smoothed by median filtering, both spectrally (over 3 spectral channels) and spatially (over boxes of 3×3 spatial pixels for 26/28 of the galaxies, and 5×5 spatial pixels for two large low surface brightness galaxies), to increase the S/N per spaxel. For each spaxel, the continuum was modelled as a straight line through spectral regions adjacent to the line region and free from skyline contamination. The Hα line was modelled as a single Gaussian convolved with the line spread function of SINFONI at the observed wavelength of the line. The spectral channels were inverse variance weighted to prevent strong sky residuals from biasing the fits. The errors on the fit kinematics and Hα flux were calculated from 100 Monte Carlo simulations, where the value of the spectrum at each wavelength was perturbed assuming a Gaussian distribution with a standard deviation given by the input error cube. Spaxels with Hα flux/error < 5 are masked in the final maps. Panel a) of Figure 2.2 shows the Hα flux map for the galaxy ZC405501, at the 0.05" pixel scale of the reduced data.

Galactocentric Distance Maps

The deprojected radial distance of each spaxel from the kinematic center of each galaxy is calculated using the galaxy position angle and axis ratio. We normalise the deprojected distance maps to the effective radii of the galaxies.

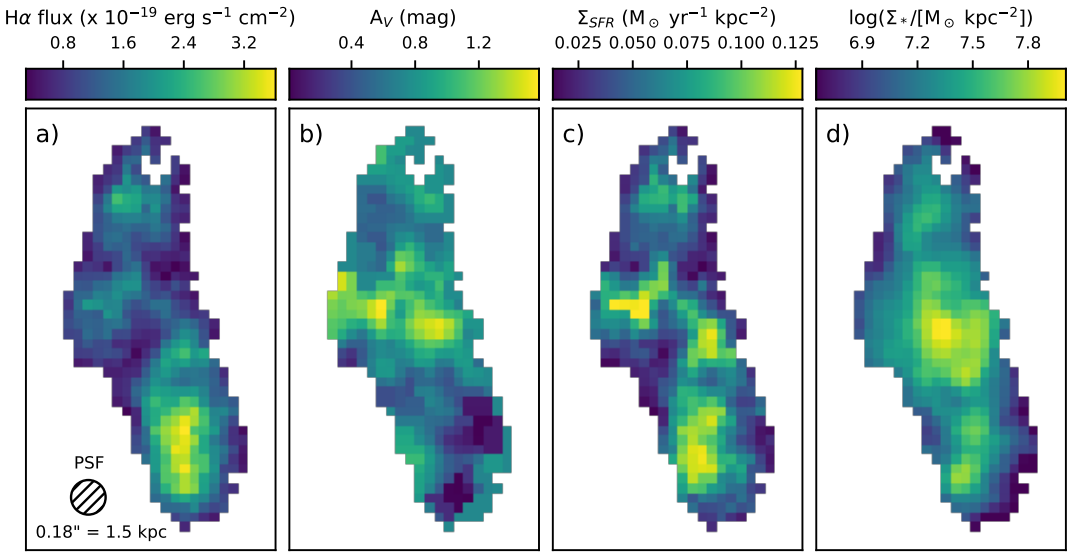

Figure 2.2: Maps of the Hα flux, A_V, $\Sigma_{\rm SFR}$ and Σ_* for ZC405501, at the 0.05" pixel scale of the reduced data. ZC405501 is at a redshift of $z = 2.154$, and has a stellar mass of $\log(M_*/M_\odot) = 9.9$ and a SFR of 85 $M_\odot$ yr^{-1}.

We also create maps of the circularized distance of each spaxel from the centre of each galaxy. The circularized radius r_{circ} is defined as the radius of the circle whose area equals the area of the ellipse with major axis radius r and minor axis radius $r \times q$ (where q is the axis ratio of the galaxy). The major axis radius is the same as the deprojected radius by definition, and therefore $r_{circ} = r_{deproj}\sqrt{q}$.

A_V and $A_{H\alpha}$ Maps

At $z \sim 2$, the observed HST F438W (B) - F814W (I) color is a proxy for the rest frame FUV-NUV color, which probes the slope of the ultraviolet continuum and is therefore a good tracer of the dust attenuation. Tacchella et al. (2018) investigated the relationship between the FUV-NUV color and the A_V, using a grid of model SEDs from Bruzual & Charlot (2003). The model SEDs cover six different metallicities (Z = 0.0001-0.05), three different star formation histories (exponentially increasing, constant, and exponentially declining), and a range of attenuations (A_V = 0-6) and redshifts (z = 2-2.5). They considered galaxy ages between 10 Myr and 3.5 Gyr (the age of the universe at $z \sim 2$) and adopted the Calzetti et al. (2000) reddening law.

Tacchella et al. (2018) showed that there is a tight, redshift-dependent correlation between the FUV-NUV color and the A_V, and used this correlation to create A_V maps for the 10 SINS/zC-SINF AO galaxies with available HST F438W and F814W imaging. 6/10 of these galaxies are included in our sample. The HST maps have similar angular resolution to the AO Hα maps, and were resampled to the same pixel grid. The A_V map for ZC405501 is shown in panel b) of Figure 2.2.

For the 22/28 galaxies without available HST F438W and F814W imaging, it is not possible to directly measure the A_V towards each spaxel. Instead, we combine the average radial A_V profiles derived by Tacchella et al. (2018) with the global A_V values measured from the SED fitting (described in Section 2.2.2) to estimate the A_V towards each spaxel. Tacchella et al. (2018) used their 10 A_V maps to create average A_V profiles (in terms of the absolute circularized radius $r_{circ,kpc}$), in two bins of stellar mass. The lower mass ($\log(M_*/M_\odot) < 11$) bin is comprised entirely of the six galaxies from our sample with A_V maps. For each of the 22 galaxies in our sample without A_V maps, we adopt the average A_V profile of the $\log(M_*/M_\odot) < 11$ galaxies from Tacchella et al. (2018), and scale the profile by a constant factor so that the A_V averaged across the individual spaxels matches the global A_V measured for the galaxy.

There is growing evidence that high redshift star forming galaxies display negative radial attenuation gradients (see also e.g. Wuyts et al., 2012; Hemmati et al., 2015; Nelson et al., 2016a; Liu et al., 2017). Therefore, the radial dust corrections that we have applied should produce more accurate Hα luminosities than global dust corrections. However, a radial attenuation profile cannot account for azimuthal A_V variations driven by the clumpy distribution of star formation in high redshift galaxies. Furthermore, high mass galaxies are observed to have steeper A_V gradients than low mass galaxies. The six galaxies from which the average profile is constructed are biased towards the high mass end of our sample ($10.0 \leq \log(M_*/M_\odot) \leq 10.7$), and therefore the average A_V profile is likely to be steeper than the intrinsic A_V profiles of the lower mass galaxies. Better constraints on the A_V towards individual spaxels of our galaxies will be crucial for obtaining more accurate Hα luminosities in the future.

The spaxel A_V values were converted to $A_{H\alpha}$ values using Equation 5 of Tacchella et al. (2018), which assumes that the stellar extinction follows the Calzetti et al. (2000) curve and that the nebular extinction follows the Cardelli et al. (1989) curve. We assume that the ratio of the E(B-V) for the stellar continuum to the E(B-V) for the nebular emission lines ($f_{*/\mathrm{neb}}$) is 0.7 (rather than $f_{*/\mathrm{neb}} = 0.44$ which is adopted in the local universe; Calzetti et al. 2000). This choice is motivated by the results of Tacchella et al. (2018), who showed that adopting $f_{*/\mathrm{neb}} = 0.7$ produces better agreement between the UV and Hα SFRs than $f_{*/\mathrm{neb}} = 0.44$, and Kashino et al. (2013), who measured $f_{*/\mathrm{neb}} = 0.7$-0.8 for star forming galaxies at $1.4 < z < 1.7$ in COSMOS. However, our main conclusions do not change if we adopt $f_{*/\mathrm{neb}} = 0.44$.

SFR and Σ_{SFR} Maps

The SFR and Σ_{SFR} maps were derived from the Hα flux maps as follows. The Hα fluxes were corrected for extinction using the calculated $A_{H\alpha}$ values, and converted to luminosities using the galaxy redshifts. The spaxel Hα luminosities were converted to SFRs using the Kennicutt (1998) calibration, adjusted to the Chabrier (2003) initial mass function (SFR $[M_\odot\ \mathrm{yr}^{-1}] = L_{\mathrm{H}\alpha}/[2.1{\times}10^{41}\ \mathrm{erg\ s}^{-1}]$). Finally, the SFRs were divided by the deprojected area of each pixel on the sky (accounting for galaxy inclination) to obtain Σ_{SFR} in units of $M_\odot\ \mathrm{yr}^{-1}\ \mathrm{kpc}^{-2}$. The Σ_{SFR} map for ZC405501 is shown in panel c) of Figure 2.2.

Σ_* Maps

Tacchella et al. (2015b) presented resolved stellar mass maps for 24/28 of the galaxies in our sample. They used HST F110W (J) - F160W (H) color maps to derive pixel mass to light ratios, assuming the Chabrier (2003) initial mass function, and multiplied the derived mass to light ratios by the pixel H band luminosities to obtain the stellar mass in each pixel. The stellar mass maps can be directly converted to Σ_* maps by dividing by the deprojected area of each pixel on the sky. The Σ_* map for ZC405501 is shown in panel d) of Figure 2.2.

The remaining 4/28 galaxies lack the F110W and/or F160W imaging required to calculate pixel mass to light ratios, and are not used in any analysis requiring Σ_* estimates. These four galaxies have intermediate stellar masses ($10.0 \leq \log(M_*/M_\odot) \leq 10.4$) and a range of SFRs ($10 - 620\ M_\odot\ \mathrm{yr}^{-1}$), and we show that the missing resolved stellar mass information is unlikely to bias our results (see Section 2.4).

2.3.2 Stacking

Creating Stacks

We stack the spectra of individual spaxels from the original (unsmoothed) datacubes in bins of the physical properties described above to create high S/N (Hα S/N = 60-170) stacks which can be used to study the relationships between those physical properties and outflow properties. Our datacubes contain a total of 9510 spaxels which have robustly measured kinematics and are therefore suitable for this analysis (see Section 2.3.1).

The spectrum of each spaxel is shifted and re-sampled so that the centroid of the Hα line is at zero velocity and the spectral channels have a width of 30 km s^{-1} (which is close to the initial velocity sampling of $\sim$30-40 km s^{-1}). The spaxels are divided into bins based on the physical property of interest. Each spaxel is assigned a single weight which is applied to all spectral channels. The weight is given by the inverse of the root mean square (rms) value of the line free channels (more than 40Å from the center of the Hα line and more than 30Å from the center of the [S II]$\lambda\lambda$6716,6731 doublet). From the spaxels in each bin, a stack is created by computing the weighted average of the spectra, subtracting a constant continuum value (given by the median value of the line free channels), and normalizing to a maximum value of 1. We also create 'unweighted' stacks (where all spaxels are given a weighting of 1), but find that the choice of weighting scheme does not impact our main conclusions.

The errors on the stacked spectra are calculated using bootstrapping. For each bin, we randomly draw half of the spaxels and stack them, and repeat the process 100 times so that we have 100 bootstrap stacks. The error on each spectral channel of the final stack is then given by the standard deviation of the values of the 100 bootstrap stacks for that channel.

Quantifying Outflow Properties

We quantify the strength and properties of the outflow component in each stack by fitting each of the Hα and [N II] lines with either one Gaussian component, or a superposition of two Gaussian components - a narrow component tracing the gas in the star forming regions, and a broader component tracing the outflows. We stress that although we sometimes refer to the outflow component as the 'broad' component, the velocity dispersion of this component is $\lesssim 300$ km s^{-1} and it is therefore much narrower than the broad components associated with e.g. AGN driven outflows or broad line regions.

When an outflow component is present, the base of the Hα line can become blended with the bases of the [N II]λ6548 and [N II]λ6584 lines which lie at separations of -670 km s^{-1} and +940 km s^{-1}, respectively. It is therefore necessary to fit the two [N II] lines simultaneously with Hα. In our fitting, we assume that all three lines have the same kinematics; i.e. for each Gaussian component all lines have a common velocity shift and velocity dispersion.

The emission line fitting is performed using the Python module EMCEE (Foreman-Mackey et al., 2013), an Affine Invariant Markov Chain Monte Carlo (MCMC) Ensemble Sampler. The MCMC provides the posterior probability distribution for each of the parameters, as well as the joint posterior probability distribution for each pair of parameters, allowing us to ensure that the parameters of interest (namely the Hα amplitude(s) and the velocity dispersion(s)) are well constrained and not degenerate with each other or other parameters in the fit. This is particularly important when fitting two kinematic components as multiple solutions may be possible (see also discussion in Freeman et al. 2019).

We adopt uniform priors on all model parameters, limiting them to ranges which are physically reasonable. Specifically, the parameters are limited to the following ranges: velocity shifts $|\Delta v| < 200$ km s^{-1}, velocity dispersion of the narrow component (σ_n) greater than 36 km s^{-1} (the spectral resolution of the data), velocity dispersion of the outflow component (σ_b) greater than 150 km s^{-1} (to minimise contamination from beam smearing; see Appendix 2.8), and line amplitudes greater than zero. The ratio of the amplitudes of the two [N II] lines ([N II]λ6584/[N II]λ6548) in each component is fixed to 3 (the theoretical value set by quantum mechanics), but the [N II]/Hα ratio is left as a free parameter.

We run the MCMC with 400 walkers, 400 burn-in steps and 1200 run steps, based on the calculated auto-correlation times for the fit parameters (110-120 steps). For each parameter, the best fit value is defined as the peak of the posterior probability distribution, and the 68 per cent confidence interval is defined as the smallest interval containing 68 per cent of the probability.

Calculating the Average $\Sigma_{\rm SFR}$ for Each Stack

To first order, the average $\Sigma_{\rm SFR}$ for each stack is simply given by the average of the $\Sigma_{\rm SFR}$ values of the spaxels that went into the stack. However, the $\Sigma_{\rm SFR}$ values measured for individual spaxels are somewhat biased. For the vast majority of spaxels it is not possible to robustly separate the star formation and outflow components, even when S/N(Hα) > 5.

Therefore, we calculate $\Sigma_{\rm SFR}$ using the single Gaussian Hα flux, which is robust and independent of S/N for S/N(Hα) > 5, regardless of the strength and width of the outflow component. However, in spaxels with significant outflow components, the single Gaussian Hα flux will be contaminated by emission from the outflow component and therefore $\Sigma_{\rm SFR}$ will be over-estimated relative to other spaxels (assuming that the dust extinction is not preferentially underestimated in regions with outflows).

We account for the contribution of the outflow component a-posteriori by calculating how much (on average) the measured $\Sigma_{\rm SFR}$ values of the spaxels in each stack are over-estimated. For each stack, we fit the Hα and [N II] lines with one Gaussian component and then with two Gaussian components. We calculate a 'correction factor', Hα(narrow)/Hα(1 comp). The denominator is the Hα flux from the single component fit, which is the biased value that was used to estimate $\Sigma_{\rm SFR}$ in Section 2.3.1. The numerator is the Hα flux of the narrow (star formation) component from the two component fit, which is the value that should be used to calculate the true $\Sigma_{\rm SFR}$.

The intrinsic average $\Sigma_{\rm SFR}$ for spaxels in each bin can therefore be calculated from the measured average $\Sigma_{\rm SFR}$ and the correction factor as follows:

$$\Sigma_{\rm SFR}({\rm intrinsic}) = \Sigma_{\rm SFR}({\rm measured}) \times \frac{{\rm H}\alpha\ ({\rm narrow})}{{\rm H}\alpha\ (1\ {\rm comp})} \tag{2.1}$$

The correction factors for our stacks range from 1.1 – 1.9. In the following sections, all quoted $\Sigma_{\rm SFR}$ values have been corrected using Equation 2.1.

2.4 Dependence of Line Width on Resolved Physical Properties

We begin by investigating how the strength of the broad component relates to different physical properties. We consider four properties which are thought to be linked to star formation driven outflows (SFR in the spaxel, $\Sigma_{\rm SFR}$, Σ_* and $\Sigma_{\rm SFR}/\Sigma_*$), and two properties related to processes which could be potential sources of contaminating broad emission (A_V and galactocentric distance). The A_V probes the amount of dust along the line of sight. If there is a large amount of dust present, some of the Hα light may be scattered to different frequencies, inducing artificial broadening of the emission line (see e.g. Scarrott et al. 1991). The Hα line could also be artificially broadened by unresolved orbital motions (beam smearing). This effect is particularly prominent in the centers of massive galaxies where velocity gradients are the largest (e.g. Epinat et al., 2010; Davies et al., 2011; Newman et al., 2013).

Figure 2.3 shows how the shape of the Hα line varies as a function of SFR, $\Sigma_{\rm SFR}$, Σ_*, $\Sigma_{\rm SFR}/\Sigma_*$, A_V and R/R_e. These properties are known to correlate with one another, so we look for the property which shows the most pronounced correlation with the strength of the broad component. For each property, the spaxels are divided into two bins (above and below the median value listed in Table 2.1), and a stack is created for each bin as described

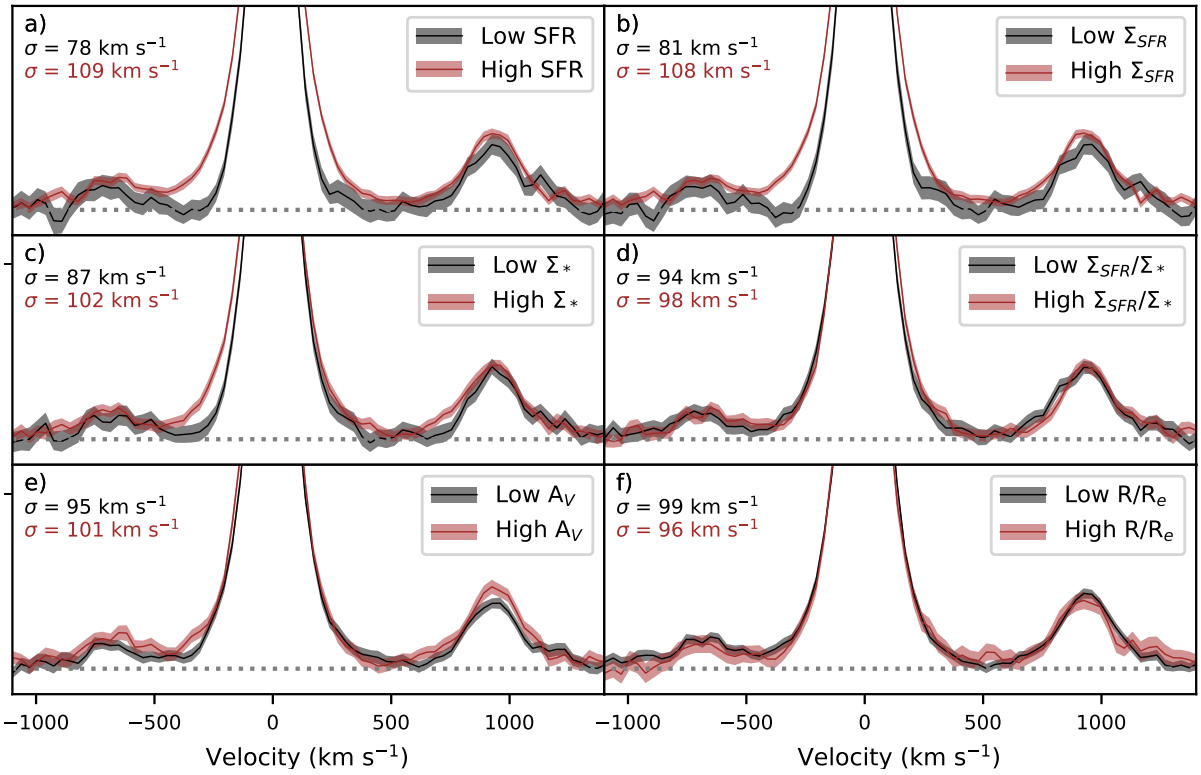

Figure 2.3: Spectra stacked in 2 bins of SFR (panel a), $\Sigma_{\rm SFR}$ (b), Σ_* (c), $\Sigma_{\rm SFR}/\Sigma_*$ (d), A_V (e) and R/R_e (f). The bins are divided by the median value of each property, listed in Table 2.1. All stacks are normalised to the same Hα amplitude. The filled regions represent the 1σ errors derived using bootstrapping. We fit a single Gaussian to the Hα and [N II] lines in each stack, and find that the line widths are primarily driven by the level of star formation (probed by the SFR and $\Sigma_{\rm SFR}$), although Σ_* may also play a significant role.

in Section 2.3.2. In each panel, the stack of spaxels above the median is shown in red, and the stack of spaxels below the median is shown in black. For each stack, the filled region indicates the 1σ error region.

We fit each of the Hα and [N II] lines in each stack with a single Gaussian, as described in Section 2.3.2. The velocity dispersions of the best fit Gaussians for all the stacks are listed in Figure 2.3. The differences between the σ values measured for the above and below median stacks for each property are listed in Table 2.1. All velocity dispersions quoted in this paper have been corrected for the spectral resolution (FWHM = 85 km s^{-1}). The formal uncertainties on the fit σ values are very small ($\sim$ 1 km s^{-1}), but do not account for the fact that a single component Gaussian model is sometimes not a good representation of the data (see also discussion at the beginning of Section 2.3), and therefore the uncertainties are not very meaningful.

Figure 2.3 shows that the shape of the emission line profiles is most strongly dependent on the level of star formation, probed by the SFR and $\Sigma_{\rm SFR}$ (panels a and b). The high SFR

Table 2.1: Quantities related to the pairs of stacked spectra in Figure 2.3.

Property	Median Value	$\Delta\sigma$ (km s^{-1})
SFR	0.08 $M_\odot$ yr^{-1}	31
Σ_{SFR}	0.19 $M_\odot$ yr^{-1} kpc^{-2}	27
Σ_*	$10^{7.78}$ $M_\odot$ kpc^{-2}	15
Σ_{SFR}/Σ_*	$10^{-8.4}$ yr^{-1}	4
A_V	0.93 mag	6
R/R_e	1.22	-3

The spaxels were divided into two bins for each of the properties in column 1, with one bin above and one bin below the median values in column 2. Column 3 lists the difference between the single component velocity dispersions fit to the above and below median stacks for each property.

stack shows a clear excess of flux at high velocities with respect to the low SFR stack, and the same is true for the $\Sigma_{\rm SFR}$ stacks. The measured velocity dispersions for the above and below median SFR stacks are σ = 109 km s^{-1} and 78 km s^{-1}, respectively, corresponding to $\Delta\sigma$ = 31 km s^{-1}. Similarly, the measured velocity dispersions for the above and below median $\Sigma_{\rm SFR}$ stacks are σ = 108 km s^{-1} and 81 km s^{-1}, respectively, corresponding to $\Delta\sigma$ = 27 km s^{-1}. The distribution of spaxels between the above and below median bins does not change significantly when dividing based on SFR or $\Sigma_{\rm SFR}$, because the SFRs of the spaxels in our sample vary by a factor of 50, but the deprojected areas of the pixels on the sky only vary by a factor of four. The $\Delta\sigma$ values measured for the SFR and $\Sigma_{\rm SFR}$ stacks are significantly larger than the $\Delta\sigma$ values measured for the Σ_*, $\Sigma_{\rm SFR}/\Sigma_*$, A_V and R/R_e stacks, suggesting that there is a direct link between the level of star formation activity and the strength of the broad emission component. This is consistent with predictions that the incidence and velocity of star formation driven outflows should increase with $\Sigma_{\rm SFR}$ (e.g. Thompson et al., 2005; Ostriker & Shetty, 2011; Faucher-Giguère et al., 2013; Hayward & Hopkins, 2017).

The shape of the emission line profiles also varies with Σ_* (panel c of Figure 2.3). The high Σ_* stack shows an excess of flux at high velocities compared to the low Σ_* stack, and we measure $\Delta\sigma$ = 15 km s^{-1} (48 per cent of the $\Delta\sigma$ between the SFR stacks). In contrast, we do not observe any significant trends in emission line width as a function of $\Sigma_{\rm SFR}/\Sigma_*$, A_V or R/R_e (panels d, e and f of Figure 2.3), and the measured $\Delta\sigma$ values are low (4, 6 and -3 km s^{-1}, respectively).

The absence of a strong correlation between A_V and σ indicates that scattered light cannot be the dominant source of broad emission in our sample. The absence of a strong correlation between galactocentric distance and σ indicates both that the broad component cannot originate primarily from beam smearing, and that the outflows are launched from a range of radii and are therefore unlikely to be AGN driven (as expected, because AGN

hosts were explicitly excluded from the sample). The impact of beam smearing on our results is further explored with the aid of dynamical models in Appendix 2.8.

We note that the Σ_* and $\Sigma_{\rm SFR}/\Sigma_*$ stacks include spectra from the 24/28 galaxies which have HST F110W and F160W imaging, whereas the SFR, $\Sigma_{\rm SFR}$, A_V and R/R_e stacks contain spectra from all 28 galaxies. To assess whether our results are biased by using different sets of galaxies in different stacks, we create SFR, $\Sigma_{\rm SFR}$, A_V and R/R_e stacks using the same 24/28 galaxies included in the Σ_* stacks, and repeat the single component Gaussian fits. The fit σ values change by a maximum of 3 km s^{-1}, indicating that our results are unlikely to be biased by the missing Σ_* measurements.

This analysis assumes that any variation in the measured σ is primarily attributable to variations in the strength and/or width of the outflow component, and is not driven by changes in the velocity dispersion of the narrow component, σ_n. The σ_n may be correlated with the level of star formation because energy injection from stellar feedback may contribute to increasing the turbulent pressure in the disk. Furthermore, Σ_* may be correlated with the gas surface density Σ_g, which regulates σ_n through the Toomre Q parameter (e.g. Förster Schreiber et al., 2006; Genzel et al., 2011; Krumholz et al., 2018). However, the pairs of stacks with the largest $\Delta\sigma$ values in Table 2.1 also have the most clearly visible differences in the strength of the broad wings in Figure 2.3, which verifies that the $\Delta\sigma$ is tracing real differences in the strength and width of the broad component, with only a minor secondary dependence on σ_n variations.

We conclude that the line width is primarily driven by the level of star formation (probed by the SFR and $\Sigma_{\rm SFR}$), but that Σ_* may also play a significant role in modulating the shapes of the line profiles (consistent with the results of Newman et al. 2012b). In this paper we choose to focus on $\Sigma_{\rm SFR}$, because it is directly linked to the star formation processes which provide the energy to drive the outflows, and because it is normalised by area, making it easier to consistently compare with measurements at different spatial scales than the SFR.

2.5 Outflow Properties as a Function of $\Sigma_{\rm SFR}$

We further quantify the difference between the line profiles of the low and high $\Sigma_{\rm SFR}$ stacks by fitting the [N II] and Hα lines as superpositions of two Gaussian components (as described in Section 2.3.2) and comparing the fit parameters. In particular, we focus on parameters which are used to calculate the outflow velocity and mass loading factor (see Sections 2.5.3 and 2.5.4): the ratio of the Hα flux in the broad component to the Hα flux in the narrow component (Hα broad flux ratio or BFR), and the velocity dispersion of the broad component (σ_b).

Figure 2.4 shows the two component fits to the above and below median $\Sigma_{\rm SFR}$ stacks (top panels), and the corresponding posterior and joint posterior distributions for the BFR and σ_b (bottom panels). It is clear that both stacks are well fit by a two component Gaussian. The fit residuals (grey) are generally smaller than the 1σ bootstrap errors on the spectra (purple shaded regions). The red shaded outflow components do not exhibit signif-

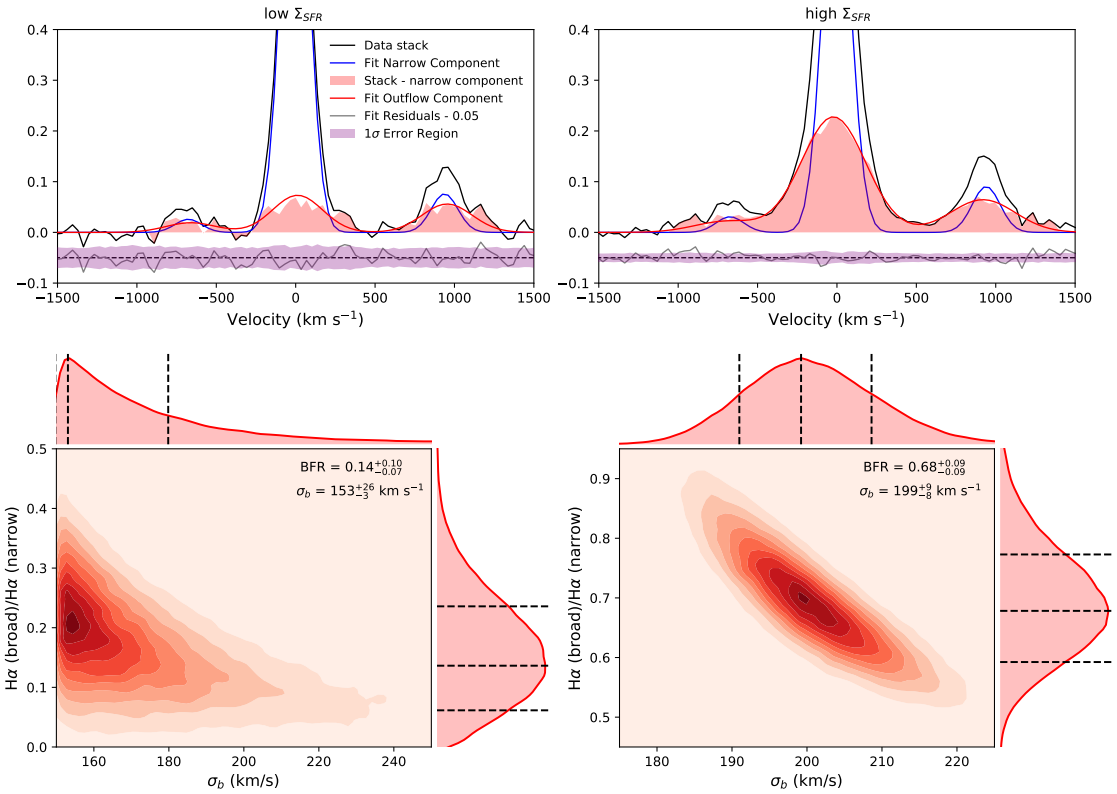

Figure 2.4: Two component Gaussian fits to the above and below median $\Sigma_{\rm SFR}$ stacks (top), and corresponding posterior and joint posterior distributions for the Hα broad-to-narrow flux ratio and the velocity dispersion of the broad component σ_b (bottom). In the top panels the stack spectra are shown in black, the best fit narrow components are shown in blue, the residuals after subtracting the fit narrow components from the stack spectra are shown by the pale red shaded regions, and the best fit outflow components are shown with red solid curves. The overall fit residuals are shown in grey and the 1σ error regions are shown in purple, and both are artificially offset below zero for clarity.

icant asymmetries and are not significantly offset in velocity space from the best fit narrow components, supporting our assumption that both the narrow and broad components are approximately Gaussian in shape.

The high $\Sigma_{\rm SFR}$ stack has a strong outflow component, with BFR = 0.68 ± 0.09 and $\sigma_b = 199^{+9}_{-8}$ km s^{-1}. The outflow parameters are well constrained and have approximately Gaussian posterior distributions. In contrast, the MCMC posteriors for the low $\Sigma_{\rm SFR}$ stack reveal that the outflow component contains a small fraction of the total Hα flux and is only marginally detected above the beam smearing limit of 150 km s^{-1}. The best fit parameters are $\sigma_b = 153^{+26}_{-3}$ km s^{-1} and BFR = $0.14^{+0.10}_{-0.07}$.

To further investigate how the properties of the outflow component vary as a function of $\Sigma_{\rm SFR}$, we split the above median $\Sigma_{\rm SFR}$ bin into 5 smaller bins and perform two component

Gaussian fitting on each of the resulting stacks. These 5 bins do not have equal numbers of spaxels - rather, they were chosen to span the range of observed $\Sigma_{\rm SFR}$ values with approximately even logarithmic spacing. The weighted average $\Sigma_{\rm SFR}$, fit parameters and derived outflow parameters for all stacks are listed in Table 2.2. In the following sections we explore trends between $\Sigma_{\rm SFR}$ and outflow properties.

2.5.1 Hα Broad-to-Narrow Flux Ratio (BFR)

Figure 2.5 shows the broad flux ratios measured for the above and below median $\Sigma_{\rm SFR}$ stacks (red circles) and for the five new $\Sigma_{\rm SFR}$ stacks (blue circles). The errors on the $\Sigma_{\rm SFR}$ values represent the 16th-84th percentile range of $\Sigma_{\rm SFR}$ values for the spaxels included in each stack, and the error bars on the BFR values represent the 68 per cent confidence intervals from the MCMC fitting.

The BFR increases from $\sim$ 0.15 at $\Sigma_{\rm SFR} < 0.2\ M_{\odot}\ {\rm yr}^{-1}\ {\rm kpc}^{-2}$ to $\sim$ 0.75 at $\Sigma_{\rm SFR} > 0.3\ M_{\odot}\ {\rm yr}^{-1}\ {\rm kpc}^{-2}$. The factor of 5 increase in the BFR over a small range in $\Sigma_{\rm SFR}$ suggests that outflows are only launched from regions with sufficiently high local $\Sigma_{\rm SFR}$.

Newman et al. (2012b) analysed the integrated spectra of many of the galaxies in our sample and found that outflows are only driven from galaxies with global $\Sigma_{\rm SFR}$ exceeding 1 $M_{\odot}\ {\rm yr}^{-1}\ {\rm kpc}^{-2}$ – a factor of 3-4 higher than the threshold local $\Sigma_{\rm SFR}$ suggested by our data. If outflows arise from the regions with the highest $\Sigma_{\rm SFR}$, then the average $\Sigma_{\rm SFR}$ across a galaxy with outflows should be lower than the $\Sigma_{\rm SFR}$ of the regions actually driving the outflows. The majority of the discrepancy can be explained by the difference between the extinction prescriptions adopted in Newman et al. (2012b) and in this work. In this work, we follow the methodology of Tacchella et al. (2018) who assume that the stellar extinction follows the Calzetti et al. (2000) curve and the nebular extinction follows the Cardelli et al. (1989) curve. We adopt $f_{*/{\rm neb}} = 0.7$, from which it follows that $A_{H\alpha} = 0.83\ A_V$. Newman et al. (2012b) assume that both the stellar and the nebular extinction follow the Calzetti et al. (2000) curve, and they adopt $f_{*/{\rm neb}} = 0.44$, from which it follows that $A_{H\alpha} = 1.86\ A_V$. If we adopt the same extinction prescription as Newman et al. (2012b), the median $\Sigma_{\rm SFR}$ of the spaxels in our sample increases by a factor of 2.2.

Another source of difference is the fact that Newman et al. (2012b) do not account for the contribution of the broad component to the measured Hα fluxes. If we did not apply the correction described in Section 2.3.2, our $\Sigma_{\rm SFR}$ values would be a factor of 1.5 higher. Therefore, the offset between our local $\Sigma_{\rm SFR}$ threshold and the global $\Sigma_{\rm SFR}$ threshold reported by Newman et al. (2012b) can be fully explained by differences in the adopted extinction prescription, and by the fact that they do not account for the contribution of the broad emission to the measured Hα fluxes.

2.5.2 Velocity Dispersion of the Broad Component (σ_b)

Figure 2.6 shows how the velocity dispersion of the broad component varies as a function of $\Sigma_{\rm SFR}$. The red shading at the bottom of the plot indicates the region at $\sigma_b < 150$ km s^{-1}

Table 2.2: Weighted average $\Sigma_{\rm SFR}$, fit parameters and derived outflow properties for each of the $\Sigma_{\rm SFR}$ stacks.

1) Σ_{SFR} ($M_\odot$ yr^{-1} kpc^{-2})	2) BFR	3) σ_b (km s^{-1})	4) Δv (km s^{-1})	5) $v_{\rm out}$	6) η	7) $\dot{E}_{out}/(10^{-3}\ L_{bol})$	8) $\dot{p}_{out}/(L_{bol}/c)$
Above and below median stacks							
0.11±0.07	$0.14^{+0.10}_{-0.07}$	153^{+26}_{-3}	9^{+7}_{-14}	296^{+54}_{-15}	0.05±0.03	0.05±0.03	0.09±0.04
$0.41^{+0.20}_{-0.23}$	0.68±0.09	199^{+9}_{-8}	-20±6	418^{+21}_{-15}	0.31±0.03	0.46±0.03	0.64±0.04
5 bin stacks							
0.25±0.04	$0.31^{+0.18}_{-0.09}$	180^{+40}_{-15}	-13±17	373^{+82}_{-35}	$0.13^{+0.05}_{-0.03}$	0.18±0.05	$0.28^{+0.05}_{-0.07}$
0.31±0.06	$0.73^{+0.33}_{-0.16}$	166^{+21}_{-7}	-22^{+8}_{-10}	355^{+43}_{-18}	$0.29^{+0.09}_{-0.05}$	0.35±0.05	$0.54^{+0.10}_{-0.07}$
0.45±0.07	$0.92^{+0.28}_{-0.11}$	183^{+13}_{-8}	-16±8	384^{+27}_{-18}	$0.40^{+0.07}_{-0.05}$	0.51±0.06	0.77±0.09
0.80±0.09	$0.62^{+0.18}_{-0.12}$	240^{+27}_{-18}	-24^{+13}_{-15}	504^{+56}_{-39}	$0.33^{+0.07}_{-0.04}$	$0.71^{+0.15}_{-0.07}$	0.85±0.10
$1.44^{+0.12}_{-0.52}$	$0.79^{+0.16}_{-0.11}$	263^{+20}_{-12}	-67^{+13}_{-16}	595^{+42}_{-30}	$0.51^{+0.07}_{-0.05}$	$1.51^{+0.20}_{-0.12}$	1.51±0.13

1) Weighted average $\Sigma_{\rm SFR}$ of the spaxels in the stack, corrected for broad emission contamination using Equation 2.1. 2) Hα broad-to-narrow flux ratio. 3) Velocity dispersion of the broad component. 4) Velocity offset between the centroids of the broad and narrow components. 5) Outflow velocity, calculated using $v_{\rm out} = \Delta$v - $2\sigma_b$. 6) Mass loading factor ($\dot{M}_{\rm out}$/SFR), assuming $n_e = 380$ cm^{-3} and $R_{\rm out} = 1.7$ kpc. 7) Ratio of the measured energy outflow rate to the predicted energy outflow rate for winds driven by energy from supernova explosions. 8) Ratio of the measured momentum outflow rate to the predicted momentum outflow rate for winds driven by radiation pressure from massive stars.

which was excluded from our analysis because broad emission components in this region could be dominated by beam smearing and/or stacking artefacts (see Sections 2.3.2 and 2.8).

There is a clear positive correlation between $\Sigma_{\rm SFR}$ and σ_b, which can be well described by a power law ($\sigma_b = c_1\ \Sigma_{SFR}^{c_2}$). We fit only the 5 bin stacks and use orthogonal distance regression to account for both the spread in $\Sigma_{\rm SFR}$ values within each bin and the errors on the σ_b measurements. The best fit power law is shown by the purple line and filled error region in Figure 2.6, and is given by

$$\sigma_b \ = \ (241 \pm 23 \text{ km s}^{-1}) \left(\frac{\Sigma_{\rm SFR}}{\text{M}_\odot \text{ yr}^{-1} \text{ kpc}^{-2}} \right)^{0.30 \ \pm \ 0.11} \tag{2.2}$$

The errors on the best fit parameters and the error region around the best fit curve were calculated using bootstrapping. We randomly perturbed the location of each stack in the $\Sigma_{\rm SFR}$-σ_b plane according to a 2D Gaussian distribution with dispersion in the two dimensions given by the errors on $\Sigma_{\rm SFR}$ and σ_b, and then re-fit the $\Sigma_{\rm SFR}$-σ_b relation using the perturbed values. This process was repeated 100 times. The quoted errors on the normalisation and power law index represent the 1σ ranges in the parameters obtained from the 100 bootstraps, and the purple shaded region in Figure 2.6 indicates the 16th-84th percentile range of the 100 best fit curves at each $\Sigma_{\rm SFR}$ value.

We confirm that the $\Sigma_{\rm SFR}$-σ_b correlation is not an artefact of beam smearing (which artificially increases the σ_b in the central regions of galaxies where $\Sigma_{\rm SFR}$ is often also the highest) by constructing and fitting another set of stacks, excluding nuclear spaxels (with galactocentric radius less than 3 kpc). Because the number of available spaxels is reduced, we also reduce the number of bins to four. The outflow component is not detected in the lowest $\Sigma_{\rm SFR}$ stack, but the σ_b values measured for the remaining 3 stacks are consistent (within the 1σ errors) with the $\Sigma_{\rm SFR}$-σ_b relation measured from the full set of spaxels.

It is important to consider the fact that separating the star formation and outflow components becomes more difficult as the σ_b and/or BFR decrease. We employ a forward modelling technique (described in Appendix 2.9) to investigate how robustly we can recover the intrinsic parameters of the outflow component in different regions of parameter space. In summary, we find that the true BFR for the below median stack could be a factor of $\sim$2 higher than measured, but is at least a factor of 2 lower than the BFRs of the high $\Sigma_{\rm SFR}$ stacks. Our modelling also indicates that the true σ_b for the below median $\Sigma_{\rm SFR}$ stack may be as high as $\sim$180 km s^{-1}, which is comparable to the σ_b values measured for the three stacks at 0.25 – 0.45 $M_\odot$ yr^{-1} kpc^{-2}, and suggests that the σ_b-$\Sigma_{\rm SFR}$ relation may flatten at low $\Sigma_{\rm SFR}$.

2.5.3 Outflow Velocity

We use the measured outflow component kinematics to investigate how the outflow velocity varies with $\Sigma_{\rm SFR}$. Heckman et al. (2000) reported that if gas is deposited into an outflow at approximately zero velocity and is then accelerated outwards, the maximum (terminal)

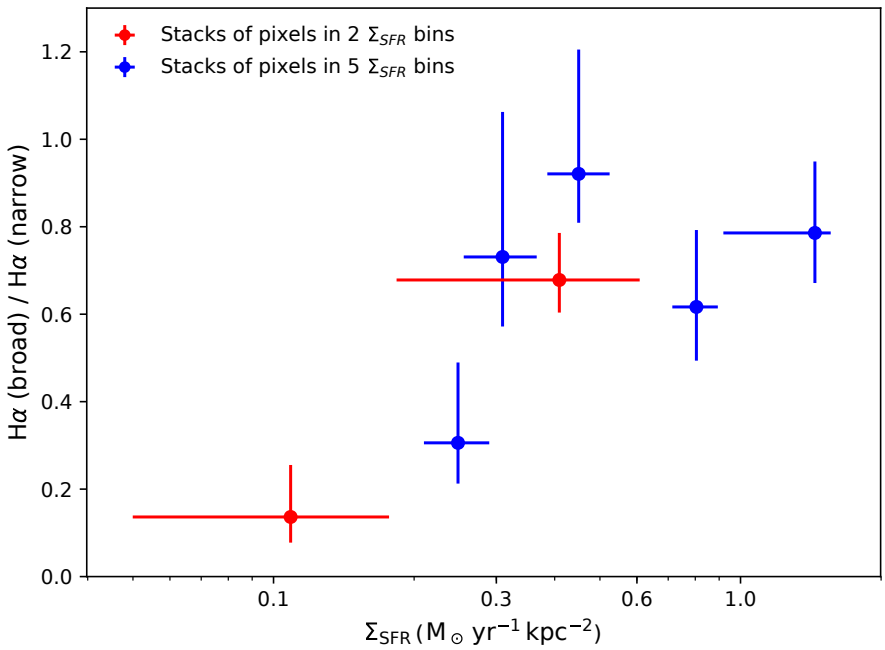

Figure 2.5: Ratio of the Hα flux in the broad component to the Hα flux in the narrow component as a function of $\Sigma_{\rm SFR}$. Red symbols represent stacks of spaxels above and below the median $\Sigma_{\rm SFR}$, and blue symbols represent stacks of spaxels in five bins of $\Sigma_{\rm SFR}$. The error bars on the $\Sigma_{\rm SFR}$ values represent the 16th-84th percentile range of $\Sigma_{\rm SFR}$ values for the spaxels included in each stack, and the error bars on the BFR values represent the 68 per cent confidence interval from the MCMC fitting. The broad component accounts for an average of ∼10% of the total Hα flux at $\Sigma_{\rm SFR} < 0.2\ M_\odot\ {\rm yr}^{-1}\ {\rm kpc}^{-2}$, but increases to ∼45% of the Hα flux at $\Sigma_{\rm SFR} > 0.3\ M_\odot\ {\rm yr}^{-1}\ {\rm kpc}^{-2}$.

velocity of the outflow is roughly $\Delta v - {\rm FWHM}_{broad}/2$ (see also Rupke et al., 2005; Veilleux et al., 2005). Genzel et al. (2011) adopted a slightly different definition for the outflow velocity ($v_{\rm out} \sim \Delta v - 2\sigma_b$), which brings the outflow velocities they measure from emission line spectra into better agreement with outflow velocities measured from absorption line spectra, for galaxies with similar stellar masses and SFRs. We adopt the Genzel et al. (2011) definition for $v_{\rm out}$, but find that the slope of the $\Sigma_{\rm SFR}$-$v_{\rm out}$ relation is independent of the chosen prescription for $v_{\rm out}$ (see discussion below).

The velocity shift of the outflow component relative to the star formation component is always < 70 km s^{-1} (see e.g. Figure 2.4), and therefore the outflow velocity is almost proportional to σ_b. Consequently $v_{\rm out}$, like σ_b, is positively correlated with $\Sigma_{\rm SFR}$ (shown in Figure 2.7). We fit a power law relation to the $\Sigma_{\rm SFR}$ and $v_{\rm out}$ values of the 5 bin stacks, and obtain

$$v_{\rm out} = (524 \pm 43\ {\rm km\ s^{-1}}) \left(\frac{\Sigma_{\rm SFR}}{{\rm M_\odot\ yr^{-1}\ kpc^{-2}}} \right)^{0.34\ \pm\ 0.10} \quad (2.3)$$

The outflow velocities for the stacks at $\Sigma_{\rm SFR} > 0.2\ M_\odot\ {\rm yr}^{-1}\ {\rm kpc}^{-2}$ range from

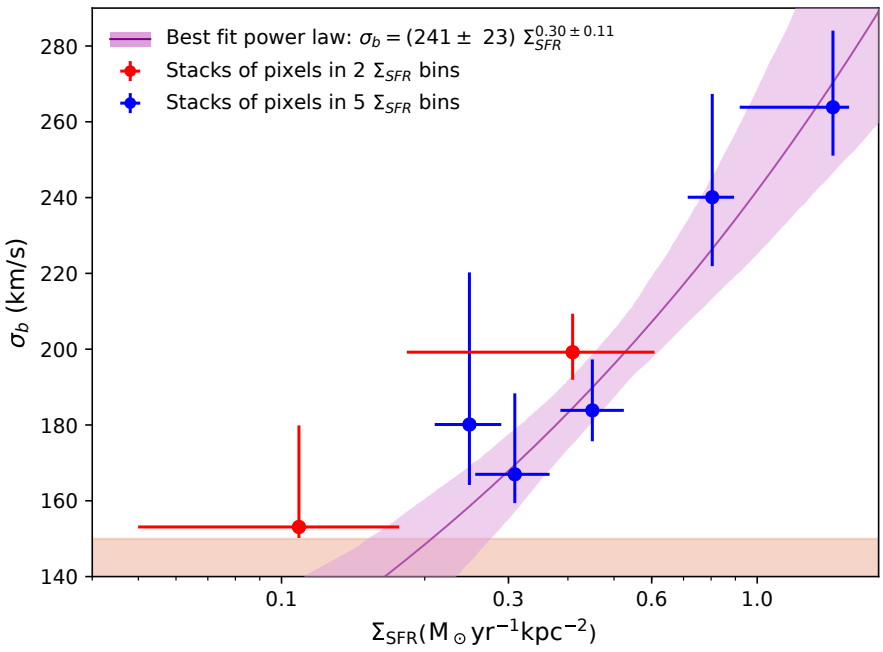

Figure 2.6: Velocity dispersion of the broad component as a function of $\Sigma_{\rm SFR}$. The purple line indicates the best fit power law relation between $\Sigma_{\rm SFR}$ and σ_b for our data, and the filled purple region indicates the 1σ error around the best fit. The red shading indicates the region at $\sigma_b < 150$ km s^{-1} which was excluded from our analysis because broad emission components in this region could be dominated by beam smearing and/or stacking artefacts.

350-600 km s^{-1}; in good agreement with the results of Förster Schreiber et al. (2019) who stacked global emission line spectra of galaxies with star formation driven outflows at $0.6 < z < 2.7$ and found a typical outflow velocity of 450 km s^{-1}. Our outflow velocities are also similar to outflow velocities measured for galaxies with similar SFRs in various absorption line studies (e.g. Weiner et al., 2009; Martin et al., 2012; Kornei et al., 2012; Heckman & Borthakur, 2016).

If we apply the $v_{\rm out}$ definition adopted by Heckman et al. (2000), Rupke et al. (2005) and Veilleux et al. (2005), the normalisation in Equation 2.3 changes to 325 ± 38 km s^{-1} – a factor of 1.6 lower than derived using the Genzel et al. (2011) definition. The best fit power law index is the same regardless of the adopted definition for $v_{\rm out}$, and is in excellent agreement with many studies reporting similar power law scalings between $v_{\rm out}$ and either $\Sigma_{\rm SFR}$ or SFR, across a range of redshifts (e.g. Martin, 2005; Weiner et al., 2009; Martin et al., 2012; Kornei et al., 2012; Heckman et al., 2015; Heckman & Borthakur, 2016).

In Figure 2.7 we also compare our derived $v_{\rm out}$-$\Sigma_{\rm SFR}$ scaling to predictions from different star formation driven outflow models. The dotted line shows the best fit to our data for a scaling of $v_{\rm out} \propto {\Sigma_{\rm SFR}}^{0.1}$, which is predicted for outflows driven by energy from supernova explosions (e.g. Strickland et al., 2004; Chen et al., 2010), and the dashed line shows the best fit to our data for a scaling of $v_{\rm out} \propto {\Sigma_{\rm SFR}}^{2}$, which is predicted for outflows driven by

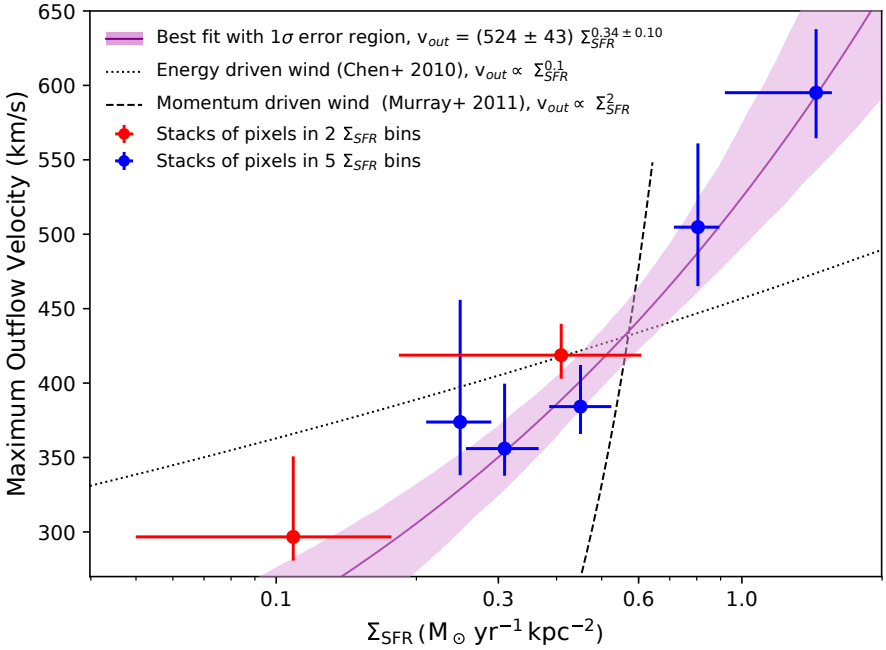

Figure 2.7: Estimated outflow velocity $v_{\rm out}$ as a function of $\Sigma_{\rm SFR}$. The dotted and dashed lines show the predicted scalings between $\Sigma_{\rm SFR}$ and $v_{\rm out}$ for energy driven and momentum driven outflow models, respectively. The scaling for our data lies between the two predictions, suggesting that the outflows may be driven by a combination of mechanical energy and momentum transport.

momentum transport through radiation pressure (e.g. Murray et al., 2011; Kornei et al., 2012). The observed relationship between $v_{\rm out}$ and $\Sigma_{\rm SFR}$ for our stacks lies between the two model predictions, suggesting that the outflows in the SINS/zC-SINF AO star forming galaxies may be driven by a combination of energy from supernova explosions and radiation pressure from massive stars.

2.5.4 Mass Loading Factor η

The mass loading factor η is defined as the ratio of the mass outflow rate to the star formation rate, and is an important parameter governing the strength of feedback in cosmological simulations (see further discussion in Section 2.6.1). η can be estimated from the outflow velocity and the Hα broad-to-narrow ratio, following the method described in Genzel et al. (2011) and Newman et al. (2012a). The model assumes that the outflow velocity and mass outflow rate are constant. The narrow component of the line emission is assumed to be associated with photoionized H II region gas, while the broad component is assumed to be associated with photoionized gas in the outflow. Under these conditions

(following Newman et al. 2012b), the mass outflow rate $\dot{M}_{\rm out}$ can be derived as follows:

$$\dot{M}_{\rm out}\ ({\rm g\ s^{-1}}) = \frac{1.36 m_H}{\gamma_{\rm H\alpha} n_e} \left(\frac{v_{\rm out}}{R_{\rm out}}\right) L_{\rm H\alpha,broad} \tag{2.4}$$

where $1.36m_H$ is the effective nucleon mass for a 10 per cent helium fraction, $\gamma_{\rm H\alpha} = 3.56 \times 10^{-25}$ erg cm^3 s^{-1} is the Hα emissivity at T = 10^4K, n_e is the local electron density in the outflow, $R_{\rm out}$ is the maximum (deprojected) radial extent of the outflow, and $L_{\rm H\alpha,broad}$ is the Hα luminosity of the outflow component. The SFR is given by

$${\rm SFR\ (g\ s^{-1})} = \frac{1.99 \times 10^{33}}{3.15 \times 10^{7}} \left(\frac{L_{\rm H\alpha,narrow}}{2.1 \times 10^{41}}\right) \tag{2.5}$$

where $L_{\rm H\alpha,narrow}$ is the Hα luminosity of the narrow component. The first term of Equation 2.5 is the number of grams per solar mass divided by the number of seconds per year, and converts the SFR from units of $M_\odot$ yr^{-1} to g s^{-1}. Equations 2.4 and 2.5 can be combined to calculate the mass loading factor as follows:

$$\eta = \left(\frac{3.15 \times 2.1 \times 10^{48}}{1.99 \times 10^{33}}\right) \frac{1.36 m_H}{\gamma_{\rm H\alpha} n_e} \left(\frac{\rm H\alpha_{broad}}{\rm H\alpha_{narrow}}\right) \frac{v_{\rm out}}{R_{\rm out}} \tag{2.6}$$

In the following sub-sections we discuss the assumption that the outflowing gas is photoionized, motivate our choice of electron density and outflow extent, and analyse the variation in η as a function of $\Sigma_{\rm SFR}$.

Ionization Mechanisms

The assumption that both components are primarily photoionized is justified by the measured emission line ratios ([N II]/Hα = 0.12±0.02 for the narrow component and [N II]/Hα = 0.27±0.04 for the broad component of the above median $\Sigma_{\rm SFR}$ stack), which are consistent with stellar photoionization (Baldwin et al., 1981; Kewley et al., 2001). The low [N II]/Hα ratio of the outflow component is surprising, because star-formation driven outflows in the local universe often show signatures of strong shocks (e.g. Sharp & Bland-Hawthorn, 2010; Rich et al., 2011; Soto et al., 2012; Ho et al., 2014). In our $z \sim 2$ star forming galaxies, the [N II]/Hα ratio of the outflow component is enhanced by 0.35 dex compared to the narrow component, which can be explained by a 30-40% contribution from shock excitation (see e.g. Rich et al., 2011; Yuan et al., 2012).

Sharp & Bland-Hawthorn (2010) argue that the shock-like line ratios in local star formation driven outflows are the result of bursty star formation. By the time the energy from supernova explosions is able to dislodge gas from the disk and launch winds, most of the massive stars have died. It is possible that our $z \sim 2$ galaxies are experiencing extended periods of star formation, so that stellar photoionization dominates over shock excitation even after winds have been launched. However, a more likely explanation for the low shock fraction is that we are simply probing material close to the galaxy disks where the large scale stellar radiation field is strong. Low shock fractions are observed close to the

disks of several prototypical starburst driven superwind galaxies including M82, NGC 1482 and NGC 253 (Shopbell & Bland-Hawthorn, 1998; Veilleux & Rupke, 2002; Westmoquette et al., 2011).

Electron Density

The electron density determines the constant of proportionality between the broad Hα luminosity and the outflow mass in Equation 2.4, but is notoriously difficult to measure. In principle, the electron density in the outflow can be calculated from the ratio of the broad component amplitudes of the [S II] doublet lines ([S II]λ6716/[S II]λ6731; Osterbrock & Ferland 2006). However, the [S II] line emission in our stacks is not strong enough to independently constrain the amplitudes of the narrow and broad components. Previous studies have faced similar issues, leading to large uncertainties on the electron densities and the resulting mass loading factors. For example, Newman et al. (2012b) measured an electron density of 10^{+590}_{-10} cm^{-3} in the broad component for a stack of 14 galaxies with star formation driven outflows from the SINS/zC-SINF survey. Other recent studies of outflows at high redshift by Freeman et al. (2019) and Leung et al. (2017) were unable to constrain the electron density and adopted the Newman et al. (2012b) value.

Important progress was made by Förster Schreiber et al. (2019), who performed the most accurate measurement to date of the electron density in star formation driven ionized gas outflows at high redshift. They started with a sample of 599 galaxies from the SINS/zC-SINF and KMOS$^{\rm 3D}$ surveys, which includes many of our galaxies and covers the main sequence of star forming galaxies at $0.6 < z < 2.7$ over a stellar mass range of $9.0 < \log(M_*/M_\odot) < 11.7$. They stacked the spectra of 33 galaxies with individual high S/N detections of star formation driven outflows, and fit two components to each of the [S II] lines in the stacked spectrum. They measured electron densities of 76^{+24}_{-23} cm^{-3} and 380^{+249}_{-167} cm^{-3} for the narrow and outflow components, respectively. The outflow component is denser than the star formation component, providing further evidence to suggest that the outflowing material may be shocked. The Förster Schreiber et al. (2019) results are consistent with several other studies of ionized gas outflows that have also found the outflowing gas to be denser than the H II region gas (e.g. Arribas et al., 2014; Ho et al., 2014; Perna et al., 2017; Kakkad et al., 2018). We therefore adopt an outflow electron density of 380 cm^{-3}. There are no observational constraints on how the electron density in the outflow varies as a function of $\Sigma_{\rm SFR}$, so we assume that it is constant.

Radial Extent of the Outflow

The $v_{\rm out}/R_{\rm out}$ term in Equation 2.4 is the inverse of the dynamical time of the outflow (see e.g. Veilleux et al. 2005), and $R_{\rm out}$ is the radial extent of the outflow from the point of launch. For the stacking analysis presented in this paper, the correct choice of $R_{\rm out}$ is not clear, because the stacks combine many spectra which trace outflows at different distances from their point of launch. Therefore, we explore two extreme cases to obtain upper and lower limits on $R_{\rm out}$, and adopt an intermediate value in our subsequent calculations.

To obtain a lower limit on $R_{\rm out}$, we assume that the outflowing material is always observed close to where it was launched. We take the minimum $R_{\rm out}$ to be the typical half width at half maximum of the PSF, which for our sample is 0.7 kpc (see also Newman et al., 2012a).

To obtain an upper limit on $R_{\rm out}$, we assume that the outflowing material could have been launched from anywhere within the galaxies. The maximum galactocentric radius to which broad emission is observed in the SINS/zC-SINF AO galaxies is 2.6 kpc (Newman et al., 2012b), so we take that as the upper limit on $R_{\rm out}$.

For our subsequent analysis we adopt the average of the lower and upper limits: $R_{\rm out} = 1.7$ kpc. As for n_e, we assume that $R_{\rm out}$ is independent of $\Sigma_{\rm SFR}$.

Trends with $\Sigma_{\rm SFR}$

Figure 2.8 shows the η values calculated for our stacks. The mass loading factor scales linearly with both BFR and $v_{\rm out}$ and consequently shows a clear positive correlation with $\Sigma_{\rm SFR}$. The positive correlation between $\Sigma_{\rm SFR}$ and η is in agreement with results from other studies of neutral and ionized gas outflows (e.g. Chen et al., 2010; Newman et al., 2012b; Arribas et al., 2014), but is in tension with models which predict that η should be inversely correlated with $\Sigma_{\rm SFR}$ (e.g Hopkins et al., 2012b; Creasey et al., 2013; Lagos et al., 2013; Li et al., 2017).

The errors on the η values shown in Figure 2.8 do not include the $\sim 50\%$ errors on $R_{\rm out}$ and n_e, which would translate to a $\sim 70\%$ uncertainty on η. If $R_{\rm out}$ and n_e are independent of $\Sigma_{\rm SFR}$ (as we have assumed), then the *shape* of the $\Sigma_{\rm SFR}$-η relationship is independent of the chosen $R_{\rm out}$ and n_e values, but there is a $\sim 70\%$ error on the normalisation of the relationship (the average η). However, if $R_{\rm out}$ and n_e vary as a function of $\Sigma_{\rm SFR}$, then the true shape of the relationship between $\Sigma_{\rm SFR}$ and η may be different.

We note that even at $\Sigma_{\rm SFR} > 0.3\ M_\odot\ {\rm yr}^{-1}\ {\rm kpc}^{-2}$, the η values are relatively low ($\eta \sim 0.3 - 0.5$), suggesting that the ionized gas outflow rates are considerably smaller than the SFRs of the clumps driving the outflows. Förster Schreiber et al. (2019) found similarly low galaxy-integrated mass loading factors for star formation driven outflows at $0.6 < z < 2.7$ in the KMOS^{3D} survey. Freeman et al. (2019) found higher mass loading factors of 0.64-1.4 for star formation driven outflows in galaxies with similar stellar masses and redshifts to the galaxies in our sample ($9.8 < \log(M_*/M_\odot) < 10.7$ at $1.37 < z < 2.61$), but this difference is due to the fact that they assumed an electron density of 50 cm^{-3}. If we re-calculate the mass loading factors for their sample assuming $n_e = 380$ cm^{-3}, the mass loading factors decrease to $\eta = 0.08$-0.18. Likewise, Newman et al. (2012b) found $\eta \sim 2$ for a very similar sample of galaxies to the one used in this paper, assuming $n_e = 50$ cm^{-2}. If we re-scale this η value for $n_e = 380$ cm^{-3}, we obtain $\eta \sim 0.26$.

We emphasise that the normalisation of the mass loading factor is impacted by uncertainties on the electron density and the radial extent of the outflow. However, if the ionized gas mass loading factors are indeed so low, the outflows would not appear to be able to remove enough gas to explain the low baryon fractions of low mass halos (e.g. Baldry et al., 2008; Moster et al., 2013; Moustakas et al., 2013; Behroozi et al., 2013).

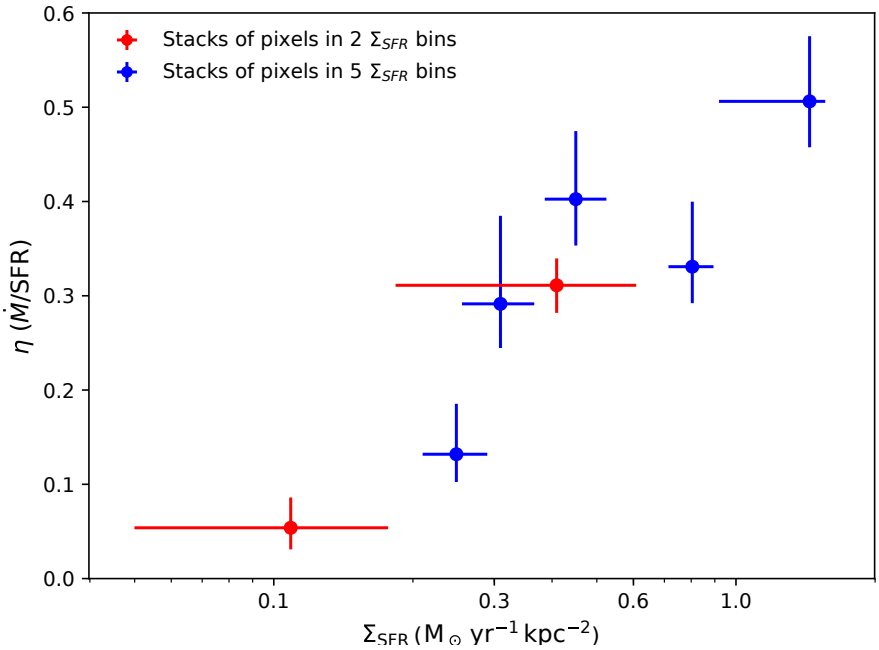

Figure 2.8: Estimated mass loading factor η as a function of $\Sigma_{\rm SFR}$. η is inversely proportional to the electron density in the outflow component, which we assume here to be 380 cm^{-3}. The derived η values are significantly lower than what is typically assumed for stellar feedback in cosmological simulations, suggesting that a significant fraction of the outflowing mass must be in other gas phases.

We have measured only the warm ionized gas phase of the outflows, and the overall mass loading factors could be higher if most of the outflowing mass is in other gas phases (see also discussion in Förster Schreiber et al. 2019). This will be discussed further in Section 2.6.1.

2.5.5 Outflow Energetics

In the absence of an AGN, galaxy scale outflows are generally thought to be driven by either the energy released through supernova explosions and radiation from young stars, or by the transport of momentum by means of radiation pressure, supernovae and stellar winds. Assuming that 1 per cent of the bolometric luminosity of the stars is released as energy in supernova explosions, and that 10 per cent of this energy is able to couple to the ISM, Murray et al. (2005) predict that for an energy driven wind, the energy outflow rate should be $\dot{E}_{\rm out} \sim 10^{-3} L_{\rm bol}$, whereas for a momentum driven wind, the momentum outflow rate should be $\dot{p}_{\rm out} \sim L_{\rm bol}/c$. We assume that $L_{\rm bol} \sim {\rm SFR} \times 10^{10} L_\odot$ (Kennicutt, 1998).

The energy and momentum outflow rates for each of the stacks can be calculated as

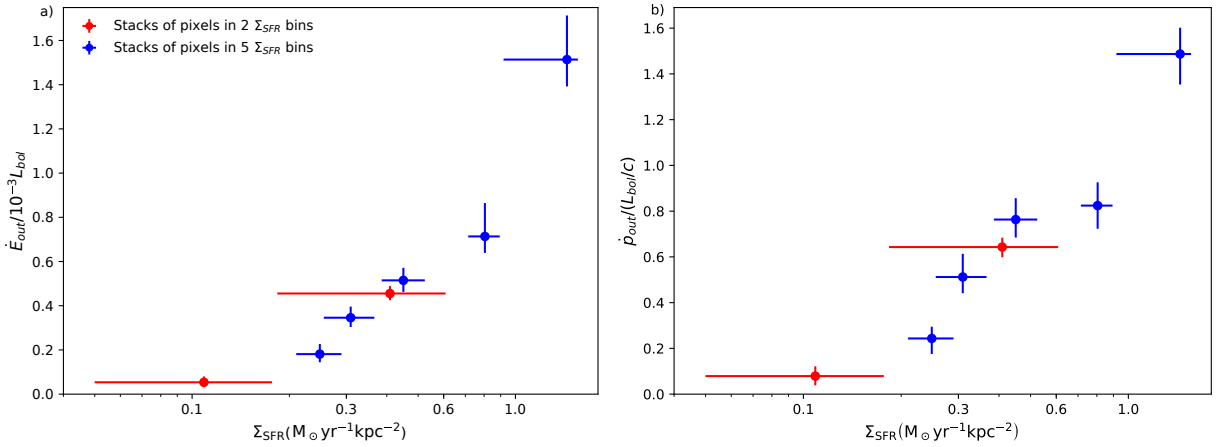

Figure 2.9: Panel a): Measured energy outflow rate $\dot{E}_{\rm out}$ as a fraction of the energy outflow rate predicted by Murray et al. (2005) for energy driven winds ($10^{-3}L_{\rm bol}$). Panel b): Measured momentum outflow rate $\dot{p}_{\rm out}$ as a fraction of the predicted momentum outflow rate for momentum driven winds ($L_{\rm bol}/c$).

follows:

$$\dot{E}_{\rm out} = \frac{1}{2}\dot{M}v_{\rm out}^2 = \frac{1}{2}\eta \times {\rm SFR} \times v_{\rm out}^2 \tag{2.7}$$

$$\dot{p}_{\rm out} = \dot{M}v_{\rm out} = \eta \times {\rm SFR} \times v_{\rm out} \tag{2.8}$$

Figure 2.9 shows the ratios of the calculated energy and momentum outflow rates for each of the stacks to the predicted energy and momentum outflow rates from Murray et al. (2005). For the stacks with $\Sigma_{\rm SFR} < 1.0\ M_\odot\ {\rm yr}^{-1}\ {\rm kpc}^{-2}$, the ratios are in the following ranges:

$$\frac{\dot{E}_{\rm out}}{10^{-3}L_{\rm bol}} = 0.05 - 0.71 \times \frac{380\ {\rm cm}^{-3}}{n_e}\frac{1.7\ {\rm kpc}}{R_{\rm out}} \tag{2.9}$$

$$\frac{\dot{p}_{\rm out}}{L_{\rm bol}/{\rm c}} = 0.09 - 0.85 \times \frac{380\ {\rm cm}^{-3}}{n_e}\frac{1.7\ {\rm kpc}}{R_{\rm out}} \tag{2.10}$$

The ratios do not exceed 1, suggesting that the current star formation activity is sufficient to power the observed outflows and that no additional energy source is required. However, the ratios show a strong correlation with $\Sigma_{\rm SFR}$ which is not explained by the Murray et al. (2005) models.

For the highest $\Sigma_{\rm SFR}$ stack, the energy and momentum outflow rates exceed the predicted rates by a factor of 1.5. There are several possible explanations for this discrepancy. A significant amount of the energy or momentum driving the outflows may come from source(s) which are not accounted for in the Murray et al. (2005) model, such as cosmic rays (see e.g. Ruszkowski et al., 2017; Girichidis et al., 2018). The SFR measured from the narrow component of the Hα emission may not be representative of the SFR at the

time and point of launch of the outflows, either because the SFR has changed over time, or because the outflows have propagated away from their launch points (which is the case for one of the outflows in ZC406690; Newman et al. 2012a). Alternatively, one or more of the assumptions made in our calculations may be incorrect: the adopted electron density or extent of the outflow may be too low, the majority of the outflowing gas may be collisionally excited rather than photoionized (which would change the coefficients in the outflow mass calculation and reduce η by a factor of $\sim$2; Genzel et al. 2011), or the emission lines may be partially broadened by mechanisms other than outflows (such as shocks or turbulent mixing layers; see further discussion in Section 2.6.2).

2.6 Discussion

2.6.1 Escape Fraction and Mass Budget

In order to gauge the impact of the star formation driven outflows on the stellar mass growth and structural evolution of their host galaxies, we investigate whether any of the outflowing material is travelling fast enough to escape the galaxy halos. The halo escape velocity is approximately three times the galaxy circular velocity (e.g. Weiner et al., 2009). We calculate the 'characteristic' circular velocity for each $\Sigma_{\rm SFR}$ bin by assigning each spaxel the circular velocity of its host galaxy (given in Förster Schreiber et al. 2018), and then averaging the circular velocities assigned to all the spaxels in the relevant bin. The characteristic circular velocities (halo escape velocities) decrease from $\sim$230 km s^{-1} (690 km s^{-1}) at the lowest $\Sigma_{\rm SFR}$ to $\sim$180 km s^{-1} (540 km s^{-1}) at the highest $\Sigma_{\rm SFR}$. The highest $\Sigma_{\rm SFR}$ bin is the only one for which the outflow velocity (595 km s^{-1}) exceeds the characteristic halo escape velocity. Therefore, if the outflows are spherically symmetric, very little of the outflowing material is likely to escape from the galaxy halos.

If the outflows are biconical and perpendicular to the galaxy disks (as suggested by observations of higher outflow velocities in face on galaxies than edge on galaxies; e.g. Heckman et al., 2000; Chen et al., 2010; Kornei et al., 2012; Newman et al., 2012b; Bordoloi et al., 2014), the outflow velocities will be under-estimated by a factor of $1/\cos(i)$, which is equivalent to the inverse of the typical galaxy axis ratio. We calculate characteristic axis ratios for each of our stacks using the same method applied to calculate the characteristic circular velocities. We find that if the outflows are biconical, the outflowing material in the two highest $\Sigma_{\rm SFR}$ bins would have sufficient velocity to escape the galaxy halos.

We note that if the outflowing material is still being accelerated, the terminal velocities will be higher than the measured outflow velocities and more material will be able to escape from the halos. On the other hand, if the outflows are ballistic, the outflow velocity will decrease over time and less material will be able to escape. Better observational constraints on the geometry and velocity structure of star formation driven outflows are required to more accurately determine the fate of the outflowing material.

We conclude that the majority of the ionized gas in the outflows is likely to decelerate and be re-accreted onto the galaxy disks. The re-accretion of gas launched in outflows is

important for the chemical evolution of galaxies because outflows carry significant amounts of heavy metals (e.g. Larson, 1974; Tremonti et al., 2004; Finlator & Davé, 2008; Peeples et al., 2014; Zahid et al., 2014). Galaxy formation simulations with star formation feedback suggest that the timescale for re-accretion of the outflowing material is approximately 1 – 2 Gyr (e.g. Oppenheimer et al., 2010; Brook et al., 2014).

The mass loading factors derived in this paper are quite low; $\eta \sim (0.3 - 0.5) \times 380$ cm$^{-3}/n_e$. η is proportional to $v_{\rm out}$, so if the outflows are bi-conical the maximum η could increase to ~ 0.7, but this would only partially resolve the tension with cosmological simulations which typically require $\eta \gtrsim 1$ to reproduce the low baryon fractions of low mass halos (e.g. Finlator & Davé, 2008; Davé et al., 2011; Hopkins et al., 2012b; Vogelsberger et al., 2014; Muratov et al., 2015).

The discrepancy between the predicted and measured mass loading factors can potentially be resolved by considering the mass contained in other phases of the outflows. Multi-wavelength observations of star formation and AGN driven outflows, both locally and at high redshift, suggest that the ionized gas phase accounts for only a small fraction of the total mass and energy expelled in outflows. The ionized gas outflow in M82 contains only ∼1-2% of the mass carried in the neutral and molecular phases of the outflow (Shopbell & Bland-Hawthorn, 1998; Walter et al., 2002; Contursi et al., 2013; Leroy et al., 2015). Similarly, in the local starburst/quasar ultra-luminous infrared galaxy Mrk 231, the ionized gas outflow rate is ∼4000 times lower than the molecular and neutral gas outflow rates (e.g. Cicone et al., 2014). In general, AGN driven outflows appear to carry more mass and energy in the neutral and molecular gas phases than in the ionized gas phase (e.g. Rupke & Veilleux, 2013; Carniani et al., 2017; Fluetsch et al., 2019; Herrera-Camus et al., 2019). There is some evidence that in local star forming galaxies the ionized gas outflow rate may be comparable to the neutral and molecular gas outflow rates (e.g. Fluetsch et al., 2019), but larger samples of galaxies with observations in multiple outflow tracers are required to overcome the large uncertainties on the mass outflow rates.

It is also important to consider the contribution of the hot X-ray emitting gas. This phase is very difficult to observe, but multi-phase simulations of star formation driven outflows predict that at distances of $\gtrsim 1$ kpc from the disk, the majority of the outflowing mass and energy will be carried by the hot phase (e.g. Li et al., 2017; Fielding et al., 2018; Kim & Ostriker, 2018).

It is clear that the total mass outflow rates and gas recycling rates are strongly dependent on the multi-phase mass budget, geometry and velocity structure of the outflows (see also discussion in Förster Schreiber et al. 2019). Better constraints on these properties are therefore key to improving our understanding of the impact of star formation feedback on the growth and evolution of $z \sim 2$ star forming galaxies.

2.6.2 Alternative Sources of Broad Emission

Throughout this paper we have assumed that the broad component of the Hα line emission traces the bulk motion of ionized gas entrained in star formation driven outflows, and therefore that the velocity dispersion of the broad component is a direct tracer of the

outflow velocity. In Section 2.4 we showed that the Hα line width is strongly correlated with $\Sigma_{\rm SFR}$, indicating that the broad emission is related to star formation. On the other hand, the shape of the Hα line is not correlated with either the A_V or the galactocentric distance, indicating that scattered light and beam smearing are unlikely to be significant sources of broad emission in our galaxies (see also discussion in Appendix 2.8).

Absorption line studies indicate that outflows are ubiquitous in star forming galaxies at $z \sim 2$ (e.g. Shapley et al., 2003; Weiner et al., 2009; Rubin et al., 2010; Steidel et al., 2010; Erb et al., 2012; Kornei et al., 2012; Bordoloi et al., 2014). It is therefore not surprising that we observe broad Hα emission associated with the ionized phase of these outflows. However, it is important to consider the possibility that the kinematics of the outflowing gas may include significant contributions from turbulent motions as well as bulk flows.

The outflowing gas may collide with material in the ISM of the galaxies and trigger shocks. The broad component of the above median $\Sigma_{\rm SFR}$ stack has an [N II]/Hα ratio of 0.27±0.04, which is significantly lower than would be expected for purely shock-excited gas (e.g. Allen et al., 2008; Rich et al., 2011), but significantly higher than the 0.12±0.02 measured for the narrow component. This suggests that up to 30-40% of the Hα emission could be shock excited, with the remaining gas photoionized by young stars in the galaxy disks (see discussion in Section 2.5.4). Förster Schreiber et al. (2019) found that the material emitting the broad Hα is denser than the H II region gas, suggesting that the broad component may trace compressed clumps of ionized gas entrained within the wind fluid. If the outflowing gas is shock excited, the width of the broad component would reflect the shock velocity, but the shock velocity is expected to be similar to the outflow velocity (see e.g. Soto et al., 2012; Ho et al., 2014; McElroy et al., 2015).

Broad emission could also arise from turbulent mixing layers at the interface between cold gas in the disk and hot wind fluid (e.g. Slavin et al., 1993; Esquivel et al., 2006; Westmoquette et al., 2007, 2009, 2011; Wood et al., 2015). In this scenario, the width of the broad component would reflect the turbulent velocity rather than the outflow velocity. We cannot rule out the possibility that the outflow components in our stacks are broadened by turbulent mixing layers in the ISM. However, the $\Sigma_{\rm SFR}$-$v_{\rm out}$ scaling we measure in Section 2.5.3 is consistent with results from absorption line studies of star-formation driven outflows at low and high redshift (e.g. Martin, 2005; Weiner et al., 2009; Heckman & Borthakur, 2016; Sugahara et al., 2017), which suggests that the kinematics of the outflowing gas are likely to be dominated by bulk flows, with only a minor contribution from turbulent motions.

2.7 Summary and Conclusions

We investigated the relationship between star formation activity and the incidence and properties of outflows on scales of 1-2 kpc in a sample of 28 star forming galaxies at $z \sim 2 - 2.6$ from the SINS/zC-SINF AO Survey. This work builds on previous studies of the relationship between *global* galaxy properties and outflow properties in the SINS/zC-SINF AO sample (Newman et al., 2012b), and the relationship between the *resolved* star

formation and outflow properties of star forming clumps in 5 SINS/zC-SINF AO galaxies (Genzel et al., 2011; Newman et al., 2012a). With the aid of stacking we are able to probe not only the actively star forming clump regions which have been studied previously, but also the fainter inter-clump regions, spanning a factor of ∼50 in $\Sigma_{\rm SFR}$.

We divided the spaxels from the 28 datacubes into bins of different physical properties (SFR, $\Sigma_{\rm SFR}$, stellar mass surface density Σ_*, $\Sigma_{\rm SFR}/\Sigma_*$, A_V and galactocentric distance), and stacked the spectra of the spaxels in each bin to obtain high signal-to-noise Hα line profiles. The Hα profiles were used to simultaneously probe the star formation (from the narrow component of the line) and the outflows (which, when present, produce an additional broader line emission component). The width of the outflow component is a tracer of the outflow velocity, and the flux of the outflow component is a tracer of the mass in the outflow. Our main results are as follows:

1. The width of the Hα line is most strongly dependent on the level of star formation (probed by the SFR and $\Sigma_{\rm SFR}$), supporting the notion that the observed broad emission is associated with star formation driven outflows. Σ_* may also play a role in governing the incidence and properties of the outflows.

2. The outflow component contains an average of ∼45% of the Hα flux emitted from the highest $\Sigma_{\rm SFR}$ regions, but is less prominent at lower $\Sigma_{\rm SFR}$.

3. The outflow velocity scales as $v_{\rm out} \propto {\Sigma_{\rm SFR}}^{0.34\pm\ 0.10}$. This scaling is shallower than the predicted ${\Sigma_{\rm SFR}}^2$ dependence for outflows driven by momentum transport through radiation pressure, but steeper than the predicted ${\Sigma_{\rm SFR}}^{0.1}$ dependence for outflows driven by kinetic energy from supernovae and stellar winds, suggesting that the observed outflows may be driven by a combination of these mechanisms.

4. The outflow velocity is lower than the halo escape velocity in all but the highest $\Sigma_{\rm SFR}$ regions, indicating that the majority of the outflowing material will not be expelled but will decelerate and fall back onto the galaxy disks. Simulations suggest that this material will likely be re-accreted after 1-2 Gyr, contributing to the chemical enrichment of the galaxies.

5. The mass loading factor η increases with $\Sigma_{\rm SFR}$. The normalisation of η is uncertain due to the large uncertainties on the radial extent and electron density of the outflowing material, but we find $\eta \sim 0.4 \times (380\ {\rm cm}^{-3}/n_e) \times (1.7\ {\rm kpc}/R_{\rm out})$. This may be in tension with cosmological simulations (which typically require $\eta \gtrsim 1$ to explain the low efficiency of formation of low mass galaxies), unless a significant fraction of the outflowing mass is in other gas phases and is able to escape the galaxy halos.

6. In 6/7 stacks the current star formation activity is powerful enough to drive the observed outflows. The energy and momentum outflow rates for the highest $\Sigma_{\rm SFR}$ stack exceed the predicted rates for star formation driven outflows by a factor of 1.5. This may indicate that other energy sources (such as cosmic rays) contribute significantly to driving the outflows, that the SFR has changed since the outflows

were launched, that the outflows have propagated away from their point of launch, that the adopted electron density or extent of the outflow is too low, and/or that the emission lines are partially broadened by mechanisms other than outflows (such as shocks or turbulent mixing layers).

Our results confirm that $\Sigma_{\rm SFR}$ is closely related to the incidence and properties of outflows on 1-2 kpc scales. In this paper we have only explored the average incidence and properties of outflows as a function of $\Sigma_{\rm SFR}$, which makes it difficult to draw strong conclusions on the relative importance of global and local galaxy properties in determining the properties of the outflows. In the future it will be important to investigate how much the outflow velocity and Hα broad flux ratio vary at fixed local $\Sigma_{\rm SFR}$, and determine which local and/or global properties are responsible for driving these variations.

2.8 Appendix A: Impact of Beam Smearing and Velocity Shifting Errors

We use dynamical models constructed with the IDL toolkit DYSMAL (Davies et al., 2011) to investigate whether a significant fraction of the broad emission in our stacks could originate from beam smearing and/or smearing introduced in the velocity shifting of the spectra. For each galaxy in our sample, we construct a rotating disk model which is tailored to the structural, kinematic and line emission properties of the galaxy (inclination, effective radius, Sérsic index, stellar mass, circular velocity, intrinsic velocity dispersion, total Hα flux, and integrated [N II]/Hα ratio, derived as described in Förster Schreiber et al. 2018). Each rotating disk model is sampled onto a mock datacube with the same field of view, pixel scale and wavelength scale as our real SINFONI data, and smoothed spectrally and spatially to match the spectral line spread function and spatial PSF of the observations. Noise is added to each mock datacube based on the exposure time and the known shape of the SINFONI K band error spectrum.

For each mock datacube we create maps of the Hα flux and kinematics, mask spaxels with Hα S/N < 5, and shift the spectra of the remaining (unmasked) spaxels to zero velocity using the same methods applied to the real datacubes. We stack the unmasked spaxels from all the mock cubes using two different weighting schemes (1/rms weighting and no weighting), and also create stacks from just the spaxels within a 3 spaxel radius of the center of a galaxy. The four mock stacks are fit using the same MCMC fitting method applied to our data, except that we do not require $\sigma_b > 150$ km s^{-1}. Instead, we only require that the outflow component is broader than the narrow component; i.e. σ_b - $\sigma_n > 20$ km s^{-1}. There are no outflows in the mock cubes, and therefore any detected 'outflow component' is purely the result of beam smearing and/or smearing introduced in the velocity shifting.

The maximum σ_b measured for any of the four mock stacks is $\sigma_b = 110 \pm 12$ km s^{-1}. Therefore, the 3σ upper limit on the velocity dispersion of a broad component that could

be primarily associated with beam smearing is 146 km s^{-1}. This is why we require the outflow components fit to our stacks to have $\sigma_b > 150$ km s^{-1}.

2.9 Appendix B: Using Forward Modelling to Investigate the Accuracy of the Recovered Outflow Parameters

2.9.1 Summary of Methodology

The analysis presented in this paper is based on the assumption that the star formation and outflow components of all the data stacks are intrinsically Gaussian, and that the parameters of these Gaussians can be robustly determined by performing two component Gaussian fitting. The fitting should indeed be robust when the wings of the outflow component are clearly detected above the wings of the narrow component and above the noise. The separation becomes more uncertain when the intrinsic σ_b is low (making the outflow component difficult to distinguish from the star formation component), and/or the intrinsic BFR is low (bringing the flux per channel in the outflow component close to the noise level) (see also Genzel et al., 2014; Freeman et al., 2019). We use forward modelling to understand the potential impact of this uncertainty on the $\Sigma_{\rm SFR}$-BFR and $\Sigma_{\rm SFR}$-σ_b trends shown in Figures 2.5 and 2.6.

A schematic summarising the steps involved in the forward modelling is shown in Figure 2.10. In brief, we generate synthetic spectra with known BFR and σ_b, add noise to mimic the error spectra of the real data stacks, and fit the synthetic stacks with two Gaussian components using the same procedure applied to our data stacks. For each data stack, we identify synthetic spectra with similar fit parameters, and use the intrinsic parameters of these synthetic stacks to estimate the intrinsic parameters of the data stack. In performing this mapping, we do not simply take the synthetic spectrum with the closest fit parameters, or weight the synthetic spectra by the Euclidean distance between their fit parameters and the fit parameters of the data stack in BFR$_{\rm fit}$-$\sigma_{\rm b,fit}$ space, because these metrics do not account for the strong covariance between the BFR and σ_b (seen in e.g. Figure 2.4). Instead, we use the joint BFR$_{\rm fit}$-$\sigma_{\rm b,fit}$ posterior probability distribution function (PDF) of the data stack to weight the synthetic spectra.

2.9.2 Detailed Description

The aim of the forward modelling (summarised in segment 1 of Figure 2.10) is to estimate the intrinsic σ_b and BFR values for each of the data stacks. Throughout this paper, we assume that *intrinsically* (if the noise was removed), each data stack is well explained by a superposition of two Gaussian components which are characterised by the *unknown* parameters BFR$_{\rm int,data}$ and $\sigma_{\rm b,int,data}$. The actual data stacks analysed in this paper (such as the example shown in panel b) of Figure 2.10) are noisy realisations of the intrinsic stacks,

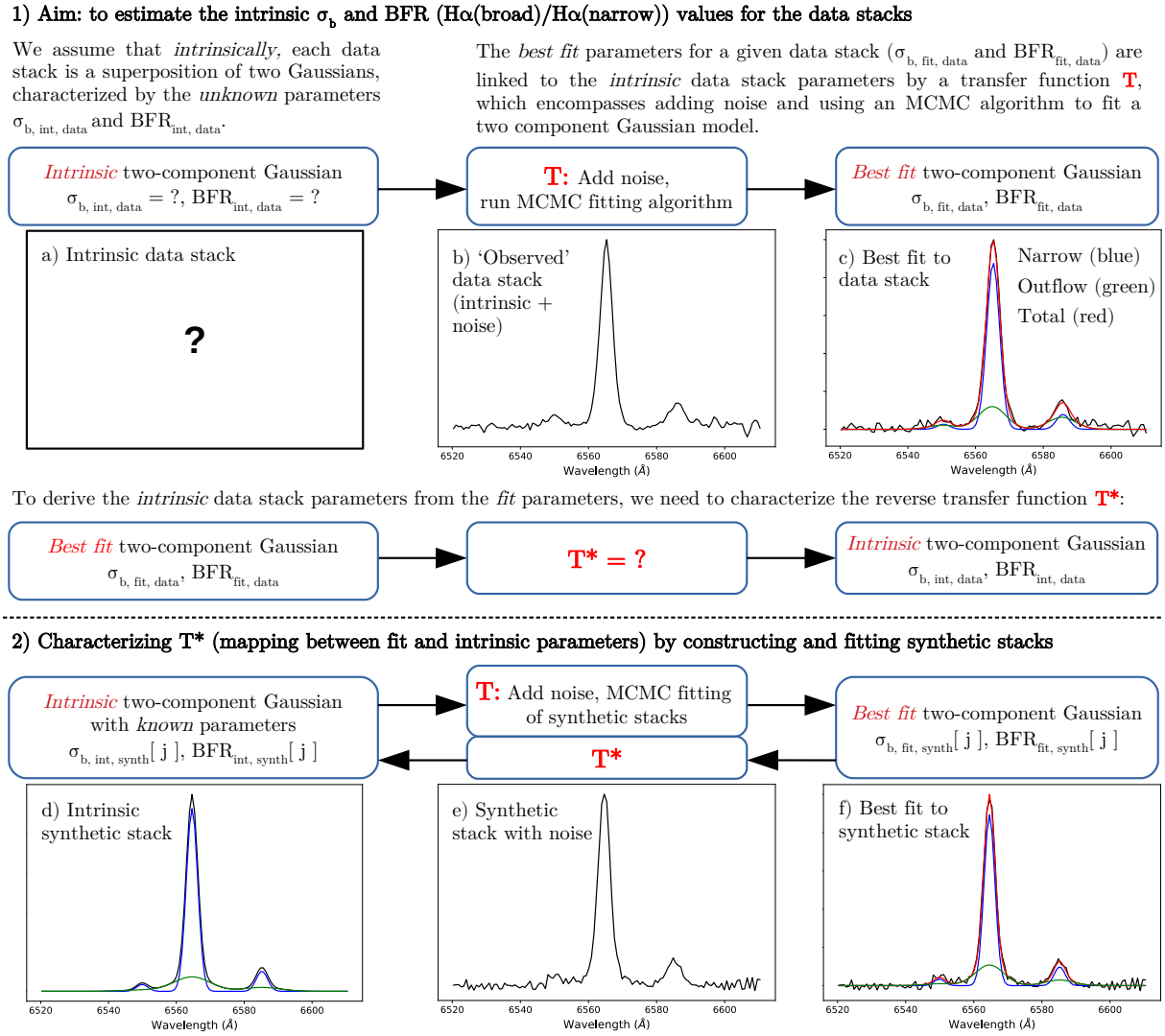

Figure 2.10: Schematic describing the forward modelling technique used to estimate the intrinsic σ_b and BFR of each data stack.

where the noise is a combination of Gaussian noise from the instrument and uncertainties introduced during the stacking process. In our analysis, these noisy stacks were fit with two Gaussian components using the MCMC algorithm described in Section 2.3.2, yielding best fit parameters $\mathrm{BFR_{fit,data}}$ and $\sigma_{\mathrm{b,fit,data}}$ (panel c).

A more mathematical expression of the relationship between the intrinsic and best fit parameters is as follows. Each intrinsic data stack, characterised by the unknown parameters $\mathrm{BFR_{int,data}}$ and $\sigma_{\mathrm{b,int,data}}$, is passed through a transfer function $\mathbf{T}$, which maps between intrinsic space and fit space by adding noise, running an MCMC fitting algorithm, and returning the best fit parameters $\mathrm{BFR_{fit,data}}$ and $\sigma_{\mathrm{b,fit,data}}$. Therefore, to obtain the unknown intrinsic parameters $\mathrm{BFR_{int,data}}$ and $\sigma_{\mathrm{b,int,data}}$, we need to characterise the reverse transfer function $\mathbf{T^*}$ which maps between fit space and intrinsic space. The relationship between the intrinsic and fit parameters and the forward and reverse transfer functions is shown by the two flowcharts in segment 1 of Figure 2.10.

To characterise $\mathbf{T^*}$, we construct a grid of 4200 synthetic stacks which mimic the data stacks but have *known* intrinsic parameters (summarised in segment 2 of Figure 2.10). Like the data stacks, each synthetic stack is intrinsically a superposition of two Gaussian components. We construct synthetic stacks with intrinsic Gaussian parameters covering and extending beyond the range of best fit parameters measured for the data stacks: $0 \leq \mathrm{BFR_{int,synth}[j]} < 1.5$ and $90 \leq \sigma_{\mathrm{b,int,synth}}[\mathrm{j}]$ (km s^{-1}) < 300. An example of an intrinsic synthetic stack and its constituent Gaussian components is shown in panel d) of Figure 2.10.

We apply the forward transfer function $\mathbf{T}$ to each of the intrinsic synthetic stacks by adding noise to mimic the error spectra of the data stacks (panel e), and then fitting two Gaussian components using the same MCMC algorithm applied to the data stacks to obtain the best fit parameters $\mathrm{BFR_{fit,synth}[j]}$ and $\sigma_{\mathrm{b,fit,synth}}[\mathrm{j}]$ (panel f). With both the intrinsic and best fit parameters for each of the synthetic stacks, it is possible to map between fit and intrinsic space, mimicking the reverse transfer function $\mathbf{T^*}$.

The final step is therefore to use the pairs of intrinsic and best fit parameters for the synthetic spectra to estimate the intrinsic parameters of each data stack (summarised in segment 3 in Figure 2.10). We assume that synthetic stacks with similar *fit* parameters to a given data stack will also have similar *intrinsic* parameters. We quantify the similarity in the output parameters between any given data stack and all the synthetic stacks by computing a non-parametric kernel density estimate of the joint posterior PDF between the fit parameters of the *data* stack ($\mathrm{BFR_{fit,data}}$ and $\sigma_{\mathrm{b,fit,data}}$), and then calculating the value of that PDF at the coordinates of the fit parameters for each synthetic stack ($\mathrm{BFR_{fit,synth}[j]}$, $\sigma_{\mathrm{b,fit,synth}}[\mathrm{j}]$). An example joint posterior PDF for one of the data stacks is shown in panel g). The calculated PDF values are used as weights ($w[\mathrm{j}]$) to apply the mapping from fit space to intrinsic space.

To estimate the *intrinsic* BFR of each data stack ($\mathrm{BFR_{int,data}}$), we simply take the weighted average of the *intrinsic* BFRs of the synthetic spectra ($\Sigma_j(\mathrm{BFR_{int,synth}[j]} \times w[\mathrm{j}])$). The same method is applied to estimate $\sigma_{\mathrm{b,int,data}}$.

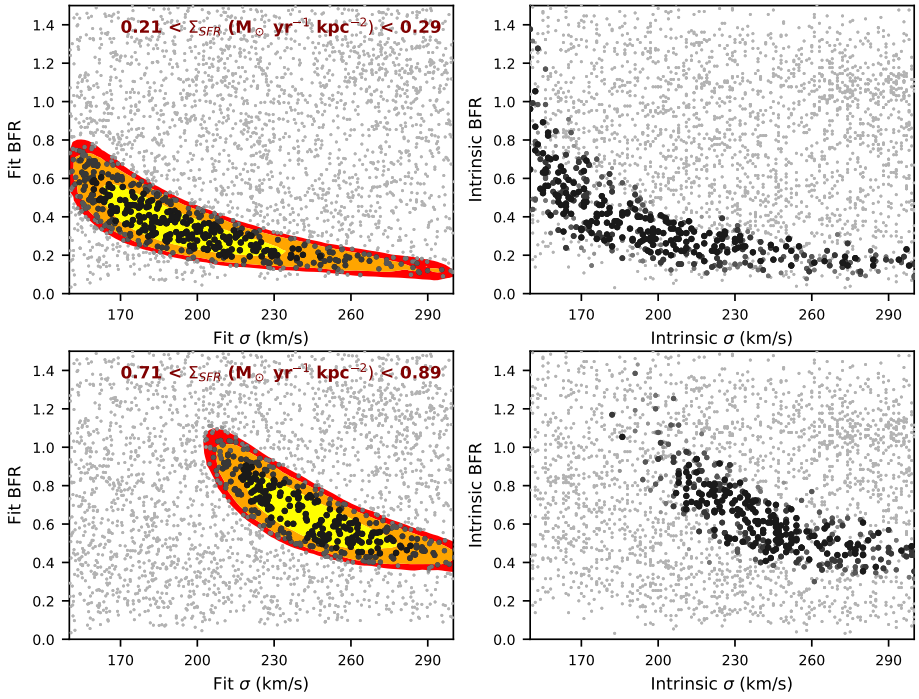

Figure 2.11: Figure illustrating the mapping between fit and intrinsic space for a low $\Sigma_{\rm SFR}$ stack (top row) and a high $\Sigma_{\rm SFR}$ stack (bottom row). The yellow, orange and red shaded regions in the background of the left hand panels show the 1σ, 2σ and 3σ levels of the joint posterior PDF of the relevant data stack. The dots in the left hand panels show the *best fit* σ_b and BFR values for all the synthetic spectra, and the dots in the right hand panels show the *intrinsic* σ_b and BFR values for all the synthetic spectra. The two left hand panels have the same set of dots, as do the two right hand panels, but the size and color of the dots in each panel indicate the weights assigned to each synthetic spectrum in the mapping for the relevant data stack (large dots with dark colors have the highest weights).

2.9.3 Results

The results of the forward modelling are summarised in Figures 2.11 and 2.12. Figure 2.11 illustrates the mapping between fit space and intrinsic space for two data stacks - one with low $\Sigma_{\rm SFR}$ (top row) and one with high $\Sigma_{\rm SFR}$ (bottom row). In each row, the left hand panel represents fit space and the right hand panel represents intrinsic space. The yellow, orange and red shaded regions in each left hand panel show the 1σ, 2σ and 3σ levels of the joint posterior PDF between the fit σ_b and the fit BFR for the relevant data stack. The dots in both left hand panels show the fit σ_b and BFR values for the complete set of synthetic stacks, but the sizes and colors of the dots differ between the panels to indicate the weighting assigned to each synthetic spectrum in the mapping for the relevant data stack (larger, darker dots indicate higher weighting). The right hand panels illustrate where the highest weighted synthetic stacks lie in the intrinsic σ_b - BFR space.

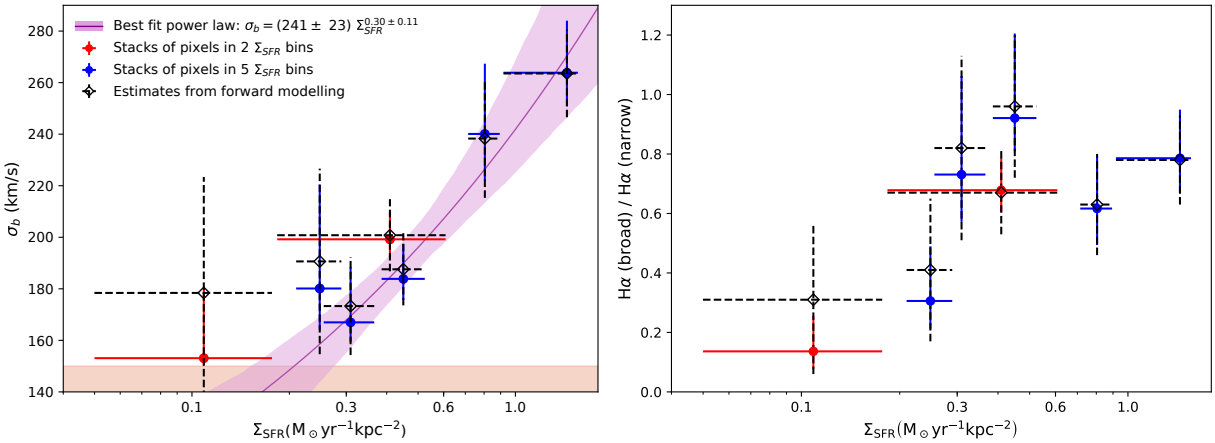

Figure 2.12: Same as Figures 2.5 and 2.6, but with the estimates from forward modelling over-plotted in black.

Figure 2.12 shows how the estimated intrinsic BFR and σ_b values for the data stacks compare to the best fit values. The errors on the estimated intrinsic values are calculated using the weighted standard deviation. For all but the lowest $\Sigma_{\rm SFR}$ stack, the best fit and intrinsic parameters match extremely well, confirming that the outflow parameters are tightly constrained in this regime. For the below median $\Sigma_{\rm SFR}$ stack, the best fit and intrinsic parameters are consistent within the 1σ errors, but there is some evidence that the best fit BFR may be under-estimated by a factor of $\sim$2, and the best fit σ_b may be under-estimated by ~ 30 km s^{-1}. Overall, the forward modelling suggests that the σ_b may flatten at low $\Sigma_{\rm SFR}$, and confirms that the BFR declines at $\Sigma_{\rm SFR} < 0.3\ M_\odot$ yr^{-1} kpc^{-2}, but indicates that the rate and shape of this decline is uncertain.

Chapter 3

From Nuclear to Circumgalactic: Zooming in on AGN-driven Outflows at $z \sim 2.2$ with SINFONI

This Chapter is a reprint of the ApJ publication *From Nuclear to Circumgalactic: Zooming in on AGN-driven Outflows at $z \sim 2.2$ with SINFONI* by Davies et al., 2020, ApJ, 894, 28. Published on May 1, 2020.

R. L. Davies performed the data analysis, developed the interpretation, and produced all of the text, figures, and tables presented in this publication, with the exception of the lens modelling and source plane reconstruction for the galaxy J0901+1814 and the associated explanatory material which is presented in Appendix A.1 (Section 3.9.1 of this thesis) and was provided by Dieter Lutz.

This work is based on observations collected at the European Organisation for Astronomical Research in the Southern Hemisphere under ESO Programme IDs 074.A-9011, 092.A-0082, 092.A-0091, 093.A-0079, 093.A-0110, 094.A-0568, 095.A-0047, 097.B-0065, 0101.A-0022. Based in part on data obtained at the LBT. The LBT is an international collaboration among institutions in the United States, Italy and Germany. LBT Corporation partners are: The University of Arizona on behalf of the Arizona Board of Regents; Istituto Nazionale di Astrofisica, Italy; LBT Beteiligungsgesellschaft, Germany, representing the Max-Planck Society, The Leibniz Institute for Astrophysics Potsdam, and Heidelberg University; The Ohio State University, and The Research Corporation, on behalf of The University of Notre Dame, University of Minnesota and University of Virginia. Based in part on observations made with the NASA/ESA Hubble Space Telescope, obtained from the data archive at the Space Telescope Science Institute. STScI is operated by the Association of Universities for Research in Astronomy, Inc. under

NASA contract NAS 5-26555. This paper makes use of the following ALMA data: ADS/JAO.ALMA#2015.1.00228.S, 2016.1.00726.S. ALMA is a partnership of ESO (representing its member states), NSF (USA) and NINS (Japan), together with NRC (Canada), MOST and ASIAA (Taiwan), and KASI (Republic of Korea), in cooperation with the Republic of Chile. The Joint ALMA Observatory is operated by ESO, AUI/NRAO and NAOJ.

Abstract - We use deep adaptive optics assisted integral field spectroscopy from SINFONI on the VLT to study the spatially resolved properties of ionized gas outflows driven by active galactic nuclei (AGN) in three galaxies at $z \sim 2.2$ – K20-ID5, COS4-11337 and J0901+1814. These systems probe AGN feedback from nuclear to circumgalactic scales, and provide unique insights into the different mechanisms by which AGN-driven outflows interact with their host galaxies. K20-ID5 and COS4-11337 are compact star forming galaxies with powerful $\sim$1500 km s^{-1} AGN-driven outflows that dominate their nuclear Hα emission. The outflows do not appear to have any impact on the instantaneous star formation activity of the host galaxies, but they carry a significant amount of kinetic energy which could heat the halo gas and potentially lead to a reduction in the rate of cold gas accretion onto the galaxies. The outflow from COS4-11337 is propagating directly towards its companion galaxy COS4-11363, at a projected separation of 5.4 kpc. COS4-11363 shows signs of shock excitation and recent truncation of star formation activity, which could plausibly have been induced by the outflow from COS4-11337. J0901+1814 is gravitationally lensed, giving us a unique view of a compact (R = 470 $\pm$ 70 pc), relatively low velocity ($\sim$650 km s^{-1}) AGN-driven outflow. J0901+1814 has a similar AGN luminosity to COS4-11337, suggesting that the difference in outflow properties is not related to the current AGN luminosity, and may instead reflect a difference in the evolutionary stage of the outflow and/or the coupling efficiency between the AGN ionizing radiation field and the gas in the nuclear regions.

3.1 Introduction

There is growing observational evidence for a direct connection between accretion onto supermassive black holes and the evolution of their host galaxies. The masses of stellar bulges are tightly correlated with the masses of their central supermassive black holes (see e.g. reviews in Alexander & Hickox, 2012; Kormendy & Ho, 2013). The redshift evolution in the black hole accretion rate density of the universe closely resembles the redshift evolution of the star formation rate (SFR) density (e.g. Madau & Dickinson, 2014; Aird et al., 2015). These relationships allude to the presence of some physical mechanism which connects the growth of supermassive black holes on parsec scales with the growth of galaxies on kiloparsec scales.

Cosmological simulations and semi-analytic models of galaxy formation have found that feedback from active galactic nuclei (AGN) can efficiently quench star formation (SF) and

account for the low baryon conversion efficiency in high mass systems (e.g. Di Matteo et al., 2005; Springel & Hernquist, 2005; Bower et al., 2006; Croton et al., 2006; Hopkins et al., 2006; Sijacki et al., 2007; Hopkins et al., 2008; Somerville et al., 2008; Schaye et al., 2015; Beckmann et al., 2017; Weinberger et al., 2017; Pillepich et al., 2018; Davé et al., 2019; Nelson et al., 2019). AGN activity can impact the host galaxy and the surrounding environment by ionizing or photodissociating the gas, heating the halo gas and reducing the rate of cold accretion onto the galaxy, and/or driving fast outflows that eject gas to large galactocentric distances and (temporarily or permanently) remove the fuel for SF (see Somerville & Davé, 2015, and references therein). Other possible mechanisms for quenching SF in high mass galaxies include morphological quenching (stabilization of the gas disk due to the presence of a stellar bulge; e.g. Martig et al. 2009), virial shock heating (e.g. Birnboim & Dekel, 2003), and cosmological starvation (reduced rate of cold gas accretion onto the dark matter halo; e.g. Feldmann & Mayer 2015).

AGN-driven outflows are expected to be most prevalent during the peak epoch of SF and black-hole growth, at $z \sim$ 1-3 (e.g. Madau & Dickinson, 2014; Aird et al., 2015). Studies of mass-selected samples of galaxies have found that AGN-driven ionized gas outflows are ubiquitous in the most massive galaxies at this redshift. Förster Schreiber et al. (2014) investigated the incidence and properties of outflows in seven massive galaxies with high quality [N II]+Hα spectra from the SINS/zC-SINF survey. They found that six out of seven galaxies have AGN-driven nuclear outflows, with a typical velocity full width half maximum (FWHM) of $\sim$ 1500 km s^{-1}. Four out of six objects observed at adaptive optics resolution ($\sim$ 1.5 kpc FWHM) have resolved outflows, with intrinsic diameters of 2-3 kpc. Statistical studies by Genzel et al. (2014) ($\sim$ 100 galaxies) and Förster Schreiber et al. (2019) ($\sim$ 600 galaxies) confirmed that AGN-driven outflows with velocities of 1000-2000 km s^{-1} are present in the majority of normal star forming galaxies above the Schechter mass, with the incidence reaching as high as 75% at $\log(M_*/M_\odot) \gtrsim 11.2$. Such statistical studies of AGN feedback across the normal galaxy population are crucial for constraining the duty cycle of AGN-driven outflows, and the role of AGN feedback in quenching SF.

There have also been extensive studies of ionized outflows in AGN-selected samples of galaxies at high redshift. Harrison et al. (2016) showed that the majority of X-ray AGN at $0.6 < z < 1.7$ drive outflows with velocities exceeding 600 km s^{-1}, and that the incidence of outflows increases with the AGN luminosity. Leung et al. (2019) found that 17% of AGN host galaxies from the MOSDEF survey show evidence for fast (400-3500 km s^{-1}), galaxy-wide outflows. Detailed studies of individual strong outflows in luminous AGN have revealed that high velocity material can often be detected to distances of $\sim$5-10 kpc; well beyond the effective radii of the host galaxies (e.g. Cano-Díaz et al., 2012; Harrison et al., 2012; Brusa et al., 2015b; Cresci et al., 2015; Carniani et al., 2016; Zakamska et al., 2016; Herrera-Camus et al., 2019). Powerful AGN-driven outflows therefore have the potential to interact with gas on galaxy scales.

It is well established that fast AGN-driven outflows are prevalent at $z \sim 2$, but the impact they have on the evolution of their host galaxies is strongly debated. Powerful outflows have the potential to exhaust the molecular gas reservoirs of their host galaxies

faster than SF, suggesting that they could be an important mechanism for quenching SF (e.g. Maiolino et al., 2012; Cicone et al., 2014). The onset of AGN-driven outflows at high stellar masses coincides with a sharp downturn in the average specific SFRs and molecular gas fractions of galaxies (Förster Schreiber et al., 2019), and there is a high incidence of AGN activity in the post-starburst region of the UVJ diagram (Belli et al., 2017), providing circumstantial evidence to suggest that AGN-driven outflows may be causally connected with SF quenching. However, direct evidence for this link is so far limited. Some studies have reported evidence for suppression of SF and molecular gas content along the trajectories of outflows from luminous quasars, but the SF outside the outflow region appears unaffected, and in some cases SF can be triggered by shocks at the boundary between the outflow and the surrounding interstellar medium (ISM) (e.g. Cano-Díaz et al., 2012; Brusa et al., 2015b; Cresci et al., 2015; Carniani et al., 2016, 2017) or can even occur in the outflow itself (Maiolino et al., 2017). Outflows driven by moderate luminosity AGN at $z \sim 2$ do not appear to have any significant impact on the instantaneous star formation activity of their host galaxies (Scholtz et al., 2020).

In this paper we use deep (5-20 hours on source) adaptive optics assisted near infrared integral field spectroscopy to characterize the resolved properties of AGN-driven outflows in three massive main sequence galaxies at $z \sim 2.2$, and study how the outflows impact their host galaxies and the surrounding environment. Our galaxy sample and datasets are outlined in Section 3.2. The methods used to measure the outflow parameters are described in Section 3.3. The results for K20-ID5, COS4-11337 and J0901+1814 are presented in Sections 3.4, 3.5 and 3.6, respectively. In Section 3.7 we discuss our results in the context of galaxy evolution, and we present our conclusions in Section 3.8.

Throughout this work we assume a flat ΛCDM cosmology with $H_0 = 70$ km s^{-1} Mpc^{-1} and $\Omega_0 = 0.3$. All galaxy properties have been derived assuming a Chabrier (2003) initial mass function.

3.2 Sample and Observations

K20-ID5, COS4-11337 and J0901+1814 (J0901 hereafter) were selected from the outflow subsample of the SINS/zC-SINF and KMOS^{3D} surveys (Förster Schreiber et al., 2014; Genzel et al., 2014; Förster Schreiber et al., 2019) because they trace AGN feedback on different spatial scales, from nuclear (hundreds of parsecs) to circumgalactic (> 5 kpc). The main properties of the galaxies are summarized in Table 3.1, and Figure 3.1 shows where the galaxies are located in the M_*-SFR plane, relative to the $z = 2$-2.5 SFR main sequence from Whitaker et al. (2014). The galaxy COS4-11363 is included because it is in a close pair with COS4-11337 and is discussed in detail in Section 3.5.

Our analysis is primarily based on high spatial resolution rest-frame optical integral field spectroscopy. Each of our galaxies was targeted with the Spectrograph for INtegral Field Observations in the Near Infrared (SINFONI; Eisenhauer et al. 2003; Bonnet et al. 2004) on the Very Large Telescope (VLT). The observations were performed using the K band filter (1.95-2.45μm), providing integral field datacubes covering the [N II]λ6548, H$\alpha\lambda$6563,

Table 3.1: Physical properties of the galaxies in our sample, derived as described in Section 3.2.

Property	K20-ID5	COS4-11337	COS4-11363	J0901
R.A.	03:32:31.4	10:00:28.70	10:00:28.71	09:01:22.4
Decl.	-27:46:23.2	+02:17:44.8	+02:17:45.4	+18:14:32.3
Redshift	2.224	2.096	2.097	2.259
$\log(M_*/M_\odot)$	11.2	11.3	11.1	11.2
$v_{\rm escape}$ (km s^{-1})	720	450	...	780
SFR$_{\rm best}$ ($M_\odot$ yr^{-1})	335	395	50	200
SFR Type	UV + IR	UV + IR	UV + IR	IR
A_V	1.3	0.8	0.9	1.2
$\log\left(\frac{L_{\rm AGN}}{\rm erg\ s^{-1}}\right)$	45.6	46.2	...	46.3

[N II]λ6584, and [S II]$\lambda\lambda$6716, 6731 lines. We used the Laser Guide Star (LGS) Adaptive Optics (AO) mode (Bonnet et al., 2003), achieving spatial resolutions of 0.18-0.24" (FWHM), or 1.5-2 kpc at $z \sim 2.2$. The high spatial resolution is required to measure the spatial extent of the outflows and to separate different line-emitting structures within the galaxies. The reduction of the SINFONI-AO data is described in detail in Förster Schreiber et al. (2018). The final K band SINFONI-AO cubes have a pixel scale of 0.05" and a spectral resolution of $\sim$ 85 km s^{-1}.

Our high resolution K band data are supplemented with seeing limited K band data, and H band data covering the [O III]λ4959, [O III]λ5007 and Hβ lines. We use the seeing limited K band observations to probe faint, extended [N II]+Hα emission that is undetected in the adaptive optics observations. The H band observations assist in decomposing the emission line profiles into multiple kinematic components, because the [O III]λ5007 line is strong in AGN host galaxies and is not blended even when a broad outflow component is present, unlike Hα which can be strongly blended with [N II]. The Hβ line, when robustly detected, is used to measure the Balmer decrement. The full set of observations used in this paper is summarized in Table 3.2.

3.2.1 K20-ID5

K20-ID5 (also known as 3D-HST GS4-30274, GS3-19791 and GMASS 0953) is a well studied star-forming galaxy at $z \sim 2.224$. It was identified as a high redshift candidate ($z_{\rm phot} > 1.7$) in the K20 survey of infrared bright galaxies (Cimatti et al., 2002), spectroscopically confirmed by Daddi et al. (2004), and followed up with deeper long slit spectroscopy as part of the GMASS survey (Kurk et al., 2013), and integral field spectroscopy as part of the SINS/zC-SINF (Förster Schreiber et al., 2009), KMOS^{3D} (Wisnioski et al., 2015) and KASHz (Harrison et al., 2016) surveys.

The left hand panel of Figure 3.2 shows an IJH color HST composite image of the region around K20-ID5. The galaxy has a bright and compact nucleus surrounded by fainter emission which is stronger and more extended on the western side of the galaxy than the

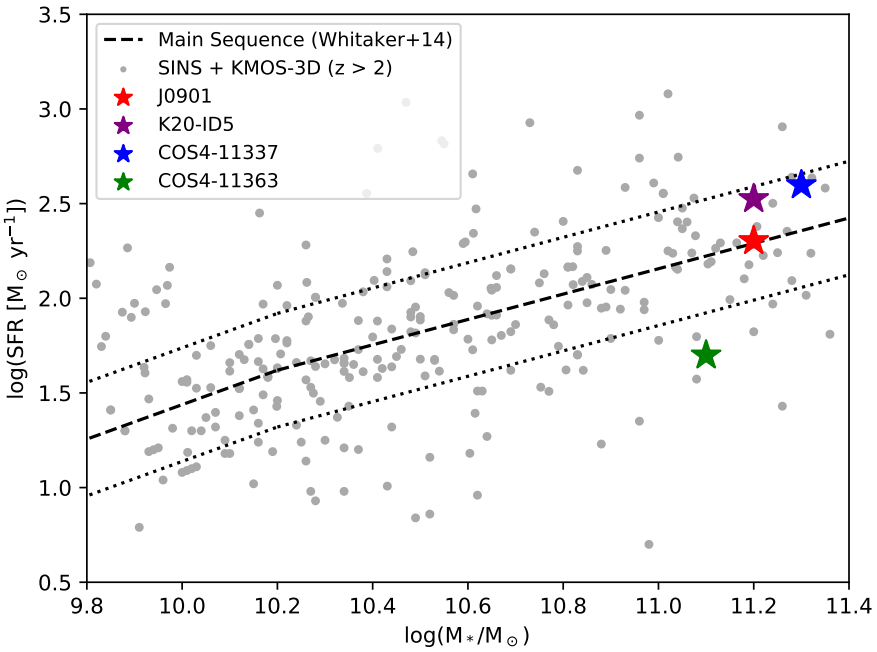

Figure 3.1: Distribution of the galaxies in our sample (colored stars) in the M_*-SFR plane. The black dashed line indicates the SFR main sequence at $z = 2 - 2.5$ from Whitaker et al. (2014), and the black dotted lines delineate the ± 0.3 dex interval around the main sequence. The grey dots show the distribution of galaxies at $z \sim 2 - 2.6$ from the KMOS^{3D} and SINS/zC-SINF surveys.

eastern side. The blue galaxy to the north of K20-ID5 is a lower redshift foreground object.

K20-ID5 has a stellar mass of $\log(M_*/M_\odot) = 11.2$ and a UV + IR SFR of 335 $M_\odot$ yr^{-1} (Wuyts et al., 2011b,a), placing it on the upper envelope of the main sequence (purple star in Figure 3.1)[1]. The galaxy is classified as an AGN host based on the X-ray luminosity, radio luminosity, mid-infrared colors and optical line ratios (e.g. van Dokkum et al., 2005; Genzel et al., 2014; Newman et al., 2014). The black hole accretion is driving a galactic wind which has been detected as a broad blueshifted component in the rest-frame optical emission lines (Genzel et al., 2014; Förster Schreiber et al., 2014; Loiacono et al., 2019; Scholtz et al., 2020), the rest-frame UV absorption lines (Cimatti et al., 2013), and tentatively in the CO(6-5) emission line (Talia et al., 2018).

K20-ID5 has an effective radius of $R_e = 2.5$ kpc (van der Wel et al., 2014) and is classified as a compact star forming galaxy (van Dokkum et al., 2015; Wisnioski et al., 2018). Molecular gas observations suggest that K20-ID5 has a starburst-like molecular gas depletion time and may therefore quench on a few hundred Myr timescale (Popping et al., 2017; Talia et al., 2018; Loiacono et al., 2019).

Our SINFONI-AO observations of K20-ID5 cover the white dashed region in the left

[1] Talia et al. (2018) and Scholtz et al. (2020) reported similar values for the stellar mass and SFR (consistent within 0.2 dex), based on SED modelling covering rest frame wavelengths of 0.1-1000 μm.

Table 3.2: Summary of the observations used in this paper.

Galaxy	Instrument	Filter	t_{int}	Pixel Scale	PSF FWHM	R	Program ID(s)
K20-ID5	SINFONI + AO	K	13h40m	0.05”	0.18”	3530	093.A-0110(B), 097.B-0065(B)
...	KMOS	K	17h30m	0.2”	0.36”	3500	092.A-0091(A), 095.A-0047(B)
...	SINFONI	H	2h00m	0.125”	0.68”	2500	074.A-9011
COS4-11337/11363	SINFONI + AO	K	5h00m	0.05”	0.24”	3530	097.B-0065(A)
...	KMOS	K	16h35m	0.2”	0.40”	3590	093.A-0079(A)
...	KMOS	H	4h25m	0.2”	0.66”	3470	0101.A-0022(A)
J0901	SINFONI + AO	K	9h30m	0.05"	0.20”	3530	093.A-0110(A), 094.A-0568(A)
...	SINFONI	K	9h00m	0.125”	∼0.6”	3530	092.A-0082(A)
...	LBT/LUCI + AO	H	2h15m	0.118”	0.37”	5470	LBT-2018A-C0208-3

The KMOS data were obtained as part of the KMOS^{3D} Survey (Wisnioski et al., 2015, 2019). The SINFONI seeing limited and adaptive optics datasets were reduced as described in Förster Schreiber et al. (2009) and Förster Schreiber et al. (2018), respectively. The LUCI longslit data for J0901 are described in Section 3.2.3. The PSF FWHM values were measured from 2D Moffat (KMOS data) or Gaussian (SINFONI and LUCI data) fits to images of standard stars obtained simultaneously (KMOS) or close in time (SINFONI and LUCI) to the science data, with the exception of the J0901 seeing limited SINFONI dataset for which the PSF FWHM was estimated by comparing the R band seeing (0.96”) to the distributions of R band seeing and K band PSF FWHM values from the KMOS^{3D} survey (Figure 2 in Wisnioski et al. 2019).

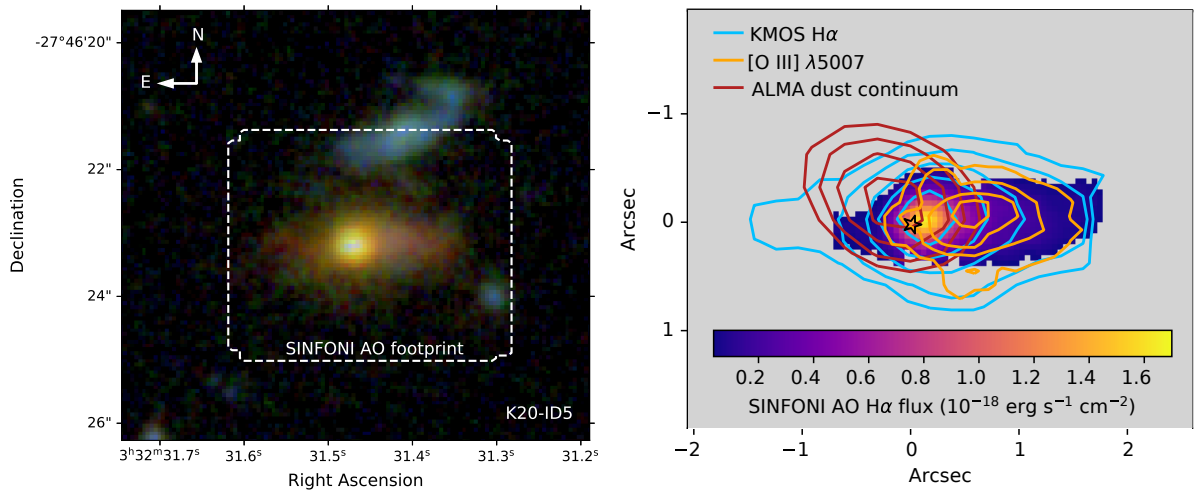

Figure 3.2: Left: K20-ID5 color composite using HST F160W (red) + F125W (green) + HST F814W (blue), with the footprint of the SINFONI-AO data overplotted. The blue galaxy to the north of K20-ID5 is a lower redshift (foreground) system. Right: SINFONI-AO Hα flux map of K20-ID5, with contours of the KMOS Hα emission (blue), [O III]λ5007 emission (from seeing limited SINFONI data, yellow) and ALMA band 4 dust continuum (brown) overplotted. The black star indicates the kinematic center of the galaxy.

hand panel of Figure 3.2. Over the same region we also have deep seeing-limited KMOS K band observations and seeing limited SINFONI H band observations. The right hand panel of Figure 3.2 shows the distribution of the SINFONI-AO Hα flux (mapped in colors), the KMOS Hα and SINFONI [O III] flux (measured from single Gaussian fits; blue and yellow contours, respectively), and the dust distribution traced by the ALMA band 4 continuum emission (program 2015.1.00228.S, PI: G. Popping) (brown contours). The SINFONI-AO Hα flux map has a similar asymmetric distribution to the broadband flux, but the KMOS^{3D} data indicate that Hα emission is indeed present on the fainter eastern side of the galaxy, and further analysis reveals that the ionized gas follows a regular rotation curve on both sides of the nucleus (Wisnioski et al., 2018). The ALMA data suggest that there is 2.5 $\times$ 10^8 $M_\odot$ of dust centered just to the east of the nucleus (Popping et al., 2017; Talia et al., 2018), and the Balmer decrement indicates significant attenuation of nebular emission in the nuclear region of the galaxy (A_V = 2.7; see Section 3.4.3). The large amount of dust could explain the asymmetry in the UV/optical emission, as well as the significant offset between the Hα and [O III] flux peaks (also seen in Loiacono et al. 2019 and Scholtz et al. 2020).

The obscuration also complicates the measurement of the AGN luminosity. Using the X-ray hardness ratio as a tracer of the obscuration yields a column density of $\log(N_{\rm H}/{\rm cm}^{-2}) = 23.2$, corresponding to an intrinsic hard (2-10 keV) X-ray luminosity of $\log(L_X/{\rm erg\ s}^{-1}) = 43.0$ and a bolometric luminosity of $\log(L_{\rm AGN}/{\rm erg\ s}^{-1}) = 44.2$ (using the bolometric correction adopted by Rosario et al. 2012; their Equation 1). However,

ongoing X-ray spectral modelling efforts suggest that the AGN may be Compton thick (M. E. Dalla Mura et al. in prep), indicating that the hard X-ray luminosity is likely to be underestimated. Therefore, we also estimate the AGN luminosity from the [N II] line (as described in Förster Schreiber et al. 2019), yielding $\log(L_{\rm AGN}/{\rm erg\ s^{-1}}) = 45.9$. This value is much closer to what one would derive from the X-ray flux if the AGN was assumed to be Compton thick. Finally, we use the Spitzer/MIPS 24μm (rest-frame 7.4μm) flux density to derive an upper limit on the AGN luminosity. Lutz et al. (2004) found a linear correlation between $\nu F_\nu(6\mu{\rm m})$ and F(2-10 keV), with a typical slope of 0.23 for Seyfert 2 AGN. The observed mid-infrared flux includes contributions from both SF and AGN activity, and therefore the total νF_ν provides an upper limit on the AGN luminosity for K20-ID5. We measure $\log(\nu L_\nu[7.4\mu{\rm m},\ {\rm AGN}]/{\rm erg\ s^{-1}}) < 45.2$, corresponding to a hard X-ray luminosity of $\log(L_X/{\rm erg\ s^{-1}}) < 44.6$ and a bolometric luminosity of $\log(L_{\rm AGN}/{\rm erg\ s^{-1}}) < 46.4$. The upper limit is 0.5 dex higher than the luminosity calculated from [N II]. Therefore, we adopt the average of the X-ray and [N II] estimates as our fiducial AGN luminosity; i.e. $\log(L_{\rm AGN}) = 45.6$.

3.2.2 COS4-11337/COS4-11363

COS4-11337 and COS4-11363 are two massive ($\log(M_*/M_\odot) \sim 11$), compact ($R_e \leq 2.5$ kpc; van der Wel et al. 2014) galaxies which lie very close in redshift ($\Delta v = 150$ km s^{-1}) and have a projected separation of only 0.65" (5.4 kpc), and may therefore be in the early stages of a major merger. The dwarf starburst galaxy COS4-11530 lies 33 kpc to the north-west of the pair at a very similar spectroscopic redshift ($z = 2.097$). The left hand panel of Figure 3.3 shows an IJH color HST composite image of the triplet.

The stellar masses and A_V values for COS4-11337 and COS4-11363 were initially derived using standard SED modelling (following Wuyts et al. 2011b), assuming an exponentially declining star formation history and considering e-folding times in the range $\log(\tau/{\rm yr}) = 8.5$-10.0. The best fit galaxy parameters for COS4-11337 are $\log(M_*/M_\odot) = 11.3$ and $A_V = 0.8$. We found that the fit for COS4-11363 could be significantly improved by adopting either a shorter e-folding time (100 Myr) or a truncated star formation history. Both models give best fit galaxy parameters of $\log(M_*/M_\odot) = 11.1$ and $A_V = 0.9$.

We calculate the IR SFR of the system using the Herschel PEP 160μm flux which we convert to $L_{\rm IR}$ using the Wuyts et al. (2008) SED template. The galaxies are strongly blended in the far infrared imaging, so it is only possible to calculate the total (combined) SFR of the system, which is 424 $M_\odot$ yr^{-1}. The SED fitting suggests that COS4-11337 has a $\sim 10\times$ higher SFR than COS4-11363, and the Hα flux ratio between the two nuclei is 47, or 14 when removing the contribution of the outflow to the Hα flux of COS4-11337 (see Section 3.5.1). Therefore, we divide the IR SFR between the galaxies in a 10:1 ratio; i.e. ${\rm SFR_{IR,11337}} = 385\ M_\odot$ yr^{-1} and ${\rm SFR_{IR,11363}} = 39\ M_\odot$ yr^{-1}. We add the UV SFRs measured from the SED fitting for the individual systems, and obtain UV + IR SFRs of 395 $M_\odot$ yr^{-1} and 50 $M_\odot$ yr^{-1} for COS4-11337 and COS4-11363, respectively.

Based on our derived parameters, COS4-11337 lies on the upper envelope of the star

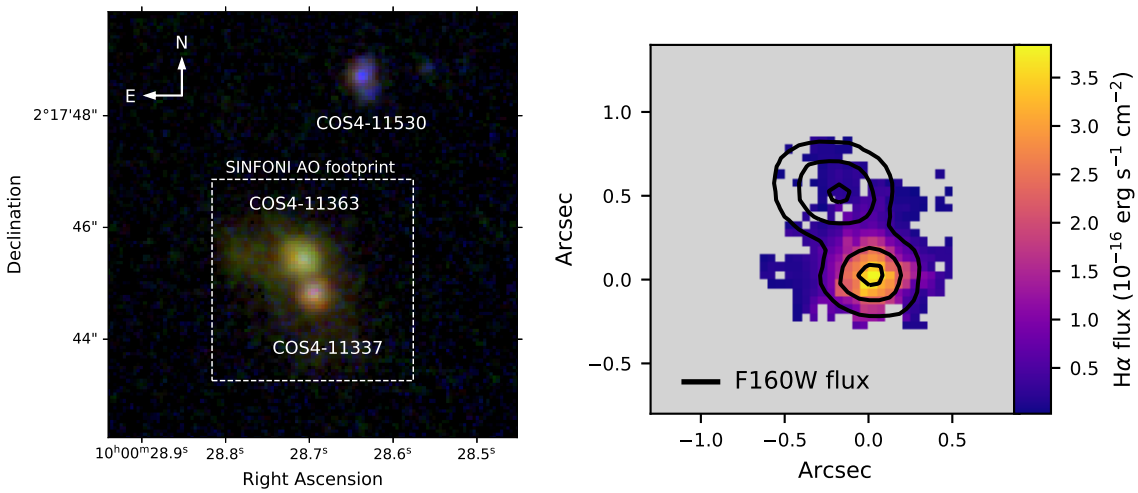

Figure 3.3: Left: Color composite of the COS4-11337/COS4-11363/COS4-11530 triplet using HST F160W (red) + F125W (green) + F814W (blue). The white box indicates the region covered by our SINFONI-AO and KMOS observations. Right: Map of the Hα flux from the SINFONI-AO cube, with contours of the F160W emission overlaid (at levels of 10%, 25% and 75% of the peak flux).

formation main sequence (blue star in Figure 3.1), and COS4-11363 lies about a factor of three below the main sequence (green star in Figure 3.1).

Grism spectroscopy from the 3D-HST survey (Brammer et al., 2012; Momcheva et al., 2016) indicates that COS4-11337 has strong [O III] emission, while COS4-11363 has very weak line emission. COS4-11337 is classified as an AGN based on both the optical line ratios (Genzel et al., 2014) and the hard X-ray luminosity ($\log(L_X/\mathrm{erg\ s^{-1}}) = 44.5$; Luo et al. 2017), which corresponds to an AGN bolometric luminosity of $\log(L_{\mathrm{bol,AGN}}/[\mathrm{erg\ s^{-1}}]) = 46.2$ (Rosario et al., 2012). We note that a very similar bolometric luminosity is obtained from the extinction-corrected [O III] luminosity, assuming a bolometric correction factor of 600 (Netzer, 2009).

Seeing limited H and K band observations of the COS4-11337/COS4-11363 system were obtained as part of the KMOS^{3D} survey (Wisnioski et al., 2015, 2019). Broad forbidden lines reveal a strong outflow originating from COS4-11337. The beam convolved line emission from COS4-11337 is dominant everywhere line emission is detected, but the [N II]/Hα ratio increases towards the nucleus of COS4-11363, indicating that COS4-11363 does have some (weak) line emission. We targeted the pair with SINFONI + AO to allow us to robustly separate the line emission from the two galaxies. The right hand panel of Figure 3.3 shows a map of the Hα flux from our SINFONI-AO data, with contours of the HST F160W emission overlaid. The Hα flux primarily originates from COS4-11337, but is also detected at the location of COS4-11363, consistent with the results from KMOS^{3D} and the 3D-HST grism spectroscopy.

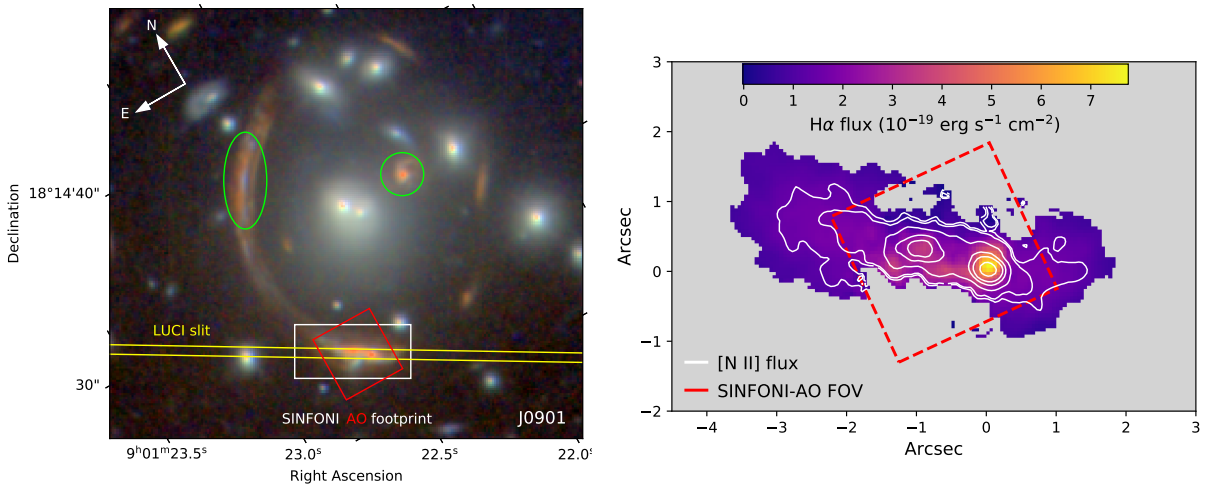

Figure 3.4: Left: J0901 color composite using HST F160W (red) + F110W (green) + F814W (blue), with the footprints of the LUCI slit (yellow), and the SINFONI seeing limited (white) and AO (red) data overplotted. J0901 is triply imaged by the lensing cluster. The south eastern image is at the center of the SINFONI footprint, and the north eastern and western images are indicated by the green ellipses. Right: Image plane Hα flux map of J0901, constructed by combining the AO data (inside the red rectangle) with the seeing limited data (outer region). The white contours trace the [N II] flux distribution.

3.2.3 J0901

SDSS J090122.37+181432.3 (abbreviated to J0901) is a strongly lensed, triply imaged galaxy at $z = 2.259$, first reported by Diehl et al. (2009). The left hand panel of Figure 3.4 shows an IJH color HST composite image of the region surrounding the lensing cluster, which is at a redshift of $z = 0.346$. The green circles indicate the locations of the north eastern (NE) and western (W) images of J0901. The south eastern (SE) image is at the center of the white and red rectangles, which indicate the coverage of our SINFONI seeing limited and adaptive optics datasets, respectively. We targeted the SE arc because the similarly bright NE fold arc is strongly distorted and images only part of the source.

Rest-frame UV and optical spectra of J0901 reveal high [N II]/Hα and [O III]/Hβ ratios (Hainline et al., 2009) and clear [N V] emission (Diehl et al., 2009), indicative of AGN activity. The [N II]+Hα emission line complex shows a clear broad component which likely traces an AGN-driven outflow (Genzel et al., 2014).

We obtained K band SINFONI observations of J0901, using the seeing limited mode to probe the extended flux of the galaxy and the adaptive optics mode to obtain a high resolution view of the center of the galaxy. The right hand panel of Figure 3.4 shows an image plane Hα flux map constructed from the combination of the seeing limited and AO datasets. The fluxes for the pixels inside the red rectangle were measured from the AO data, and the fluxes for the pixels in the outer region were measured from the seeing limited data. The white contours show the spatial distribution of the [N II] emission.

We also observed J0901 in the H band using the LUCI long slit spectrograph on the Large Binocular Telescope (LBT), aided by the Advanced Rayleigh guided Ground-layer adaptive Optics System (ARGOS; Rabien et al., 2019). The observations consist of one 45 minute block from LUCI-1 on 2018-03-02 and one 45 minute block from each of LUCI-1 and LUCI-2 on 2018-03-03. The three blocks were reduced independently using the Flame pipeline (Belli et al., 2018), and then combined, weighted by the uncertainty on each pixel. The spatial resolution of the combined dataset is 0.37", and the spectral resolution calculated from a stack of skylines close to the wavelength of [O III]λ5007 is 55 km s^{-1}. The final 2D spectrum was flux calibrated using the slit alignment star.

The strong gravitational lensing causes magnification and distortion of the light which must be accounted for in order to derive the intrinsic properties of J0901. We use Lenstool and archival HST imaging to build a model for the mass distribution of the lensing cluster, as described in Appendix 3.9.1. This model allows us to convert from observed (image plane) flux distributions to intrinsic (source plane) flux distributions, and derive the intrinsic properties of the galaxy.

We measure an intrinsic [O III] luminosity of $\log(L_{[\mathrm{OIII}]}/[\mathrm{erg\ s^{-1}}]) = 43.5$, corresponding to an AGN bolometric luminosity of $\log(L_{\mathrm{bol,AGN}}/[\mathrm{erg\ s^{-1}}]) = 46.3$ (see Appendix 3.9.2). We note that the AGN luminosity is relatively uncertain due to both the lack of hard X-ray observations and the uncertainties associated with the source plane reconstruction. We fit SED models to the magnification corrected F160W, F814W and F435W fluxes, yielding a stellar mass of $\log(M_*/M_\odot) = 11.2$ and an A_V of 1.2 (Appendix 3.9.3). Using the 160μm flux measurement presented in Saintonge et al. (2013) we derive a SFR of 200 $M_\odot$ yr^{-1} (Appendix 3.9.4) which places J0901 on the SFR main sequence (red star in Figure 3.1).

3.3 Measuring Outflow Parameters

3.3.1 Isolating Emission Associated with Outflows

Ionized gas outflows are generally observed as broadened (FWHM $\gtrsim$ a few hundred km/s) emission line components underneath the narrower emission produced by gas in the disk of the galaxy. The outflow and disk components can be robustly separated for individual spaxels in integral field observations of local galaxies, but even with our deep observations the emission line signal-to-noise (S/N) is only high enough to permit a robust disk-outflow decomposition in the brightest spaxels. Therefore, we calculate the properties of the AGN-driven outflows in K20-ID5, COS4-11337 and J0901 using spectra integrated across the nuclear regions of the galaxies.

The method used to extract the nuclear spectra is described in detail in Section 2.5.1 of Förster Schreiber et al. (2019). In short, each datacube was median subtracted to remove continuum emission, σ-clipped to remove skyline residuals, and smoothed spatially using a Gaussian filter with a FWHM of 3-4 pixels. For each spaxel in each datacube, we simultaneously fit the [N II]λ6548, Hα and [N II]λ6583 lines as single Gaussians with a

common velocity offset and velocity dispersion, and then shifted the spectrum so that the narrow line cores were centered at zero velocity. This velocity shifting removes (and therefore prevents artificial line profile broadening associated with) large scale gravitationally driven velocity gradients, but has minimal impact on the shapes of the outflow line profiles because their line widths are $\sim$ 5-10$\times$ larger than the maximum velocity shifts. From the velocity shifted cubes we extracted spectra integrated over the region where broad outflow emission was detected ($\sim$ 1-3 kiloparsecs in radius).

We fit the line profiles in each nuclear spectrum as a superposition of two kinematic components - one for the galaxy and one for the outflow. An example fit (to the nuclear spectrum of COS4-11337) can be seen in the left hand panel of Figure 3.8. We again assumed a common velocity offset and velocity dispersion for all lines in each kinematic component, and fixed the [N II]λ6583/[N II]λ6548 and [O III]λ5007/[O III]λ4959 ratios to 3 (the theoretical value set by quantum mechanics).

3.3.2 Outflow Extent

We use the two component fits to the nuclear spectra to determine which spectral channels are dominated by the outflow component, and integrate the flux over the outflow channels in each spaxel to create maps of the outflow emission. We compare the curves of growth of the outflow emission and the point spread function (PSF) to confirm that the outflows are resolved. We calculate the intrinsic (PSF-corrected) size of the outflows by modelling the observed outflow emission as a 2D Gaussian (representing the intrinsic outflow emission) convolved with the PSF, and adopt the half width at half maximum (HWHM) of the Gaussian as the radius of the outflow. In this modelling we use the empirically-derived average AO PSF from the SINS/zC-SINF AO Survey (Förster Schreiber et al., 2018), which has sufficiently high S/N that both the core (AO corrected) and wing (uncorrected) components of the PSF can be robustly characterized. The average PSF is constructed from datasets obtained under similar conditions to our targets, and the FWHM measured from the curve of growth of the average PSF is 0.18", which is similar to the FWHM values measured for our datasets (see Table 3.2).

3.3.3 Outflow Velocity

The outflow velocity is calculated by taking the full width at zero power (FWZP) of the entire [N II]+Hα complex, subtracting the velocity separation of the [N II] doublet lines (1600 km s^{-1}), and dividing by two (following Förster Schreiber et al., 2019). This measurement yields the maximum line-of-sight velocity of the outflowing material, which should be close to the true outflow velocity for a constant velocity wide angle outflow.

3.3.4 Mass Outflow Rate ($\dot{M}_{\rm out}$) and Mass Loading Factor (η)

The mass outflow rate $\dot{M}_{\rm out}$ of a constant velocity spherical or (multi-)conical outflow can be calculated from the Hα luminosity of the outflow ($L_{\rm H\alpha,out}$) as follows:

$$\dot{M}_{\rm out}\,({\rm M}_\odot\,{\rm yr}^{-1}) \;=\; 33\left(\frac{1000\ {\rm cm}^{-3}}{n_e}\right)\left(\frac{v_{\rm out}}{1000\ {\rm km\ s}^{-1}}\right)\times\left(\frac{1\ {\rm kpc}}{R_{\rm out}}\right)\left(\frac{L_{\rm H\alpha,out}}{10^{43}\ {\rm erg\ s}^{-1}}\right) \quad (3.1)$$

$R_{\rm out}$ is the radial extent of the outflow, $v_{\rm out}$ is the outflow velocity and n_e is the local electron density of the ionized gas in the outflow (Genzel et al., 2011; Newman et al., 2012a)[2]. The mass loading factor η is defined as $\eta = \dot{M}_{\rm out}/{\rm SFR}_{\rm best}$.

The biggest uncertainty in the calculation of $\dot{M}_{\rm out}$ and η is the electron density, which is extremely challenging to constrain for AGN-driven outflows at z$\sim$2. In principle, the electron density of the ionized gas in the outflow can be measured from the [S II]λ6716/[S II]λ6731 ratio in the outflow component (Osterbrock & Ferland, 2006). However, the [S II] lines are weak compared to Hα and [N II], and become strongly blended in the presence of a broad outflow component, making it very difficult to constrain a two component decomposition of the [S II] line profile. Förster Schreiber et al. (2019) fit two kinematic components to a high S/N stacked spectrum of 30 AGN-driven outflows at $0.6 < z < 2.6$, and found that the average electron density of the outflowing material is ~ 1000 cm^{-3}. Their stack includes two of the three galaxies in our sample. Several recent studies of AGN-driven outflows at low and intermediate redshift have found similarly high densities in the outflowing gas (e.g. Perna et al., 2017; Kakkad et al., 2018; Husemann et al., 2019; Shimizu et al., 2019). We therefore adopt $n_e = 1000$ cm^{-3}.

3.3.5 Extinction Correction

The Hα emission from the outflowing gas is attenuated by dust along the line of sight to the nuclear regions of the galaxies. To calculate the intrinsic mass outflow rates, we need to correct the observed Hα fluxes for extinction.

Our observations cover both the Hα and Hβ emission lines. When Hβ is detected, the best method for correcting emission line luminosities for extinction is to use the Balmer decrement, which directly probes the attenuation along the line of sight to the nebular line emitting regions. The Hβ line is too weak to robustly separate into disk and outflow components, and therefore we adopt the integrated Balmer decrement. The theoretical unattenuated Balmer decrement for Case B recombination at T = 10^4 K is 2.86 (Osterbrock & Ferland, 2006). However, this value can increase to 3.1 in the presence of an AGN (Gaskell & Ferland, 1984). Therefore, we adopt an intrinsic Balmer decrement of 3.1. We assume the nebular extinction follows the Cardelli et al. (1989) curve.

In cases where the Balmer decrement cannot be measured, we correct for extinction using the global continuum A_V of the galaxy, and account for extra attenuation

[2]Equation 3.1 assumes that the outflowing gas is photoionized. If the ionized gas in the outflow is primarily collisionally excited and has a temperature of $\sim 2 \times 10^4$ K, the mass outflow rates would scale by a factor of ~ 0.6 (see Appendix B of Genzel et al., 2011).

of the nebular emission using the empirical formula presented by Wuyts et al. (2013) ($A_{H\alpha}$ = 1.9 A_{stars} - 0.15 A^2_{stars}). The empirical correction assumes that the extinction follows the Calzetti et al. (2000) curve, but the functional form was chosen to produce the best agreement between the Hα and UV + IR SFRs for SFGs at 0.7 < z < 1.5 (i.e. $A_{H\alpha} \sim$ -2.5 $\log_{10}$ ($SFR_{H\alpha}/SFR_{UV+IR}$)), and therefore the derived $A_{H\alpha}$ should be largely independent of the chosen attenuation curve.

We note that in both cases we assume that the outflow emission and galaxy nebular emission experience similar attenuation, which may not be the case if the two components have different spatial distributions. Higher S/N and/or space-based observations of the Hβ line are required to calculate the Balmer decrements of the galaxy and outflow components separately.

3.4 K20-ID5: A Powerful Galaxy Scale Outflow

3.4.1 Velocity Field and Kinematic Modelling

Our SINFONI-AO data reveal previously unresolved kinematic structures in K20-ID5, providing key insights into the nature of the line emission in the nuclear region of the galaxy. The kinematic properties of K20-ID5 are summarized in Figure 3.5.

The first row of panels shows the velocity fields measured from the KMOS and SINFONI-AO data. At the lower resolution and coarser spatial sampling of the KMOS data, the velocity field looks quite regular, but the higher resolution SINFONI-AO data reveal a twist and a steepening of the velocity gradient in the central 0.4". The bottom panel of Figure 3.5 shows the 1D velocity profile, extracted in 5×5 spaxel apertures along the kinematic major axis of the galaxy (PA = -84.5°). The colored dots trace the velocity of the ionized gas as a function of galactocentric distance in the SINFONI-AO data, and the purple squares show the velocity profile extracted from the KMOS data. The velocities are derived from single component Gaussian fits to the Hα and [N II] lines, but we verified that very similar profiles are recovered when performing two component fitting to account for the presence of the broad emission component in the nuclear region. Therefore, the SINFONI-AO data reveal irregular narrow component kinematics in the nuclear region of K20-ID5.

We exploit the regularity of the KMOS velocity field to model the kinematics of the extended disk. We model the velocity field using DYSMALPY, a python implementation of the dynamical fitting code DYSMAL (Cresci et al., 2009; Davies et al., 2011; Wuyts et al., 2016; Übler et al., 2018). DYSMAL is a forward modeling code which builds a model for the mass distribution (including one or more of a disk, bulge and dark matter halo), produces a mock datacube with a given spatial and spectral sampling, convolves the datacube with the given line spread function and spatial PSF, produces model velocity and velocity dispersion fields, and compares the model to the data. We fit the KMOS velocity field using an exponential disk model with the mass, effective radius, inclination and position angle of the disk as free parameters. We do not fit the velocity dispersion

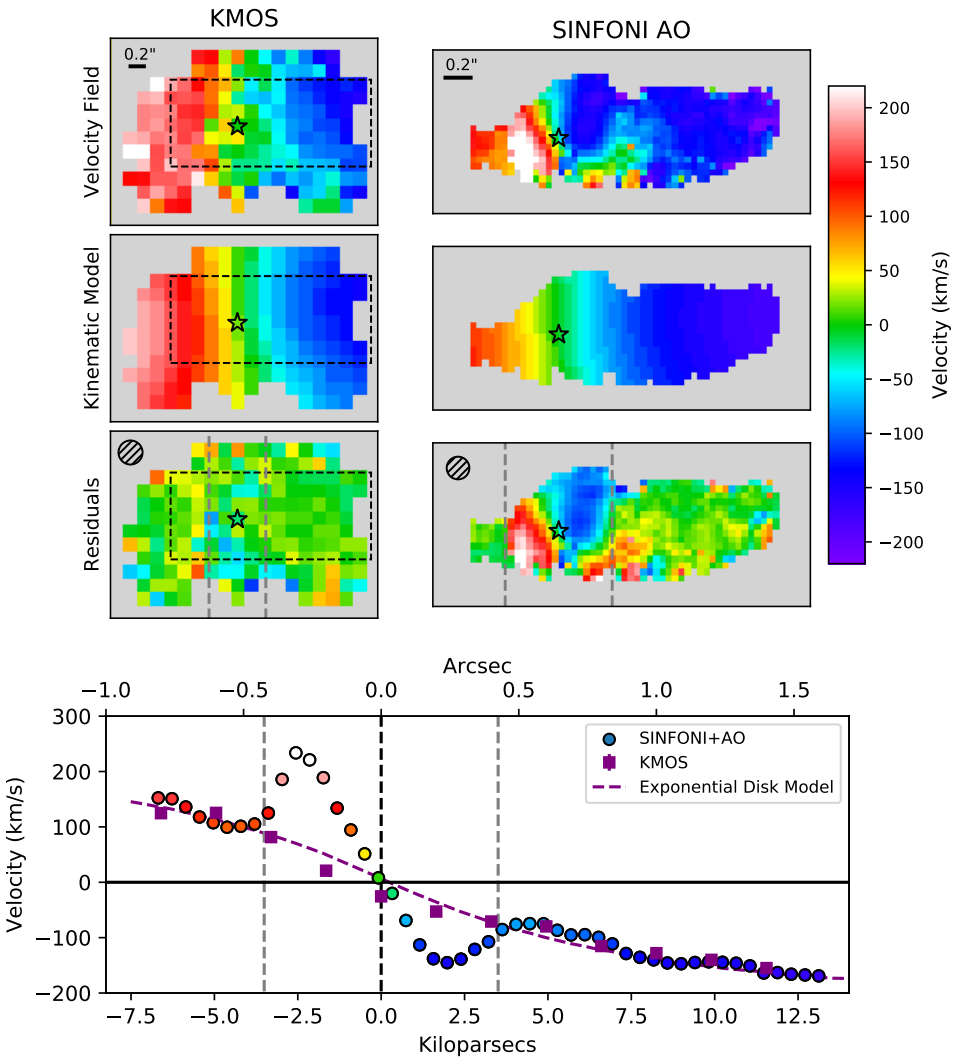

Figure 3.5: Top: Summary of the 2D kinematic modelling for K20-ID5. The first row of panels shows the velocity fields measured from the KMOS (left) and SINFONI-AO (right) data. The SINFONI-AO data covers a sub-region of the KMOS data, indicated by the black dashed rectangle. The black stars indicate the kinematic center of the galaxy. The second row shows the exponential disk model fit to the KMOS velocity field, mock observed at the spatial resolution and sampling of both datasets. The third row shows the residuals after subtracting the best fit model from the measured velocity fields. A strong nuclear velocity gradient is visible in the SINFONI-AO residuals, across the region bounded by the grey dashed lines. Bottom: 1D velocity profiles extracted along the kinematic major axis (PA = -84.5°). The colored dots trace the velocity profile measured from single component fits to SINFONI-AO spectra, where the colors represent the velocity on the same color scale used for the velocity field maps. The purple squares indicate the velocity profile measured from the KMOS data, and the purple dashed line shows the profile of the exponential disk model fit to the KMOS velocity field.

field because it is heavily influenced by the outflow in the central regions.

The best fit model for the extended velocity field of K20-ID5 is shown in the second row of Figure 3.5, at the resolution/sampling of the KMOS data in the left column and at the resolution/sampling of the SINFONI-AO data in the right column. The third row of panels shows the residuals after subtracting the best fit model from the measured velocity field for each of the datasets. The best fit model reproduces the KMOS velocity field very well, leaving only small amplitude residuals (less than 55 km s^{-1} in 90% of spaxels) with no clear spatial structure. On the other hand, the discontinuity in the SINFONI-AO velocity field is visible as a strong velocity gradient in the residuals, going from -120 km s^{-1} to +240 km s^{-1} at an angle of $\sim 25°$ to the major axis of the disk.

The twist in the narrow component kinematics could trace either a misaligned core or an outflow. In order to determine which of these is more likely, we examine how the line profiles and the single component [N II]/Hα ratio and velocity dispersion differ between the nuclear region and the extended disk of the galaxy. The left hand panels of Figure 3.6 show maps of the single component [N II]/Hα ratio (top) and velocity dispersion (bottom) from the SINFONI-AO data. The [N II]/Hα ratio is elevated in the nucleus compared to the extended disk region, and more interestingly shows a sharp boundary between the nucleus and the extended disk on the eastern (receding) side of the galaxy. This sharp boundary coincides with an abrupt change in the magnitude of the velocity residuals. The velocity dispersion is also elevated in the nuclear region, but decreases gradually with increasing galactocentric distance.

The right hand panels of Figure 3.6 show a position-velocity (p-v) diagram extracted along the E-W direction (i.e. the p-v diagram and the maps on the left side of the figure share the same x-axis), and spectra extracted in eight slices which are numbered on both the p-v diagram and the corresponding panels. Slices 1, 6, 7 and 8 trace the regularly rotating extended disk of the galaxy and show narrow line emission and low [N II]/Hα ratios. Slices 2-4 trace the kinematically anomalous nuclear region, and show strong broad emission and high [N II]/Hα ratios. Slice 5 traces the western edge of the nuclear region where the broad outflow emission is still visible but is overpowered by narrow emission from the galaxy disk. The [N II]/Hα ratio is intermediate between the nuclear and extended disk regions, but the narrow lines follow the velocity field of the extended disk.

The kinematically anomalous nuclear region of K20-ID5 is characterized by broad line profiles and high [N II]/Hα ratios, whereas the regularly rotating regions at larger radii are dominated by narrow disk emission with much lower [N II]/Hα ratios. This provides strong circumstantial evidence that the residual nuclear velocity gradient is tracing the outflow.

The nuclear velocity gradient reflects the kinematics of the narrow line peaks, leading to the conclusion that both the narrow and broad line emission in the nuclear region of K20-ID5 must be primarily associated with outflowing material. In other words, the outflow has a non-Gaussian line-of-sight velocity distribution which can be approximated by the superposition of a narrow and a broad Gaussian component. 3D biconical outflow models suggest that outflow emission line profiles can have non-Gaussian shapes, and may

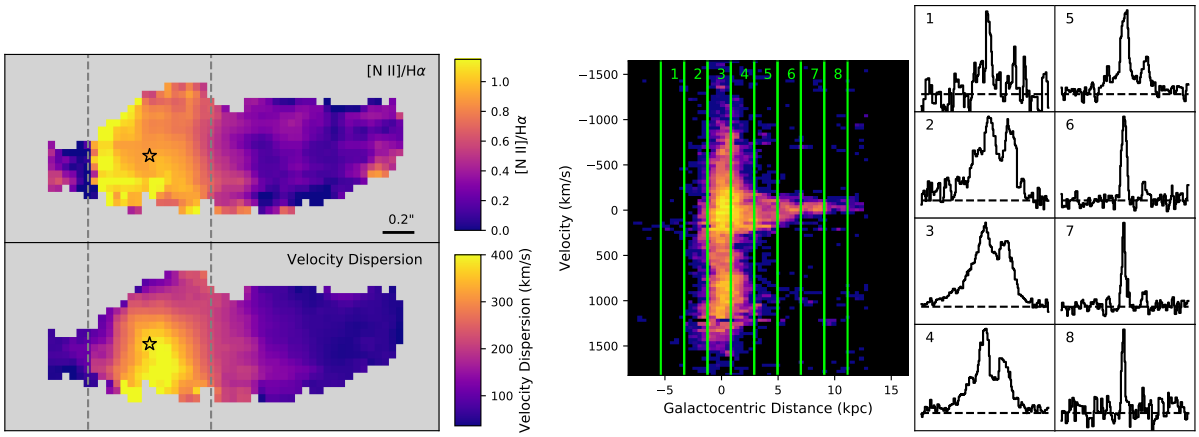

Figure 3.6: Left: Maps of the [N II]/Hα ratio (top) and single component velocity dispersion (bottom) for K20-ID5. The grey dashed lines delineate the region where strong velocity residuals are observed (see Figure 3.5). Right: Position-velocity (p-v) diagram for K20-ID5 (constructed by collapsing the cube along the N-S direction), and 1D spectra extracted in eight slices along the p-v diagram.

resemble the superposition of a narrow and a broad component depending on the outflow velocity and geometry (e.g. Bae & Woo, 2016). AGN driven outflows with non-Gaussian line profiles and/or requiring multiple Gaussian components have been observed both in the local universe (e.g. Fischer et al., 2018; Shimizu et al., 2018; Davies et al., 2020b) and at high redshift (e.g. Liu et al., 2013; Vayner et al., 2017). There are also many examples of AGN host galaxies with outflow-dominated narrow line region kinematics (e.g. Fischer et al., 2013; Liu et al., 2013), similar to what we observe in K20-ID5.

We note that the clear distinction between the kinematics and line ratios of the nuclear outflow and the extended gas in K20-ID5 confirm that the extended gas is tracing the rotating disk of the galaxy rather than a galaxy-scale outflow (see discussion in Loiacono et al. 2019).

3.4.2 Outflow Velocity

We measure the properties of the nuclear outflow from a deep K band spectrum extracted over the kinematically anomalous nuclear region of K20-ID5, where the outflow dominates the line emission (see Section 3.4.1). We combine the SINFONI-AO and KMOS datasets for a total on-source integration time of 31 hours. The spectrum is shown in the left hand panel of Figure 3.7.

Based on the FWZP of the [N II]+Hα complex, we measure an outflow velocity of 1410 $\pm$ 56 km s^{-1}.[3] Our best-fit exponential disk model yields a circular velocity

[3]We note that our outflow velocity is a factor of $\sim$3 higher than the outflow velocity reported in Genzel et al. (2014). This difference likely arises because 1) the dataset used in this work has a factor of seven longer integration time, significantly improving the S/N in the high velocity wings of the line profile, 2) the

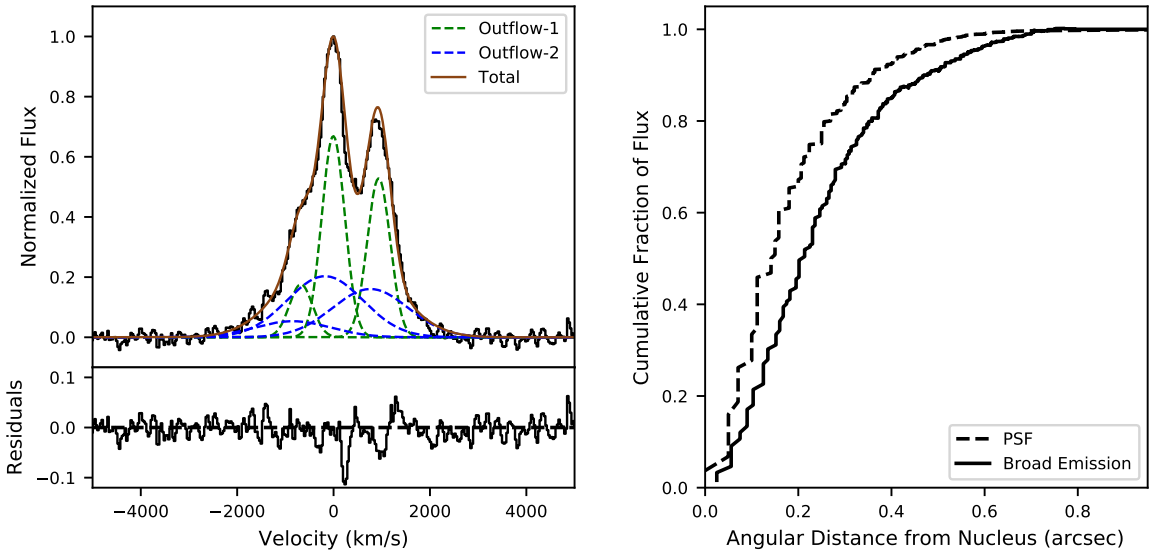

Figure 3.7: (Left) Deep SINFONI-AO + KMOS nuclear spectrum of K20-ID5 (black) with the best fit two component Gaussian model over-plotted. The green and blue curves represent the narrow and broad components respectively, and the brown curve represents the total best fit line profile. In this spectrum, both components are attributed to the outflow. The bottom panel shows the fit residuals. (Right) Curve of growth of the SINFONI-AO PSF (dotted) and the broad emission (solid) as a function of radius.

of $\sim$ 240 km s^{-1}, corresponding to a halo escape velocity of $\sim$ 720 km s^{-1} (assuming $v_{\rm escape} \sim 3\ v_{\rm circ}$; Weiner et al. 2009). The outflow velocity is a factor of two larger than the escape velocity, suggesting that a significant fraction of the outflowing material could be ejected from the halo.

3.4.3 Outflow Energetics

The mass outflow rate is derived from the Hα luminosity of the outflow, as described in Section 3.3.4. Our analysis in Section 3.4.1 revealed that the vast majority of the (narrow and broad) line emission in the nuclear region of K20-ID5 is associated with the outflow. Therefore, we calculate the outflow properties assuming that 100% of the nuclear Hα flux originates from the outflow ("outflow" model).

Even though the outflow dominates the line emission, it is necessary to fit two Gaussian components to recover the shape of the line profiles, as shown in the left hand panel of Figure 3.7. We sum the Hα fluxes of the two components to obtain the total Hα flux. We do not use the seeing limited SINFONI H band data to constrain the emission line fitting,

Genzel et al. (2014) measurement was based on the KMOS nuclear spectrum, and the broad component is significantly more prominent in the SINFONI-AO nuclear spectrum because the higher spatial resolution allows the outflow-dominated nuclear region to be better separated from the surrounding disk-dominated regions, and 3) they adopted a more conservative definition of the outflow velocity.

because the nuclear [O III] emission is strongly attenuated (see Figure 3.2) and we do not find any evidence for a broad or blueshifted component in the [O III] line profile.

There is a significant amount of dust attenuating the nebular line emission from the nuclear region of K20-ID5 (see Section 3.2.1). We use the SINFONI H band data to measure the Hβ flux, and find Hα/Hβ = 8.0 $\pm$ 0.7, corresponding to an A_V of 2.7. This is significantly larger than the global continuum A_V of 1.3, but is consistent with the results of Loiacono et al. (2019) who measured a global Balmer decrement of 8.3 $\pm$ 1.8, and Scholtz et al. (2020) who measured a nuclear Balmer decrement of $8.7^{+2.3}_{-1.8}$. We use the measured Balmer decrement to correct the Hα luminosity of the outflow for extinction.

The outflow is well resolved (see right hand panel of Figure 3.7), and has a PSF-deconvolved HWHM of 1.0 $\pm$ 0.2 kpc. Combining all these quantities, we measure a mass outflow rate of 262 $\pm$ 76 $M_\odot$ yr^{-1}, corresponding to a mass loading factor of $\eta = 0.78 \pm 0.23$.

For comparison, we also calculate the outflowing mass using just the Hα luminosity of the broad component ("galaxy + outflow" model). In this case, we measure $\dot{M}_{\rm out} = 103 \pm 30$ $M_\odot$ yr^{-1} and $\eta = 0.31 \pm 0.09$. The outflow parameters for the outflow only (fiducial) and galaxy + outflow models are listed in Columns 2 and 3 of Table 3.3, respectively.

3.4.4 Outflow Geometry and Velocity Structure

The detection of a velocity gradient across the nucleus of K20-ID5 makes it possible to place some constraints on the geometry of the outflowing material. The velocity difference between the approaching and receding sides of the outflow is $\Delta v \sim 360$ km s^{-1} (see Figure 3.5), which is significantly smaller than the outflow velocity (1410 km s^{-1}). This suggests that the outflow is quasi-spherical, because a large opening angle ($\gtrsim 60°$) is required to produce a large range of projected outflow velocities at every radius, while maintaining a similar average velocity across the entire outflow (see e.g. models in Liu et al., 2013). The small Δv could also be produced by a collimated outflow almost perpendicular to the line of sight, but in a collimated outflow there would only be a small range of velocities at each radius, and therefore this scenario cannot account for the large observed line width.

It is also possible to place some constraints on the velocity profile of the outflowing material. There is no evidence for any radial variation in the FWZP of the [N II]+Hα complex, suggesting that the outflow velocity is approximately constant out to the maximum radius at which it is detected (at least $\sim$ 5 kpc; see Figure 3.6).

3.5 COS4-11337: An Outflow in a Galaxy Pair

3.5.1 Outflow Velocity and Energetics

We measure the properties of the outflow from COS4-11337 by fitting the KMOS H and K band nuclear spectra as a superposition of two Gaussian components. We use the KMOS

Table 3.3: Derived outflow parameters.

Galaxy	K20-ID5		COS4-11337	J0901
Model Type	**Outflow**	Galaxy + Outflow	**Galaxy + Outflow**	**Galaxy + Outflow**
(1)	(2)	(3)	(4)	(5)
a) $R_{\rm out}$ (kpc)		1.0 ± 0.2	0.9 ± 0.2	0.47 ± 0.07
b) $v_{\rm out}$ (km s^{-1})		1410 ± 56	1459 ± 66	650 ± 46
c) $\dot{M}_{\rm out}$ ($M_\odot$ yr^{-1})	262 ± 76	103 ± 30	61 ± 6	25 ± 8
d) η ($= \dot{M}_{\rm out}/{\rm SFR}_{\rm best}$)	0.78 ± 0.23	0.31 ± 0.09	0.15 ± 0.03	0.12 ± 0.04

For COS4-11337 and J0901 we consider only a Galaxy + Outflow model, whilst for K20-ID5 we also consider a model where all of the nuclear line emission is associated with the outflow (Outflow). Boldface font indicates the fiducial model for each galaxy. The rows are as follows: a) Half light radial extent of the outflow emission. b) Outflow velocity, defined as (FWZP$_{\rm [NII]+H\alpha}$ - 1600)/2. c) Mass outflow rate, calculated using Equation 3.1. d) Mass loading factor.

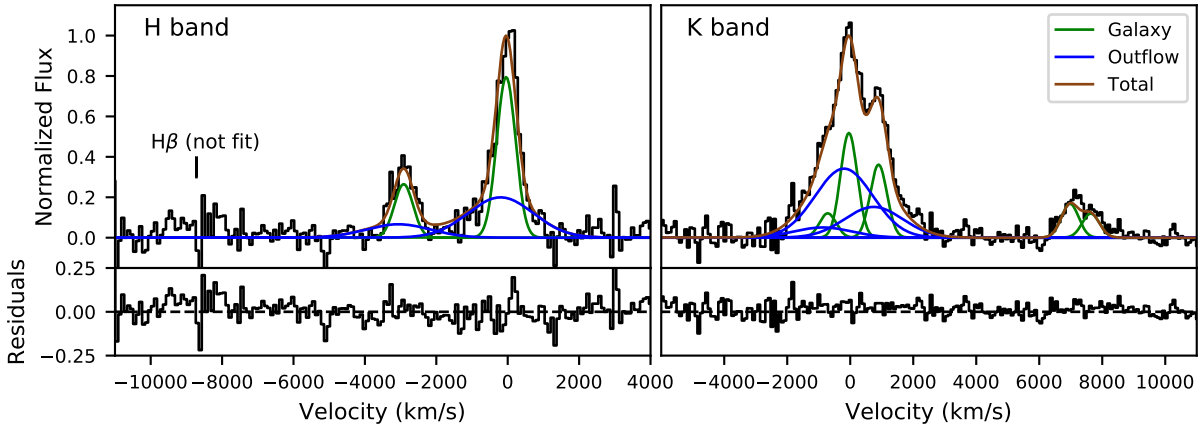

Figure 3.8: KMOS H and K band nuclear spectra of COS4-11337, plotted in independent normalized flux units. The green and blue curves indicate the best fit narrow (galaxy) and broad (outflow) components for a two component Gaussian fit, respectively. The brown curve represents the sum of the narrow and broad components, and the lower panels show the fit residuals in each band.

K band data in favour of the SINFONI-AO K band data because the KMOS K band observations have 3.3 times the integration time and therefore a factor of ∼1.8 higher S/N, and allow us to perform a robust galaxy + outflow decomposition of the nuclear line profile which is not possible using the SINFONI data alone. Although COS4-11363 and COS4-11337 are partially blended in the KMOS data, the SINFONI-AO data indicate that the line emission from COS4-11363 is weak and is confined to the nucleus of the galaxy (see Figure 3.3). Therefore, the contribution of COS4-11363 to the nuclear spectrum of COS4-11337 should be negligible.

The two component fit to the spectrum of COS4-11337 is shown in Figure 3.8. The K band spectrum shows very broad wings, revealing the presence of a fast outflow. Based on the FWZP of the [N II]+Hα complex, we measure an outflow velocity of 1459 ± 66 km s^{-1}. COS4-11337 has a circular velocity of 150 ± 60 km s^{-1} (Wisnioski et al., 2018), corresponding to an escape velocity of ∼ 450 km s^{-1}. The outflow velocity is more than a factor of three larger than the escape velocity, indicating again that a significant fraction of the outflowing material could potentially be expelled from the host halo.

3.5.2 Outflow Energetics

The redshift of this system places the Hβ line at a wavelength with bad skyline residuals (see Figure 3.8), and as a result we cannot derive a reliable Balmer decrement for COS4-11337. Therefore, we correct the Hα luminosity of the outflow for extinction using the global A_V, as described in Section 3.3.5. The outflow is resolved (see Figure 3.9) and has a PSF-deconvolved HWHM of 0.9 ± 0.2 kpc. We find a mass outflow rate of 61 ± 6 $M_\odot$ yr^{-1} and a mass loading factor of $\eta = 0.15 \pm 0.03$. The derived outflow parameters are listed

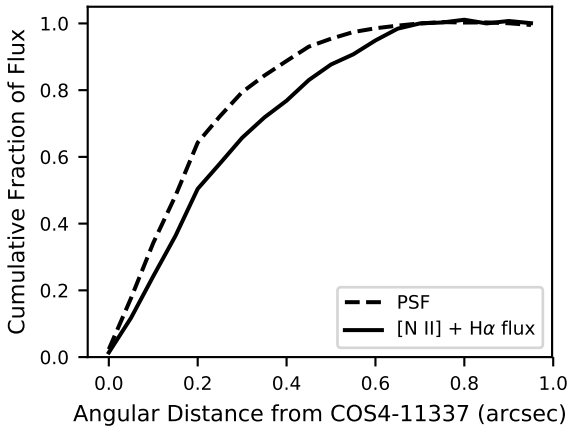

Figure 3.9: Curve of growth of the SINFONI-AO PSF (dashed) and [N II]+Hα flux (solid) as a function of distance from the center of COS4-11337.

in Column 4 of Table 3.3.

3.5.3 Redshift of COS4-11363

COS4-11337 and COS4-11363 are resolved and clearly separated in the SINFONI-AO K band data, allowing us to extract and analyse the spectrum of COS4-11363, which is shown in the left hand panel of Figure 3.10. Only one emission line is detected. It is relatively narrow and lies close to the observed wavelength of [N II]λ6583 in COS4-11337, which is indicated by the blue dashed line. The single emission line in the spectrum of COS4-11363 could trace either [N II]λ6583 at $z = 2.097$, in which case the dv between the galaxies would be ~ 140 km s^{-1}, or Hα at $z = 2.107$, in which case the dv would be ~ 1100 km s^{-1}. The 3D-HST grism redshift is $z_{\rm grism} = 2.103$, in between the two possible spectroscopic redshifts.

We break the redshift degeneracy by utilising archival ALMA observations. COS4-11337/11363 was observed for 90 minutes in Band 4 as part of program 2016.1.00726.S (PI: A. Man). The observations cover the CO(4-3) line, and have a spatial resolution of 0.39" which is sufficient to resolve the two galaxies. The left hand panel of Figure 3.11 shows the F160W image of the system, with contours of the CO(4-3) emission (at levels of 2σ and 3σ) overlaid. Despite the relatively short integration time, CO(4-3) emission is detected near the nucleus of COS4-11363[4]. The right hand panel shows the CO(4-3) spectrum associated with the peak of the emission. The spectrum is plotted as a function of velocity offset from COS4-11337. The purple and green dashed lines indicate where CO(4-3) would fall if the redshift of COS4-11363 were $z = 2.097$ or $z = 2.107$, respectively.

[4]We note that the offset between the CO and F160W centroids may be the result of a small offset in the HST RAs. We compared the HST and Gaia positions of the two Gaia stars in 3D-HST COSMOS tile 12, and found that the HST RAs were lower by 0.14" and 0.28". There were no significant DEC offsets. The white arrow in Figure 3.11 indicates how the HST data would shift relative to the ALMA data if the RAs were to increase by 0.28".

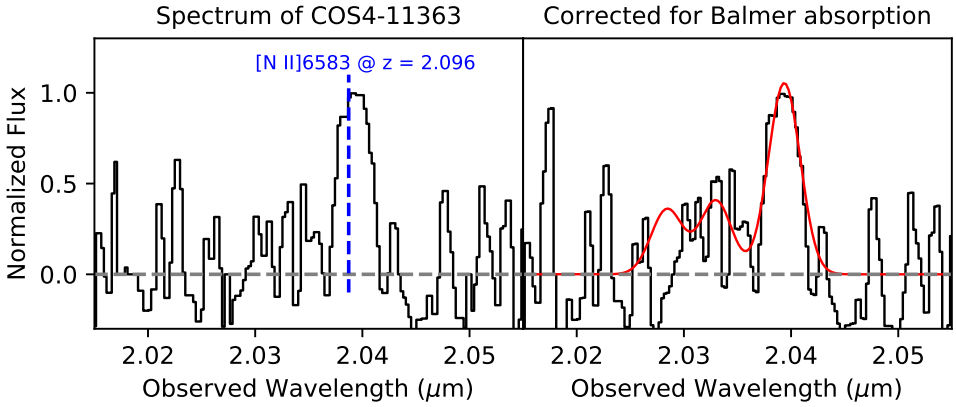

Figure 3.10: (Left) SINFONI-AO K band nuclear spectrum for COS4-11363. One emission line is detected at $\lambda \sim 2.039$ μm. This emission line lies close to the wavelength of the [N II] line at the redshift of COS4-11337, which is indicated by the blue dashed line. (Right) Spectrum corrected for stellar absorption, with the fit to the [N II]+Hα line emission shown in red.

The ALMA data clearly favour the $z = 2.097$ scenario, indicating that the line detected in the SINFONI-AO K band spectrum is [N II]λ6583, and that the Δv between COS4-11363 and COS4-11337 is ≤ 150 km s^{-1}.

3.5.4 Nature of the Line Emission in COS4-11363

The detection of [N II]λ6583 emission without strong Hα emission indicates that the [N II]/Hα ratio in this galaxy must be significantly higher than observed in normal star forming galaxies. The average [N II]/Hα ratio for a pure star forming, $\log(M_*/M_\odot) = 11.1$ galaxy on the mass-metallicity relation at $z = 2.1$ is [N II]/H$\alpha \sim 0.4$ (based on the mass-redshift-metallicity parametrization in Tacconi et al. (2018) and the [N II]/Hα-metallicity calibration from Pettini & Pagel 2004). However, to determine the intrinsic [N II]/Hα ratio in the nucleus of COS4-11363, we must account for the fact that the Hα emission line coincides with a deep photospheric absorption feature in the spectrum of A stars. The best fit SED models for COS4-11363 support the presence of strong Balmer absorption features, regardless of whether we adopt a truncated or exponentially declining star formation history. We scale the best fit SED to match the continuum level of COS4-11363, and subtract this scaled best-fit SED from the observed spectrum (shown in the left hand panel of Figure 3.10) to obtain a pure emission line spectrum (right panel of Figure 3.10). We fit the [N II] and Hα lines in this emission line spectrum as single Gaussians, using the same fitting algorithm with the same parameter restrictions as described for our multi-component fitting process (see Section 3.3.1). We measure an [N II]/Hα ratio of 2.6 ± 0.4 - a factor of 6.5 higher than expected for a pure star forming galaxy.

The high [N II]/Hα ratio indicates that the line-emitting gas must be collisionally excited and/or ionized by sources other than young stars. We measure an Hα equivalent

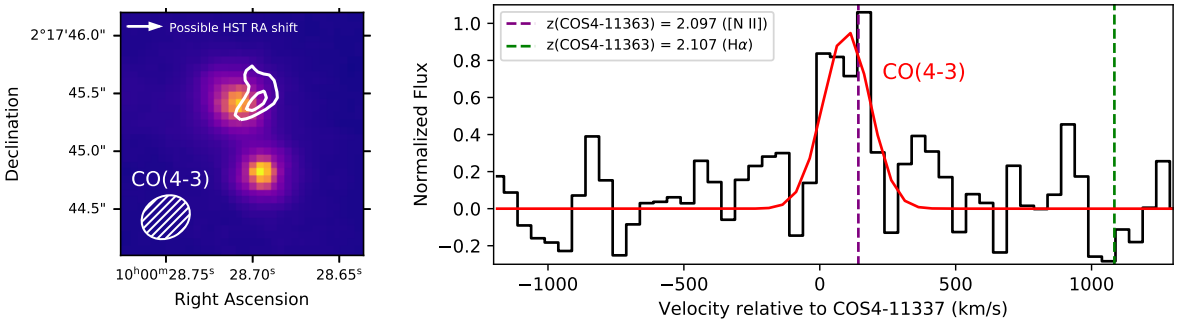

Figure 3.11: Left: HST F160W image of the COS4-11337/11363 system, with 2σ and 3σ contours of the CO(4-3) emission overlaid. The CO(4-3) emission is clearly associated with COS4-11363. The offset between the CO and F160W centroids may be an artefact of a small offset in the HST RAs. Right: CO(4-3) spectrum extracted over the region where the line is detected, plotted as a function of velocity relative to COS4-11337. The red line indicates the best fit to the line emission and is centered at $z = 2.097$. The purple and green lines indicate the possible redshifts of COS4-11363 from the SINFONI-AO data (see Figure 3.10), assuming the detected emission line is [N II]λ6583 at $z = 2.097$, or Hα at $z = 2.107$, respectively. The CO(4-3) detection is strongly in favour of the detected line being [N II]λ6583.

width of 5.8 ± 2.5 Å, which exceeds the maximum value of 3 to be consistent with ionization by evolved stellar populations (e.g. Cid Fernandes et al., 2011; Belfiore et al., 2016). We therefore suggest that the line emission is most likely to be powered by either shock excitation or AGN activity.

The strongest evidence for the source of the line emission comes from the velocity dispersion map, shown in Figure 3.12. The velocity dispersion peaks at $\sim$ 800 km s^{-1} at the nucleus of COS4-11337, where the outflow is launched. However, it remains elevated above 500 km s^{-1} along the entire region connecting COS4-11363 and COS4-11337, before dropping to $\sim$ 250 km s^{-1} at the nucleus of COS4-11363. This suggests that the outflow from COS4-11337 may be propagating towards its companion. Based on the outflow velocity and the projected separation between the galaxies, the travel time between the nuclei is $\sim$ 4 Myr. If the outflow collided with the ISM of COS4-11363, it is likely to have driven large scale shocks, producing the high observed [N II]/Hα ratios. This is a potential example of AGN feedback acting on both galactic scales (by transporting mass and energy in the outflow) and circumgalactic scales (by driving shocks through the ISM of the companion galaxy).

Tidal torques are likely to be an additional source of shock excitation in both COS4-11363 and COS4-11337. In the local universe, interacting/merging systems show prominent line emission from shock excited gas with a typical FWHM of 250-500 km s^{-1} (e.g. Monreal-Ibero et al., 2006; Farage et al., 2010; Rich et al., 2011, 2015). This FWHM is similar to the width of the line emission from COS4-11363, but a factor of $\sim$4 narrower than the broad line emission from COS4-11337, suggesting that an outflow is most likely

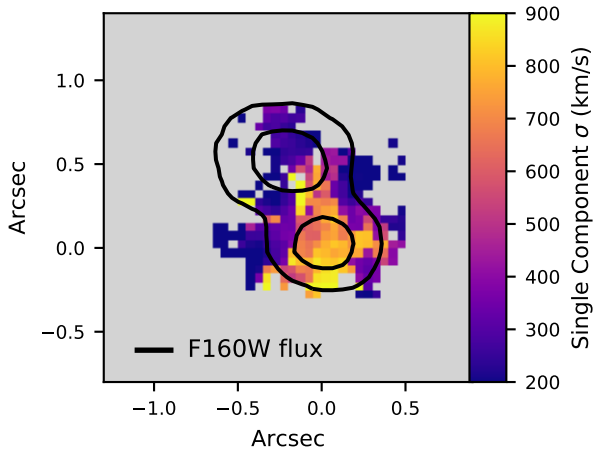

Figure 3.12: Map of the single component velocity dispersion across the COS4-11337/11363 system. The velocity dispersion peaks at the nucleus of COS4-11337 but remains elevated in the region between the two galaxies, suggesting that the outflow from COS4-11337 may be propagating towards COS4-11363.

required to explain the kinematics of the gas in COS4-11337. However, we cannot rule out a scenario where the shock excitation in COS4-11363 is purely induced by the interaction.

It is interesting to speculate on the possible impact that the outflow from COS4-11337 may have had on the star formation activity of COS4-11363. The 3D-HST grism spectrum and the best fit SED for COS4-11363 both support the presence of a prominent Balmer break, and the SED fitting favours a rapid decrease in the SFR over the last hundred Myr. From the Hα flux, we measure an instantaneous SFR of $< 2\ M_{\odot}\ \mathrm{yr}^{-1}$, which places the galaxy two orders of magnitude below the main sequence SFR. The detection of CO associated with this galaxy indicates that the recent truncation of the SF activity was not simply the consequence of an exhausted gas reservoir. The quenching could plausibly have been triggered by the outflow from COS4-11337 ploughing into the ISM of COS4-11363, driving large scale shocks and preventing the gas from collapsing to form stars. However, the galaxy-galaxy interaction is also likely to have had a significant impact on the SF activity in this system. Deep spectroscopy covering the region around 4000Å will assist to more accurately constrain the star formation history and evolution of this galaxy.

3.6 J0901: A Centrally Confined Outflow

3.6.1 Outflow Velocity

The nuclear spectrum of J0901 was extracted from the source plane datacube (which was created by applying the source plane reconstruction to each spectral channel individually), and is shown in Figure 3.13. The [N II] line is significantly broader than the Hα line, and our two component fitting reveals that this is because the Hα emission peak is dominated

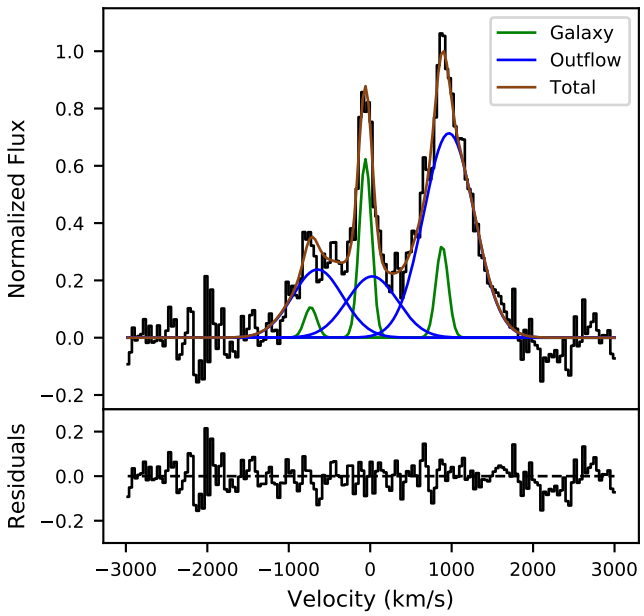

Figure 3.13: Source plane nuclear spectrum of J0901 (black), with the best two component fit over-plotted. The narrow (galaxy) and broad (outflow) components are shown in green and blue, respectively, and the total fit is shown in brown. The bottom panel shows the fit residuals.

by the galaxy component whereas the [N II] emission peak is dominated by the broader outflow component. From the FWZP of the [N II]+Hα complex, we measure an outflow velocity of 650 $\pm$ 46 km s^{-1}. This is a factor of $\sim$2 smaller than the outflow velocities measured for K20-ID5 and COS4-11337. Kinematic modelling indicates that J0901 has an inclination-corrected circular velocity of $\sim$ 260 km s^{-1} (Rhoads et al., 2014; Sharon et al., 2019), corresponding to an escape velocity of 780 km s^{-1}. The outflow velocity is approximately 85% of the escape velocity, and therefore the majority of the outflowing material detected in our data is unlikely to be able to escape from the galaxy halo.

3.6.2 Outflow Extent

Figure 3.14 shows source plane maps of the narrow galaxy emission (left) and the broad outflow emission (middle) over the region covered by the SINFONI-AO data. The approximate shape of the source plane PSF at the location of the nucleus is indicated by the hatched ellipse at the bottom right of the middle panel. Both the galaxy and outflow emission show a single peak in the nucleus, unlike the image plane [N II] map (white contours in the right hand panel of Figure 3.4) in which two clear peaks are visible. Our lens modelling reveals that the secondary peak in the image plane flux distribution is a re-image of the northern side of the nucleus. This result is confirmed by Sharon et al. (2019), who independently developed a lens model for the J0901 lensing cluster in parallel

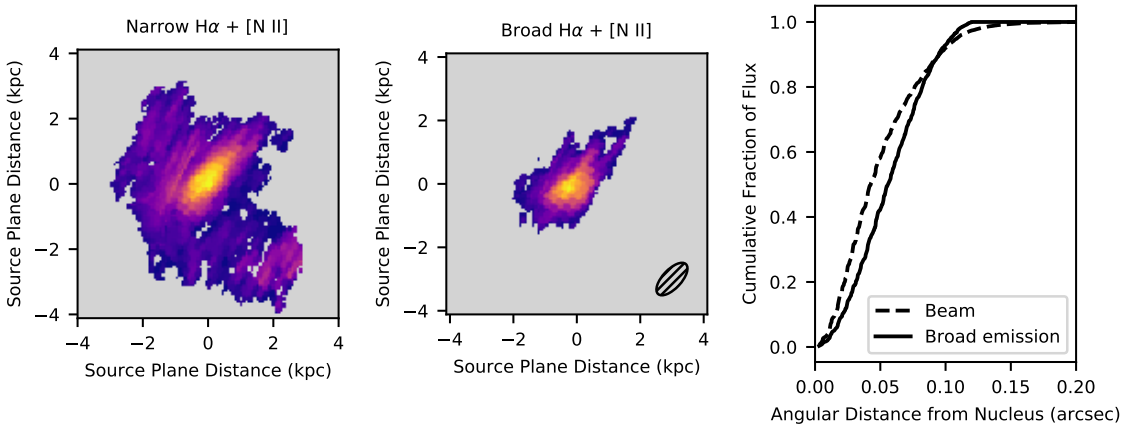

Figure 3.14: Left and middle: Source plane maps of the narrow and broad Hα and [N II] emission across J0901, at a pixel scale of 0.005". The hatched ellipse at the bottom right of the middle panel indicates the approximate shape and size of the source plane PSF. Right: Curves of growth for the beam and the broad component. The broad component is slightly more extended than the beam, indicating that it is marginally resolved.

with our team.

The narrow emission is extended and traces the disk of the galaxy. We note that this figure only shows the central region of the galaxy covered by our AO data, and the true extent of the disk is significantly larger. In contrast, the broad outflow emission is very centrally concentrated. The right hand panel of Figure 3.14 compares the curves of growth for the outflow emission and the PSF. The source plane spatial resolution of the SINFONI-AO data at the nucleus is 122 $\times$ 56 mas (FWHM), corresponding to a circularized FWHM of 83 mas and a physical resolution of 680 pc. Despite the factor of two improvement in spatial resolution due to the lensing, the outflow emission is only slightly more extended than the PSF, indicating that it is marginally resolved. The de-convolved Gaussian HWHM of the outflow emission is 470 $\pm$ 70 pc - a factor of $\sim$ 2 smaller than the outflows from K20-ID5 and COS4-11337.

3.6.3 Outflow Energetics

The outflowing mass is calculated from the source plane Hα luminosity of the outflow component. We robustly detect the Hβ line in our LUCI long slit spectrum of J0901, and therefore we correct the Hα luminosity for extinction using the Balmer decrement. We measure a Balmer decrement of Hα/Hβ = 6.8 $\pm$ 0.6, corresponding to A_V = 2.2. We find a mass outflow rate of 25 $\pm$ 8 $M_\odot$ yr^{-1}, and a mass loading factor of η = 0.12 $\pm$ 0.04 (listed in Column 5 of Table 3.3).

3.7 Discussion

3.7.1 Outflow Driving Mechanisms

Although all three of our galaxies host AGN, the observed ionized gas outflows could plausibly be driven by SF, AGN activity, or both. Outflows can be energy conserving or momentum conserving depending on how fast the hot wind material cools as it interacts with the ISM (e.g. King, 2010; King & Pounds, 2015).

The AGN ionizing radiation field injects momentum into the surrounding material, driving a hot wind with a momentum rate of $\dot{p}_{\rm wind} \sim L_{\rm AGN}/{\rm c}$. If the kinetic energy of the wind couples efficiently to the ISM, it can drive a galaxy scale energy conserving outflow with kinetic power $\dot{E}_{\rm out} \lesssim 0.05\ L_{\rm AGN}$ and momentum rate $\dot{p}_{\rm out} \lesssim$ (5-20) $L_{\rm AGN}/{\rm c}$ (Faucher-Giguère & Quataert, 2012; Zubovas & King, 2012). On the other hand, if the wind kinetic energy is efficiently radiated away, the result is a smaller scale momentum conserving outflow with $\dot{E}_{\rm out} \lesssim 10^{-3} L_{\rm AGN}$ and $\dot{p}_{\rm out} \lesssim L_{\rm AGN}/{\rm c}$ (King, 2010; King & Pounds, 2015).

Supernovae and stellar winds deposit energy at a rate of $\dot{E}_{\rm out} \lesssim 10^{-3}\ L_{\rm SF}$ (Murray et al., 2005). Momentum is deposited through both radiation pressure from massive stars ($\dot{p}_{\rm rad} \sim L_{\rm SF}/{\rm c}$) and supernova explosions. The initial momentum of the ejecta from a single supernova is $p_{\rm i,SN} \sim 3000\ M_\odot$ km s^{-1}, and assuming one supernova per 100 years per solar mass of SF, this corresponds to a total momentum injection rate by supernovae of $\dot{p}_{\rm i,SN} \sim 0.7\ L_{\rm SF}/{\rm c}$ (Murray et al., 2005). However, if the cooling time of the supernova ejecta is sufficiently long, the hot wind can sweep up a significant amount of ISM, and the final momentum rate of the outflow can be a factor of ~ 10 larger than the initial wind momentum rate ($\dot{p}_{\rm f,SN} \sim 6\ L_{\rm SF}/{\rm c}$; Kim & Ostriker 2015). SF driven outflows have been observed to propagate to distances of a few kiloparsecs at $z \sim 2$ (e.g. Newman et al., 2012a,b; Davies et al., 2019).

We calculate the kinetic powers and momentum rates of the outflows in our three galaxies and compare them to $L_{\rm SF}$ and $L_{\rm AGN}$ to determine if the outflows are driven by SF or AGN activity and if they are momentum or energy conserving (see Table 3.4).

In this comparison it is important to account for the $1/n_e$ dependence of the mass outflow rate. In our calculations we have adopted $n_e = 1000$ cm^{-3}, under the assumption that the outflows are AGN-driven. However, the typical electron density of the ionized gas in SF-driven outflows at $z \sim 2$ is 380 cm^{-3} (Förster Schreiber et al., 2019), a factor of 2.6 lower. Therefore, when calculating $\dot{E}_{\rm out}/L_{\rm SF}$ and $\dot{p}_{\rm out}/(L_{\rm SF}/{\rm c})$, we multiply the mass outflow rates by a factor of 2.6. It is also important to consider that $L_{\rm SF}$ represents the *global* bolometric output of the young stars, but the AGN-driven outflows are launched from the nuclear regions of the galaxies, and therefore only some fraction of $L_{\rm SF}$ will be available to drive the outflows.

The kinetic powers of the outflows from K20-ID5 and COS4-11337 are too large for the outflows to be SF-driven. The kinetic power of the K20-ID5 outflow is $0.04(\pm0.01)\ \times L_{\rm AGN}$ and the momentum rate is $17(\pm5)\ \times L_{\rm AGN}/c$, suggesting that the outflow is energy conserving. However, we note that the energy and momentum ratios vary inversely with the AGN luminosity which is poorly constrained due to the probable high column densities

Table 3.4: Outflow kinetic powers and momentum rates, and comparison to the bolometric luminosities of the AGN and the young stars.

Galaxy	K20-ID5		COS4-11337	J0901
Model Type	**Outflow**	Galaxy + Outflow	**Galaxy + Outflow**	**Galaxy + Outflow**
(1)	(2)	(3)	(4)	(5)
$\log(\dot{E}_{\mathrm{out},n_e=1000}/(\mathrm{erg\ s^{-1}}))$	44.2 ± 0.1	43.8 ± 0.1	43.6 ± 0.1	42.5 ± 0.2
$\log(\dot{p}_{\mathrm{out},n_e=1000}/\mathrm{dyn})$	36.4 ± 0.1	36.0 ± 0.1	35.7 ± 0.1	35.0 ± 0.1
$\dot{E}_{\mathrm{out},n_e=1000}/L_{\mathrm{AGN}}$	$(4.0 \pm 1.2)\times10^{-2}$	$(1.6 \pm 0.5)\times10^{-2}$	$(2.8 \pm 0.3)\times10^{-3}$	$(1.5 \pm 0.9)\times10^{-4}$
$\dot{p}_{\mathrm{out},n_e=1000}/(L_{\mathrm{AGN}}/c)$	17 ± 5	6.8 ± 2.0	1.1 ± 0.1	0.14 ± 0.08
$\dot{E}_{\mathrm{out},n_e=380}/L_{\mathrm{SF,best}}$	$(3.4 \pm 1.0)\times10^{-2}$	$(1.3 \pm 0.4)\times10^{-2}$	$(7.1 \pm 1.2)\times10^{-3}$	$(1.1 \pm 0.5)\times10^{-3}$
$\dot{p}_{\mathrm{out},n_e=380}/(L_{\mathrm{SF,best}}/c)$	14 ± 4	5.6 ± 1.7	2.9 ± 0.5	1.0 ± 0.4

The columns are the same as in Table 3.3. When comparing to L_{AGN} we adopt $n_e = 1000\ \mathrm{cm^{-3}}$, and when comparing to L_{SF} we adopt $n_e = 380\ \mathrm{cm^{-3}}$, reflecting the different ionized gas densities of AGN-driven and SF-driven outflows at $z \sim 2$ (see discussion in Section 3.7.1).

towards the nucleus (see Section 3.2.1). The coupling between the AGN radiation field and the outflow is less efficient in COS4-11337, which has an outflow kinetic power of $2.8(\pm0.3) \times 10^{-3} L_{\rm AGN}$ and a momentum rate of $1.1(\pm0.1) \times L_{\rm AGN}/c$. The inefficient coupling suggests that the outflow could plausibly be momentum driven. However, the outflow extends to a distance of ~ 5 kpc (see Section 3.5.4 and Figure 3.12), which is more in favour of the energy driving scenario.

The J0901 outflow has a smaller kinetic power than the outflows from K20-ID5 and COS4-11337, primarily due to the lower outflow velocity. The outflow has a kinetic power of $1.1(\pm0.5) \times 10^{-3} L_{\rm SF}$ and a momentum rate of $1.0(\pm0.4) \times L_{\rm SF}/c$, and could therefore potentially be SF-driven. However, the spatial distribution of the Hα emission suggests that only $\gtrsim 1/3$ of the SF is occurring within the outflow region, in which case the bolometric luminosity of the young stars would likely be insufficient to power the observed outflow. In addition, the outflow emission has a very high [N II]/Hα ratio (3.3; see Figure 3.13), which is typical of AGN-driven outflows but is not observed in SF-driven outflows at $z \sim 2$ (e.g. Newman et al., 2012a; Davies et al., 2019; Genzel et al., 2014; Förster Schreiber et al., 2019). Therefore, we suggest that the outflow is most likely to be AGN-driven, although we cannot rule out a significant contribution from the SF. Only a very small fraction of the energy released by the AGN needs to couple to the ISM in order to drive the observed outflow. Given the very low coupling efficiency and fact that the outflow is confined to the circumnuclear regions, it seems likely that the outflow in J0901 is a momentum conserving AGN-driven outflow.

3.7.2 Extents of AGN-Driven Outflows

An important ingredient in our understanding of how AGN-driven outflows interact with their host galaxies is accurate measurements of the radial extents of AGN-driven outflows. In all three of our systems we find that the majority of the outflow emission is concentrated within approximately the central kiloparsec, consistent with the findings of Förster Schreiber et al. (2014). However, with the exception of J0901, the outflows are not confined to the nuclear regions, but extend well beyond the effective radii of the galaxies. In K20-ID5 the outflow propagates at an approximately constant velocity to a radius of at least 5 kpc (see Section 3.4.4). In COS4-11337, we see compelling evidence that the outflow has travelled beyond the galaxy, and is shock heating the ISM in its companion galaxy COS4-11363 (see Section 3.5.4). Other studies of luminous AGN at similar redshifts have found evidence that ionized outflows can propagate 5-10 kpc from the galaxy nuclei (e.g. Nesvadba et al., 2006, 2008; Harrison et al., 2012; Cresci et al., 2015; Brusa et al., 2018; Herrera-Camus et al., 2019). Put together, these results suggest that AGN-driven outflows have steep luminosity profiles, with a luminous core component in the central kpc and a faint tail extending to several kpc, which may reflect a decrease in the surface brightness and/or density of the outflowing material as it expands out from the galaxy nuclei (e.g. Kakkad et al., 2018).

However, the detection of a confined ($R_e = 470 \pm 70$ pc) outflow in J0901 emphasises that not all AGN-driven outflows extend beyond the nuclear region. Fischer et al. (2019)

reported another hundred parsec scale, $\sim$ 500 km s^{-1} AGN-driven outflow in the lensed galaxy SGAS J003341.5+024217 (SGAS 0033+02 hereafter) at $z = 2.39$. The outflows in both J0901 and SGAS 0033+02 are so compact that they would not be resolved without gravitational lensing. Fischer et al. (2019) state that the outflow in SGAS 0033+02 would probably not be detectable if the system was not lensed, because the outflow emission would be overpowered by emission from the galaxy. The J0901 outflow is clearly visible even in an 0.6" (source plane) diameter aperture, primarily because the large [N II]/Hα ratio in the broad component increases the contrast between the broad component and the surrounding continuum. However, it is possible that confined nuclear outflows are present but undetected in a non-negligible fraction of massive galaxies at $z \sim 2$.

The similarity in the AGN luminosities measured for COS4-11337 and J0901 suggests that the outflow extent is not determined by the *current* AGN luminosity, although we re-iterate that the uncertainty on the AGN luminosity of J0901 is relatively large. The AGN in J0901 and SGAS 0033+02 could potentially have 'switched on' relatively recently, so that the outflows have not yet had time to propagate beyond the circumnuclear regions. Alternatively, the AGN accretion energy may not couple efficiently to the gas in the nuclear regions (as appears to be the case for J0901), giving the outflows insufficient energy to propagate to larger radii. In their current states, these outflows are unable to directly impact gas on kiloparsec scales. However, the outflows are depositing a significant amount of kinetic energy within a few hundred parsecs of the galaxy nuclei. This deposition of energy will increase the amount of turbulence in the circumnuclear regions, and if the turbulent pressure becomes large enough, the star-forming gas could become stabilized against collapse (e.g. Guillard et al., 2012; Alatalo et al., 2015). Therefore, these small, lower velocity outflows could potentially lead to a reduction of the star formation efficiency in the nuclear regions of their host galaxies. Further studies of confined outflows will assist to better characterize this unique class of objects.

3.7.3 Mass and Energy Budget of AGN-Driven Outflows

The near infrared spectroscopic data analyzed in this paper probe only the ionized gas phase of the AGN-driven outflows in K20-ID5, COS4-11337 and J0901. However, galaxy scale outflows are intrinsically multi-phase, and contain not only warm ionized gas, but also cooler molecular and atomic gas, and hotter X-ray emitting gas. Multi-phase observations of outflows in local AGN host galaxies suggest that on galaxy scales, the molecular and neutral phases dominate the outflow mass and the mass outflow rate, but the ionized gas has a higher outflow velocity (e.g. Rupke & Veilleux, 2013; Veilleux et al., 2013; Fiore et al., 2017; Fluetsch et al., 2019; Husemann et al., 2019; Shimizu et al., 2019; Herrera-Camus et al., 2020). In two quasar-driven outflows at $z \sim 1.5$, the molecular phase has a factor of $\sim$2-5 higher mass outflow rate than the ionized phase but a factor of $\sim$2-4 lower outflow velocity (e.g. Vayner et al., 2017; Brusa et al., 2018). For a typical star forming galaxy at $z \sim 2$, Herrera-Camus et al. (2019) found that the molecular outflow rate is a factor of $\sim$5 higher than the ionized outflow rate.

Simulations predict that the hot ($\sim 10^7$ K) phase should carry at least as much mass as

the cooler gas phases (e.g. Nelson et al., 2019), but so far the majority of the observational constraints come from studies of X-ray Broad Absorption Line (BAL) winds and Ultra-Fast Outflows (UFOs) on very small spatial scales, and these appear to have mass outflow rates similar to or lower than those of ionized gas outflows (e.g. Feruglio et al., 2015; Fiore et al., 2017; Tombesi et al., 2017).

Even when outflows can be observed in multiple phases, constructing an accurate budget of the mass and energy in the different phases is very challenging. Ionized gas outflow masses scale with the inverse of the electron density, which is a relatively poorly constrained quantity. Recent studies suggest that the luminosity-weighted density of ionized gas in AGN-driven outflows is ~ 1000 cm^{-3} (e.g. Perna et al., 2017; Kakkad et al., 2018; Husemann et al., 2019; Förster Schreiber et al., 2019; Shimizu et al., 2019), but many studies in the literature adopt $n_e \lesssim 100$ cm^{-3}, indicating potential discrepancies on the order of magnitude level. CO-based molecular gas outflow rates scale with the CO-to-H_2 conversion factor ($\alpha_{\rm CO}$), for which the typically adopted values vary between 0.8 (the 'ULIRG' value; e.g. Cicone et al. 2014) and 4.3 (the Milky Way value; Bolatto et al. 2013), and optically thin outflows with even lower conversion factors have been reported in two objects (Dasyra et al., 2016; Lutz et al., 2020).

Although the exact distribution of mass and energy between different outflow phases is poorly constrained, it is clear that the mass outflow rates and mass loading factors listed in Table 3.3 and the outflow coupling efficiencies listed in Table 3.4 are only lower limits. This must be taken into consideration when evaluating the potential impact of outflows on the evolution of their host galaxies.

The $M_{\rm BH}$-σ (Ferrarese et al., 2001) and $M_{\rm BH}$-$M_{\rm bulge}$ (Magorrian et al., 1998) relations provide indirect evidence to suggest that black holes co-evolve with their host galaxies. The gravitational energy released by accretion onto supermassive black holes greatly exceeds the binding energy of the bulge, and therefore AGN feedback is widely considered an important mechanism for shaping this relationship. Analytical theories predict that AGN driven winds should have $\dot{E}_{\rm out} \sim 0.05\ L_{\rm edd}$, and that this relationship should naturally give rise to the $M_{\rm BH}$-σ relation as a locus of balance between the momentum injection rate from the AGN and the gravitational potential of the bulge. Black holes above the M-σ relation are predicted to drive galaxy-scale energy conserving outflows which eject gas from the bulge and prevent further black hole growth (e.g. King, 2003; Zubovas & King, 2012; Lapi et al., 2014). Various studies based on numerical simulations have reported that a 5% coupling efficiency is sufficient to drive strong outflows which halt star formation and black hole growth, and leave galaxies on the M-σ relation (e.g. Di Matteo et al., 2005).

Figure 3.15 shows the relationship between the outflow kinetic power and the AGN bolometric luminosity for K20-ID5, COS4-11337 and J0901. For comparison, we also plot data for a literature compilation of AGN-driven ionized outflows at $z \sim$ 1-3 (Genzel et al., 2014; Harrison et al., 2016; Fiore et al., 2017; Leung et al., 2019; Herrera-Camus et al., 2019; Fischer et al., 2019; Förster Schreiber et al., 2019). All the literature measurements have been scaled to $n_e = 1000$ cm^{-3} for consistency.

There is a clear correlation between the AGN bolometric luminosity and the outflow kinetic power. The average ratio of the outflow kinetic power to the AGN bolometric lumi-

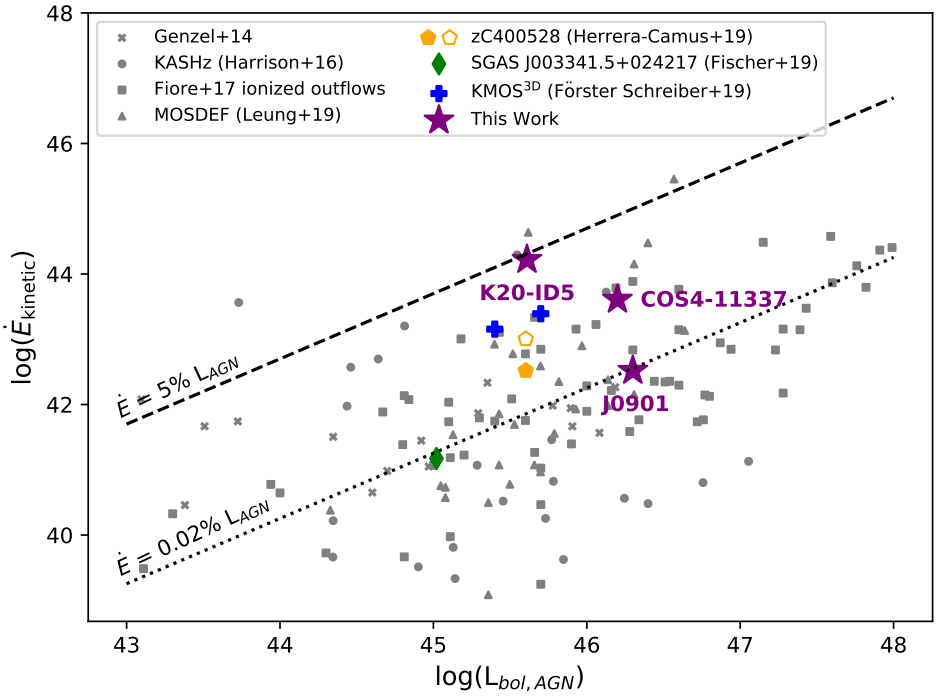

Figure 3.15: Ionized outflow kinetic power as a function of AGN bolometric luminosity for K20-ID5, COS4-11337 and J0901, compared to a compilation of AGN-driven outflows at $z \sim$ 1-3 from the literature (see Section 3.7.3 for details). The literature values have been scaled to an electron density of $n_e = 1000$ cm^{-3}. The dotted and dashed lines show the scalings for ionized outflows with kinetic power equivalent to 0.02% and 5% of the AGN bolometric luminosity, respectively. The filled and open points for zC400528 indicate measurements made from ionized gas only and from the sum of the ionized and molecular gas components, respectively.

nosity is 0.02% (black dotted line). There is a large scatter around the average (primarily driven by variations in outflow velocity at a fixed AGN luminosity), but in the vast majority of cases the coupling efficiency is well below the 5% level suggested by the models (black dashed line). K20-ID5 is one of the extreme cases falling close to the 5% line, but the coupling factor for COS4-11337 is a factor of ten lower at 0.3%. J0901 is another factor of ten lower at 0.02%, but this is not surprising given the likely momentum conserving nature of the outflow. Even if we were to assume an electron density of 100 cm^{-3}, the average coupling factor for the full sample would be 0.2% - still a factor of 25 too low. The coupling between the AGN ionizing radiation field and the ionized gas outflows does not appear to be efficient enough for the M-σ relation to be the consequence of self-regulating black hole feedback. Anglés-Alcázar et al. (2013) showed that a torque-limited accretion model (in which the inflow rate onto the black hole accretion disk is driven by gravitational instabilities in the galaxy disk) naturally reproduces the M-σ relation without the need for any coupling between the AGN accretion energy and gas on galaxy scales.

Accounting for the mass and energy in other phases of the outflows would result in higher $\dot{E}_{\rm out}$ values and may partially alleviate the discrepancy with first order expectations for self-regulated black hole growth. However, for zC400528, a normal AGN host galaxy at $z \sim 2$, the molecular and ionized phases have similar kinetic power (Herrera-Camus et al., 2019), and therefore the overall coupling efficiency does not change significantly depending on whether only the ionized phase (filled yellow pentagon in Figure 3.15) or both the ionized and molecular phases (open yellow pentagon) are considered. Further multi-phase studies of outflows in individual galaxies as well as better constraints on uncertain parameters such as n_e and $\alpha_{\rm CO}$ will be crucial for gaining further insights into the primary mode of black hole growth and the degree of coupling between the AGN accretion energy and gas in the host galaxy.

3.7.4 Strong AGN-Driven Outflows in Compact Star Forming Galaxies

K20-ID5 and COS4-11337 are particularly interesting systems because they provide insights into the role of AGN feedback in driving the evolution of compact star forming galaxies (cSFGs). cSFGs lie on or above the SFR main sequence but have sizes more similar to those of compact quiescent galaxies. There is growing evidence that the build up of large stellar mass surface densities is closely linked to the quenching of star formation (e.g. Martig et al., 2009; Bluck et al., 2014; Lang et al., 2014), and cSFGs may represent an intermediate population of galaxies that have already undergone morphological transformation but have not yet ceased forming stars (e.g. Barro et al., 2013; Nelson et al., 2014; Williams et al., 2014). Most cSFGs appear to have lower gas fractions and shorter depletion times than normal star forming galaxies, suggesting that they will indeed quench on relatively short timescales (e.g. Barro et al., 2016; Spilker et al., 2016; Popping et al., 2017; Tadaki et al., 2017; Talia et al., 2018).

Compaction occurs when a large amount of gas is funneled towards the center of a galaxy - for example as a result of disk instabilities (e.g. Bournaud et al., 2007; Dekel & Burkert, 2014; Brennan et al., 2015) or galaxy-galaxy interactions (e.g. Hopkins & Quataert, 2010). The presence of a large nuclear gas reservoir can trigger star formation and/or AGN activity, which can subsequently drive outflows. cSFGs exhibit a higher incidence of AGN activity than normal star forming galaxies at fixed stellar mass (Kocevski et al., 2017), and are also expected to have a high incidence of AGN-driven outflows based on their large stellar masses and central stellar mass densities (e.g. Förster Schreiber et al., 2019). Therefore, it is important to consider the potential role of AGN feedback in quenching star formation in cSFGs.

K20-ID5 and COS4-11337 are both classified as 'Strong Outflows' by Förster Schreiber et al. (2019) because an unusually large fraction of their [N II]+Hα emission is associated with their $\sim$1500 km s^{-1} AGN-driven outflows. This is exemplified in K20-ID5, for which our analysis suggests that almost all of the nuclear line emission is associated with the outflow. Strong Outflows are rare, occurring in $\sim$5% of massive ($\log(M_*/M_\odot) \gtrsim 10.7$)

galaxies, and accounting for ∼10% of AGN-driven outflows. They have similar outflow velocities and global mass loading factors to normal AGN-driven outflows, but have $\sim 2.5\times$ higher mass outflow rates and are found in galaxies that are smaller and have higher SFRs and specific AGN luminosities (sometimes used as a proxy for Eddington ratio) compared to typical AGN host galaxies at the same redshift. Strong Outflows may therefore trace a 'blowout' phase which is also associated with strong SF and black hole accretion activity.

The impact of these extreme outflow phases on SF in the host galaxy is unclear. The sub-dominant contribution of SF to the Hα emission in the nuclear regions could indicate either that there is very little nuclear SF, or that the nuclear SF is heavily obscured, which would be expected if the gas mass surface densities in the central regions are high. The Strong Outflows on average have similar global mass loading factors to normal AGN-driven outflows, suggesting that the SF activity in the host galaxy is relatively unaffected by the extreme nuclear blowout, at least in the early stages. However, the outflows carry significant amounts of kinetic energy into the circumgalactic medium, which may help to maintain the presence of a hot halo and therefore impede replenishment of the molecular gas reservoir (e.g. Bower et al., 2006; Croton et al., 2006; Bower et al., 2017; Pillepich et al., 2018).

The outflows from K20-ID5 and COS4-11337 decrease the already short molecular gas depletion times in these systems. K20-ID5 has a molecular gas mass of $\log(M_{H_2}/M_\odot) = 11.0$ (calculated by re-scaling the CO-based gas mass from Popping et al. 2017 to the metallicity-dependent α_{CO} from Tacconi et al. 2018), corresponding to a SF depletion time of 280 Myr. If we assume that the molecular gas outflow rate is at least as large as the ionized gas outflow rate (see discussion in Section 3.7.3), the overall depletion time (including the contribution of the outflow) is $\leq$ 160 Myr, compared to an average depletion time of 520 Myr for galaxies at the same stellar mass, SFR and redshift (Tacconi et al., 2018). There are no existing gas mass measurements for COS4-11337, but using the upper limit on the CO(4-3) flux (Figure 3.11), we find a 3σ upper limit on the gas mass of $\log(M_{H_2}/M_\odot) < 9.9$ (assuming CO(1-0)/CO(4-3) = 2.4, and the metallicity-dependent α_{CO} from Tacconi et al. 2018). The gas mass upper limit corresponds to a SF depletion time of $<$ 18 Myr, and an overall molecular gas depletion time of $<$ 16 Myr, compared to an average of 540 Myr for galaxies at the same stellar mass, SFR and redshift. The molecular gas depletion time for COS4-11337 is very short, and may indicate that the AGN radiation field is heating some of the molecular gas and causing it to emit primarily in higher excitation CO transitions (e.g. Gallerani et al., 2014; Mingozzi et al., 2018; Rosario et al., 2019).

Both K20-ID5 and COS4-11337 could deplete their entire molecular gas reservoir within a couple of hundred Myr, and the kinetic energy injected into the halos by the AGN-driven outflows could suppress the accretion of fresh molecular gas, supporting the notion that these galaxies may be the direct progenitors of compact quiescent systems. However, both galaxies are currently located on the upper envelope of the star-forming main sequence, suggesting that the outflows have not yet had any significant impact on the SF activity in their host galaxies.

3.8 Summary and Conclusions

We have used deep SINFONI-AO data to characterize the AGN-driven outflows in three massive ($\log(M_*/M_\odot) \sim 11$) main sequence galaxies at $z \sim 2.2$ – K20-ID5, COS4-11337 and J0901. These galaxies probe AGN feedback acting on nuclear, disk, and circumgalactic scales, and therefore provide important insights into the different mechanisms through which AGN-driven outflows can interact with their host galaxies and surrounding environment.

K20-ID5 has a luminous compact core and a fainter, regularly rotating extended disk. Our SINFONI-AO data reveal strong deviations from regular disk kinematics in the central 0.4" (3.3 kpc), spatially coincident with elevated line widths and large [N II]/Hα ratios. We conclude that the majority of the line emission in the nuclear region traces the AGN-driven outflow, with a minor contribution from star formation. The outflow can be traced well beyond the effective radius of the galaxy, to a distance of ∼5 kpc, at an approximately constant velocity of ∼1400 km s^{-1}.

COS4-11337 is a compact star forming galaxy in a close pair with COS4-11363, at a projected separation of only 5.4 kpc. COS4-11337 shows very strong and broad line emission, whereas COS4-11363 has very little line emission and is likely to have experienced a rapid decrease in SFR in the last hundred Myr. We identified CO(4-3) emission at the location of COS4-11363 in archival ALMA data, confirming that it lies close in velocity space to COS4-11337 ($\Delta v < 150$ km s^{-1}). The SINFONI-AO spectrum of COS4-11363 reveals a very high [N II]/Hα ratio of 2.6, indicative of shock excitation. We showed that the ∼1500 km s^{-1} outflow driven by the AGN in COS4-11337 is propagating towards COS4-11363 and may therefore be responsible for shock heating the ISM in the companion galaxy. However, we cannot rule out a scenario where most or all of the shock excitation in COS4-11363 is due to tidal torques induced by the galaxy-galaxy interaction.

The outflows in K20-ID5 and COS4-11337 have small half-light radii (∼1 kpc) but can be traced to large galactocentric distances ($\gtrsim 5$ kpc). Combined with previous results, this suggests that AGN-driven outflows have steep luminosity profiles, with luminous cores and faint extended tails, perhaps driven by a decrease in the surface brightness and/or density of the outflowing material as it propagates away from the galaxy nuclei.

K20-ID5 and COS4-11337 are unique objects because they are classified as compact star forming galaxies and show abnormally strong outflow signatures in their nuclear spectra. The lack of prominent galaxy emission in the nuclear regions may indicate that there is very little nuclear star formation or that the nuclear region is heavily obscured, the latter of which is plausible in the case of high nuclear gas mass surface densities. The galaxies are located on the upper envelope of the star forming main sequence, suggesting that the outflows do not have any significant impact on the instantaneous SF activity in their host galaxies. However, the outflows carry a large amount of kinetic energy which will be injected into the circumgalactic medium, and could contribute to the maintenance of a hot halo. The resulting suppression of cold gas accretion combined with the already short depletion times in these systems could perhaps lead to rapid exhaustion of the molecular gas reservoirs on timescales of a few hundred Myr.

The outflow in J0901 has very different properties to the outflows in K20-ID5 and COS4-11337. J0901 is gravitationally lensed, providing us with a magnified view of the nuclear region. Despite the factor of two enhancement in spatial resolution, the nuclear outflow is barely resolved, and has a half light radius of 470 $\pm$ 70 pc and a velocity of $\sim$ 650 km s^{-1}.

The AGN in J0901 has a similar luminosity to the AGN in COS4-11337, and therefore the difference in outflow extent and velocity does not appear to be related to the *current* AGN luminosity. We postulate that the J0901 outflow may be in an early stage of its evolution (i.e. it has not yet had sufficient time to break out of the nuclear region), or the conditions in the nuclear region may lead to inefficient coupling between the AGN radiation field and the gas in the host galaxy. In its current state, the outflow in J0901 is not able to transfer a significant amount of mass or energy out of the nuclear region. However, the dissipation of kinetic energy from the outflow could potentially increase the turbulence in the circumnuclear region enough to stabilise molecular gas against collapse, and therefore decrease the star formation efficiency in the center of the galaxy.

Finally, we investigated whether the efficiency of the coupling between the AGN radiation field and the ionized gas outflows is sufficiently strong for the M-σ relation to be explained by self-regulating black hole feedback. We combined our measurements with a compilation of ionized outflows at z $\sim$1-3 from the literature, and found an average coupling factor ($\dot{E}_{\rm out}/L_{\rm AGN}$) of 0.02%. K20-ID5 has one of the highest coupling factors in the sample at 4%, J0901 lies at the average value of 0.02%, and COS4-11337 has an intermediate coupling factor of 0.3%. The low average coupling factor may lend support to alternative origins for the M-σ relation such as torque-limited black hole accretion. However, we emphasise that there are many uncertainties in the calculation of the coupling factors. The outflow kinetic energy scales inversely with the electron density, which is a poorly constrained quantity. In this work we have only probed the ionized gas phase of the outflows, and it is unclear what fraction of the outflow kinetic power is carried in the molecular, neutral and hot phases. In the future it will be critical to gather a large sample of AGN-driven outflows with robust measurements of the outflow mass in multiple gas phases, in order to better determine what fraction of the mass and kinetic power is found in the ionized phase, and whether this varies as a function of AGN luminosity or other galaxy properties.

3.9 Appendix: J0901 Lens Modelling, Source Plane Reconstruction and Physical Properties

3.9.1 Lens Modelling with Lenstool

J0901 at $z = 2.2586$ (Hainline et al., 2009) is lensed by a poor cluster at $z \sim 0.3459$ (Diehl et al., 2009). Three images are apparent in Figure 3.16: the southeast (SE) arc that is the target of our high resolution SINFONI observations, a relatively undistorted western (W) arc, and the northeastern (NE) arc which is a fold arc that images part of the

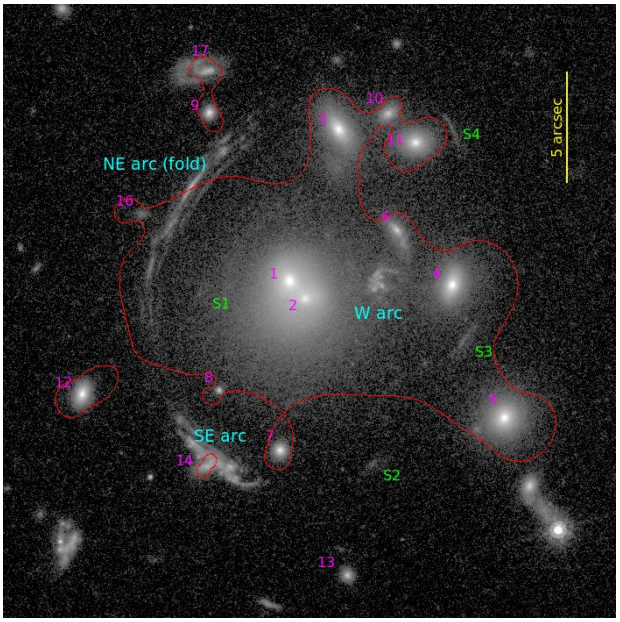

Figure 3.16: HST F814W image of J0901, with overplotted information related to the lens modelling. N is on top. Cyan labels identify the three J0901 arcs. S1 to S4 (green labels) label the four images of the $z \approx 3.1$ 'Sith' lensed background object. Foreground cluster objects used in the lens model are labelled in magenta. No. 14 is the perturber near the SE arc. The outer critical line for the J0901 redshift is overplotted in red.

source twice, but misses the H-band nucleus (see also Tagore, 2014; Sharon et al., 2019). To construct a lens model for interpretation of the SINFONI adaptive optics and HST data, we rely on archival HST F814W (rest frame UV) and F160W (rest frame optical) images, and use version 7.0 of the parametric gravitational lens modelling code LENSTOOL (Kneib et al., 1996; Jullo et al., 2007; Jullo & Kneib, 2009). All HST data have been astrometrically registered for consistency with each other and with five stars from GAIA DR1 (Gaia Collaboration et al., 2016).

The model is constrained by the locations of 15 I-band (rest UV) emission knots (Figure 3.17), with positions that have been manually measured in the W arc, in the SE arc (one of them imaged three times within the SE arc), and for five of them in the NE fold arc (all of these imaged twice). In addition, we use the four HST H-band images of a reddish second lensed object with unknown redshift, nicknamed 'Sith' by Tagore (2014). The redshift of this object is left free for the lens modelling and is estimated at $z \approx 3.1$ by the adopted LENSTOOL model.

The lens model includes a general cluster potential for which we adopt an NFW profile (Navarro et al., 1997). We fix the NFW concentration parameter at $c = 6$, reasonable for a $M_{200} \approx 10^{14}\ M_{\odot}$ cluster reported below (Dutton & Macciò, 2014; Merten et al., 2015; Umetsu et al., 2016), and considering some bias towards more concentrated halos for strong lensing clusters. The position, axial ratio, position angle and radius of the cluster

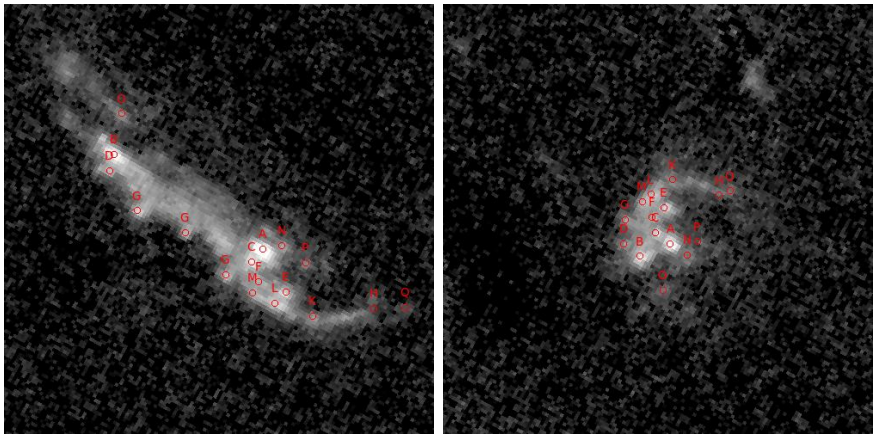

Figure 3.17: Identification of I-band knots used to constrain the lens model, overplotted on foreground object subtracted F814W images of the SE arc (left) and W arc (right). Note that the H-band nucleus coincides with knot C rather than the I-band brighter knot A. Knot G is triply imaged in the SE arc, due to the nearby foreground perturber galaxy which is already subtracted for this image. Residual from foreground galaxy subtraction are visible towards the top of the right panel.

potential are left free for the fit. We note that our data do not strongly test or constrain this adopted cluster radial profile shape, since all J0901 and Sith constraints are at similar clustercentric radii.

Galfit (Peng et al., 2002, 2010a) was applied to the HST I-band and H-band images in order to derive parameters of the foreground cluster members. For the two galaxies near the cluster center, we adopt dPIE (Elíasdóttir et al., 2007) profiles with fixed position and core radius but fit the axial ratio, position angle, velocity dispersion, and cut radius. Close proximity to the cluster center makes their individual parameters less constrained. For the perturber galaxy near the J0901 SE arc, we fix position and position angle to the I band observed values but fit axial ratio, velocity dispersion, and cut radius. For 13 additional foreground cluster galaxies, we follow the common procedure (e.g., Limousin et al., 2007) of fixing position, position angle, and axial ratio individually to the I band observed values, but fitting $\propto L^{1/4}$ relations for velocity dispersion and cut radius, with L based on the H band magnitude. Finally, we use the crossing of the NE fold arc by the critical line and the arc orientation at that point as constraints. Table 3.5 lists resulting parameters.

The model fits the overall lens morphology. The RMS difference in the image plane between observed position of a knot and position predicted from the knot's location in another arc plus lens model is $0.45''$. This reduces to $0.16''$ when comparing only SE and W arc, i.e. excluding the strongly distorted NE arc and Sith. The overall morphology and in particular the need to consider the perturber near the SE arc match the findings that Sharon et al. (2019) obtained from a lens model that is based on $1.1''$ resolution IRAM CO data. Since our focus is on interpretation of higher spatial resolution SINFONI adaptive optics data, we adopt the model built from high resolution HST data. Figure 3.18 provides

Table 3.5: Best-fit lens model parameters.

Halo	R.A.	Decl.	e	PA	r_{core}	r_{cut}	σ_0
	$''$	$''$		(deg)	(kpc)	(kpc)	(km s^{-1})
Cluster	-1.53	1.48	NFW e=0.32, PA=82.7, [c=6], $r_{scale} = 127$ kpc, $M_{200} = 7.3 \times 10^{13}\ M_\odot$				
Galaxy 1	[-0.79]	[2.13]	0.22	35.4	[0.25]	211.5	270.0
Galaxy 2	[-1.51]	[1.33]	0.22	77.0	[0.25]	221.5	172.6
Perturber	[2.93]	[-6.25]	0.01	77.0	[0.25]	384.6	85.9
Galaxy scaling	...	...	...	...	[0.15]	5.5	235.9

Coordinates are in arcseconds relative to a fiducial RA 135.343500 deg DEC 18.241792 deg (ICRS). Values in square brackets are fixed to the input. Ellipticities are $e = (a^2 - b^2)/(a^2 + b^2)$. All halos except the NFW 'cluster' one are dPIE potentials. Positions angles are quoted degrees east of north (i.e., not in the LENSTOOL convention). 'Galaxy scaling' values refer to those galaxies where r_{cut} and σ_0 are not individually fitted but scaled $\propto L^{1/4}$. Values listed refer to a galaxy with H=17.3mag.

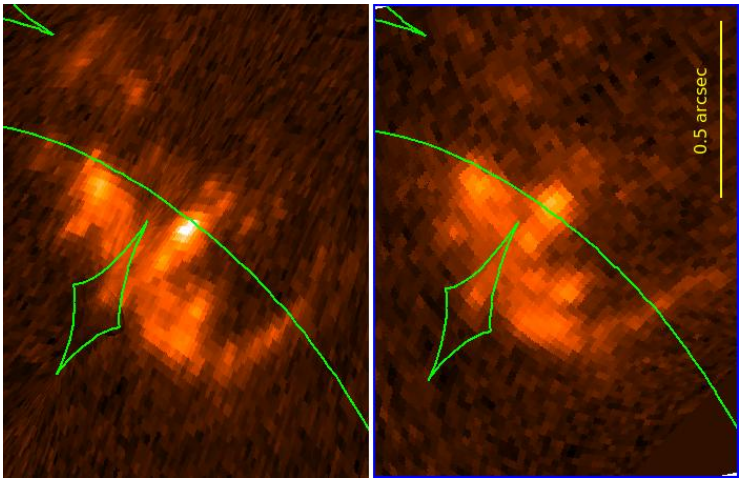

Figure 3.18: I band source plane projections of the SE arc (left) and W arc (right). The source plane image for the W arc has been scaled $\times 0.955$ and rotated by 11.6°. Outer caustics are overplotted in green, the small diamond-shaped caustic is related to the perturber near the SE arc and encloses knot G.

a sanity check of the lens model, by comparing the SE and W I-band arcs, projected back to the source plane and applying a small scaling/rotation correction to the W reconstruction. Before applying the lens model to SINFONI data, we shifted the astrometry of the SINFONI cubes to obtain a K-band continuum position consistent with the HST F160W image.

3.9.2 AGN Luminosity

We calculate the luminosity of the AGN in J0901 from the [O III] luminosity. It is not possible to directly compute the source plane [O III] luminosity because we only have long slit data. Instead, we assume that the [N II] and [O III] emission have similar spatial distributions, and multiply the image plane [O III] luminosity by the ratio of the [N II] flux in the source plane nuclear spectrum to the [N II] flux in the image plane long slit spectrum. We correct the [O III] luminosity for extinction using the Balmer decrement (described in Section 3.6.3), and convert the [O III] luminosity to the AGN bolometric luminosity using a bolometric correction factor of 600 (Netzer, 2009), yielding an AGN luminosity of $\log(L_{\rm AGN}) = 46.3$.

3.9.3 Stellar Mass

Saintonge et al. (2013) estimated the stellar mass of J0901 by making use of empirical correlations between the 3.6μm and 4.5μm luminosities and the stellar mass. The observed luminosities were corrected for lensing magnification using a single wavelength-independent correction factor. We re-calculate the stellar mass and A_V for J0901 by

utilising archival HST imaging in the F475W (λ_{rest} = 1481Å), F814W (λ_{rest} = 2500Å) and F160W (λ_{rest} = 4959Å) bands (Program ID 11602, PI: S. Allam). The imaging has a spatial resolution of 0.1-0.15", which is sufficient to apply the source plane reconstruction and calculate the magnification factor for each band individually. We calculate the source plane luminosities in these three bands and fit the SED using the FAST code (Kriek et al., 2009). We consider solar metallicity models from the Bruzual & Charlot (2003) library, with dust extinction following the Calzetti et al. (2000) curve and A_V = 0-3. We assume an exponentially declining star formation history (τ model), allowing for ages between 50 Myr and 2.86 Gyr (the age of the universe at $z = 2.259$), and $\log(\tau/\mathrm{yr}) = 8.5$-10.0. The best fit model gives $\log(M_*/M_\odot) = 11.2$ and $A_V = 1.2$. Our stellar mass estimate is close to the value that is obtained by scaling the Saintonge et al. (2013) value to our Hα magnification factor ($\log(M_*/M_\odot) = 11.03 \pm 0.14$).

3.9.4 SFR

We calculate the SFR of J0901 from the 160μm flux presented in Saintonge et al. (2013). We scale the total 160μm flux by a factor of 0.4 to isolate the flux originating from the SE arc (Saintonge et al., 2013). We cannot measure the magnification factor in the FIR, because the spatial resolution of the imaging is insufficient to perform the source plane reconstruction. Instead, we adopt the Hα magnification factor ($\mu = 9.9$), which provides a good first order approximation of the lensing correction. We convert the 160μm luminosity to $L_{\rm IR}$ using the SED template from Wuyts et al. (2008), and convert the $L_{\rm IR}$ to a SFR using $\mathrm{SFR} = 1.09 \times 10^{-10} L_{\rm IR}/L_\odot$ (Wuyts et al., 2011a). The resulting SFR is 200 $M_\odot$ yr^{-1}.

Chapter 4

The KMOS^{3D} Survey: Investigating the Origin of the Elevated Electron Densities in Star-forming Galaxies at $1 \lesssim z \lesssim 3$

This Chapter is a reprint of the paper *The KMOS^{3D} Survey: Investigating the Origin of the Elevated Electron Densities in Star-forming Galaxies at $1 \lesssim z \lesssim 3$*, which has been submitted to ApJ. © AAS. Reproduced with permission.

R. L. Davies performed the data analysis, developed the interpretation, and produced all of the text, figures, and tables presented in the main text and appendices of this publication.

Based on observations collected at the European Organisation for Astronomical Research in the Southern Hemisphere under ESO Programme IDs 073.B-9018, 074.A-9011, 075.A-0466, 076.A-0527, 077.A-0527, 078.A-0600, 079.A-0341, 080.A-0330, 080.A-0339, 080.A-0635, 081.A-0672, 081.B-0568, 082.A-0396, 183.A-0781, 087.A-0081, 088.A-0202, 088.A-0209, 090.A-0516, 091.A-0126, 092.A-0082, 092.A-0091, 093.A-0079, 093.A-0110, 093.A-0233, 094.A-0217, 094.A-0568, 095.A-0047, 096.A-0025, 097.A-0028, 098.A-0045, 099.A-0013, and 0100.A-0039. Also based on observations taken at the Large Binocular Telescope on Mt. Graham in Arizona. The LBT is an international collaboration among institutions in the United States, Italy and Germany. LBT Corporation partners are: The University of Arizona on behalf of the Arizona university system; Istituto Nazionale di Astrofisica, Italy; LBT Beteiligungsgesellschaft, Germany, representing the Max-Planck Society, the Astrophysical Institute Potsdam, and Heidelberg University; The Ohio State University, and The Research Corporation, on

behalf of The University of Notre Dame, University of Minnesota and University of Virginia.

Abstract - We investigate the physical processes driving the evolution of the typical electron density (n_e) in star-forming galaxies from $z \sim 2.6$ to $z \sim 0$, using a sample of 611 galaxies drawn primarily from the KMOS^{3D} ($0.6 < z < 2.6$) and SAMI ($z < 0.113$) integral field surveys. We select galaxies that do not show evidence of AGN activity or outflows in order to constrain the average gas conditions within H II regions. The galaxy spectra are stacked in four redshift bins and the [S II] doublet ratio is used to measure the local n_e in the line-emitting material. We find that n_e([S II]) decreases from 187^{+140}_{-132} cm^{-3} at $z \sim 2.2$ to 32^{+4}_{-9} cm^{-3} at $z \sim 0$, consistent with previous results. We also use the Hα luminosity to estimate the root-mean-square (rms) n_e averaged over the volumes of star-forming disks at each redshift. The local and volume-averaged n_e evolve at similar rates, hinting that the volume filling factor of the line-emitting gas may be approximately constant across $0 \lesssim z \lesssim 2.6$. There is a roughly monotonic trend between n_e and star formation rate across the redshift range probed by our samples, but the KMOS^{3D} galaxies have systematically higher n_e than the SAMI galaxies at fixed offset from the star-forming main sequence, suggesting a link between the n_e evolution and the evolving main sequence normalization. We explore potential drivers of the density evolution and find that n_e(rms) $\simeq n_{H_2}$, suggesting that the elevated electron densities in H II regions at high-z could plausibly be the direct result of higher gas densities in the parent molecular clouds. There is also tentative evidence to suggest that n_e could be influenced by the balance between stellar feedback, which drives the expansion of H II regions, and the ambient pressure, which resists their expansion.

4.1 Introduction

The average properties of star-forming galaxies have evolved significantly from the peak epoch of star formation to the present day universe. The cosmic star formation rate (SFR) density and the normalization of the star-forming main sequence (MS) have both decreased by an order of magnitude since $z \sim 2$ (e.g. Daddi et al., 2007; Elbaz et al., 2007; Madau & Dickinson, 2014; Sobral et al., 2014; Speagle et al., 2014; Whitaker et al., 2014), primarily driven by the declining rate of cosmological cold gas accretion and the subsequent reduction in the molecular gas fractions of galaxies (e.g. Genzel et al., 2015; Scoville et al., 2017; Liu et al., 2019; Millard et al., 2020; Tacconi et al., 2020). The high gas fractions at $z \sim 2$ drive galaxy-wide gravitational instabilities, resulting in elevated gas velocity dispersions (e.g. Genzel et al., 2006, 2008; Law et al., 2009; Newman et al., 2013; Wisnioski et al., 2015; Johnson et al., 2018; Krumholz et al., 2018; Übler et al., 2019) and triggering the formation of massive star-forming clumps (e.g. Elmegreen & Elmegreen, 2005; Bournaud et al., 2007; Dekel et al., 2009; Genzel et al., 2011; Genel et al., 2012; Wisnioski et al., 2012; Wuyts et al., 2012).

It is then perhaps not surprising that we also observe significant evolution of the properties of the interstellar medium (ISM). The first near-infrared spectroscopic surveys of high-redshift star-forming galaxies revealed that they do not lie along the locus of local star-forming galaxies on the [N II]/Hα vs. [O III]/Hβ diagnostic diagram, but are offset to higher line ratios (e.g. Shapley et al., 2005; Erb et al., 2006a; Kriek et al., 2007). The physical origin of this offset remains highly debated, with proposed explanations including a harder ionizing radiation field (e.g. Steidel et al., 2016; Strom et al., 2017; Sanders et al., 2020), higher N/O abundance ratio (e.g. Masters et al., 2014; Jones et al., 2015; Shapley et al., 2015), elevated electron density and ISM pressure (e.g. Dopita et al., 2016; D'Agostino et al., 2019), higher ionization parameter (e.g. Kashino et al., 2017; Bian et al., 2020), an increased contribution from shocks and/or Active Galactic Nuclei (AGN; e.g. Newman et al., 2014; Freeman et al., 2019), and/or a decreased contribution from diffuse ionized gas within the regions sampled by the observations (e.g. Shapley et al., 2019). It is very difficult to distinguish between different possible drivers based on the [N II]/Hα and [O III]/Hβ ratios alone (e.g. Kewley et al., 2013), and it is necessary to quantify the evolution of each property in order to build a full picture of how the physical conditions in star-forming regions have evolved over time.

A number of observational studies have found that the typical electron densities of star-forming galaxies have decreased from $n_e \sim 200 - 300$ cm^{-3} at $z \sim 2 - 3$ (e.g. Steidel et al., 2014; Shimakawa et al., 2015; Sanders et al., 2016) to $n_e \sim 100 - 200$ cm^{-3} at $z \sim 1.5$ (e.g. Kaasinen et al., 2017; Kashino et al., 2017) and to $n_e \sim 30$ cm^{-3} at $z \sim 0$ (e.g. Herrera-Camus et al., 2016; Kashino & Inoue, 2019). However, the physical mechanism(s) responsible for driving this evolution are difficult to identify, and to date no quantitative models have been proposed to explain the density evolution.

When interpreting n_e measurements it is important to consider the geometry of the line-emitting material and the volume over which n_e is measured. The electron density is typically measured using density-sensitive line ratios, such as [S II]λ6716/[S II]λ6731 and [O II]λ3729/[O II]λ3726 (e.g. Osterbrock & Ferland, 2006), which probe the local electron density in the line-emitting material. Consider an H II region containing a collection of line-emitting structures with electron densities $n_{e,i}$, volumes V_i, and [S II] luminosities $L_{[\mathrm{SII}],i}$. The [S II]λ6716/[S II]λ6731 ratio probes the approximate luminosity-weighted average n_e of these structures[1]; i.e.

$$n_e([\mathrm{SII}]) \simeq \sum_i \left(n_{e,i} \times L_{[\mathrm{SII}],i}\right) \; / \; \sum_i L_{[\mathrm{SII}],i} \tag{4.1}$$

The root-mean-square (rms) number of electrons per unit volume in the H II region, also known as the rms electron density or n_e(rms), can be calculated from the Hα luminosity and volume of the H II region:

$$L(\mathrm{H}\alpha, \mathrm{HII}) = \gamma_{H\alpha} V_{\mathrm{HII}} \; n_e^2(\mathrm{rms}) \tag{4.2}$$

[1]This is true if the majority of the $n_{e,i}$ values fall in the regime where the relationship between n_e and [S II]λ6716/[S II]λ6731 is approximately linear; i.e. $n_e \simeq 40 - 5000$ cm^{-3} (e.g. Osterbrock & Ferland, 2006; Kewley et al., 2019).

where $\gamma_{H\alpha}$ is the volume emissivity of Hα (3.56×10^{-25} erg cm^3 s^{-1} for Case B recombination). The total Hα luminosity of this hypothetical H II region can also be written as the sum of the Hα luminosities of the individual line-emitting structures:

$$L(\mathrm{H}\alpha, \mathrm{HII}) = \gamma_{H\alpha} \sum_i \left(V_i \; n_{e,i}^2 \right) \tag{4.3}$$

By combining Equations 4.2 and 4.3 we can derive an expression for the volume filling factor (ff) of these structures:

$$ff \equiv \left(\sum_i \; V_i \right) / \; V_{\mathrm{HII}} = n_e^2(\mathrm{rms}) \times \frac{\sum_i V_i}{\sum_i \left(n_{e,i}^2 \times V_i \right)} \tag{4.4}$$

Assuming that all of the line-emitting structures have roughly similar electron densities, and that the volume-weighted and light-weighted average densities are approximately equal, Equation 4.4 can be re-written as

$$ff \simeq \left[n_e(\mathrm{rms}) / n_e([\mathrm{SII}]) \right]^2 \tag{4.5}$$

Observations of local H II regions have found that n_e([S II]) and n_e([O II]) are much larger than n_e(rms), implying that the majority of the line emission originates from clumps with relatively low volume filling fractions of $\sim$ 0.1 – 10% (e.g. Osterbrock & Flather, 1959; Kennicutt, 1984; Elmegreen & Hunter, 2000; Hunt & Hirashita, 2009; Cedrés et al., 2013). It is therefore likely that the physical processes governing the ionized gas densities occur on spatial scales far below what can be resolved at high-z. However, global trends between n_e and galaxy properties provide constraints on what types of physical processes are most likely to drive the evolution of the global, luminosity-weighted average n_e in SFGs over cosmic time.

The electron density appears to be closely linked to the level of star formation in galaxies. Kaasinen et al. (2017) found that there is no difference in the electron densities of galaxies at $z \sim 0$ and $z \sim 1.5$ when they are matched in SFR. The electron density has been found to correlate with specific SFR (sSFR) and SFR surface density (Σ_{SFR}), at both low and high redshift (e.g. Shimakawa et al., 2015; Jiang et al., 2019; Kashino & Inoue, 2019). There is also evidence for a spatial correlation between enhanced star formation activity and enhanced electron density in local galaxies (e.g. Westmoquette et al., 2011, 2013; McLeod et al., 2015; Herrera-Camus et al., 2016; Kakkad et al., 2018).

Several scenarios have been proposed to explain the correlation between n_e and the level of star formation. Σ_{SFR} sets the rate of energy injection by stellar winds and supernovae (e.g. Ostriker & Shetty, 2011; Kim et al., 2013), and may therefore also govern the pressure and density in H II regions (e.g. Groves et al., 2008; Krumholz & Matzner, 2009; Kaasinen et al., 2017; Jiang et al., 2019). Alternatively, the density of the parent molecular cloud, which determines Σ_{SFR} through the Kennicutt-Schmidt relation, may also set the initial n_e (e.g. Hunt & Hirashita, 2009; Shimakawa et al., 2015; Kashino & Inoue, 2019). A related possibility is that the ambient density and pressure could significantly influence

the dynamical evolution of H II regions. Oey & Clarke (1997, 1998) proposed that H II regions undergo energy conserving expansion powered by stellar winds and supernovae (see also Weaver et al., 1977) until the internal pressure is on the order of the ambient pressure. H II regions in denser environments may expand less, resulting in larger electron densities (e.g. Shirazi et al., 2014; Herrera-Camus et al., 2016). Finally, it has been suggested that galaxies or regions with higher $\Sigma_{\rm SFR}$ may have a larger fraction of young H II regions which are still over-pressured with respect to their surroundings (e.g. Herrera-Camus et al., 2016; Jiang et al., 2019). It is important to note that while any of these scenarios could potentially explain a link between the level of star formation and the *volume averaged* electron density, the relationship between n_e(rms) and n_e([S II]) as a function of redshift has not yet been established observationally.

Quantitative tests of these scenarios have been hindered by the limited dynamic range of individual galaxy samples. Measurements of n_e([S II]) and n_e([O II]) in high-z galaxies have large associated uncertainties because the [S II] and [O II] emission lines are relatively weak, and the [O II] doublet lines can be significantly blended in galaxies with large integrated line widths. In addition, the measurements could be biased by emission from ionized gas outflows, which are prevalent at high-z. The line-emitting gas in star formation driven outflows at $z \sim 2$ is $\sim 5\times$ denser than the line-emitting gas in the H II regions of the galaxies driving the outflows (e.g. Förster Schreiber et al., 2019). In order to recover intrinsic correlations between galaxy properties and the electron densities in H II regions, and to place stronger constraints on the physical driver(s) of the n_e evolution, it is necessary to assemble a large sample of galaxies spanning a wide range in redshift and galaxy properties, while also minimizing the degree of contamination from line emission produced outside of H II regions.

In this paper we use a sample of 611 galaxies with no evidence of AGN activity or broad line emission associated with outflows, drawn primarily from the KMOS$^{\rm 3D}$ (Wisnioski et al., 2015, 2019) and SAMI (Bryant et al., 2015; Scott et al., 2018) integral field surveys, to investigate the physical processes driving the evolution of the typical electron density in star-forming galaxies (SFGs) from $z \sim 2.6$ to $z \sim 0$. The KMOS$^{\rm 3D}$ sample is distributed across three redshift bins at $z \sim 0.9$, $z \sim 1.5$ and $z \sim 2.2$, allowing us to examine the evolution of n_e over ~ 5 Gyr of cosmic history with a single dataset. We apply the same sample selection, spectral extraction and stacking methodology to the SAMI sample to obtain a self-consistent measurement of n_e at $z \lesssim 0.1$. The combined sample is centered on the star-forming MS at each redshift and spans more than three orders of magnitude in SFR.

The paper is structured as follows. In Section 4.2 we outline the properties of our galaxy samples and describe the methods used to stack spectra, measure the [S II] doublet ratio and calculate the H II region electron densities and pressures. We present our results on the redshift evolution of n_e([S II]), n_e(rms) and ionized gas filling factors in Section 4.3, and explore how n_e([S II]) varies as a function of global galaxy properties in Section 4.4. In Section 4.5 we compare our density measurements to quantitative predictions for various potential drivers of the n_e evolution, and evaluate the most likely causes of the elevated electron densities in SFGs at high-z. Our conclusions are summarized in Section

4.6.

Throughout this work we assume a flat ΛCDM cosmology with $H_0 = 70$ km s^{-1} Mpc^{-1} and $\Omega_0 = 0.3$. All galaxy properties have been derived assuming a Chabrier (2003) initial mass function.

4.2 Data and Methodology

4.2.1 KMOS^{3D}+ Parent Sample

The high-z SFG sample used in this paper is primarily drawn from the KMOS^{3D} survey, a VLT/KMOS IFU survey focused on investigating the emission line properties of primarily mass-selected galaxies at $0.6 < z < 2.7$ (Wisnioski et al., 2015, 2019). The KMOS^{3D} sample was drawn from the subset of 3D-HST galaxies with $\log(M_*/M_\odot) > 9$ and $K_{AB} \leq 23$ mag, with the aim to achieve a homogeneous coverage of the star-forming population as a function of stellar mass and redshift. In this paper, we focus on the subset of 525 KMOS^{3D} galaxies that were included in the Förster Schreiber et al. (2019) study of outflows across the high-z galaxy population. These objects were selected to have Hα emission detected at a signal-to-noise (S/N) per spectral channel > 3, and no strong telluric line contamination in the region around the [N II]+Hα complex. Förster Schreiber et al. (2019) visually inspected the spectra of all galaxies to search for broad emission line components indicative of outflows, allowing us to isolate a sample of galaxies with no evidence of outflows for our analysis (see Section 4.2.3).

We supplement our KMOS^{3D} sample with galaxies from other high-z surveys that were also included in the Förster Schreiber et al. (2019) analysis. 47 galaxies were drawn from the SINS/zC-SINF Survey (Förster Schreiber et al., 2009, 2018; Mancini et al., 2011), a VLT/SINFONI survey of 84 galaxies at $1.5 < z < 2.5$ selected on the basis of having secure spectroscopic redshifts and expected Hα fluxes $\geq 5 \times 10^{-17}$ erg s^{-1} cm^{-2}. Again, objects with low Hα S/N or bad telluric contamination were excluded. Finally, we included six galaxies at $2 < z < 2.5$ from the K band selected sample of Kriek et al. (2007, 2008) observed with VLT/SINFONI and Gemini/GNIRS, and the galaxy EGS-13011166 at $z \sim 1.5$ observed with LBT/LUCI (Genzel et al., 2013, 2014). Our combined high-z parent sample consists of 579 galaxies, of which $\sim 90\%$ are drawn from KMOS^{3D}, and therefore this sample is henceforth referred to as the KMOS^{3D}+ parent sample.

Stellar masses were derived for all galaxies using population synthesis modeling of the rest-UV to optical/near-IR spectral energy distributions (SEDs), and SFRs were calculated from the rest-frame UV + IR luminosities using standard procedures, as described in Wuyts et al. (2011b). Galaxy stellar disk effective radii (R_e) were derived from two dimensional Sérsic fits to *HST H* band imaging (van der Wel et al., 2012; Lang et al., 2014).

Figure 4.1 shows the redshift distribution of the KMOS^{3D}+ parent sample (left, grey histogram) and how the galaxies are distributed in the $M_* - \mathrm{SFR}$ (center) and $M_* - R_e$ (right) planes. Marker colors and symbols identify different subsets of the sample which

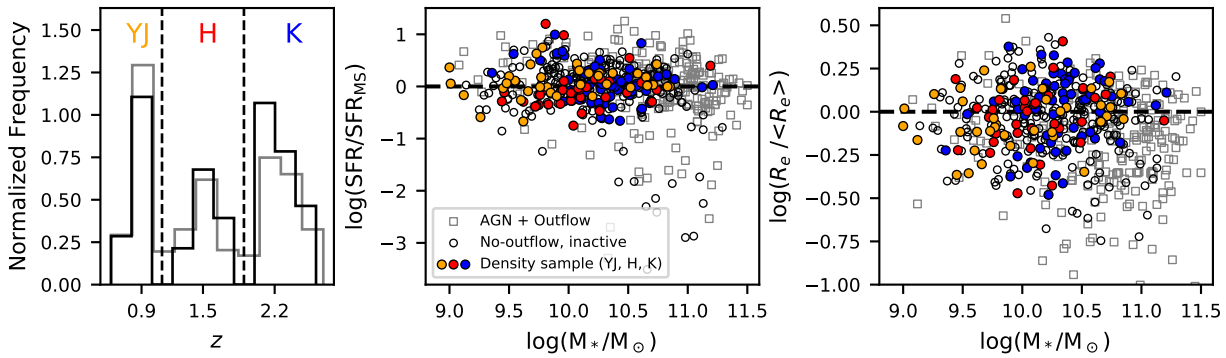

Figure 4.1: Left: Normalized redshift distributions of the KMOS^{3D}+ parent sample (grey) and our density sample (black). Center and right: Distribution of our density sample (solid markers) in (center) offset from the star-forming MS and (right) offset from the galaxy mass-size relation, both as a function of stellar mass, compared to the distribution of the parent no-outflow inactive (open black circles) and AGN + outflow (open grey squares) samples. Orange, red and blue markers indicate galaxies in the YJ, H and K redshift slices, respectively.

are discussed later. The 'density sample', shown in solid markers, is the primary sample used in our analysis and consists of inactive galaxies that do not show evidence of outflows and have high quality [S II] spectra (described in Section 4.2.3). In the center and right panels we have removed the average trends in SFR and R_e as a function of stellar mass and redshift, adopting the Speagle et al. (2014) parametrization of the star-forming MS (their Equation 28; chosen for consistency with the Tacconi et al. 2020 molecular gas depletion time scaling relation which is later used to estimate molecular gas masses) and the van der Wel et al. (2014) mass-size relation for late type galaxies as a function of the Hubble parameter $H(z)$.

The galaxies are grouped in three distinct redshift slices, corresponding to the redshift ranges where Hα falls into the KMOS YJ ($z \sim 0.9$), H ($z \sim 1.5$) and K ($z \sim 2.2$) band filters. The KMOS^{3D}+ parent sample spans the average SFR and size distributions of normal SFGs at $9.0 \lesssim \log(M_*/M_\odot) \lesssim 11.5$, and also extends into the starburst, quiescent and compact galaxy regimes.

4.2.2 Extracting Integrated Spectra

Integrated spectra for the KMOS^{3D} and SINS/zC-SINF galaxies were extracted from the integral field datacubes as described in Section 2.5.1 of Förster Schreiber et al. (2019). Briefly, the datacubes were median subtracted to remove stellar continuum, 4σ-clipped blueward and redward of the strong emission lines to mask skyline residuals, and smoothed over the spatial dimensions using a Gaussian kernel with a typical full width at half maximum (FWHM) of 3 pixels (0.6", similar to the typical point spread function FWHM of $\sim$ 0.5"; Wisnioski et al. 2019). A single Gaussian line profile was fit to the Hα emission in each

spaxel of the smoothed cubes to create velocity field maps, and the velocity field maps were used to shift the (unsmoothed) spectra of all spaxels within each galaxy to the same velocity centroid. The velocity shifting minimizes broadening of the integrated emission line profiles induced by the presence of large scale, gravitationally driven line-of-sight velocity gradients across rotating disks. Integrated spectra were extracted by summing the velocity shifted spectra of all spaxels within a galactocentric radius of 0.25 – 0.6" (corresponding to a physical aperture diameter of 2 – 5 kpc, similar to the median R_e of 3.4 kpc), where the aperture size was adjusted based on the galaxy size to optimize the S/N of the extracted spectrum.

4.2.3 Selection of the KMOS^{3D}+ Density Sample

In this work, we focus on star-forming galaxies with no evidence of AGN activity or broad line emission indicative of outflows. Förster Schreiber et al. (2019) created a single stacked spectrum of inactive galaxies with strong outflows spanning $0.6 < z < 2.6$, and measured the [S II] ratios and electron densities of the narrow ISM component and the broader outflow component individually. They found that ionized gas in star formation driven outflows is typically $\sim 5\times$ denser than the ionized ISM of the galaxies driving the outflows (see also Arribas et al., 2014; Ho et al., 2014; Perna et al., 2017; Kakkad et al., 2018; Fluetsch et al., 2020), suggesting that ISM material is shocked and compressed as it is swept up by the hot wind fluid. For these galaxies, the density measured from a single component fit to the full (ISM + outflow) [S II] line profiles would be a luminosity-weighted average of the ISM density and the outflow density. Therefore, including galaxies with detected outflows could bias the measured H II region electron densities toward artificially large values.

AGN host galaxies are removed because 1) outflows are prevalent in AGN host galaxies (e.g. Genzel et al., 2014; Förster Schreiber et al., 2014; Harrison et al., 2016; Leung et al., 2019; Förster Schreiber et al., 2019), and 2) we calculate the electron density using H II region photoionization models (discussed in Section 4.2.6), which cannot be applied to the spectra of AGN host galaxies because the AGN ionizing radiation field is significantly harder than an O star spectrum and will produce a very different ionization and temperature structure (see e.g. discussion in Kewley et al. 2019; Davies et al. 2020b).

Förster Schreiber et al. (2019) classified all galaxies in the KMOS^{3D}+ sample as either AGN or inactive, and outflow or no-outflow. Galaxies were classified as AGN if their hard X-ray luminosity, radio luminosity, mid-IR colors, or [N II]/Hα ratio exceeded the threshold for pure star formation. Outflows were identified visually based on the presence of broad or asymmetric features in the integrated emission line profiles. The velocity shifting that was performed prior to spectral extraction increases the sharpness and S/N per spectral channel of the line emission from the galaxy disk (see e.g. Figure 1 of Swinbank et al. 2019), and therefore maximizes the outflow detection fraction by pushing the detection limit to lower outflow velocities and mass outflow rates. The majority (356/579 or 61%) of the galaxies were classified as inactive with no visually identifiable outflow component in the line emission ('no-outflow'). A further 87 galaxies (15%) were classified as inactive with

outflows, and the remaining 136 (23%) galaxies were classified as AGN hosts (of which 94, or 16% of the parent sample, have detected outflows).

Of the 356 inactive galaxies with no outflows, 320 have spectra covering the [S II] doublet. The [S II] emission lines are relatively weak (with a typical peak amplitude ∼5% that of the Hα line at $z \sim 1-2$), and small changes in the [S II]λ6716/[S II]λ6731 ratio correspond to relatively large differences in the derived electron density, so it is very important to create a sample of spectra without significant sky contamination in the [S II] doublet region. We visually inspected the spectra of all 320 no-outflow inactive galaxies and removed objects with elevated errors or bad systematics in the [S II] region. This quality cut leaves us with a final sample of 140 galaxies (the 'density sample').

The left panel of Figure 4.1 compares the redshift distribution of the density sample (black) and the parent sample (grey). Of our 140 galaxies, 39 galaxies fall in the $z \sim 0.9$ slice, 36 galaxies fall in the $z \sim 1.5$ slice, and 65 galaxies fall in the $z \sim 2.2$ slice. The density sample covers a wide redshift range and allows us to probe the n_e evolution over ~ 5 Gyr in cosmic history with consistent data and analysis.

Colored circles in the center and right panels of Figure 4.1 show where the $z \sim 0.9$ (YJ, orange), $z \sim 1.5$ (H, red) and $z \sim 2.2$ (K, blue) subsets of our density sample are located in the $M_* -$ SFR and $M_* - R_e$ planes, compared to the full sample of no-outflow inactive galaxies (open black circles) and the galaxies with outflows and/or AGN activity (open grey squares). The density sample probes typical SFGs spanning ~ 2 dex in both M_* and sSFR, and has a median stellar mass of $\log(M_*/M_\odot) = 10.2$, with a slight trend towards higher stellar masses at higher redshift (the median stellar masses in the individual redshift bins are $\log(M_*/M_\odot) = 9.9$ at $z \sim 0.9$, $\log(M_*/M_\odot) = 10.1$ at $z \sim 1.5$, and $\log(M_*/M_\odot) = 10.3$ at $z \sim 2.2$).

By nature of the selection criteria the density sample does not extend to the highest stellar masses or into the compact, quiescent and starburst galaxy regimes where AGN and outflows are most frequent (see Förster Schreiber et al., 2019). The removal of the highest stellar mass objects, which also have the highest SFRs, means that the density sample has a slightly lower median SFR than the parent sample at fixed z. The most actively star-forming galaxies are expected to have the highest n_e (e.g. Shimakawa et al., 2015; Kaasinen et al., 2017; Jiang et al., 2019; Kashino & Inoue, 2019), and therefore there is a possibility that the electron densities measured from the density sample could under-estimate the true average n_e in H II regions at each redshift. However, we perform a test which suggests that the n_e values measured from our density sample are likely to reflect the average gas conditions in H II regions across the wider SFG population (see full description in Appendix 4.7.1).

4.2.4 $z \sim 0$ Comparison Sample: SAMI Galaxy Survey

We measure the zero-point of the n_e evolution using a sample of galaxies from the SAMI Galaxy Survey (Bryant et al., 2015), an integral field survey of ~ 3000 galaxies at $z \lesssim 0.1$. We choose an IFU sample rather than the much larger set of SDSS fiber spectra because the IFU data can be analysed using exactly the same methods applied to the KMOS^{3D}+ data,

allowing us to obtain a self-consistent measurement of n_e at $z \sim 0$. We specifically choose the SAMI survey because 1) it is mass selected and 2) the spectral resolution ($R \sim 4300$) is comparable to that of our KMOS^{3D}+ data ($R \sim 3500$ – 4000).

The most recent data release (DR2) includes blue and red data cubes (covering 3750 – 5750Å and 6300 – 7400Å observed, respectively) for 1559 galaxies, and velocity maps for 1526/1559 galaxies (Scott et al., 2018). We start with 1197 galaxies that lie in the same stellar mass range as our KMOS^{3D}+ targets ($\log(M_*/M_\odot) = 9.0$ – 11.2). Using the published emission line catalogues, we select 839 galaxies for which Hα is detected at $\geq 10\sigma$ and Hβ, [N II]λ6584 and [O III]λ5007 are all detected at $\geq 3\sigma$. We remove 280 galaxies with significant contributions from non-stellar sources (lying above the Kauffmann et al. 2003 classification line on the [N II]/Hα vs. [O III]/Hβ diagnostic diagram). For each of the remaining 559 galaxies we velocity shift the blue and red datacubes and extract integrated spectra by summing the spectra of all spaxels with detected line emission[2], as described in Section 4.2.2. Stellar continuum fitting and subtraction is performed by running the Penalized Pixel-Fitting (pPXF) method (Cappellari & Emsellem, 2004; Cappellari, 2017) on the full (blue + red) spectrum for each galaxy, using the MILES library of stellar templates (Vazdekis et al., 2010). The blue spectra are only used to constrain the continuum fitting and are not used in any further analysis. We visually inspect all integrated spectra and continuum fits, and reject galaxies with strong skyline residuals near any of the primary emission lines (Hα, [N II] and [S II]), evidence for outflow emission (broad or asymmetric emission in multiple lines), or bad continuum fits. The final sample consists of 471 galaxies.

We calculate the global SFRs of the SAMI galaxies by summing the publicly available dust-corrected Hα SFR maps (described in Medling et al. 2018). The left hand panel of Figure 4.2 shows how the SAMI galaxies are distributed in the M_* – SFR plane. The SAMI sample spans ~ 2 dex in M_* and ~ 3.5 dex in sSFR, and has a median stellar mass of $\log(M_*/M_\odot) = 9.6$; significantly lower than the median stellar mass of the KMOS^{3D}+ sample ($\log(M_*/M_\odot) = 10.2$) despite covering the same stellar mass range. The differences between the median stellar masses of the samples are accounted for when relevant to our analysis.

The red dotted line in Figure 4.2 shows the Speagle et al. (2014) star-forming main sequence. The SAMI galaxies follow a slightly steeper relation indicated by the red dashed line, which is the best fit to the full sample of galaxies with $\log(\text{sSFR}\ [\text{yr}^{-1}]) > -11.2$ (the approximate boundary between the star-forming and quiescent populations). The discrepancy in the main sequence slope is attributed to the fact that spaxels with significant contributions from non-stellar excitation sources are masked in the SAMI SFR maps, meaning that the calculated SFRs are lower limits (Medling et al., 2018). Throughout the paper the main sequence offset of the SAMI galaxies is defined with respect to the best fit (red dashed) line.

[2]The integrated spectra cover a median galactocentric radius of $\sim 2R_e$. This is larger than the typical radius covered by the KMOS^{3D}+ spectra, but excluding spaxels outside $1R_e$ does not have any significant impact on the electron densities measured from the SAMI spectra.

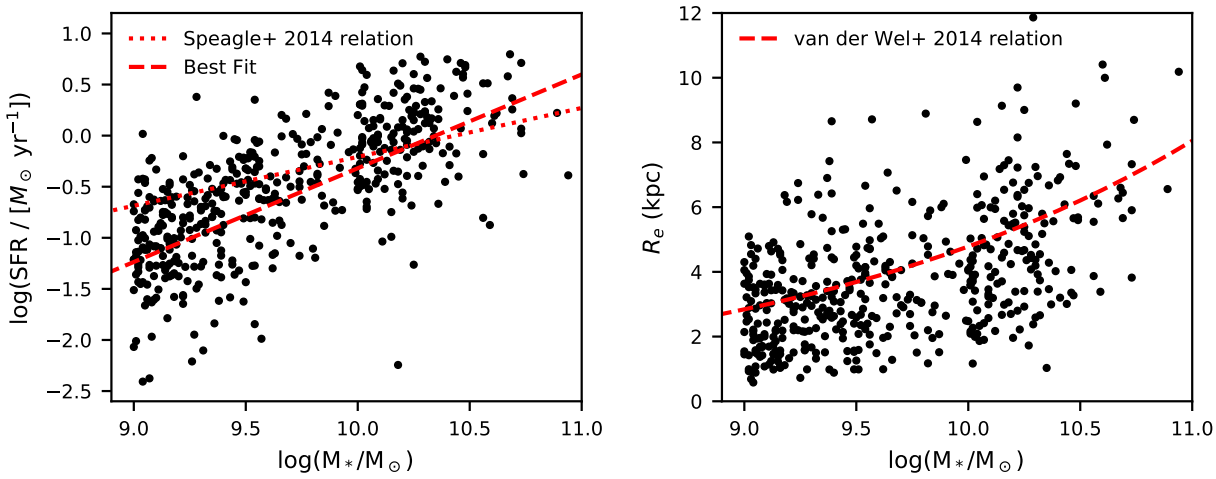

Figure 4.2: Distribution of SAMI galaxies in the (left) M_*- SFR and (right) $M_* - R_e$ planes. The van der Wel et al. (2014) mass-size relation shown in the right hand panel has been adjusted to the rest-frame central wavelength of the SDSS r-band filter ($\lambda \simeq 6020$ Å) using their Equation 1.

The effective radii of the SAMI galaxies were derived from two dimensional Sérsic fits to the GAMA r band imaging (Kelvin et al., 2012). The right hand panel of Figure 4.2 shows where the SAMI galaxies lie in the $M_* - R_e$ plane, compared to the van der Wel et al. (2014) mass-size relation (red dashed line) which has been adjusted to the rest-frame central wavelength of the SDSS r-band filter ($\lambda \simeq 6020$ Å) using their Equation 1. The SAMI galaxies follow the expected increase in average size with increasing stellar mass but are $\sim 10\%$ smaller than predicted by the van der Wel et al. (2014) relation.

4.2.5 Stacking

We stack the integrated spectra of different sets of galaxies to produce high S/N composite spectra that can be used to make robust measurements of n_e and thermal pressure. Before stacking, each spectrum is normalized to a peak Hα amplitude of one to prevent the stacks being biased towards galaxies with brighter Hα emission (i.e. galaxies at lower redshifts and/or with higher SFRs). The normalized galaxy spectra are averaged to obtain the stacked spectrum. When averaging, values lying more than 3σ away from the median in each spectral channel are masked to ensure that the final stacks are not disproportionately affected by any possible remaining outliers.

4.2.6 Electron Density and Thermal Pressure Calculations

[S II]λ6716/[S II]λ6731 Ratio and Model Grids

We measure the electron density and the thermal pressure from each stacked spectrum using the [S II]λ6716/[S II]λ6731 ratio (also referred to as the '[S II] ratio' and '$R_{\rm SII}$'). [S II]λ6716 and [S II]λ6731 originate from excited states that have similar excitation energies but different collision strengths and radiative decay rates, meaning that the [S II] ratio is strongly dependent on n_e but only weakly dependent on temperature. In the low density limit, the timescale for collisional de-excitation is significantly longer than the timescale for radiative decay and the population ratio is determined by the ratio of the collision strengths, resulting in $R_{\rm SII} \sim 1.45$. In the high density limit, collisions govern transitions between the excited states and the electrons are distributed in a Boltzmann population ratio, resulting in $R_{\rm SII} \sim 0.45$. At densities similar to the critical density (where the probability of collisional de-excitation and radiative decay are approximately equal), $R_{\rm SII}$ varies almost linearly with n_e. The [S II] ratio is most sensitive to densities in the range $\sim 40 - 5000$ cm^{-3} (e.g. Osterbrock & Ferland, 2006; Kewley et al., 2019), and is therefore a good probe of the electron density in the line-emitting material within H II regions which typically ranges from tens to hundreds cm^{-3}.

We convert from $R_{\rm SII}$ to electron density and thermal pressure using the constant density and constant pressure model grids presented in Kewley et al. (2019), respectively. The grids are outputs of plane-parallel H II region models run with the MAPPINGS 5.1 photoionization code. The constant density models allow for a radially varying temperature and ionization structure within the nebula, and the constant pressure models additionally allow for radially varying density structure. Real H II regions can have strong density gradients (e.g. Binette et al., 2002; Phillips, 2007) but are expected to have approximately constant pressure (e.g. Field, 1965; Begelman, 1990), and therefore the pressure provides a more meaningful description of the conditions within H II regions than the electron density.

Outputs of the constant density and constant pressure models are provided for $\log(n_e/{\rm cm}^{-3}) = 1.0 - 5.0$ and $\log(P/k) = 4.0 - 9.0$, respectively, with a sampling of 0.5 dex in both quantities. Throughout this paper, P/k is in units of K cm^{-3}. For each value of n_e and $\log(P/k)$, the grids include outputs of models run at five metallicities ($12 + \log({\rm O/H}) = 7.63$, 8.23, 8.53, 8.93 and 9.23) and nine ionization parameters ($\log q = 6.5 - 8.5$ in increments of 0.25 dex). The metallicity and ionization parameter determine the temperature structure of the nebula. The [S II] ratio has a weak dependence on electron temperature because the collisional de-excitation rate scales with $T^{-1/2}$ (from the Maxwell-Boltzmann electron temperature distribution), and therefore the critical density scales with $T^{1/2}$ (e.g. Dopita & Sutherland, 2003; Kewley et al., 2019).

Measurements

We derive n_e([S II]) and $\log(P_{\rm th}/k)$([S II]) for each stacked spectrum by interpolating the model grids in q, Z and $R_{\rm SII}$. The [S II] ratio is measured by fitting a single Gaussian to each of the [S II] lines. We require both lines to have the same velocity centroid and

velocity dispersion.

We estimate the average metallicity of the galaxies in each stack using the [N II]+[S II]+Hα calibration from Dopita et al. (2016). This diagnostic is relatively insensitive to variations in the density/pressure and ionization parameter, making it well suited for use with high redshift galaxies. Dopita et al. (2016) calibrated the diagnostic using MAPPINGS 5.0 H II region models run with the same abundance set as the Kewley et al. (2019) models, which is crucial because of the large systematic discrepancies between different metallicity calibrations in the literature. We simultaneously fit all the strong emission lines ([N II]λ6548, Hα, [N II]λ6584, [S II]λ6716, [S II]λ6716) to measure the [N II]/Hα and [S II]/Hα ratios and obtain an estimate of the metallicity. The metallicity estimates for the KMOS^{3D}+ stacks are listed in Table 4.4.

Our high-z spectra do not cover the [O III]λ5007 and [O II]$\lambda\lambda$3726,3729 emission lines which are required to make a direct measurement of the ionization parameter. We adopt typical ionization parameters of $\log(q) = 7.8$ for the KMOS^{3D}+ galaxies based on measurements of star-forming galaxies at $z \sim 1 - 2$ from the COSMOS-[O II] and MOSDEF surveys (Sanders et al., 2016; Kaasinen et al., 2018), and $\log(q) = 7.3$ for the SAMI galaxies (Poetrodjojo et al., 2018). However, varying the ionization parameter by a factor of three changes the derived pressures and densities by at most 0.1 dex (a factor of 1.2), and therefore the choice of ionization parameter has a minimal impact on our results.

We estimate the errors on the derived $R_{\rm SII}$, n_e([S II]) and $\log(P_{\rm th}/k)$([S II]) values using a combination of bootstrapping and Monte Carlo sampling to account for both sample variance and measurement uncertainties. For a given stack of N galaxies, we randomly perturb the spectrum of each galaxy by its measurement errors, draw N perturbed spectra allowing for duplicates (bootstrapping), stack the drawn spectra, and measure $R_{\rm SII}$, n_e([S II]) and $\log(P_{\rm th}/k)$([S II]). This process is repeated 600 times[3], and the 16th and 84th percentile values of the 600 measurements of $R_{\rm SII}$, n_e([S II]) and $\log(P_{\rm th}/k)$([S II]) are taken as the lower and upper boundaries of the 1σ confidence interval for each quantity. We note that due to the relatively high S/N of the input spectra, the error budget is dominated by sample variance in all cases.

4.3 Redshift Evolution of H II Region Electron Densities

4.3.1 Typical [S II] Electron Density at $z \sim 0.9$, $z \sim 1.5$ and $z \sim 2.2$ with KMOS^{3D}+

We begin by using our 'density sample' of inactive galaxies with no outflows to measure the average n_e([S II]) and $\log(P_{\rm th}/k)$([S II]) in each of the KMOS^{3D}+ redshift slices. The stacked [S II] doublet profiles and best Gaussian fits are shown in Figure 4.3. The grey

[3]This number was empirically verified to result in consistent error estimates between trials.

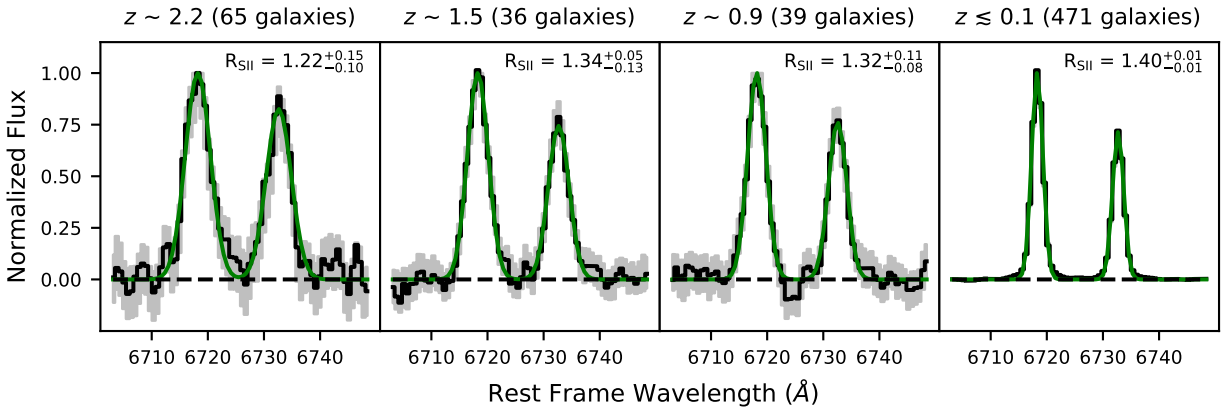

Figure 4.3: Stacked [S II] doublet profiles of galaxies with no evidence for outflows or AGN activity, in four redshift slices: $z \sim 2.2$ (KMOS K band), $z \sim 1.5$ (KMOS H band), $z \sim 0.9$ (KMOS YJ band), and $z \lesssim 0.1$ (SAMI). The grey shaded regions indicate the 1σ spread of the 600 bootstrap stacks generated for each redshift slice (described in Section 4.2.6). The green curves indicate the best fit Gaussian profiles.

shaded regions indicate the 1σ spread of the 600 bootstrap stacks generated for each redshift slice.

The left hand panel of Figure 4.4 illustrates how the measured [S II] ratios are converted to electron densities. For each redshift slice we interpolate the $q - Z - n_e - R_{\rm SII}$ photoionization model output grid at the measured Z and adopted q to produce a set of (n_e, $R_{\rm SII}$) pairs, plotted as grey circles. The grey dashed lines are linear interpolations between the sampled electron densities. We generate and plot the circles and lines for each stack individually but the differences between the sets of interpolated outputs are barely visible. The green stars and error bars show the $R_{\rm SII}$ measurements for the KMOS$^{\rm 3D}$+ stacks and the corresponding n_e([S II]) values derived from the outputs of the constant density models. The $\log(P_{\rm th}/k)$([S II]) values are derived from the outputs of the constant pressure models using the same method. All of the measured and derived quantities are listed in Table 4.4.

We find n_e([S II]) $= 101^{+59}_{-85}$ cm^{-3} at $z \sim 0.9$, consistent with results from the KROSS survey (Swinbank et al., 2019), and n_e([S II]) $= 79^{+120}_{-40}$ cm^{-3} at $z \sim 1.5$, in agreement with measurements from the COSMOS-[O II] (Kaasinen et al., 2017) and FMOS-COSMOS (Kashino et al., 2017) surveys. At $z \sim 2.2$ we measure n_e([S II]) $= 187^{+140}_{-132}$ cm^{-3}, similar to the values reported by the KBSS-MOSFIRE (Steidel et al., 2014) and MOSDEF (Sanders et al., 2016) surveys.

The choice to remove galaxies with outflows from our sample was motivated by the observation of enhanced electron densities in outflowing material (Förster Schreiber et al., 2019). However, the electron densities measured from our sample of no-outflow inactive galaxies match the electron densities measured from other galaxy samples that likely include star formation driven outflows. This suggests that the increased incidence of outflows

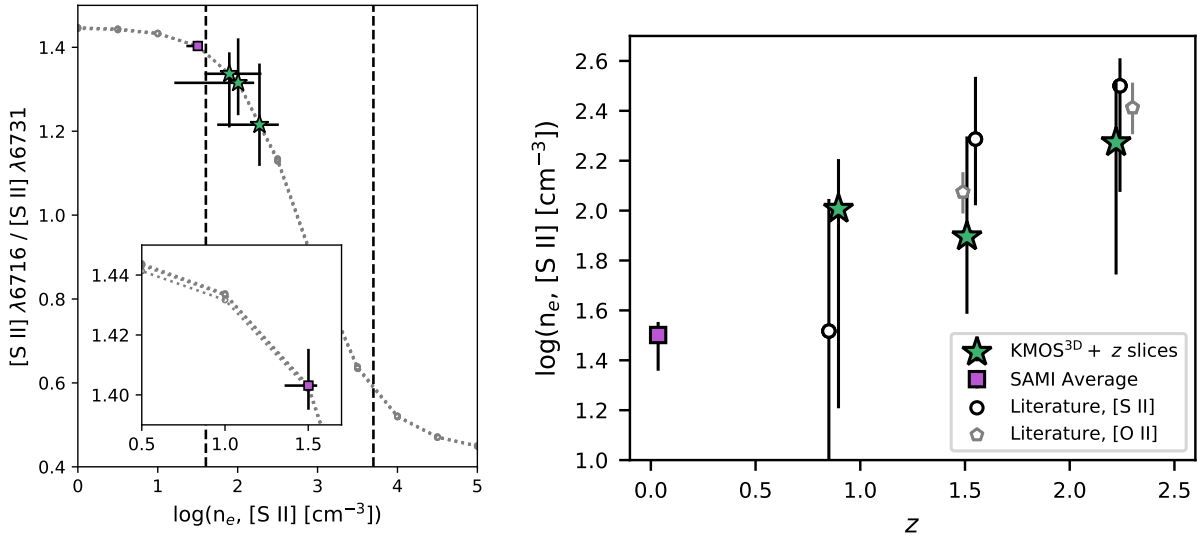

Figure 4.4: Left: Illustration of the conversion between $R_{\rm SII}$ and n_e([S II]). For each redshift slice, we interpolate the $q - Z - n_e - R_{\rm SII}$ photoionization model output grid at the measured Z and adopted q to produce a set of (n_e, $R_{\rm SII}$) pairs. The (n_e, $R_{\rm SII}$) pairs are plotted as open grey circles, and the grey dashed lines are linear interpolations between the sampled electron densities. We generate and plot the circles and lines for each stack individually but the differences between the four sets of interpolated outputs are barely visible. Black dashed lines indicate the boundaries of the region where $R_{\rm SII}$ is most sensitive to n_e. The green stars and purple square show the measured $R_{\rm SII}$ and the derived n_e([S II]) for the KMOS^{3D}+ and SAMI stacks, respectively. The inset in the bottom left is a zoom-in on the region around the SAMI measurement, showing that the measured $R_{\rm SII}$ is inconsistent with the theoretical maximum value. Right: The redshift evolution of n_e([S II]) based on the combination of the KMOS^{3D}+, SAMI and high-z literature ([S II]: black circles, [O II]: grey pentagons) samples.

at high redshift does not have a significant impact on the magnitude of the density evolution inferred from single component Gaussian fits to the [S II] doublet lines. In Appendix 4.7.2 we confirm that including sources with star formation driven outflows (in proportion to their population fraction) has a minimal impact on the measured average densities.

We also investigate the impact of AGN contamination on the measured densities. Uniform identification of AGN host galaxies at high redshift is challenging due to the varying availability and depth of multi-wavelength ancillary data between extragalactic deep fields. In Appendix 4.7.3 we present tentative evidence to suggest that the measured densities could be up to a factor of ~ 2 larger when AGN host galaxies are included.

4.3.2 Typical [S II] Electron Density at $z \sim 0$ with SAMI

We use the velocity shifted spectra of the sample of 471 SAMI galaxies to obtain a self-consistent measurement of the electron density at $z \sim 0$. The stacked [S II] doublet profile

and best Gaussian fit are shown in the right-most panel of Figure 4.3. The purple square in the left hand panel of Figure 4.4 indicates that the SAMI stack lies in the low n_e regime of the [S II] diagnostic where $R_{\rm SII}$ asymptotes towards the theoretical maximum value, causing the n_e – $R_{\rm SII}$ curve to become quite flat. However, the inset shows that due to the very high S/N of the stacked spectrum, the measured $R_{\rm SII}$ is inconsistent with the theoretical maximum value at the $\sim 5\sigma$ level.

The measured $R_{\rm SII}$ corresponds to an electron density of $n_e([\text{S II}]) = 32^{+4}_{-9}$ cm^{-3}. This value is in very good agreement with electron densities measured for resolved regions of local spiral galaxies using the [N II]122μm/[N II]205μm ratio which is a robust tracer of electron density down to $n_e \sim 10$ cm^{-3} (Herrera-Camus et al., 2016), and with the typical n_e([S II]) derived from stacked SDSS fiber spectra of local galaxies (Kashino & Inoue, 2019).

4.3.3 Redshift Evolution of the [S II] Electron Density, and the Impact of Diffuse Ionized Gas

We combine the SAMI and KMOS$^{\rm 3D}$+ measurements to investigate how n_e evolves as a function of redshift, as shown in the right hand panel of Figure 4.4. We also gather [S II] and [O II] ratio measurements from other surveys of high-z galaxies in the literature (KBSS-MOSFIRE; Steidel et al. 2014, MOSDEF; Sanders et al. 2016, KROSS; Stott et al. 2016, COSMOS-[O II]; Kaasinen et al. 2017, and FMOS-KMOS; Kashino et al. 2017). We require that the median SFR of each sample lies within 0.5 dex of the star-forming MS to ensure that the galaxies are representative of the underlying SFG population at the relevant redshifts. The majority of the literature measurements are based on slit spectra with the exception of the data from KROSS, a KMOS IFU survey of SFGs at $0.6 < z < 1.0$ (Stott et al., 2016). A more complete description of the literature samples is given in Appendix 4.8. We re-calculate the electron densities from the published line ratio measurements to avoid systematic biases in the conversion between line ratios and n_e arising from differences in atomic data or assumed electron temperature (see e.g. discussions in Sanders et al. 2016 and Kewley et al. 2019). We do not calculate $\log(P_{\rm th}/k)([\text{S II}])$ for the literature samples because we do not have the line ratio measurements required to obtain self-consistent metallicity estimates.

The [S II] and [O II] lines originate from different regions of the nebula and will only give consistent densities if the electron temperature does not vary significantly between the [S II] and [O II] emitting regions. Sulfur exists as S^+ for photon energies in the range 10.4 – 23.3 eV[4], and therefore [S II] emission is expected to originate primarily from dense clumps and the partially ionized zone at the edge of the H II region (e.g. Proxauf et al., 2014). On the other hand, O^+ exists for photon energies in the range 13.6 – 35.1 eV and therefore [O II] is emitted over a much larger fraction of the H II region (Kewley et al., 2019). However, Sanders et al. (2016) showed that there is a good correspondence between

[4]Ionization energies taken from the NIST Atomic Spectra Database (ver. 5.7.1); https://physics.nist.gov/asd.

the global [S II] and [O II] densities measured for star-forming galaxies at $z \sim 2$. In our plots, we distinguish between densities measured from the [S II] ratio (circles with black outlines) and the [O II] ratio (pentagons with grey outlines).

Figure 4.4 clearly suggests that the typical electron densities inferred from the [S II] and [O II] doublet ratios have decreased by a factor of $\sim 6 - 10$ over the last 10 Gyr, consistent with previous studies. However, to understand whether this reflects an evolution in the typical properties of ionized gas inside H II regions, we must consider the origin of the line emission. It is well established that around 50% of the Hα emission from local galaxies originates from diffuse ionized gas (DIG) between H II regions (e.g. Thilker et al., 2002; Oey et al., 2007; Poetrodjojo et al., 2019; Chevance et al., 2020). The DIG is thought to be ionized by a combination of leaked ionizing photons from H II regions, radiation from low mass evolved stars, and shock excitation (e.g. Martin, 1997; Ramirez-Ballinas & Hidalgo-Gámez, 2014; Zhang et al., 2017). DIG dominated regions have larger [N II]/Hα and [S II]/Hα ratios than H II regions (e.g. Rand, 1998; Haffner et al., 1999; Madsen et al., 2006), and it is therefore likely that a significant fraction of the [S II] emission from the SAMI galaxies is associated with the DIG rather than H II regions.

The line-emitting clumps in the DIG have a typical density of $n_e \sim 0.05$ cm^{-3} (e.g. Reynolds, 1991), meaning that DIG contamination could potentially have a significant impact on the measured [S II] ratios. Fortunately the [S II] ratio saturates for densities below $n_e \sim 40$ cm^{-3} (see the left hand panel of Figure 4.4), such that the [S II] ratios measured for H II regions at or below this density will be relatively unimpacted by DIG contamination. Recent surveys of resolved H II regions in nearby spiral galaxies have found that the majority of H II regions have [S II] ratios in the low density limit (e.g. Cedrés et al., 2013; Berg et al., 2015; Kreckel et al., 2019). In NGC 7793, the distributions of [S II] ratios in H II regions and the DIG are indistinguishable (Della Bruna et al., 2020). These results suggest that the impact of DIG contamination on the derived n_e([S II]) at $z \sim 0$ may be relatively small.

The situation is different at higher redshift where the measured electron densities are significantly above the low density limit of the [S II] ratio. However, the fractional contribution of the DIG to the Hα emission is anti-correlated with the Hα surface brightness (e.g. Oey et al., 2007), and is predicted to decrease with increasing redshift until it becomes negligible at $z \sim 2$ (e.g. Sanders et al. 2017; Shapley et al. 2019, and see discussion in the following section). We therefore assume that the measured electron density evolution shown in Figure 4.4 is most likely to reflect a change in the intrinsic n_e([S II]) of H II regions over cosmic time.

We note that even though DIG contamination is not expected to have a significant impact on the measured $R_{\rm SII}$, the derived n_e([S II]) and $\log(P_{\rm th}/k)$([S II]) do not reflect the *average* properties of gas in H II regions. Galaxies commonly display negative radial gradients in H II region electron density (e.g. Gutiérrez & Beckman, 2010; Cedrés et al., 2013; Herrera-Camus et al., 2016) and metallicity (e.g. Zaritsky et al., 1994; Moustakas et al., 2010; Ho et al., 2015), the latter of which directly corresponds to positive electron temperature gradients because metal lines are the primary source of cooling in the 10^4 K ISM (e.g. Osterbrock & Ferland, 2006). The derived n_e([S II]) and $\log(P_{\rm th}/k)$([S II]) rep-

resent the luminosity-weighted average properties of the gas within each aperture, and will therefore likely be biased towards the densest H II regions in the central regions of the galaxies.

4.3.4 Redshift Evolution of the Volume-Averaged Electron Density and Ionized Gas Filling Factor

Background

The electron densities in H II regions can be measured using two complementary methods. The measurements presented thus far have been based on $R_{\rm SII}$, a density sensitive line ratio that probes the *local* n_e in the line-emitting material. The second approach is to use the Hα luminosity, which is proportional to the volume emission measure, to calculate the rms number of electrons per unit volume, n_e(rms) (Equation 4.2). The ratio of n_e(rms) to n_e([S II]) scales with the square root of the volume filling factor of the line-emitting material (Equation 4.5).

There is some evidence to suggest that the rms electron densities (and by extension, the volume averaged thermal pressures) of local H II regions may be approximately proportional to the external ambient pressure (e.g. Elmegreen & Hunter, 2000; Gutiérrez & Beckman, 2010), hinting that the local environment may play an important role in regulating H II region properties (e.g. Kennicutt, 1984). Measurements of n_e(rms) therefore represent a crucial link in our understanding of how global galaxy properties impact the local electron density of the line-emitting material.

The spatial resolution of our integral field observations is far below what is required to resolve individual H II regions, and with our data we can only estimate the rms number of electrons per unit volume on galactic scales. This provides a lower limit on the rms number of electrons per unit volume within the H II regions themselves, because H II regions do not fill the entire volumes of star-forming disks. The rms electron density within the H II regions is related to the measured n_e(rms) within R_e by the inverse of the volume ratio: n_e(rms, H II) = n_e(rms, R_e) $\times$ $V_{\rm R_e}/V_{\rm HII}$. The same scaling applies to the volume filling factors.

We use the SAMI and KMOS$^{\rm 3D}$+ datasets to estimate n_e(rms) and the volume filling factor of the line-emitting gas within R_e at $z \sim 0$, 0.9, 1.5 and 2.2. These calculations require a measurement of the Hα luminosity within R_e (described in Section 4.3.4) and an estimate of the disk scale height (discussed in Section 4.3.4).

Hα Luminosities

The total Hα luminosities within R_e for the KMOS$^{\rm 3D}$+ galaxies are derived from the published integrated Hα fluxes (Kriek et al., 2007; Förster Schreiber et al., 2009, 2018; Wisnioski et al., 2019) as follows. The Hα fluxes are corrected for extinction using the continuum A_V obtained from SED fitting and adopting the Wuyts et al. (2013) prescription for extra attenuation towards nebular regions. The Hα and H band (observed frame)

effective radii of SFGs at $z \sim 1 - 2$ are approximately equal (e.g. Nelson et al., 2016a; Förster Schreiber et al., 2018; Wilman et al., 2020), and therefore we divide the integrated Hα fluxes by two to obtain the fluxes within R_e. For the SAMI galaxies we directly use the published Hα fluxes and dust correction factors within R_e from the 'recommend component' emission line flux catalogue (Scott et al., 2018). The Hα and r-band sizes of the SAMI galaxies are typically consistent to within ~ 0.1 dex (Schaefer et al., 2017).

The Hα emission includes contributions from both H II regions and DIG, as discussed in Section 4.3.3. To isolate the Hα emission from H II regions, we assume that the fraction of Hα emission associated with the DIG ($f_{\mathrm{H}\alpha,\mathrm{DIG}}$) follows the relationship calibrated by Sanders et al. (2017):

$$f_{\mathrm{H}\alpha,\mathrm{DIG}} = -1.5 \times 10^{-14} \left(\frac{\Sigma_{H\alpha}}{\mathrm{erg\ s^{-1}\ kpc^{-2}}} \right)^{1/3} + 0.748 \tag{4.6}$$

This expression is the best fit to measurements of $\Sigma_{H\alpha}$ and $f_{\mathrm{H}\alpha,\mathrm{DIG}}$ for local galaxies. The power law index is fixed to 1/3, motivated by the assumption that there is a constant volume of gas available to be ionized, so that an increase in the total volume occupied by H II regions (as a result of an increase in the SFR) directly corresponds to a decrease in the volume occupied by the DIG (Oey et al., 2007). This assumption of density bounded ionization is likely to be unphysical because the implied escape fraction of ionizing photons from local starburst galaxies would be much larger than what is observed (Oey et al., 2007). However, the functional form reproduces the general shape of the observed $\Sigma_{H\alpha} - f_{\mathrm{H}\alpha,\mathrm{DIG}}$ trend.

Using Equation 4.6 we estimate $f_{\mathrm{H}\alpha,\mathrm{DIG}} \simeq 58\%$ at $z \sim 0$, $\sim 33\%$ at $z \sim 0.9$, $\sim 16\%$ at $z \sim 1.5$ and $\sim 0\%$ at $z \sim 2.2$. The decrease in the estimated DIG contribution with increasing redshift is consistent with the [S II]/Hα ratios measured from our stacked spectra, which decrease from 0.38 ± 0.01 at $z \sim 0$ to 0.19 ± 0.01 at $z \sim 2$ (see also Shapley et al., 2019).

Volume of the Star Forming Disk

The volume of the star-forming disk within R_e is computed as $V_{R_e} = 2\pi R_e^2 h_{\mathrm{HII}}$, where h_{HII} is the scale height of the star-forming disk. Ideally, h_{HII} would be directly measured from Hα observations of edge-on disk galaxies. However, $z \sim 0$ disk galaxies show strong extraplanar Hα emission associated with DIG (e.g. Rossa & Dettmar, 2003; Miller & Veilleux, 2003; Bizyaev et al., 2017; Levy et al., 2019), meaning that the scale height of the star-forming disk cannot be measured from Hα alone.

A reasonable alternative is to take the typical scale height of the molecular gas disk out of which the H II regions form, and correct this value upwards for the extra pressure support experienced by the ionized gas in the star-forming disk. The scale height and velocity dispersion of a thick and/or truncated gas disk are related by $h \simeq R_d \times \sigma_0 / v_{\mathrm{rot}}$ where R_d is the disk scale length, σ_0 is the intrinsic velocity dispersion and v_{rot} is the rotational velocity (e.g. Genzel et al., 2008). Assuming that H II regions and molecular

clouds have similar radial distributions across galaxies, the kinematics and scale heights of the molecular and star-forming disks are related by

$$h_{\rm HII} = h_{\rm mol} \times (\sigma_0/v_{\rm rot})_{\rm HII} \; / \; (\sigma_0/v_{\rm rot})_{\rm mol} \tag{4.7}$$

At fixed redshift, the typical velocity dispersion of ionized gas in SFGs is $\sim 10 - 15$ km s^{-1} larger than the average $\sigma_{0,\rm mol}$ (Übler et al., 2019). The majority of this difference can be explained by the higher temperature of the ionized phase and the additional contribution of H II region expansion to the measured velocity dispersion, which together are expected to contribute ~ 15 km s^{-1} in quadrature (e.g. Krumholz & Burkhart, 2016). Therefore, we assume that $\sigma_{0,\rm HII} = (\sigma_{0,\rm mol}^2 + 15^2)^{1/2}$.

Surveys of CO line emission in local spiral galaxies have found typical molecular gas velocity dispersions of $\sim 12 - 13$ km s^{-1} (Caldú-Primo et al., 2013; Levy et al., 2018). We adopt $\sigma_{0,\rm mol} = 12.5$ km s^{-1}, from which we estimate $\sigma_{0,\rm HII} = 19.5$ km s^{-1}. The ionized gas is expected to have a slightly lower $v_{\rm rot}$ than the molecular gas because of the extra pressure support (e.g. Burkert et al., 2010), but the percentage difference is observed to be small (e.g. Levy et al., 2018), so we assume that $v_{\rm rot,HII}/v_{\rm rot,mol} \simeq 1$. Molecular gas disks in the local universe have typical scale heights of $100 - 200$ pc (e.g. Scoville et al., 1993; Pety et al., 2013; Kruijssen et al., 2019), so we adopt $h_{\rm mol} = 150$ pc. Combining all these numbers, we estimate $h_{\rm HII} \simeq 230$ pc.

At high-z the contribution of DIG to the Hα emission is subdominant, but measurements of Hα scale heights are very challenging due to surface brightness dimming. Elmegreen et al. (2017) measured an average rest-UV continuum scale height of 0.63 ± 0.24 kpc for galaxies at $z \sim 2$, suggesting that high-z disks are significantly thicker than their low-z counterparts. This is consistent with the elevated ionized gas velocity dispersions in high-z disks (e.g. Genzel et al., 2006, 2008; Wisnioski et al., 2015; Johnson et al., 2018; Übler et al., 2019).

We use measurements of R_d, $v_{\rm rot}$ and σ_0 to estimate the median $h_{\rm HII}$ at $z \sim 0.9$, 1.5 and 2.2. The Hα flux profiles are assumed to be approximately exponential (motivated by studies of SFGs at similar redshifts; e.g. Nelson et al. 2013, 2016b; Wilman et al. 2020), which implies that $R_d = R_e/1.67$. The $v_{\rm rot}$ and σ_0 values are measured by forward modeling the one dimensional velocity and velocity dispersion profiles extracted along the kinematic major axis of each galaxy, accounting for instrumental effects, beam smearing, and pressure support as described in Übler et al. (2019). Their sample of galaxies with reliable kinematic measurements includes 18/39 of the galaxies in our $z \sim 0.9$ stack, 13/36 galaxies in our $z \sim 1.5$ stack, and 16/65 galaxies in our $z \sim 2.2$ stack. We estimate $h_{\rm HII}$ for each galaxy that is included in both our density sample and the Übler et al. (2019) kinematic sample and then calculate the median $h_{\rm HII}$ for each redshift slice, yielding approximate ionized gas scale heights of 280 pc, 460 pc, and 540 pc at $z \sim 0.9$, 1.5, and 2.2, respectively. The $h_{\rm HII}$ estimated for the $z \sim 2.2$ sample is consistent with the rest-UV continuum scale heights measured by Elmegreen et al. (2017) for galaxies at the same redshift.

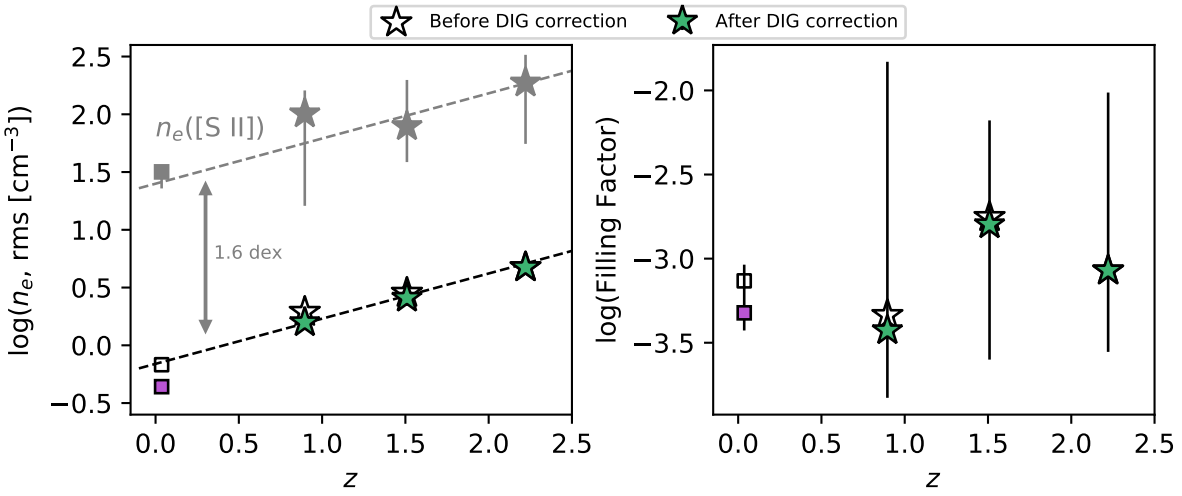

Figure 4.5: Redshift evolution of the rms electron density (left) and the volume filling factor of the line-emitting gas (right). Grey markers in the left hand panel show the n_e([S II]) measurements for comparison. The plotting symbols are the same as in Figure 4.4. Open and colored solid markers indicate values before and after correcting for the contribution of DIG to the Hα emission, respectively. Error bars are omitted from the open markers for clarity. The formal errors on the n_e(rms) measurements are too small to be seen. The two dashed lines in the left hand panel have the same slope and are offset by 1.6 dex.

Results

The calculated rms electron densities and volume filling factors are shown in Figure 4.5 and listed in Table 4.1. We give the values before and after correcting for the DIG contribution to indicate the magnitude of the correction, which is relatively small because n_e(rms) scales with $(1 - f_{\mathrm{H}\alpha,\mathrm{DIG}})^{1/2}$.[5] The quoted errors on n_e(rms) indicate the standard error on the mean based on the Hα flux uncertainties, but in reality the error is dominated by the unknown systematic uncertainty on the line-emitting volume.

Figure 4.5 indicates that n_e(rms) evolves at a very similar rate to n_e([S II]), increasing by a factor of $\sim 6 - 10$ from $z \sim 0$ to $z \sim 2.2$. Consequently, our estimates suggest that there is no significant evolution of the volume filling factor over the probed redshift range. These conclusions hold independent of whether or not the DIG correction is applied.

The line-emitting volume is calculated assuming that h_{HII} does not vary as a function of galactocentric radius. However, observations of constant ionized gas velocity dispersions across high-z disks (e.g. Genzel et al., 2006, 2011, 2017; Cresci et al., 2009) suggest that the scale height may grow exponentially with increasing galactocentric radius (e.g. Burkert et al., 2010). If we adopted a flared geometry the derived line-emitting volume would increase by a factor of 1.35. This would have a negligible impact on the derived rms electron

[5] We note that the rms density becomes lower after correcting for the DIG contribution, even though the DIG is less dense than the ionized gas in the H II regions, because there is no adjustment in the adopted line-emitting volume.

Table 4.1: Thermal pressure and electron density calculated from the [S II] doublet ratio, root-mean-square (volume averaged) electron density, and volume filling factor of the line-emitting gas in each of the four redshift slices.

Redshift Bin	$\log(P_{\rm th}/k)$([S II])	n_e([S II], cm^{-3})	n_e(rms, cm^{-3})		$ff_{\rm R_e} \times 10^3$	
			Original	DIG corrected	Original	DIG Corrected
$z \sim 0$ (SAMI)	$5.78^{+0.01}_{-0.19}$	32^{+4}_{-9}	0.7 ± 0.1	0.4 ± 0.1	$0.7^{+0.7}_{-0.2}$	$0.5^{+0.4}_{-0.1}$
$z \sim 0.9$ (KMOS$^{\rm 3D}$+ YJ)	$6.29^{+0.28}_{-0.73}$	101^{+59}_{-85}	1.9 ± 0.2	1.6 ± 0.1	$0.5^{+17.8}_{-0.3}$	$0.4^{+14.4}_{-0.2}$
$z \sim 1.5$ (KMOS$^{\rm 3D}$+ H)	$6.23^{+0.43}_{-0.26}$	79^{+120}_{-40}	2.8 ± 0.3	2.6 ± 0.3	$1.8^{+5.6}_{-1.5}$	$1.6^{+5.0}_{-1.3}$
$z \sim 2.2$ (KMOS$^{\rm 3D}$+ K)	$6.62^{+0.20}_{-0.53}$	187^{+140}_{-132}	4.7 ± 0.4	4.7 ± 0.4	$0.8^{+8.9}_{-0.6}$	$0.8^{+8.9}_{-0.6}$

P/k is in units of K cm^{-3}. The [S II] doublet ratio traces the local properties of the line-emitting gas. The rms electron density gives the average number of electrons per unit volume over the star-forming disk within R_e. We provide the values before and after correcting the Hα luminosities for the contribution of diffuse ionized gas, as described in Section 4.3.4.

densities (which scale with $h_{\rm HII}^{-1/2}$) and a minor impact on the derived filling factors (which scale with $h_{\rm HII}^{-1}$). For the same reason, the relatively large uncertainties on the ionized gas scale heights have a limited impact on our results. A factor of 2 change in any or multiple of the adopted scale height values would not change the basic conclusion that n_e(rms) evolves much more rapidly than the ionized gas volume filling factor.

The consistency between the rate of evolution of n_e([S II]) and n_e(rms) seen in the left hand panel of Figure 4.5 suggests that the distribution of line-emitting material inside H II regions may be approximately constant over cosmic time. This finding considerably reduces one major uncertainty in our understanding of the physical processes linking the evolution of n_e([S II]) to the evolution of galaxy properties.

The similarity between the redshift evolution of n_e([S II]) and n_e(rms) also provides further evidence to suggest that we are indeed observing a change in the density of the ionized material within H II regions over cosmic time. The [S II]-emitting gas in an H II region with a radial n_e gradient will have a different n_e distribution depending on whether the nebula is ionization bounded or density bounded. Galaxies in the local group contain both ionization and density bounded H II regions (e.g. Pellegrini et al., 2012), and the elevated [O III]/[O II] and [O III]/Hβ ratios characteristic of high-z Lyα emitters could potentially be explained by density bounded nebulae (e.g. Nakajima & Ouchi, 2014). In a density bounded nebula the partially ionized zone is truncated, meaning that the observed [S II] emission would originate from material at smaller radii which could have a higher average n_e compared to the ionization bounded case. It is therefore hypothetically possible that some or all of the measured n_e([S II]) evolution could be driven by a decrease in the fraction of ionization bounded regions with increasing redshift, rather than by a change in the average gas conditions within H II regions. However, the strong evolution of n_e(rms) suggests that changing gas conditions are the dominant source of the observed n_e([S II]) evolution.

4.4 Trends between Electron Density and Galaxy Properties

We begin our investigation into the physical origin of the density evolution by exploring how the electron density varies as a function of various galaxy properties, first within the KMOS^{3D}+ sample (Section 4.4.1) and then using the extended dataset (Section 4.4.2).

4.4.1 Trends in Electron Density Within KMOS^{3D}+

We explore which galaxy properties are most closely linked to the density variation within the KMOS^{3D}+ sample by dividing the galaxies into two bins (below and above the median) in various star formation, gas and structural properties: M_*, SFR, sSFR, $\Sigma_{\rm SFR}$, offset from the star-forming main sequence (SFR/SFR$_{\rm MS(z)}$), molecular gas fraction μ_{H_2} ($= M_{H_2}/M_*$), molecular gas mass surface density Σ_{H_2}, baryonic surface density $\Sigma_{\rm baryon}$, and R_e. The molecular gas properties are estimated by assuming that the galaxies lie along the Tacconi

et al. (2020) scaling relation for the molecular gas depletion time $t_{\rm depl}$ as a function of z, offset from the star-forming MS and M_*. The derived $t_{\rm depl}$ is multiplied by SFR to obtain the molecular gas mass M_{H_2}. $\Sigma_{\rm SFR}$ is defined as SFR/$(2\pi R_e^2)$, and similar definitions apply to all other surface density quantities. The calculated surface densities represent the conditions in the central regions of the galaxies.

We stack the spectra of the galaxies below and above the median in each property, and measure $R_{\rm SII}$, n_e([S II]) and $\log(P_{\rm th}/k)$([S II]) for each stack. Table 4.2 lists the median value of each galaxy property, the [S II] ratios measured for the below median and above median stacks, the differences between the [S II] ratios measured for the below and above median stacks, and the statistical significance of these differences. We note that the median values are calculated for each property individually and therefore the combination of these parameters does not necessarily represent a 'typical' galaxy. Table 4.3 lists the n_e([S II]) and $\log(P_{\rm th}/k)$([S II]) values calculated from the [S II] ratios listed in Table 4.2, as well as the differences and statistical significance of the differences between the values measured for the below and above median stacks.

We find the most significant differences between the [S II] ratios of galaxies below and above the median in $\Sigma_{\rm SFR}$, SFR, $\Sigma_{\rm baryon}$, and sSFR. The galaxies with comparably weak star formation and/or low $\Sigma_{\rm baryon}$ have electron densities and ISM pressures similar to those of local star-forming galaxies, whereas the galaxies with strong star formation and/or high $\Sigma_{\rm baryon}$ have densities and pressures which are comparable to or exceed the typical values for $z \sim 2$ SFGs (see Figure 4.3). $R_{\rm SII}$ is also mildly anti-correlated with Σ_{H_2} and μ_{H_2}. There is a weak trend towards lower $R_{\rm SII}$ at higher SFR/SFR$_{\rm MS(z)}$ and M_*, the latter of which is likely driven by the positive correlation between M_* and SFR. Our results are consistent with previous findings that the electron density is positively correlated with the level of star formation in galaxies (e.g. Shimakawa et al., 2015; Kaasinen et al., 2017; Jiang et al., 2019; Kashino & Inoue, 2019). However, the trend with $\Sigma_{\rm baryon}$ suggests that the weight of the stars and ISM may also influence the density of the ionized gas in H II regions.

Within the KMOS$^{\rm 3D}$+ sample there is no evidence that the density is correlated with R_e, suggesting that the n_e([S II]) evolution is unlikely to be explained solely by the size evolution of galaxies.

4.4.2 Trends in Electron Density Across $0 \lesssim z \lesssim 2.6$

We use the extended dataset to investigate the relationship between electron density and global galaxy properties over a much larger dynamic range. Figure 4.6 shows how $R_{\rm SII}$ (top) and n_e([S II]) (bottom) vary as a function of sSFR, SFR, $\Sigma_{\rm SFR}$, and SFR/SFR$_{\rm MS(z)}$. The galaxy samples are color-coded by median redshift.

We explore the trends within the SAMI and KMOS$^{\rm 3D}$+ samples by measuring the [S II] ratio in sliding bins. For the KMOS$^{\rm 3D}$+ sample, we sort the galaxies by the quantity on the x-axis (e.g. sSFR), stack the first 50 galaxies, and calculate $R_{\rm SII}$ and n_e. The bin boundary is then moved across by 10 galaxies, and the stacking is repeated for galaxies number 10 – 60, followed by galaxies number 20 – 70, etc., resulting in a total of 9 bins.

Table 4.2: [S II]λ6716/[S II]λ6731 measurements for stacks of KMOS^{3D}+ galaxies in bins below and above the median in various galaxy properties.

Property	Median Value	Below Median $R_{\rm SII}$	Above Median $R_{\rm SII}$	Difference	Significance (σ)
$\Sigma_{\rm SFR}$ ($M_\odot$ yr^{-1} kpc^{-2})	0.3	$1.38^{+0.06}_{-0.10}$	$1.16^{+0.09}_{-0.09}$	-0.22	1.6
SFR ($M_\odot$ yr^{-1})	23	$1.37^{+0.09}_{-0.07}$	$1.21^{+0.09}_{-0.12}$	-0.16	1.4
$\log(\Sigma_{\rm baryon}/(M_\odot$ kpc$^{-2}))$	8.7	$1.39^{+0.07}_{-0.13}$	$1.17^{+0.11}_{-0.06}$	-0.22	1.3
$\log({\rm sSFR/yr}^{-1})$	-8.9	$1.39^{+0.04}_{-0.12}$	$1.17^{+0.14}_{-0.08}$	-0.21	1.2
$\log(\Sigma_{H_2}/(M_\odot$ kpc$^{-2}))$	8.4	$1.36^{+0.04}_{-0.13}$	$1.19^{+0.09}_{-0.08}$	-0.17	1.1
$\log(M_{H_2}/M_*)$	0.06	$1.36^{+0.04}_{-0.11}$	$1.19^{+0.12}_{-0.09}$	-0.17	1.0
$\log({\rm SFR/SFR_{MS(}}_z{\rm)})$	0.0	$1.34^{+0.03}_{-0.16}$	$1.21^{+0.12}_{-0.05}$	-0.13	0.7
$\log(M_*/M_\odot)$	10.2	$1.33^{+0.08}_{-0.09}$	$1.24^{+0.09}_{-0.10}$	-0.09	0.7
R_e (kpc)	3.4	$1.28^{+0.08}_{-0.08}$	$1.27^{+0.10}_{-0.09}$	-0.01	0.1

Each bin contains 70 galaxies. The rows are sorted by decreasing significance of the difference between the [S II] ratios measured for the below and above median bins.

Table 4.3: Electron densities and ISM pressures calculated from the $R_{\rm SII}$ measurements presented in Table 4.2.

Property	Below Median		Above Median		Difference		Significance (σ)	
	$\log(P/k)$	n_e (cm^{-3})	$\log(P/k)$	n_e (cm^{-3})	$\log(P/k)$	n_e (cm^{-3})	$\log(P/k)$	n_e (cm^{-3})
$\Sigma_{\rm SFR}$ ($M_\odot$ yr^{-1} kpc^{-2})	$6.03^{+0.46}_{-1.25}$	44^{+86}_{-41}	$6.73^{+0.19}_{-0.20}$	257^{+138}_{-109}	0.70	213	1.4	1.5
SFR ($M_\odot$ yr^{-1})	$6.09^{+0.33}_{-2.09}$	52^{+64}_{-51}	$6.62^{+0.25}_{-0.27}$	193^{+170}_{-82}	0.54	141	1.3	1.4
$\log(\Sigma_{\rm baryon}/(M_\odot$ kpc$^{-2}))$	$5.96^{+0.59}_{-1.96}$	38^{+108}_{-37}	$6.72^{+0.13}_{-0.28}$	252^{+98}_{-121}	0.76	214	1.2	1.3
$\log({\rm sSFR/yr}^{-1})$	$5.94^{+0.57}_{-0.52}$	39^{+99}_{-27}	$6.73^{+0.17}_{-0.41}$	246^{+125}_{-141}	0.79	207	1.1	1.2
$\log(\Sigma_{H_2}/(M_\odot$ kpc$^{-2}))$	$6.13^{+0.48}_{-0.35}$	58^{+115}_{-29}	$6.65^{+0.17}_{-0.26}$	214^{+125}_{-91}	0.52	156	1.0	1.1
$\log(M_{H_2}/M_*)$	$6.09^{+0.46}_{-0.29}$	55^{+99}_{-22}	$6.68^{+0.20}_{-0.37}$	216^{+143}_{-113}	0.59	161	1.0	1.1
$\log({\rm SFR/SFR_{MS(}}_z{\rm)})$	$6.19^{+0.52}_{-0.14}$	72^{+159}_{-23}	$6.63^{+0.10}_{-0.42}$	192^{+63}_{-109}	0.44	120	0.7	0.6
$\log(M_*/M_\odot)$	$6.26^{+0.34}_{-0.56}$	85^{+81}_{-62}	$6.55^{+0.22}_{-0.31}$	160^{+130}_{-70}	0.28	75	0.6	0.7
R_e (kpc)	$6.46^{+0.20}_{-0.38}$	128^{+81}_{-73}	$6.51^{+0.20}_{-0.43}$	139^{+100}_{-84}	0.05	11	0.1	0.1

We perform measurements in sliding bins because it minimizes biases associated with the arbitrary choice of bin boundaries and gives a much clearer picture of the overall trends. However, the sliding bin measurements are highly correlated and are therefore not used in any quantitative analysis.

The same procedure is applied to the SAMI galaxies, except that we stack in bins of 100 galaxies and move the bin boundary by 20 galaxies at a time, resulting in a total of 18 bins. The larger bin size is chosen to mitigate the effects of line ratio fluctuations in the low density limit. At the typical densities of the SAMI galaxies, $R_{\rm SII}$ changes very slowly as a function of n_e (see left hand panel of Figure 4.4). Small line ratio fluctuations can lead to disproportionately large density fluctuations, which are partially smoothed out by the larger bins.

We find that the electron density is positively correlated with sSFR, SFR and $\Sigma_{\rm SFR}$, in good agreement with previous results (e.g. Shimakawa et al., 2015; Herrera-Camus et al., 2016; Kashino & Inoue, 2019). The trends among the high-z samples appear to be much steeper than the trends within the SAMI sample, but it is unclear whether this reflects an intrinsic difference in the relationship between n_e and the level of star formation at different cosmic epochs, or whether it is an artefact of the flattening of the n_e – $R_{\rm SII}$ relationship at $n_e \lesssim 40$ cm^{-3}.

From Figure 4.6, it appears that the electron density is not intrinsically related to offset from the star-forming main sequence. The KMOS$^{\rm 3D}$+ galaxies have systematically higher n_e([S II]) (lower $R_{\rm SII}$) than the SAMI galaxies at fixed main sequence offset. This, combined with the overall roughly monotonic variations in $R_{\rm SII}$ and n_e as a function of SFR, sSFR, and $\Sigma_{\rm SFR}$ (see also Kaasinen et al., 2017), suggests that the redshift evolution of the electron density is likely to be linked to the evolving normalization of the star-forming MS.

Figure 4.7 shows $R_{\rm SII}$ (top) and n_e([S II]) (bottom) vary as a function of μ_{H_2}, Σ_{H_2}, $\Sigma_{\rm baryon}$, and Σ_*. μ_{H_2} is directly related to sSFR through the molecular gas depletion time and therefore the two quantities show very similar trends with n_e. The same is true for Σ_{H_2} and $\Sigma_{\rm SFR}$. Our data are consistent with a single positive correlation between $\Sigma_{\rm baryon}$ and n_e across $0 \lesssim z \lesssim 2.6$, but the KMOS$^{\rm 3D}$+ galaxies are clearly offset to higher n_e([S II]) than the SAMI galaxies at fixed Σ_*. This supports our earlier hypothesis that any correlation between n_e and M_* is primarily driven by the M_*- SFR relation, and provides further evidence to suggest that the evolving gas content of galaxies – which drives the evolution of the normalization of the star-forming MS – may also be an important driver of the n_e evolution.

4.5 What Drives the Redshift Evolution of Galaxy Electron Densities?

We use our measurements to investigate possible physical driver(s) of the evolution of the electron density and thermal pressure across $0 \lesssim z \lesssim 2.6$. We focus on four scenarios

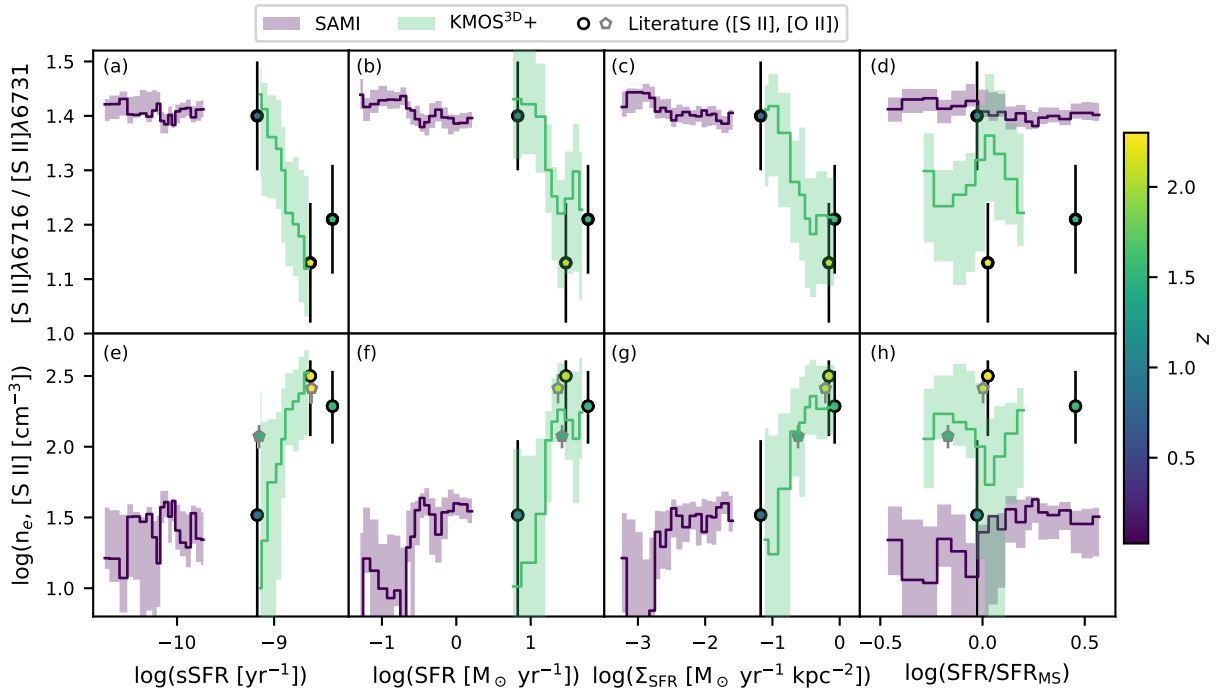

Figure 4.6: [S II] ratio (top) and n_e([S II]) (bottom) as a function of sSFR (a and e), SFR (b and f), $\Sigma_{\rm SFR}$ (c and g) and SFR/SFR$_{\rm MS(z)}$ (d and h). The solid lines and shaded error regions represent the average properties of the SAMI (purple) and KMOS$^{\rm 3D}$+ (green) galaxies, computed in sliding bins as described in Section 4.4.2. The individual data points are measurements for literature samples of high-z SFGs, introduced in Section 4.3.3. The color-coding indicates the median redshift of each galaxy sample.

that are commonly discussed in the literature: that the electron density is governed by 1) the density of the parent molecular cloud (Section 4.5.1), 2) the pressure injected by stellar feedback (Section 4.5.2), 3) the pressure of the ambient medium (Section 4.5.3), or 4) the dynamical evolution of the H II region (Section 4.5.4). In this analysis we explicitly account for the average properties of the galaxies in each stack, meaning that the presented interpretation does not rely on the assumption that our samples are representative of the underlying SFG population at each redshift, or that the samples probe the same subset of the galaxy population at each redshift.

4.5.1 Scenario 1: H II Region Density and Thermal Pressure Governed by Molecular Cloud Density

Stars form in the centers of molecular clouds and radiate high energy photons that ionize the surrounding ISM material to form H II regions. Therefore, the initial electron densities of H II regions are likely to be set by the molecular hydrogen number density. In this case, since each H_2 molecule contributes two electrons, $n_e \simeq 2\ n_{H_2}$.

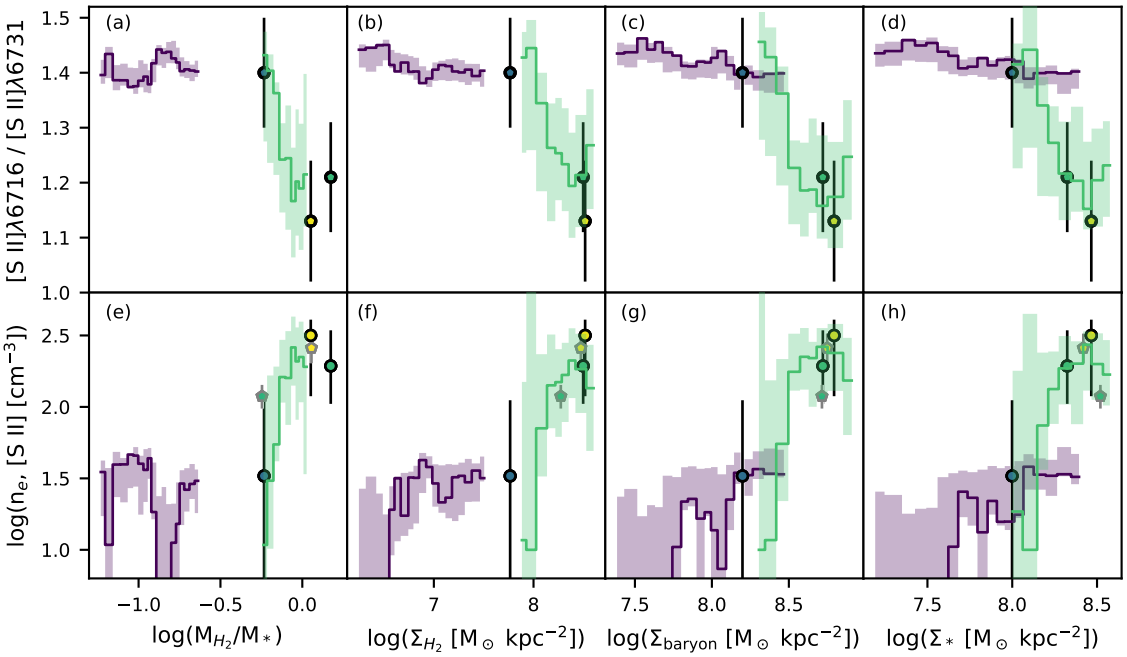

Figure 4.7: [S II] ratio (top) and n_e([S II]) (bottom) as a function of μ_{H_2} (a and e), Σ_{H_2} (b and f), $\Sigma_{\rm baryon}$ (c and g), and Σ_* (d and h). The color-coding, symbols, and data representation are the same as in Figure 4.6.

The mass volume density of molecular hydrogen (ρ_{H_2}) within R_e is derived by dividing Σ_{H_2} by the molecular gas scale height $h_{\rm mol}$, which is estimated using the procedures described in Section 4.3.4. We adopt $h_{\rm mol} = 150$ pc at $z \sim 0$, and estimate the median $h_{\rm mol}$ at $z \sim 0.9$, 1.5 and 2.2 assuming $h_{\rm mol} \simeq R_d \times \sigma_{0,\rm mol}/v_{\rm rot,mol}$. The molecular gas kinematics are estimated from the measured ionized gas kinematics accounting for the expected difference in the pressure support experienced by the two gas phases (e.g. Burkert et al., 2010). These calculations yield typical molecular gas scale heights of ~ 180 pc, ~ 420 pc and ~ 490 pc at $z \sim 0.9$, 1.5 and 2.2, respectively.

We divide ρ_{H_2} by the molecular mass of H_2 to obtain n_{H_2}. Column a) of Figure 4.8 compares the evolution of n_{H_2} to the evolution of n_e([S II]) (top), $\log(P_{\rm th}/k)$([S II]) (middle), and n_e(rms) (bottom). The dashed lines, anchored to the $z \sim 0$ measurements, show where the data would be expected to lie if the quantities on the x and y axes had a 1:1 relationship in log space at all redshifts (equivalent to a linear relationship in linear space). The dotted lines are offset from the dashed lines by $\pm$ 0.3 dex. Any significant systematic deviation from the dashed lines would suggest that the relationship between n_e and n_{H_2} changes over cosmic time, meaning that additional physical processes would need to be considered in order to explain the n_e evolution.

There is an approximately linear relationship between n_e(rms) and n_{H_2}, with a mean ratio (across all four redshift slices) of $n_e({\rm rms})/n_{H_2} \simeq 0.6$. This relationship is averaged over the assumed volumes of the star-forming and molecular disks, and to obtain the

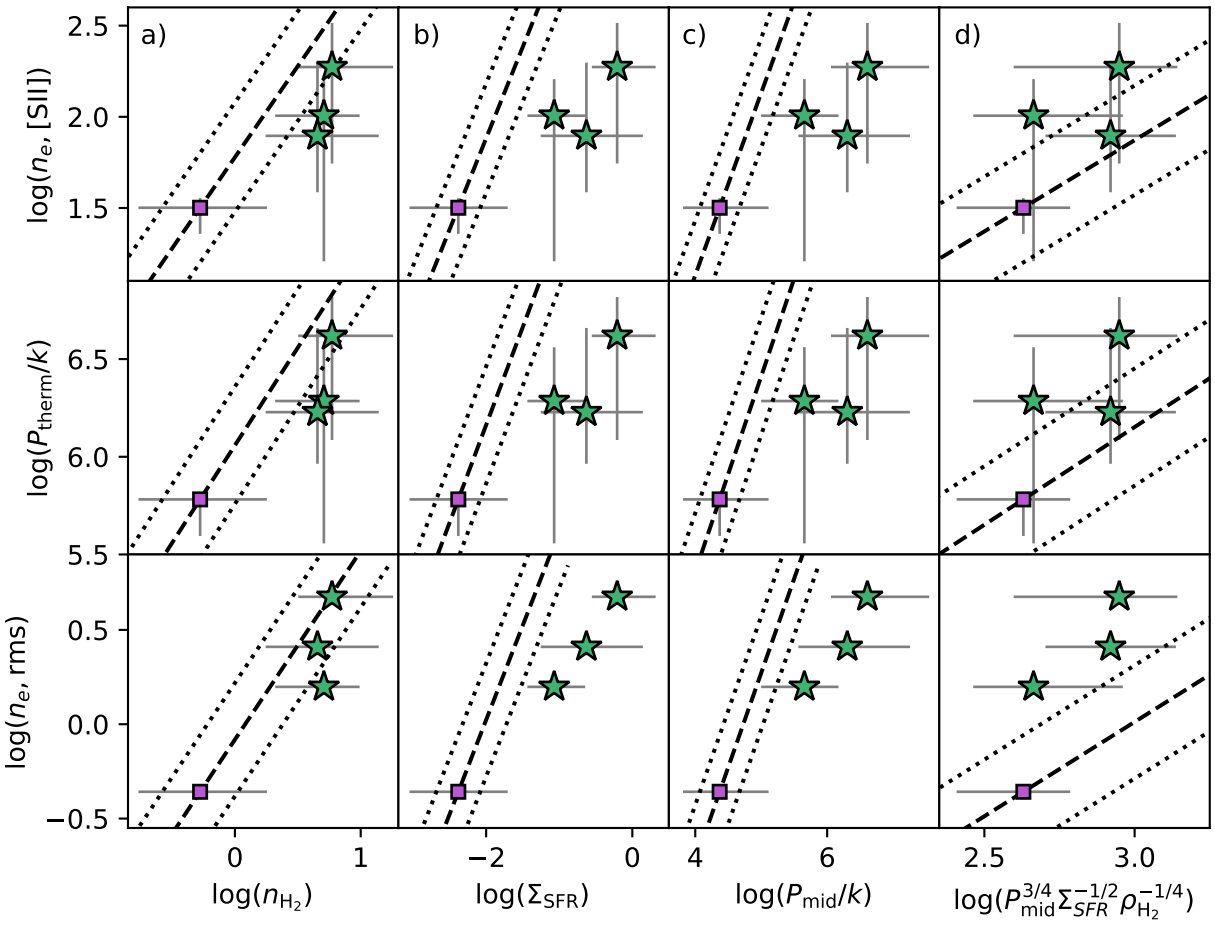

Figure 4.8: Relationships between the thermal properties of the ionized gas – probed by (top) n_e([S II]), (middle) $\log(P_{\rm th}/k)$([S II]), and (bottom) n_e(rms) – and selected galaxy properties: a) n_{H_2}, b) $\Sigma_{\rm SFR}$, c) midplane pressure $P_{\rm mid}$, and d) $\Sigma_{\rm SFR}^{-1/2}$ $\rho_{H_2}^{-1/4}$ $P_{\rm mid}^{3/4}$, which is proportional to the inverse of the predicted H II region stall radius. The dashed lines, anchored to the $z \sim 0$ measurements, show where the data would be expected to lie if the quantities on the x and y axes had a 1:1 relationship (in log space) at all redshifts. The dotted lines are offset by ±0.3 dex. Plotting symbols are the same as in Figure 4.4. Error bars on the x axes indicate the 16th-84th percentile range in galaxy properties within each stack.

average coefficient for individual star-forming regions one would need to multiply by the ratio of the volume filling factor of molecular clouds within $2\pi R_e^2 h_{\rm mol}$ to the volume filling factor of H II regions within $2\pi R_e^2 h_{\rm HII}$. The discrepancy between the estimated coefficient of 0.6 and the predicted coefficient of 2 could very likely be accounted for by the systematic uncertainties introduced by the various assumptions made in our calculations. Therefore, we suggest that the elevated electron densities in H II regions at high-z could plausibly be the direct result of larger molecular hydrogen densities in the parent molecular clouds.

4.5.2 Scenario 2: H II Region Density and Thermal Pressure Governed by Stellar Feedback

It has been suggested that the strong correlation between n_e and the level of star formation in galaxies may arise because n_e is governed by stellar feedback (e.g. Kaasinen et al., 2017; Jiang et al., 2019). Stellar winds and supernovae inject energy into H II regions, increasing the pressure and electron density (e.g. Groves et al., 2008; Krumholz & Matzner, 2009).

The turbulent pressure injected by stellar feedback can be parametrized as $P_{\rm inj} = \Sigma_{\rm SFR}\ (p_*/m_*)/4$, where p_*/m_* is the amount of momentum injected into the ISM per solar mass of star formation, and the factor of 1/4 represents the fraction of the total momentum in the vertical component on one side of the disk (Ostriker & Shetty, 2011; Kim et al., 2013). The value of p_*/m_* scales with the number of supernovae per solar mass of star formation and is therefore strongly dependent on the initial mass function. ISM simulations have not yet reached a consensus on the amount of momentum injected per supernova explosion. It has been suggested that the momentum injection may be sensitive to small scale properties such as the spatial clustering of supernovae (e.g. Gentry et al., 2019) and the interaction between the hot ejecta and the surrounding ISM (e.g. Kim & Ostriker, 2015), but differences in numerical methods lead to large discrepancies between different simulation results. Sun et al. (2020) find a linear correlation between $\Sigma_{\rm SFR}$ and the turbulent pressure of molecular clouds in local spiral galaxies, suggesting that p_*/m_* is approximately constant. We assume that p_*/m_* is constant and independent of redshift, meaning that $P_{\rm inj} \propto \Sigma_{\rm SFR}$. In other words, we can investigate the link between n_e and pressure injection by stellar feedback without needing to assume a specific value for p_*/m_*.

Column b) of Figure 4.8 shows that the electron density and thermal pressure increase much more slowly than $\Sigma_{\rm SFR}$. This suggests that the increase in the rate of turbulent pressure injection towards higher redshifts does not directly lead to the observed increase in n_e. The sub-linearity of the relationship could potentially indicate that the fraction of injected pressure that is confined within H II regions decreases towards higher redshifts. In order for the data to be consistent with a linear relationship between n_e and the confined pressure, the fraction of pressure leaking out of H II regions would have to increase by an order of magnitude from $z \sim 0$ to $z \sim 2.2$. The increased incidence of outflows at high-z (e.g. Steidel et al., 2010; Newman et al., 2012b; Förster Schreiber et al., 2019) could lead to a significant reduction in the pressure confinement efficiency, although our explicit removal of objects with detected galaxy scale outflows limits the possible magnitude of such an

effect in our dataset.

Alternatively, the relationship between n_e and the confined feedback pressure could be intrinsically sublinear, perhaps because a) the fraction of the injected turbulent pressure that cascades into the thermal pressure of the 10^4 K gas decreases steeply with increasing $\Sigma_{\rm SFR}$ and/or z, b) n_e is *not* governed by the internal H II region pressure, or c) n_e *is* governed by the internal pressure, but stellar feedback is not the primary source of internal pressure across some or all of the parameter space covered by our sample. The total pressure within an H II region is the sum of many components including the turbulent and thermal pressure of the 10^4 K gas, the hot gas pressure associated with supernova ejecta and shocked stellar winds, and radiation pressure (e.g. Krumholz & Matzner, 2009; Murray et al., 2010). Quantitative predictions for the relationship between n_e and $P_{\rm inj}$ from multi-phase simulations of H II regions including outflows and all major pressure components (e.g. Rahner et al., 2017, 2019), as well as more complete observational censuses of the relative contributions of different pressure components within H II regions (e.g. Lopez et al., 2014; McLeod et al., 2019, 2020), would assist to determine which of these scenarios is most likely.

4.5.3 Scenario 3: H II Region Density and Thermal Pressure Governed by the Ambient Pressure

H II regions are initially over-pressured and expand towards lower pressures and densities until they reach pressure equilibrium with their surroundings. Analytic models suggest that in populations of H II regions with average ages $\gtrsim 1$ Myr, the majority should be close to their equilibrium sizes and pressures (e.g. Oey & Clarke, 1997; Nath et al., 2020).

The relationship between n_e(rms), n_e([S II]) and the pressure of the external ambient medium depends on the balance between the different internal pressure components. There is some observational evidence to suggest that in local H II regions, n_e(rms) scales linearly with the disk midplane pressure. Elmegreen & Hunter (2000) noted that the volume averaged thermal pressures of the largest H II regions in nearby massive spiral galaxies are comparable to the average disk midplane pressures (assuming $T_e = 10^4$ K). Gutiérrez & Beckman (2010) measured n_e(rms) for individual H II regions in a spiral galaxy and a dwarf irregular galaxy and found that in both galaxies, the electron density declines exponentially with a scale length similar to that of the H I column density profile. The roughly linear relationship between n_e(rms) and the ambient pressure suggests that the thermal pressure of the 10^4 K gas must account for an approximately constant fraction of the total H II region pressure.

If the majority of H II regions at $0 \leq z \leq 2.6$ are in pressure equilibrium with their surroundings, and the balance between the different internal pressure components does not change significantly over time, then n_e(rms) $\times$ T_e should evolve at approximately the same rate as the midplane pressure. We do not expect the average T_e to vary significantly between our four redshift slices because we measure similar gas-phase metallicities from all four stacks (the increase in median stellar mass towards higher redshift offsets the evolution

of the mass-metallicity relation). Therefore, we estimate the average midplane pressure within R_e at each redshift and test whether the midplane pressure evolves at a similar rate to n_e.

The pressure at the midplane of a disk in hydrostatic equilibrium is given by:

$$P_{\rm mid} \simeq \frac{\pi G}{2} \Sigma_{HI+H_2} \left(\Sigma_{HI+H_2} + \frac{\sigma_g}{\sigma_*} \Sigma_* \right) \tag{4.8}$$

where Σ_* is the stellar mass surface density, Σ_{HI+H_2} is the atomic + molecular gas mass surface density, σ_g is the velocity dispersion of the neutral gas (which we assume to be given by $\sigma_{0,\rm mol}$), and σ_* is the stellar velocity dispersion (Elmegreen, 1989). The stellar velocity dispersion is estimated from Σ_* assuming hydrostatic equilibrium, as outlined in Appendix 4.9. We adopt a constant atomic gas mass surface density of $\Sigma_{HI} = 6.9\ M_\odot\ {\rm pc}^{-2}$ based on the tight observed relationship between the masses and diameters of H I disks in the local universe (Broeils & Rhee, 1997; Wang et al., 2016). The gas reservoirs in the star-forming disks of high-z SFGs are expected to be dominated by H_2 (Tacconi et al., 2018, 2020, and references therein), and therefore the assumption of a redshift-invariant Σ_{HI} is unlikely to have any significant impact on the midplane pressures derived for the KMOS$^{\rm 3D}$+ galaxies (see discussion in Appendix 4.10).

Column c) of Figure 4.8 compares the evolution of $P_{\rm mid}$ to the evolution of the electron density and thermal pressure. The midplane pressure evolves much more rapidly than n_e(rms), n_e([S II]) and $\log(P_{\rm th}/k)$([S II]), suggesting that the thermal pressure of the 10^4 K gas accounts for a decreasing fraction of the total H II region pressure with increasing redshift.

The implied change in the H II region internal pressure balance can be understood by considering the sources of the different pressure components. The electron density increases by a factor of $\sim 6-10$ from $z \sim 0$ to $z \sim 2.2$, which drives a similar change in the thermal pressure of the 10^4 K gas. The ratio of turbulent to thermal pressure in the 10^4 K gas is given by $\sigma^2_{0,\rm ion}/c_s^2$. The sound speed c_s scales with $T_e^{1/2}$ and is therefore not expected to vary significantly with redshift, but $\sigma^2_{0,\rm ion}$ increases by a factor of ~ 4 from $z \sim 0$ to $z \sim 2.2$ (e.g. Genzel et al., 2006; Wisnioski et al., 2015; Johnson et al., 2018; Übler et al., 2019), driven by gravitational instabilities in marginally stable gas-rich disks (e.g. Krumholz et al., 2018; Übler et al., 2019). The radiation pressure and hot gas pressure both scale almost linearly with the average SFR (e.g. Oey & Clarke, 1997; Murray et al., 2010; Ostriker & Shetty, 2011) which is approximately two orders of magnitude larger for a $\log(M_*/M_\odot) = 10.3$ galaxy at $z \sim 2.2$ than for a $\log(M_*/M_\odot) = 9.6$ galaxy at $z \sim 0$. Therefore, the ratio of the thermal pressure of the 10^4 K gas to the total H II region pressure could easily change by at least an order of magnitude over the probed redshift range.

We conclude that n_e could plausibly be set by the interplay between the external ambient pressure and the internal pressure balance, but not by the ambient pressure alone.

4.5.4 Scenario 4: H II Region Density and Thermal Pressure Governed by Dynamical Evolution

There is an inverse linear correlation between the diameter and n_e(rms) of local H II regions (e.g. Kim & Koo, 2001; Dopita et al., 2006; Hunt & Hirashita, 2009), suggesting that the dynamical evolution of H II regions may play an important role in regulating their electron densities. Oey & Clarke (1997, 1998) presented an analytic model for the size evolution of an H II region assuming that the internal pressure is dominated by shocked stellar winds and supernova ejecta. They postulated that the H II region will expand as an energy-driven bubble until the internal pressure is comparable to the ambient pressure, at which point the H II region 'stalls'. The stall radius scales as $R_{\rm stall} \propto \Sigma_{\rm SFR}^{1/2}\ \rho_{H_2}^{1/4}\ P_{\rm mid}^{-3/4}$ (see derivation in Appendix 4.11). The final size of the H II region is determined by the balance between the combined mechanical luminosity of the central star cluster and the internal gas pressure, which both drive the expansion of the H II region, and the ambient pressure which resists the expansion.

Oey & Clarke (1997) used their model to predict the slope of the H II region size distribution, and showed that the majority of H II regions are expected to be close to their maximum sizes. The predicted size distribution is consistent with the observed size distribution of H I holes in local spiral galaxies (Oey & Clarke, 1997; Bagetakos et al., 2011). If the majority of H II regions at $0 \leq z \leq 2.6$ have sizes close to the stall radii predicted by Oey & Clarke (1997), and the size – n_e(rms) correlation observed in the local universe extends to higher redshifts, then we might expect to observe an inverse linear correlation between n_e(rms) and $R_{\rm stall}$, or equivalently, a (positive) linear correlation between n_e(rms) and $\Sigma_{\rm SFR}^{-1/2}\ \rho_{H_2}^{-1/4}\ P_{\rm mid}^{3/4}$.

We investigate whether or not such a correlation exists in Column d) of Figure 4.8. The rms electron densities of the high-z SFGs are slightly higher than what would be predicted based on their estimated stall radii, but the [S II] electron densities could potentially be consistent with an inverse linear relationship between n_e and $R_{\rm stall}$. This suggests that the elevated electron densities in high-z SFGs could plausibly be driven by a decrease in the ratio of the injected hot gas pressure (which drives H II region expansion) to the midplane pressure (which resists the expansion).

However, we note that the adopted expression for the stall radius is based on a few simplifying assumptions which may not reflect the conditions in H II regions at high-z. The most basic assumption is that each star cluster ionizes a spherical H II region that does not overlap with regions ionized by adjacent clusters. Extreme star-forming regions in the local universe often show more complex geometries, with neighbouring star clusters ionizing overlapping areas within a single giant molecular cloud (e.g. Förster Schreiber et al., 2001; Snijders et al., 2007). If these conglomerations of H II regions reflect the typical conditions in rapidly star-forming galaxies at high-z, the stall radius may indicate the typical extent of the ionized region associated with an individual star cluster, rather than a characteristic spherical H II region size.

The second key assumption is that the H II region expansion is primarily driven by mechanical energy from stellar winds and supernovae. These processes produce highly

pressurized hot gas which, if confined, can efficiently drive the expansion of an H II region (e.g. Castor et al., 1975). However, observations of Milky Way H II regions indicate that the pressure in the hot gas is comparable to the pressure in the 10^4 K gas (e.g. McKee et al., 1984; Dorland & Montmerle, 1987; Harper-Clark & Murray, 2009), suggesting that much of the hot gas may escape through holes in the expanding bubbles (e.g. Murray et al., 2010). If the hot gas pressure is significantly lower than predicted, the dynamics of H II regions may be governed by other forms of pressure, such as the thermal pressure of the 10^4 K gas (e.g. Spitzer, 1978; Dyson & Williams, 1980) or radiation pressure. Photons trapped in the expanding shell of an H II region will provide an extra source of acceleration, increasing the expansion velocity of the shell and the final stall radius. Radiation is predicted to govern the dynamics of H II regions around luminous massive clusters (e.g. Krumholz & Matzner, 2009; Murray et al., 2010) and may therefore be significant at high-z. However, thermal pressure and mechanical feedback are observed to be dominant in more typical local H II regions (e.g. Lopez et al., 2014; McLeod et al., 2019, 2020).

It is unclear how the relationship between n_e and $R_{\rm stall}$ would change if a different expansion mechanism was considered. Stall radius expressions have been derived for thermal pressure driven expansion assuming that the expansion stalls when thermal pressure equilibrium is achieved (Dyson & Williams, 1980), and for radiation pressure driven expansion assuming that the expansion stalls when the expansion velocity becomes comparable to the velocity dispersion in the parent cloud (Krumholz & Matzner, 2009). An investigation of how these stall conditions relate to the total pressure equilibrium condition for different ratios of thermal to total pressure is beyond the scope of this paper. Simulations of H II region evolution including all major internal pressure components as well as varying fractions of turbulent pressure in the ambient medium (such as those presented in Rahner et al. 2017, 2019) will help to better understand how the dynamical evolution and stall radii of H II regions vary as a function of the luminosity and evolutionary stage of the cluster and the properties of the surrounding medium.

4.5.5 Implications

In this section we have compared the observed n_e evolution to quantitative predictions for four potential drivers of the density evolution. We found that $n_e \simeq n_{H_2}$, suggesting that the elevated electron densities in H II regions at high-z could plausibly be the direct result of higher gas densities in the parent molecular clouds. We investigated whether the strong relationship between n_e and the level of star formation in galaxies could arise because n_e is governed by pressure injection from stellar feedback. Our data suggest that the increase in the amount of turbulent pressure injected by stellar winds and supernovae towards higher redshifts does not directly lead to the observed increase in n_e. Further constraints from observations and simulations are required to determine which additional parameters control the relationship between these two quantities.

We explored whether the n_e evolution could be driven by a change in the equilibrium internal pressure of H II regions. We found that the ambient pressure evolves much faster than n_e, suggesting that n_e could be governed by the interplay between the ambient pres-

sure and the balance between different sources of pressure within H II regions, but not by the ambient pressure alone. Finally, motivated by the existence of a strong inverse correlation between n_e(rms) and H II region size in the local universe, we investigated whether the n_e evolution could be linked to a change in the balance between the energy injection from stellar feedback (which drives H II region expansion) and the ambient pressure (which resists the expansion). We found tentative evidence for an inverse linear correlation between n_e and the H II region stall radius $R_{\rm stall}$, but noted that the functional form of $R_{\rm stall}$ relies on some assumptions that may not hold at high-z.

The evolution of $R_{\rm stall}$ is governed by the balance between the increase in $\Sigma_{\rm SFR}$ and ρ_{H_2} (which lead to larger $R_{\rm stall}$) and the increase in $P_{\rm mid}$ (which leads to smaller $R_{\rm stall}$). The fact that the predicted $R_{\rm stall}$ decreases with increasing redshift indicates that the $P_{\rm mid}$ term is dominant. Of the terms that contribute to $P_{\rm mid}$, the typical values of Σ_{HI} and σ_g/σ_* do not vary significantly across the redshift range probed by our samples, whereas the median Σ_* in our $z \sim 2.2$ sample is ~ 0.7 dex higher than the median Σ_* in our $z \sim 0$ sample, and the median Σ_{H_2} is 1.5 dex higher in our $z \sim 2.2$ sample than in our $z \sim 0$ sample. Therefore, the increase in $P_{\rm mid}$ is primarily driven by the increase in Σ_{H_2}.

We conclude that, in the plausible scenario that the electron density is governed by either n_{H_2} or $1/R_{\rm stall}$, the increase in electron density from $z \sim 0$ to $z \sim 2.6$ would be primarily driven by the increase in the molecular gas fractions of galaxies. This is consistent with our earlier hypothesis that the n_e evolution is linked to the evolving normalization of the star-forming MS (Section 4.4.2), which is also driven by the evolution of galaxy molecular gas reservoirs (e.g. Tacconi et al., 2020).

Finally, we note that the three rows of panels in Figure 4.8 indicate that n_e([S II]), $\log(P_{\rm th}/k)$([S II]) and n_e(rms) evolve at very similar rates. The thermal pressure is expected to be approximately constant within any given H II region and is therefore likely to be a more meaningful description of the gas conditions than n_e which can show strong radial gradients (see e.g. Kewley et al. 2019 and references therein). However, the conclusions presented in this section are not strongly dependent on which of the three quantities is considered.

4.6 Conclusions

We have investigated the evolution of the typical electron density in SFGs from $z \sim 2.6$ to $z \sim 0$, using a sample of 140 galaxies at $0.6 < z < 2.6$ drawn primarily from the KMOS^{3D} survey and a sample of 471 galaxies at $z \sim 0$ from the SAMI Galaxy Survey. The KMOS^{3D} sample is distributed in three redshift bins ($z \sim 0.9$, 1.5, and 2.2) and allows us to analyse the density evolution over ~ 5 Gyr of cosmic history with a single dataset. We select galaxies that do not show evidence of AGN activity or broad line emission indicative of outflows in order to minimize contamination from line emission originating outside of star forming regions. We also examine the effects of diffuse ionized gas, which is expected to account for a decreasing fraction of the nebular line emission towards higher redshifts, and argue that this is unlikely to be the dominant driver of the observed redshift evolution of

$R_{\rm SII}$ and of the derived n_e([S II]) and $\log(P_{\rm th}/k)$([S II]).

The galaxy spectra are stacked in bins of redshift and galaxy properties and the [S II] doublet ratio is used to measure the local n_e in the line-emitting gas. Based on these measurements, we find that:

- The electron density of the line-emitting gas in SFGs has decreased by a factor of ~ 6 over the last ~ 10 Gyr. We measure $n_e([\text{S II}]) = 187^{+140}_{-132}$ cm^{-3} at $z \sim 2.2$, $n_e([\text{S II}]) = 79^{+120}_{-40}$ cm^{-3} at $z \sim 1.5$, $n_e([\text{S II}]) = 101^{+59}_{-85}$ cm^{-3} at $z \sim 0.9$, and $n_e([\text{S II}]) = 32^{+4}_{-9}$ cm^{-3} at $z \sim 0$, consistent with results from previous surveys of SFGs at similar redshifts.

- Combining the SAMI and KMOS$^{\rm 3D}$+ datasets, we find that n_e([S II]) shows roughly monotonic correlations with sSFR, SFR and $\Sigma_{\rm SFR}$ across $0 \lesssim z \lesssim 2.6$. However, the KMOS$^{\rm 3D}$+ galaxies have systematically higher n_e than the SAMI galaxies at fixed offset from the star-forming MS, suggesting that the n_e evolution is linked to the evolving main sequence normalization. There is also a roughly monotonic trend between n_e and $\Sigma_{\rm baryon}$, but n_e is correlated with z at fixed Σ_*, suggesting that the gas reservoir plays an important role in regulating galaxy electron densities.

We investigate how the n_e([S II]) measurements are impacted by contamination from non-stellar sources by comparing the [S II] ratios measured from the spectra of galaxies with outflows and/or AGN activity to the [S II] ratios measured for the primary sample. We measure higher n_e([S II]) for inactive galaxies with outflows than for no-outflow inactive galaxies, but only ~ 10 – 30% of inactive SFGs at $0.6 < z < 2.6$ have outflows that are strong enough to be detectable in line emission, and this fraction is too low to have a significant impact on the measured average properties of the overall inactive SFG population. AGN host galaxies have lower [S II] ratios than inactive SFGs and should be excluded to avoid over-estimating the average electron densities in star-forming regions.

We compare the local n_e([S II]) measurements to estimates of the rms number of electrons per unit volume across star-forming disks at each redshift. The rms electron density n_e(rms) is calculated from the Hα luminosity (which is proportional to the volume emission measure) and the line-emitting volume (which we define as $2\pi R_e^2 h$). The typical flattening ratios (R_e/h) of the high-z disks are estimated from the measured $v_{\rm rot}/\sigma_0$ ratios. We find that n_e(rms) decreases by an order of magnitude from $z \sim 2.2$ to $z \sim 0$. The local and volume-averaged electron densities evolve at similar rates, suggesting that the volume filling factor of the line-emitting gas may be approximately constant across $0 \lesssim z \lesssim 2.6$.

Finally, we use our measurements of n_e([S II]), $\log(P_{\rm th}/k)$([S II]), and n_e(rms) to explore different potential drivers of the n_e evolution. We quantitatively test whether the electron density could plausibly be primarily governed by a) the density of the parent molecular cloud, b) the pressure injected by stellar feedback, c) the pressure of the ambient medium, or d) the dynamical evolution of the H II region. We find that n_e(rms) $\simeq n_{H_2}$, suggesting that the elevated electron densities in H II regions at high-z could perhaps be the direct result of higher gas densities in the parent molecular clouds. There is also tentative evidence to suggest that n_e could be influenced by the balance between stellar

feedback, which drives the expansion of H II regions, and the ambient pressure, which resists their expansion.

Further studies are required to confirm the feasibility of these scenarios. Our molecular gas mass estimates are based on scaling relations and therefore the relationships between n_e, n_{H_2}, and $R_{\rm stall}$ should be verified using samples of galaxies with both optical spectroscopy and molecular gas measurements. The H II region stall radii are estimated from analytic scalings which rely on many simplifying assumptions. Detailed comparisons between observed and predicted sizes for local H II regions would help to establish whether such scalings can be meaningfully applied to predict the typical sizes of ionized regions in more distant galaxies.

Our conclusions fit with the growing picture that the evolution of the properties of SFGs from the peak epoch of star formation to the present day universe is primarily driven by a change in the rate of cold gas accretion onto galaxies. SFGs at $z \sim 2$ are thought to have elevated cold gas accretion rates, allowing them to maintain large molecular gas reservoirs which fuel rapid star formation, drive enhanced velocity dispersions, trigger the formation of massive clumps (see Tacconi et al. 2020 and Förster Schreiber et al. in press for reviews), and based on our work, may also be responsible for the elevated electron densities in H II regions.

4.7 Appendix A: Impact of Sample Selection on the Measured Electron Densities

4.7.1 Star Formation Rate Bias

Our sample selection explicitly excludes AGN host galaxies and inactive galaxies with outflows because we are primarily interested in investigating what drives the evolution of the electron densities in H II regions over cosmic time. However, a significant fraction of the excluded galaxies are located at high stellar masses and/or above the star-forming MS, and as a result, the density sample has a slightly lower median SFR than the parent sample at fixed z (see Section 4.2.3). The most actively star-forming galaxies are expected to have the highest n_e (e.g. Shimakawa et al., 2015; Kaasinen et al., 2017; Jiang et al., 2019; Kashino & Inoue, 2019), and therefore the electron densities measured from the density sample could potentially under-estimate the true average n_e in H II regions of $\log(M_*/M_\odot) \gtrsim 9 - 9.5$ galaxies at a given redshift.

We investigate the impact of the small SFR bias on the derived electron densities by estimating the average n_e of the narrow-line-emitting gas in different subsamples of galaxies with [S II]-clean spectra. We produce stacks including no-outflow inactive galaxies, AGN hosts and/or inactive galaxies with outflows, and then fit the emission lines in the stacked spectra as superpositions of a narrow ISM component and a broader outflow component. The [S II] ratio of the narrow component can be used to calculate the average n_e in the disks of the stacked galaxies. However, a high S/N detection of the outflow component is

required to obtain a meaningful two component decomposition of the emission line profiles.

We perform the two component emission line fitting using EMCEE, a Markov Chain Monte Carlo (MCMC) Ensemble Sampler implemented in PYTHON (Foreman-Mackey et al., 2013). EMCEE returns the posterior probability distribution function (PDF) for each of the fit parameters and therefore allows us to evaluate whether or not the [S II] ratio of the narrow component is well constrained by the data. Within each kinematic component, all emission lines are tied to the same velocity offset and dispersion. We fit all five emission lines simultaneously to obtain the best possible constraints on the kinematics of the two components. We adopt flat priors on all fit parameters and impose a top-hat prior on the [S II] ratio that has a value of 1 within the theoretically allowed range of $0.45 \leq R_{\rm SII} \leq 1.45$ and 0 outside of this range. The MCMC is run with 300 walkers, 300 burn-in steps and 1000 run steps.

We obtain meaningful two component emission line decompositions for stacks of galaxies at $z \sim 2.2$. At lower redshifts, the outflow emission is not strong enough to break degeneracies between the fit parameters. For the $z \sim 2.2$ stacks, we use the posterior PDFs of the emission line narrow component amplitudes to derive the posterior PDF of n_e following the method described in Section 4.2.6. From the stack of all inactive galaxies with [S II]-clean spectra at $z \sim 2.2$ (96 galaxies) we measure a disk n_e of 181^{+123}_{-86} cm^{-3}, and from the stack additionally including AGN host galaxies (110 galaxies in total) we measure a disk n_e of 207^{+134}_{-100} cm^{-3}. These values are in very good agreement with the fiducial n_e measured from the density sample ($n_e = 187^{+140}_{-132}$ cm^{-3}). Förster Schreiber et al. (2019) performed similar two component line fitting on the stack of the 33 inactive outflow host galaxies with the highest S/N spectra across $0.6 < z < 2.6$ (from the KMOS$^{\rm 3D}$+ sample). They reported a narrow [S II] ratio of 1.33 ± 0.09, almost identical to the ratio of 1.34 ± 0.03 obtained from the single component fit to the stack of all no-outflow inactive galaxies in the same redshift range.[6] Together, these results suggest that the electron densities measured from the stacks of no-outflow inactive galaxies are likely to reflect the average conditions in H II regions across the population of SFGs with $\log(M_*/M_\odot) \gtrsim 9 - 9.5$ at the probed redshifts.

4.7.2 Star Formation Driven Outflows

Recent observational results suggest that star formation driven ionized gas outflows at high redshift are approximately five times denser than the ionized ISM of the galaxies driving the outflows (Förster Schreiber et al., 2019). The line emission from galaxies hosting outflows traces a combination of H II region gas and outflowing material, and therefore the densities measured for these galaxies may be artificially enhanced and not representative of the conditions in H II regions. We compare the densities measured from *single* component emission line fits to stacked spectra of inactive galaxies with and without outflows (rather than the two component fitting method described in Appendix 4.7.1), and

[6] The narrow [S II] ratios reported by Förster Schreiber et al. (2019) are higher than those derived from our two component fitting because they include galaxies across the full redshift range ($0.6 \lesssim z \lesssim 2.6$) whereas we focus only on galaxies at $1.9 \lesssim z \lesssim 2.6$.

test how including galaxies hosting outflows in our stacks impacts the average density measured for each redshift slice.

The KMOS^{3D}+ parent sample includes 87 inactive galaxies hosting outflows, of which 82 have spectra covering the [S II] doublet and 42 pass the quality control cut. 8/42 fall in the YJ redshift slice, 3/42 fall in the H slice and 31/42 fall in the K slice. Due the relatively large sample variance (see e.g. Table 4.1), at least $\sim$ 10 galaxies are required to obtain a meaningful measurement of the average [S II] ratio, which in this case is only possible for the K subsample. Table 4.4 compares the pressures and densities measured for different subsamples of galaxies in each redshift slice. At $z \sim 2$, we measure somewhat higher densities and pressures in inactive galaxies with outflows compared to those with no outflows, although the two sets of measurements are consistent within the errors.[7]

We also investigate how the inclusion of inactive galaxies hosting outflows in the primary sample would change the average measured pressure and density at each redshift. The fraction of inactive galaxies with outflows in our [S II]-clean sample is similar to the fraction in the KMOS^{3D}+ parent sample. Galaxies hosting outflows account for 8/47 or 17% of inactive galaxies in our YJ slice compared to 14% in the parent sample, 3/39 or 8% in our H slice compared to 13% in the parent sample, and 31/96 or 32% in our K slice compared to 29% in the parent sample. Therefore, the trends observed in our [S II]-clean sample should reflect the trends in the overall inactive galaxy population at $z \sim 0.9$ and $z \sim 2.2$, but may slightly under-estimate the impact of outflows at $z \sim 1.5$. The measurements shown in Table 4.4 indicate that including inactive galaxies hosting outflows in the primary sample leads to modest enhancements in the inferred electron density (of up to $\sim$ 35 cm^{-3}) and ISM pressure (up to 0.2 dex), but the values derived from the full inactive sample and the no outflow subsample are consistent within the errors. These results confirm that the increased incidence of star formation driven outflows at high-z is unlikely to have a significant impact on the magnitude of the density evolution inferred from single component Gaussian fits to the [S II] doublet lines.

The relatively small impact of outflows on the measured average densities can be explained by the modest fraction of inactive galaxies with detectable broad velocity components in their nebular emission line profiles. The [S II] emission from the galaxies hosting outflows is a combination of an ISM component and an outflow component. For the $z \sim 2$ outflow galaxies, we measure a typical [S II] ratio of 1.16. Assuming that the outflow component has a typical [S II] ratio of 1.07 (as measured by Förster Schreiber et al., 2019), and that the ISM component has a typical [S II] ratio of 1.22 (as measured from our stack of no-outflow inactive galaxies), the measured [S II] ratio of 1.16 implies that $\sim$ 40% of the

[7]We note that the density measured from the outflow stack is $\sim$ 49 cm^{-3} higher than the density measured from the no outflow stack, but the ISM pressures derived from the two stacks differ by only 0.02 dex. This is because the outflow stack has a higher [N II]/Hα ratio, which results in a higher inferred metallicity and a lower inferred electron temperature compared to the no outflow stack. In reality, the enhanced [N II]/Hα ratio in the outflow stack is likely due to a small contribution from shock excitation rather than a higher metallicity (e.g. Davies et al., 2019; Freeman et al., 2019), but this observation highlights the importance of accounting for metallicity differences between galaxy populations when studying ISM pressure.

[S II] flux originates from outflowing material. If we take this 40% outflow flux fraction and multiply it by the fraction of inactive galaxies with outflows (32% in our K slice), we would expect 13% of the [S II] emission from the full inactive galaxy population at $z \sim 2.2$ to be associated with outflowing material, corresponding to an expected [S II] ratio of ~ 1.20 – in very good agreement with the value measured from the 'all inactive' stack. Performing a similar exercise for the H and YJ bands predicts that the average [S II] ratios in the overall inactive galaxy population should 1.33 and 1.30, respectively, again in good agreement with the measured values.

Overall, we find that the presence of high density outflowing material enhances the densities measured for galaxies hosting outflows over those measured for galaxies without outflows, but the incidence of outflows in the inactive galaxy population is not sufficient to have a significant impact on the measured average densities. The outflow fraction is highest at $z \sim 2.2$ ($\sim$30%), but at this redshift the typical ISM density is only a factor of ~ 2 lower than the typical density of the outflowing material, with the consequence that including sources with outflows still has a limited impact on the measured average density.

4.7.3 AGN Contamination

There is growing observational evidence to suggest that AGN-driven outflows have [S II] densities of $\gtrsim 1000$ cm^{-3} (e.g. Perna et al., 2017; Kakkad et al., 2018; Husemann et al., 2019; Förster Schreiber et al., 2019; Shimizu et al., 2019); significantly denser than the ISM of typical inactive galaxies at high-z. Furthermore, outflows appear to be almost ubiquitous in AGN-host galaxies at $z \sim 1 - 2$ (e.g. Genzel et al., 2014; Förster Schreiber et al., 2014; Harrison et al., 2016; Förster Schreiber et al., 2019; Leung et al., 2019). We perform tests similar to those described in the previous section to investigate the impact of AGN contamination on measurements of the ISM pressure and electron density at high-z.

The KMOS^{3D}+ parent sample contains 136 AGN host galaxies, of which 112 have spectra covering the [S II] doublet. One of the galaxies is classified as a Type 1 AGN and excluded, and 33 of the remaining 111 galaxies pass the quality control cut. 3/33 fall in the YJ redshift slice, 16/33 fall in the H slice and 14/33 fall in the K slice. We note that only 6/33 are classified as no-outflow systems (consistent with the high outflow fraction), so we analyze all of the AGN hosts together. AGN hosts account for 3/50 or 6% of galaxies in our YJ slice compared to 23% in the parent sample, 16/55 or 29% in our H slice compared to 29% in the parent sample, and 14/110 or 13% in our K slice compared to 20% in the parent sample. The AGN fraction in our [S II]-clean sample is very similar to the fraction in the parent sample for the $z \sim 1.5$ slice, but is significantly lower than the fraction in the parent sample for the other two redshift slices, indicating that our tests may underestimate the true impact of AGN contamination in these redshift ranges.

The [S II] ratios measured for the AGN host galaxies in the H and K slices are listed in Table 4.4. We do not present density or pressure measurements for the AGN host galaxies because the grids that are used to convert the [S II] ratios to densities and pressures are outputs of H II region photoionization models. The hard ionizing radiation field of the AGN will change the ionization and temperature structure of the nebula, resulting in a

Table 4.4: Measured [S II]λ6716/[S II]λ6731, [S II]/Hα and [N II]/Hα ratios and calculated metallicities, electron densities and thermal pressures for different subsamples of KMOS^{3D}+ galaxies in each redshift slice.

Subsample	$n_{\rm gal}$	$R_{\rm SII}$	[N II]/Hα	[S II]/Hα	12 + log(O/H)	log(P/k)	n_e([S II]) (cm^{-3})
YJ ($z \sim 0.9$)							
Inactive (no outflow)	39	$1.32^{+0.11}_{-0.08}$	0.19	0.23	8.50	$6.29^{+0.28}_{-0.73}$	101^{+59}_{-85}
Inactive (with outflow)	8	...	...	...			
All inactive	47	$1.27^{+0.10}_{-0.06}$	0.18	0.22	8.47	$6.48^{+0.14}_{-0.43}$	132^{+60}_{-83}
AGN hosts	3	...	...	...			
Inactive (no outflow) + AGN	42	$1.28^{+0.09}_{-0.09}$	0.20	0.24	8.51	$6.42^{+0.24}_{-0.39}$	123^{+87}_{-77}
H ($z \sim 1.5$)							
Inactive (no outflow)	36	$1.34^{+0.05}_{-0.13}$	0.16	0.24	8.39	$6.23^{+0.43}_{-0.26}$	79^{+120}_{-40}
Inactive (with outflow)	3	...	...	...			
All inactive	39	$1.33^{+0.05}_{-0.13}$	0.16	0.24	8.39	$6.27^{+0.41}_{-0.22}$	89^{+120}_{-43}
AGN hosts	16	$1.18^{+0.11}_{-0.09}$	...	...			
Inactive (no outflow) + AGN	52	$1.25^{+0.07}_{-0.08}$	0.17	0.27	8.37	$6.58^{+0.16}_{-0.25}$	157^{+92}_{-53}
K ($z \sim 2.2$)							
Inactive (no outflow)	65	$1.22^{+0.15}_{-0.10}$	0.15	0.19	8.47	$6.62^{+0.20}_{-0.53}$	187^{+140}_{-132}
Inactive (with outflow)	31	$1.16^{+0.17}_{-0.09}$	0.22	0.18	8.68	$6.64^{+0.16}_{-0.52}$	236^{+130}_{-160}
All inactive	96	$1.19^{+0.12}_{-0.07}$	0.18	0.19	8.56	$6.63^{+0.14}_{-0.37}$	207^{+104}_{-105}
AGN hosts	14	$1.11^{+0.26}_{-0.19}$	...	...			
Inactive (no outflow) + AGN	79	$1.22^{+0.13}_{-0.10}$	0.16	0.20	8.46	$6.61^{+0.17}_{-0.55}$	182^{+142}_{-122}

In each section of the table, the top row gives the 'fiducial' ISM pressure and electron density measured from the stack of inactive galaxies with no outflows. Subsequent rows list measurements for inactive galaxies with outflows and AGN host galaxies, and show how the density and pressure measurements change when these subpopulations are included in the primary sample. We did not make measurements for stacks with less than ten galaxies due to the relatively large sample variance. Densities and pressures are not calculated for AGN hosts because the H II region model grids that are used to convert from $R_{\rm SII}$ to density and pressure cannot be meaningfully applied to spectra excited by non-stellar sources.

different relationship between $R_{\rm SII}$ and density/pressure. AGN host galaxies appear to have lower [S II] ratios than inactive galaxies with and without outflows at the same redshift, although the differences between the line ratios measured for the different K stacks are not statistically significant. There is some evidence to suggest that AGN contamination may impact the measured ISM densities and pressures, particularly in the H slice where both quantities increase by a factor of ~ 2 when AGN are included. The inclusion of AGN host galaxies has only a minor impact on measured average density in the YJ redshift slice, and does not have any significant impact on the measurements in the K slice, but we emphasise that for these redshift slices, the AGN fractions in our [S II]-clean sample are a factor of $\sim 2-4$ lower than in the parent sample, and therefore our test likely only provides a lower limit on the impact of AGN contamination.

In studies of high-redshift star-forming galaxies, AGN are commonly identified using X-ray, radio and/or mid-IR data. However, Förster Schreiber et al. (2019) showed that these classical selection techniques may miss up to $\sim 50\%$ of AGN at $z \sim 1-2$, likely due to both the varying availability and depth of ancillary data between different extragalactic fields, and the impact of AGN variability and small-scale nuclear obscuration on the different diagnostic tracers (e.g Padovani et al., 2017). Our results indicate that it is important to use conservative AGN selection criteria (e.g. including optical line ratios) to minimize the probability of contamination from non-stellar excitation sources when measuring electron densities and ISM pressures.

4.8 Appendix B: High-z Literature Samples

We supplement our KMOS$^{\rm 3D}$+ results with measurements from other surveys of high-z galaxies in the literature. Specifically, we select samples of galaxies at $z \gtrsim 0.6$ that lie within ~ 0.5 dex of the Speagle et al. (2014) star-forming MS and have published [S II]λ6716/[S II]λ6731 or [O II]λ3726/[O II]λ3729 measurements. All stellar masses and SFRs are scaled to the Chabrier (2003) initial mass function for consistency with our measurements. We require published line ratios to avoid systematic biases in the conversion between line ratios and densities arising from differences in the atomic data or assumed electron temperature (see e.g. discussions in Sanders et al. 2016, Kewley et al. 2019). We only include datasets with at least 20 galaxies to minimize the impact of variance within the galaxy population. Our final high-z comparison sample contains measurements from KROSS (Swinbank et al., 2019), COSMOS-[O II] (Kaasinen et al., 2017), FMOS-COSMOS (Kashino et al., 2017), MOSDEF (Sanders et al., 2016), and KBSS-MOSFIRE (Steidel et al., 2014). Table 4.5 summarizes the properties of the high-z literature samples as well as the line ratio measurements and the derived electron densities. We do not have size measurements for the galaxies in these samples, so the average surface density quantities used in Figures 4.6 and 4.7 are estimated assuming that the galaxies lie on the redshift-dependent mass-size relation from van der Wel et al. (2014).

Table 4.5: Literature Samples

Sample/Reference	Median z	Median $\log(M_*/M_\odot)$	Density Diagnostic	Line Ratio	n_e (cm^{-3})
KROSS (Swinbank et al., 2019)	0.85	10.0	[S II]	1.4 ± 0.1	33^{+78}_{-32}
COSMOS-[O II] (Kaasinen et al., 2017)	1.5	10.6	[O II]	1.29 ± 0.03	119^{+24}_{-21}
FMOS-COSMOS (Kashino et al., 2017)	1.55	10.2	[S II]	1.21 ± 0.1	193^{+150}_{-88}
MOSDEF (Sanders et al., 2016)	2.24	10.1	[S II]	$1.13^{+0.16}_{-0.06}$	316^{+92}_{-197}
KBSS-MOSFIRE (Steidel et al., 2014)	2.3	10.0	[O II]	1.16 ± 0.04	258^{+67}_{-56}

Line ratio measurements were taken directly from the listed references and electron densities were re-calculated adopting the metallicity of the KMOS^{3D} stack lying closest in redshift. In cases where both the [S II] and the [O II] ratio were quoted we calculate the density from the [S II] ratio for consistency with our analysis.

4.9 Appendix C: Stellar Velocity Dispersion Estimates

For a disk in hydrostatic equilibrium, the vertical stellar velocity dispersion is given by:

$$\sigma_{*,z} = h_* \sqrt{2\pi G \rho} \tag{4.9}$$

where h_* is the scale height of the stellar disk and ρ is the midplane mass volume density (van der Kruit, 1988; Leroy et al., 2008). We assume that, for the relatively high mass galaxies considered in this analysis, ρ is dominated by the stellar and gas components.

In the local universe, the average 'flattening' (ratio of scale length to scale height, $R_{d,*}/h_*$) of the stellar disk is 7.3 (Kregel et al., 2002; Sun et al., 2020). For the SAMI galaxies at $z \sim 0$ we adopt $h_* = R_{d,*}/7.3$, and approximate $R_{d,*}$ from R_e using the relationship for an exponential disk ($R_{d,*} \simeq R_e/1.67$).

High-z disks are significantly thicker than $z \sim 0$ disks, both photometrically (e.g. Elmegreen et al., 2017) and kinematically (e.g. Förster Schreiber et al., 2009; Wisnioski et al., 2015; Johnson et al., 2018), and therefore we cannot use the $z \sim 0$ flattening to derive h_* from R_e. Instead, we assume that the stellar scale heights of the KMOS^{3D}+ galaxies are approximately equivalent to their ionized gas scale heights. This is plausibly a reasonable assumption (to first order) given that the majority of the ionized gas is likely to be associated with H II regions (see discussion in Section 4.3.4) and that the stellar populations of galaxies at $z \sim 1 - 2$ must be relatively young. The scale heights of stellar disks increase over time as a result of mergers and gravitational interactions with massive objects in the disk (such as giant molecular clouds, globular clusters and black holes). These encounters randomly perturb the momentum of individual stars, leading to the diffusion of stellar orbits and an increase in the vertical velocity dispersion and scale height of the stellar disk (e.g. Wielen, 1977). The scale height of the star-forming disk also changes over time (see discussion in Section 4.3.4). Therefore, the stellar and ionized gas scale heights will be most similar in galaxies with young stellar populations. We note that varying h_* by a factor of 2 changes the midplane pressures derived in Section 4.5.3 by < 0.15 dex and therefore the uncertainties on h_* have a relatively limited impact on our results.

We have a single value of ρ per galaxy which can be used to estimate the average stellar velocity dispersion within R_e. We assume that the scale height is constant as a function of radius (for consistency with the n_e(rms) calculations in Section 4.3.4), but note that the average scale height within R_e for a flared disk (i.e. with constant disk velocity dispersion; e.g. Burkert et al. 2010) is almost identical to the scale height at R_d, and therefore the choice of geometry has a negligible impact on the derived midplane pressure.

4.10 Appendix D: Constraints on Atomic Gas Reservoirs at $z \sim$ 1-3

The redshift evolution of galaxy atomic gas reservoirs is poorly constrained because current radio telescopes can only detect H I emission from galaxies at $z \lesssim 0.4$. At higher redshifts,

the atomic gas mass volume density can be estimated from Lyα absorption in quasar spectra, but this probes gas both in galaxies and in the circumgalactic medium around galaxies. Current observational compilations suggest that the neutral hydrogen volume density of the universe has decreased by a factor of $\sim$ 1.5 since $z \sim 2$ (see Péroux & Howk 2020 and references therein), whereas the molecular hydrogen volume density has decreased by a factor of $\sim$ 4 (e.g. Decarli et al., 2016; Scoville et al., 2017; Riechers et al., 2019; Lenkić et al., 2020; Tacconi et al., 2020). Therefore, the fraction of the ISM in the molecular phase is expected to increase towards higher redshifts.

H I mapping surveys of local spiral galaxies have found that Σ_{HI} has a relatively constant value of $\sim 6\ M_{\odot}\ \mathrm{pc}^{-2}$ at all galactocentric radii (e.g. Leroy et al., 2008) and rarely exceeds $\sim 10\ M_{\odot}\ \mathrm{pc}^{-2}$ (e.g. Bigiel et al., 2008; Leroy et al., 2008; Schruba et al., 2018), most likely because H I is converted to H_2 at higher gas mass surface densities (see e.g. discussion in Tacconi et al. 2020). The maximal Σ_{HI} is inversely correlated with the gas phase metallicity (e.g. Schruba et al., 2018). The metallicities measured from our four stacked spectra (see Section 4.2.6) are consistent with each other within 0.1 dex, because the average stellar mass of the probed galaxies increases towards higher redshifts. Therefore, the maximal Σ_{HI} is not expected to vary significantly between our samples. On the other hand, Σ_{H_2} increases from the outskirts to the centers of local spiral galaxies and no saturation is observed (e.g. Schruba et al., 2011).

There is a tight relationship between the masses and diameters of local H I disks which implies a uniform characteristic Σ_{HI} of 6.9 $M_{\odot}\ \mathrm{pc}^{-2}$ (Broeils & Rhee, 1997; Wang et al., 2016) (assuming a standard helium mass fraction of 36%). In comparison, the Tacconi et al. (2020) molecular gas depletion time scaling relation suggests that the SAMI and KMOS^{3D}+ galaxies have median molecular gas mass surface densities of $\sim 8\ M_{\odot}\ \mathrm{pc}^{-2}$ and $\sim 200\ M_{\odot}\ \mathrm{pc}^{-2}$, respectively (see Figure 4.7). The typical Σ_{H_2} for the KMOS^{3D}+ galaxies is more than an order of magnitude above the surface density at which Σ_{HI} is observed to saturate in local galaxies, suggesting that the ISM in the central regions of high-z SFGs is likely to be strongly dominated by molecular gas. On the other hand, the gas reservoirs within R_e for the SAMI galaxies are likely to be approximately equal parts H I and H_2. We adopt $\Sigma_{HI} = 6.9\ M_{\odot}\ \mathrm{pc}^{-2}$ at all redshifts, but note that the average total gas mass surface densities of the KMOS^{3D}+ galaxies are insensitive to the adopted Σ_{HI} within any reasonable range of values. Varying Σ_{HI} by a factor of 2 would change the median midplane pressure at $z \sim 0$ (Section 4.5.3) by $\lesssim 0.2$ dex and the inverse of the H II region stall radius (Section 4.5.4) by $\lesssim 0.15$ dex.

4.11 Appendix E: Derivation of H II Region Stall Radius

The time evolution of the internal pressure of an adiabatically expanding bubble driven by stellar winds and supernovae is given in Equation 25 of Oey & Clarke (1997):

$$P_{\rm int}(t) = \frac{7}{(3850\pi)^{2/5}}\ L_{\rm mech}^{2/5}\ \rho_0^{3/5}\ t^{-4/5} \tag{4.10}$$

where $L_{\rm mech}$ is the mechanical luminosity of the central star cluster and ρ_0 is the mass volume density of the material surrounding the H II region. Assuming that the expansion of the bubble stalls when $P_{\rm int}$ reaches the ambient pressure P_0, the stall time $t_{\rm stall}$ is related to $L_{\rm mech}$, ρ_0 and P_0 as follows:

$$t_{\rm stall} \propto L_{\rm mech}^{1/2}\ \rho_0^{3/4}\ P_0^{-5/4} \tag{4.11}$$

The time evolution of the radius of the expanding bubble is given in Equation 24 of Oey & Clarke (1997):

$$R(t) = \left(\frac{250}{308\pi}\right)^{1/5}\ L_{\rm mech}^{1/5}\ \rho_0^{-1/5}\ t^{3/5} \tag{4.12}$$

The expression for the stall time (Equation 4.11) can be substituted into Equation 4.12 to derive the stall radius $R_{\rm stall}$ as a function of $L_{\rm mech}$, ρ_0 and P_0:

$$\begin{aligned} R_{\rm stall} &\propto L_{\rm mech}^{1/5}\ \rho_0^{-1/5}\ \left(L_{\rm mech}^{1/2}\ \rho_0^{3/4}\ P_0^{-5/4}\right)^{3/5} \\ &\propto L_{\rm mech}^{1/2}\ \rho_0^{1/4}\ P_0^{-3/4} \end{aligned} \tag{4.13}$$

We assume that the ambient pressure is equivalent to the hydrostatic equilibrium midplane pressure $P_{\rm mid}$ (discussed in Section 4.5.3), that the mechanical luminosity of the central star cluster is proportional to $\Sigma_{\rm SFR}$ (discussed in Section 4.5.2), and that the mass volume density of the material surrounding the H II region is proportional to ρ_{H_2} (discussed in Section 4.5.1). Under these conditions, the stall radius can be expressed as

$$R_{\rm stall} \propto \Sigma_{\rm SFR}^{1/2}\ \rho_{H_2}^{1/4}\ P_{\rm mid}^{-3/4} \tag{4.14}$$

Chapter 5

Conclusions and Outlook

5.1 Summary of this Thesis

This thesis investigates the driving mechanisms of outflows and the impact of feedback processes on the properties of the ISM and the evolution of galaxies. The focus is on galaxies at the peak epoch of cosmic star formation activity and black hole growth ($1 \lesssim z \lesssim 3$) where the rate of energy injection and the frequency and strength of outflows are expected to reach a maximum. State-of-the-art near infrared integral field spectroscopy is combined with unique analysis techniques to gain valuable new insights into long-standing problems relating to the physics of outflows and their impact on the growth of galaxies.

In Chapter 2, the largest sample of $z \sim 2$ SFGs resolved on the scales of massive star-forming clumps is used to investigate how the typical velocities and mass loading factors of star formation driven outflows vary as a function of local star formation properties across galaxy disks. The high spatial resolution of the observations maximizes the contrast between the observed properties of the actively star-forming clumps and the more quiescent inter-clump regions. The measured outflow scaling relations are compared with theoretical predictions to determine the most likely driving mechanisms of the outflows.

Chapter 3 presents a detailed analysis of deep, high spatial resolution, multi-wavelength data for three AGN host galaxies at $z \sim 2.2$. These data are used to map the outflows, star formation, and ISM properties across the galaxies, and to explore how the outflows couple the AGN accretion energy to the surrounding gas over an order of magnitude in spatial scales (from nuclear to circumgalactic). The SFRs of the AGN host galaxies are compared to the average SFRs of inactive galaxies at the same stellar masses to evaluate the instantaneous impact of outflows on star formation in their host galaxies.

In Chapter 4, integrated spectra of more than 600 SFGs spanning 11 billion years of cosmic history ($0 \lesssim z \lesssim 2.6$) are used to investigate the physical processes driving the redshift evolution of galaxy electron densities. Stacked spectra of galaxies with no evidence of AGN activity or broad emission line components indicative of outflows are used to measure the typical [S II]λ6716/[S II]λ6731 ratio and n_e([S II]) in H II regions at $z \sim 0$, 0.9, 1.5, and 2.2. Hα luminosity measurements are used to estimate the average number of

electrons per unit volume across star-forming disks at each redshift, and to examine the link between the small scale properties of the [S II]-emitting gas and the global star formation properties of galaxies. Finally, the n_e measurements are compared to quantitative predictions for several potential drivers of the n_e evolution.

These investigations provide important new insights relating to the questions posed in Section 1.6:

1. *How do the velocities and mass loading factors of star formation driven outflows scale with the local properties at their launch sites? What does this reveal about the launching and driving mechanisms of the outflows?*

The velocities and mass loading factors of star formation driven outflows are positively correlated with the local $\Sigma_{\rm SFR}$. The observed correlation between $\Sigma_{\rm SFR}$ and $v_{\rm out}$ is steeper than the relationship predicted for outflows powered by mechanical energy injection from stellar winds and supernovae, but flatter than the relationship predicted for momentum driven outflows powered by radiation pressure, suggesting that both of these mechanisms may contribute to driving the observed outflows. The light-weighted average outflow strength increases by a factor of five over a relatively small range in $\Sigma_{\rm SFR}$ ($\sim 0.2 - 0.3\ M_{\odot}\ {\rm yr}^{-1}\ {\rm kpc}^{-2}$), suggesting that strong outflows may only be launched once the stellar feedback is powerful enough to overcome the local gravitational potential.

2. *How do outflows couple AGN accretion energy to gas in the interstellar medium and the circumgalactic medium? How does this coupling affect star formation in the host galaxy?*

The impact of AGN driven outflows on the gas in the surrounding environment varies significantly from system to system. Two of the three AGN driven outflows studied in Chapter 3 have propagated several kiloparsecs from their point of launch and offer a means to couple the AGN accretion energy to gas in the outer regions of their host galaxies. There is some evidence to suggest that one of these ~ 1400 km s^{-1} outflows may have ploughed directly into a nearby massive companion galaxy, driving large-scale shocks through the ISM and plausibly leading to a sudden truncation of star formation in this system. In contrast, the third target has a relatively low velocity (~ 650 km s^{-1}) outflow that is confined to the circumnuclear region and is barely resolved even with the aid of gravitational lensing. This small scale outflow is depositing a large amount of kinetic energy within a radius of a few hundred parsecs, and the resulting increase in ISM turbulence could potentially prevent the circumnuclear gas from collapsing to form stars. However, all three of the studied AGN host galaxies lie on the star-forming main sequence, suggesting that the outflows do not have any significant impact on the instantaneous integrated star formation rates of their host galaxies. These findings are consistent with the currently favored hypothesis that AGN feedback quenches star formation primarily by heating gas in the halo, compounding the effects of virial shock heating to prevent the halo gas from being (re-)accreted and replenishing the reservoir of neutral gas in the ISM.

3. *How do the electron densities in H II regions vary as a function of cosmic time? What is the role of star formation feedback in driving this evolution?*

Both the local n_e of the [S II]-emitting gas in H II regions and the average number of electrons per unit volume across star-forming disks decrease by a factor of $\sim 6 - 10$ from $z \sim 2.6$ to $z \sim 0$, suggesting that the volume filling factor of the line-emitting gas may be approximately constant across $0 \lesssim z \lesssim 2.6$. The data suggest that the enhanced electron densities in SFGs at $z \sim 1 - 3$ are most likely to be the result of either an increase in the density of the parent molecular clouds, or a decrease in the ratio of the pressure injected by stellar feedback (which drives H II region expansion) to the pressure of the ambient medium (which resists the expansion). The reduction in the amount of turbulent pressure injected by stellar feedback between $z \sim 2$ and $z \sim 0$ does not appear to lead directly to the observed decrease in n_e over the same period. However, further studies of detailed H II region simulations are required to gain a deeper understanding of the relationship between stellar feedback and the electron density of the line-emitting gas.

5.2 Outlook: Probing the Impact of Outflows on Halo Scales

The research presented in this thesis makes important contributions to our understanding of how the energy produced by young stellar populations and accretion onto supermassive black holes couples to, and ejects gas from, galaxies. However, one important topic that has not yet been discussed is how outflows impact star formation and the evolution of galaxies over long timescales.

Outflows and the ISM are just two components of the 'cosmic baryon cycle'. Intergalactic gas that falls into galaxy halos becomes part of the circumgalactic medium (CGM). CGM gas can be accreted into the ISM of galaxies and then either remains in the ISM, forms stars and is locked up until it is released by stellar winds or supernovae, or is ejected in outflows. Outflowing material may be expelled beyond the virial radius of the halo and returned to the intergalactic medium (IGM), or may remain in the CGM where it can cool and be recycled back into the ISM. In order to permanently quench star formation in a galaxy, it is necessary to consume and/or eject the existing neutral ISM reservoir, prevent the accretion of fresh gas to replenish this reservoir, and/or prevent the ISM from forming stars. Therefore, understanding how feedback leads to star formation quenching requires detailed knowledge of the cosmic baryon cycle and how it is impacted by outflows (see e.g. discussion in Tumlinson et al., 2017).

Over the last decades astronomers have conducted extensive censuses of several key components of the cosmic baryon cycle: star formation (Madau & Dickinson, 2014; Speagle et al., 2014), the neutral ISM (Catinella et al., 2018; Péroux & Howk, 2020; Tacconi et al., 2020), and outflows (e.g. Chen et al., 2010; Steidel et al., 2010; Harrison et al., 2016; Förster Schreiber et al., 2019). In comparison, the properties of the CGM and the IGM are relatively poorly understood, primarily because these gas components are much more

diffuse than the ISM and therefore have much lower surface brightnesses. However, in recent years there has been a rapid increase in research efforts and instruments focused on the galaxy-halo connection and what this reveals about the cosmic baryon cycle.

Cosmological simulations suggest that the CGM could hold important clues regarding the strength and nature of feedback. In the *Evolution and Assembly of GaLaxies and their Environments* (EAGLE) simulation, the mass outflow rates across the virial radii of halos are up to 100 times larger than the mass outflow rates from galaxies, suggesting that outflows may be able to efficiently entrain and expel CGM gas (Mitchell et al., 2020). Similarly, several simulations find that AGN feedback could be capable of heating halo gas and pushing it away from galaxies (e.g. van de Voort & Schaye, 2012; Suresh et al., 2017; Oppenheimer et al., 2020a). The sub-grid feedback models implemented in modern cosmological simulations are designed to reproduce the observed stellar properties of the galaxy population at $z \sim 0$, but the type and strength of feedback vary widely between models (Naab & Ostriker, 2017), resulting in very different predictions for the mass, metal content and temperature distribution of the CGM (e.g. Davies et al., 2020a). An observational census of CGM properties as a function of galaxy properties would therefore provide unique constraints on sub-grid feedback models.

The CGM is most often studied using absorption lines in quasar spectra. Quasar continuum photons pass through the halos of foreground galaxies on their way to our telescopes, and some of the photons lying at the redshifted wavelengths of hydrogen and metal lines are absorbed by gas in the foreground halos. Statistical studies of large samples of such absorbers spanning a wide range of impact parameters have revealed that the halos of massive galaxies are metal-enriched out to radii of $\gtrsim 100$ kpc (e.g. Tumlinson et al., 2011; Nielsen et al., 2013; Werk et al., 2013; Peek et al., 2015). The CGM contains 20 – 30% of all of the metals synthesized in stars over the lifetimes of galaxies (e.g. Peeples et al., 2014), suggesting that outflows must be able to efficiently transport metals from the ISM to the CGM (e.g. Oppenheimer & Davé, 2006; Scannapieco et al., 2006; Shen et al., 2010). There is more hot gas in the halos of SFGs than in the halos of quiescent galaxies at fixed stellar mass (e.g. Tumlinson et al., 2011), providing preliminary evidence for a link between the expulsion of halo gas and the cessation of star formation. Kinematic studies of the CGM around massive galaxies at $z \sim 2$ suggest that the majority of the neutral hydrogen within ~ 50 kpc of these galaxies is outflowing (e.g. Chen et al., 2020). Such studies provide important information about the spatial extents and velocity structures of outflows on spatial scales that are currently inaccessible (in the majority of cases) by emission line studies. For example, the characteristic velocities of the absorption lines can be compared with the average outflow velocities inferred from emission line studies (e.g. Davies et al., 2019; Förster Schreiber et al., 2019) to determine whether the typical velocity structures of outflows are more consistent with ballistic or accelerated trajectories.

Direct observations of gas flows into and out of the CGM require spatially resolved measurements of gas kinematics, which can only be obtained with sensitive integral field spectroscopy. The *Multi Unit Spectroscopic Explorer* (MUSE) and the *Keck Cosmic Web Imager* (KCWI) both probe Lyα emission at $z \gtrsim 3$, and have enabled detections of inflows from the cosmic web (e.g. Martin et al., 2019), halo-scale outflows (e.g. Erb et al., 2018;

Travascio et al., 2020), and extended Lyα halos around high-z galaxies (e.g. Wisotzki et al., 2018; Leclercq et al., 2020). The capabilities of both of these instruments will be extended in the second half of the 2020s through the *BlueMUSE* and *Keck Cosmic Reionization Mapper* (KCRM) projects, opening up possibilities to probe the multi-phase structure of the CGM by mapping it in hydrogen and metal line emission simultaneously, to study the kinematics of the CGM at $z \sim 2 - 3$, and to detect emission from the CGM and the IGM all the way back to the epoch of reionization (Richard et al., 2019).

The hot ($\gtrsim 10^6$ K) phase of the CGM can be observed in soft X-ray emission. The X-ray halos around disk galaxies have luminosities that are much lower than what is predicted for a radiatively cooling hot corona (e.g. Benson et al., 2000; Li et al., 2006). This discrepancy has been interpreted as evidence that strong outflows remove hot gas from the inner regions of halos (e.g. Crain et al., 2010). However, statistics are limited because the X-ray emission from the CGM is so weak that only the most massive halos can be detected directly. The improved sensitivity and angular resolution of next generation X-ray telescopes (such as *eROSITA*, launched in 2019, and in the future, the *Advanced Telescope for High ENergy Astrophysics* or ATHENA, to launch in 2031) will substantially increase the number of galaxies with individual X-ray halo detections. These facilities will also have sufficient spatial resolution to measure how the (average) radial distribution of hot gas varies as a function of galaxy and halo properties, providing important constraints on AGN feedback models (e.g. Oppenheimer et al., 2020b).

The main limitation of studying the CGM using the quasar absorption technique described earlier is that each spectrum probes a single line of sight through each foreground halo. The space density of quasars is relatively low, and it is rare for more than one quasar sightline to pass within the virial radius of a given halo. Therefore, studies of the spatial variation in CGM properties across halos currently rely on statistical samples of quasar-galaxy pairs at a range of impact parameters. Observational facilities with higher point source sensitivities would make it possible to detect absorption lines in the continuum of fainter and more numerous background sources, which combined with multiplexing capabilities would enable efficient tomographic mapping of the CGM around low redshift galaxies. This is a key science goal of many planned and proposed facilities including the *High Resolution Spectrograph* (HIRES), the *Wide Field Optical Spectrograph* (WFOS), and the *GMT Multi-object Astronomical and Cosmological Spectrograph* (GMACS), all of which are expected to begin operating on thirty meter class telescopes in $\sim 2025 - 2030$, and the *Large UV/Optical/IR Surveyor* (LUVOIR), which if approved and built would be expected to become available in the late 2040s.

The CGM contains a wealth of information about the long term evolution of outflows and their impact on star formation and galaxy evolution. With new and upcoming observational facilities it will be possible to probe the properties of outflows on halo scales and to investigate how the mass, temperature structure, kinematics, and morphology of the CGM evolve as galaxies quench. Ultimately, future surveys of CGM and ISM properties targeting shared samples of galaxies will significantly improve our understanding of how baryons cycle through halos and galaxies, and will offer unique insights into how feedback processes shape the evolution of entire galaxy ecosystems over billions of years.

References

Abbott, D. C. 1982, ApJ, 263, 723

Abraham, R. G., Glazebrook, K., McCarthy, P. J., et al. 2004, AJ, 127, 2455

Aird, J., Coil, A. L., Georgakakis, A., et al. 2015, MNRAS, 451, 1892

Aird, J., Nandra, K., Laird, E. S., et al. 2010, MNRAS, 401, 2531

Alatalo, K., Lacy, M., Lanz, L., et al. 2015, ApJ, 798, 31

Alexander, D. M., & Hickox, R. C. 2012, NAR, 56, 93

Allen, M. G., Groves, B. A., Dopita, M. A., Sutherland, R. S., & Kewley, L. J. 2008, ApJS, 178, 20

Anglés-Alcázar, D., Özel, F., & Davé, R. 2013, ApJ, 770, 5

Arribas, S., Colina, L., Bellocchi, E., Maiolino, R., & Villar-Martín, M. 2014, A&A, 568, A14

Bae, H.-J., & Woo, J.-H. 2016, ApJ, 828, 97

Bagetakos, I., Brinks, E., Walter, F., et al. 2011, AJ, 141, 23

Baldry, I. K., Glazebrook, K., & Driver, S. P. 2008, MNRAS, 388, 945

Baldwin, J. A., Phillips, M. M., & Terlevich, R. 1981, PASP, 93, 5

Balogh, M. L., Pearce, F. R., Bower, R. G., & Kay, S. T. 2001, MNRAS, 326, 1228

Barro, G., Faber, S. M., Pérez-González, P. G., et al. 2013, ApJ, 765, 104

Barro, G., Kriek, M., Pérez-González, P. G., et al. 2016, ApJ, 827, L32

Beckmann, R. S., Devriendt, J., Slyz, A., et al. 2017, MNRAS, 472, 949

Begelman, M. C. 1990, Astrophysics and Space Science Library, Vol. 161, Thermal phases of the interstellar medium in galaxies, ed. J. Thronson, Harley A. & J. M. Shull, 287–304

Behroozi, P., Wechsler, R. H., Hearin, A. P., & Conroy, C. 2019, MNRAS, 488, 3143

Behroozi, P. S., Wechsler, R. H., & Conroy, C. 2013, ApJ, 770, 57

Belfiore, F., Maiolino, R., Maraston, C., et al. 2016, MNRAS, 461, 3111

Belli, S., Contursi, A., & Davies, R. I. 2018, MNRAS, 478, 2097

Belli, S., Genzel, R., Förster Schreiber, N. M., et al. 2017, ApJ, 841, L6

Benson, A. J., Bower, R. G., Frenk, C. S., & White, S. D. M. 2000, MNRAS, 314, 557

Berg, D. A., Skillman, E. D., Croxall, K. V., et al. 2015, ApJ, 806, 16

Béthermin, M., Daddi, E., Magdis, G., et al. 2015, A&A, 573, A113

Bian, F., Kewley, L. J., Groves, B., & Dopita, M. A. 2020, MNRAS, 493, 580

Bigiel, F., Leroy, A., Walter, F., et al. 2008, AJ, 136, 2846

Binette, L., González-Gómez, D. I., & Mayya, Y. D. 2002, Rev. Mexicana Astron. Astrofis., 38, 279

Birnboim, Y., & Dekel, A. 2003, MNRAS, 345, 349

Bizyaev, D., Walterbos, R. A. M., Yoachim, P., et al. 2017, ApJ, 839, 87

Bluck, A. F. L., Mendel, J. T., Ellison, S. L., et al. 2014, MNRAS, 441, 599

Bolatto, A. D., Warren, S. R., Leroy, A. K., et al. 2013, Nature, 499, 450

Bonnet, H., Ströbele, S., Biancat-Marchet, F., et al. 2003, in Society of Photo-Optical Instrumentation Engineers (SPIE) Conference Series, Vol. 4839, Adaptive Optical System Technologies II, ed. P. L. Wizinowich & D. Bonaccini, 329–343

Bonnet, H., Abuter, R., Baker, A., et al. 2004, The Messenger, 117, 17

Bordoloi, R., Rigby, J. R., Tumlinson, J., et al. 2016, MNRAS, 458, 1891

Bordoloi, R., Lilly, S. J., Hardmeier, E., et al. 2014, ApJ, 794, 130

Bouché, N., Cresci, G., Davies, R., et al. 2007, ApJ, 671, 303

Bournaud, F., Elmegreen, B. G., & Elmegreen, D. M. 2007, ApJ, 670, 237

Bournaud, F., Daddi, E., Elmegreen, B. G., et al. 2008, A&A, 486, 741

Bower, R. G., Benson, A. J., Malbon, R., et al. 2006, MNRAS, 370, 645

Bower, R. G., Schaye, J., Frenk, C. S., et al. 2017, MNRAS, 465, 32

Boyle, B. J., Shanks, T., Croom, S. M., et al. 2000, MNRAS, 317, 1014

Brammer, G. B., van Dokkum, P. G., Franx, M., et al. 2012, ApJS, 200, 13

Brennan, R., Pandya, V., Somerville, R. S., et al. 2015, MNRAS, 451, 2933

Brinchmann, J., Charlot, S., White, S. D. M., et al. 2004, MNRAS, 351, 1151

Broeils, A. H., & Rhee, M. H. 1997, A&A, 324, 877

Brook, C. B., Stinson, G., Gibson, B. K., et al. 2014, MNRAS, 443, 3809

Brusa, M., Feruglio, C., Cresci, G., et al. 2015a, A&A, 578, A11

Brusa, M., Bongiorno, A., Cresci, G., et al. 2015b, MNRAS, 446, 2394

Brusa, M., Cresci, G., Daddi, E., et al. 2018, A&A, 612, A29

Bruzual, G., & Charlot, S. 2003, MNRAS, 344, 1000

Bryant, J. J., Owers, M. S., Robotham, A. S. G., et al. 2015, MNRAS, 447, 2857

Burkert, A., Genzel, R., Bouché, N., et al. 2010, ApJ, 725, 2324

Caldú-Primo, A., Schruba, A., Walter, F., et al. 2013, AJ, 146, 150

Calzetti, D., Armus, L., Bohlin, R. C., et al. 2000, ApJ, 533, 682

Cano-Díaz, M., Maiolino, R., Marconi, A., et al. 2012, A&A, 537, L8

Cantó, J., Raga, A. C., & Rodríguez, L. F. 2000, ApJ, 536, 896

Capak, P., Aussel, H., Ajiki, M., et al. 2007, ApJS, 172, 99

Cappellari, M. 2017, MNRAS, 466, 798

Cappellari, M., & Emsellem, E. 2004, PASP, 116, 138

Cardelli, J. A., Clayton, G. C., & Mathis, J. S. 1989, ApJ, 345, 245

Carniani, S., Marconi, A., Maiolino, R., et al. 2016, A&A, 591, A28

—. 2017, A&A, 605, A105

Castor, J., McCray, R., & Weaver, R. 1975, ApJ, 200, L107

Catinella, B., Saintonge, A., Janowiecki, S., et al. 2018, MNRAS, 476, 875

Cedrés, B., Beckman, J. E., Bongiovanni, Á., et al. 2013, ApJ, 765, L24

Chabrier, G. 2003, PASP, 115, 763

Chen, H.-W., McCarthy, P. J., Marzke, R. O., et al. 2002, ApJ, 570, 54

Chen, Y., Steidel, C. C., Hummels, C. B., et al. 2020, arXiv e-prints, arXiv:2006.13236

Chen, Y.-M., Tremonti, C. A., Heckman, T. M., et al. 2010, AJ, 140, 445

Chevalier, R. A., & Clegg, A. W. 1985, Nature, 317, 44

Chevance, M., Kruijssen, J. M. D., Hygate, A. P. S., et al. 2020, MNRAS, 493, 2872

Chisholm, J., Tremonti, C. A., Leitherer, C., & Chen, Y. 2017, MNRAS, 469, 4831

Chisholm, J., Tremonti, C. A., Leitherer, C., Chen, Y., & Wofford, A. 2016, MNRAS, 457, 3133

Cicone, C., Maiolino, R., Sturm, E., et al. 2014, A&A, 562, A21

Cid Fernandes, R., Stasińska, G., Mateus, A., & Vale Asari, N. 2011, MNRAS, 413, 1687

Cimatti, A., Mignoli, M., Daddi, E., et al. 2002, A&A, 392, 395

Cimatti, A., Brusa, M., Talia, M., et al. 2013, ApJ, 779, L13

Contursi, A., Poglitsch, A., Grácia Carpio, J., et al. 2013, A&A, 549, A118

Cox, D. P. 1972, ApJ, 178, 159

Crain, R. A., McCarthy, I. G., Frenk, C. S., Theuns, T., & Schaye, J. 2010, MNRAS, 407, 1403

Crain, R. A., Theuns, T., Dalla Vecchia, C., et al. 2009, MNRAS, 399, 1773

Creasey, P., Theuns, T., & Bower, R. G. 2013, MNRAS, 429, 1922

Cresci, G., Hicks, E. K. S., Genzel, R., et al. 2009, ApJ, 697, 115

Cresci, G., Mainieri, V., Brusa, M., et al. 2015, ApJ, 799, 82

Croton, D. J., Springel, V., White, S. D. M., et al. 2006, MNRAS, 365, 11

Daddi, E., Cimatti, A., Renzini, A., et al. 2004, ApJ, 600, L127

Daddi, E., Dickinson, M., Morrison, G., et al. 2007, ApJ, 670, 156

D'Agostino, J. J., Kewley, L. J., Groves, B., et al. 2019, ApJ, 878, 2

Dasyra, K. M., Combes, F., Oosterloo, T., et al. 2016, A&A, 595, L7

Davé, R., Anglés-Alcázar, D., Narayanan, D., et al. 2019, MNRAS, 486, 2827

Davé, R., Finlator, K., & Oppenheimer, B. D. 2012, MNRAS, 421, 98

Davé, R., Oppenheimer, B. D., & Finlator, K. 2011, MNRAS, 415, 11

Davé, R., Rafieferantsoa, M. H., Thompson, R. J., & Hopkins, P. F. 2017, MNRAS, 467, 115

Davies, J. J., Crain, R. A., Oppenheimer, B. D., & Schaye, J. 2020a, MNRAS, 491, 4462

Davies, R., Förster Schreiber, N. M., Cresci, G., et al. 2011, ApJ, 741, 69

Davies, R., Baron, D., Shimizu, T., et al. 2020b, arXiv e-prints, arXiv:2003.06153

Davies, R. I., Agudo Berbel, A., Wiezorrek, E., et al. 2013, A&A, 558, A56

Davies, R. L., Förster Schreiber, N. M., Übler, H., et al. 2019, ApJ, 873, 122

Davies, R. L., Förster Schreiber, N. M., Lutz, D., et al. 2020c, ApJ, 894, 28

Decarli, R., Walter, F., Aravena, M., et al. 2016, ApJ, 833, 69

Dekel, A., & Burkert, A. 2014, MNRAS, 438, 1870

Dekel, A., Sari, R., & Ceverino, D. 2009, ApJ, 703, 785

Dekel, A., & Silk, J. 1986, ApJ, 303, 39

Della Bruna, L., Adamo, A., Bik, A., et al. 2020, A&A, 635, A134

Delvecchio, I., Gruppioni, C., Pozzi, F., et al. 2014, MNRAS, 439, 2736

Di Matteo, T., Springel, V., & Hernquist, L. 2005, Nature, 433, 604

Dicke, R. H., Peebles, P. J. E., Roll, P. G., & Wilkinson, D. T. 1965, ApJ, 142, 414

Diehl, H. T., Allam, S. S., Annis, J., et al. 2009, ApJ, 707, 686

Dopita, M. A., Kewley, L. J., Sutherland, R. S., & Nicholls, D. C. 2016, Ap&SS, 361, 61

Dopita, M. A., & Sutherland, R. S. 2003, Astrophysics of the diffuse universe

Dopita, M. A., Fischera, J., Sutherland, R. S., et al. 2006, ApJS, 167, 177

Dorland, H., & Montmerle, T. 1987, A&A, 177, 243

Dutton, A. A., & Macciò, A. V. 2014, MNRAS, 441, 3359

Dyson, J. E., & Williams, D. A. 1980, Physics of the interstellar medium

Efstathiou, G. 2000, MNRAS, 317, 697

Einasto, J., Saar, E., Kaasik, A., & Chernin, A. D. 1974, Nature, 252, 111

Eisenhauer, F., Abuter, R., Bickert, K., et al. 2003, in Proc. SPIE, Vol. 4841, Instrument Design and Performance for Optical/Infrared Ground-based Telescopes, ed. M. Iye & A. F. M. Moorwood, 1548–1561

Eisenstein, D. J., Zehavi, I., Hogg, D. W., et al. 2005, ApJ, 633, 560

Elbaz, D., Daddi, E., Le Borgne, D., et al. 2007, A&A, 468, 33

Elíasdóttir, Á., Limousin, M., Richard, J., et al. 2007, arXiv e-prints, arXiv:0710.5636

Elmegreen, B. G. 1989, ApJ, 338, 178

Elmegreen, B. G., & Elmegreen, D. M. 2005, ApJ, 627, 632

Elmegreen, B. G., Elmegreen, D. M., Tompkins, B., & Jenks, L. G. 2017, ApJ, 847, 14

Elmegreen, B. G., & Hunter, D. A. 2000, ApJ, 540, 814

Epinat, B., Amram, P., Balkowski, C., & Marcelin, M. 2010, MNRAS, 401, 2113

Erb, D. K. 2015, Nature, 523, 169

Erb, D. K., Quider, A. M., Henry, A. L., & Martin, C. L. 2012, ApJ, 759, 26

Erb, D. K., Shapley, A. E., Pettini, M., et al. 2006a, ApJ, 644, 813

Erb, D. K., Steidel, C. C., & Chen, Y. 2018, ApJ, 862, L10

Erb, D. K., Steidel, C. C., Shapley, A. E., et al. 2006b, ApJ, 646, 107

Esquivel, A., Benjamin, R. A., Lazarian, A., Cho, J., & Leitner, S. N. 2006, ApJ, 648, 1043

Fabian, A. C. 2012, ARA&A, 50, 455

Farage, C. L., McGregor, P. J., Dopita, M. A., & Bicknell, G. V. 2010, ApJ, 724, 267

Faucher-Giguère, C.-A., & Quataert, E. 2012, MNRAS, 425, 605

Faucher-Giguère, C.-A., Quataert, E., & Hopkins, P. F. 2013, MNRAS, 433, 1970

Feldmann, R., & Mayer, L. 2015, MNRAS, 446, 1939

Ferrara, A., & Ricotti, M. 2006, MNRAS, 373, 571

Ferrarese, L., & Merritt, D. 2000, ApJ, 539, L9

Ferrarese, L., Pogge, R. W., Peterson, B. M., et al. 2001, ApJ, 555, L79

Feruglio, C., Fiore, F., Carniani, S., et al. 2015, A&A, 583, A99

Field, G. B. 1965, ApJ, 142, 531

Fielding, D., Quataert, E., & Martizzi, D. 2018, MNRAS, 481, 3325

Finlator, K., & Davé, R. 2008, MNRAS, 385, 2181

Fiore, F., Feruglio, C., Shankar, F., et al. 2017, A&A, 601, A143

Fischer, T. C., Crenshaw, D. M., Kraemer, S. B., & Schmitt, H. R. 2013, ApJS, 209, 1

Fischer, T. C., Kraemer, S. B., Schmitt, H. R., et al. 2018, ApJ, 856, 102

Fischer, T. C., Rigby, J. R., Mahler, G., et al. 2019, ApJ, 875, 102

Fluetsch, A., Maiolino, R., Carniani, S., et al. 2019, MNRAS, 483, 4586

—. 2020, arXiv e-prints, arXiv:2006.13232

Foreman-Mackey, D., Hogg, D. W., Lang, D., & Goodman, J. 2013, PASP, 125, 306

Förster Schreiber, N. M., Genzel, R., Lutz, D., Kunze, D., & Sternberg, A. 2001, ApJ, 552, 544

Förster Schreiber, N. M., Genzel, R., Lehnert, M. D., et al. 2006, ApJ, 645, 1062

Förster Schreiber, N. M., Genzel, R., Bouché, N., et al. 2009, ApJ, 706, 1364

Förster Schreiber, N. M., Shapley, A. E., Genzel, R., et al. 2011, ApJ, 739, 45

Förster Schreiber, N. M., Genzel, R., Newman, S. F., et al. 2014, ApJ, 787, 38

Förster Schreiber, N. M., Renzini, A., Mancini, C., et al. 2018, ApJS, 238, 21

Förster Schreiber, N. M., Übler, H., Davies, R. L., et al. 2019, ApJ, 875, 21

Freeman, W. R., Siana, B., Kriek, M., et al. 2019, ApJ, 873, 102

Gaia Collaboration, Brown, A. G. A., Vallenari, A., et al. 2016, A&A, 595, A2

Gallerani, S., Ferrara, A., Neri, R., & Maiolino, R. 2014, MNRAS, 445, 2848

Gaskell, C. M., & Ferland, G. J. 1984, PASP, 96, 393

Gebhardt, K., Bender, R., Bower, G., et al. 2000, ApJ, 539, L13

Genel, S., Naab, T., Genzel, R., et al. 2012, ApJ, 745, 11

Gentry, E. S., Krumholz, M. R., Madau, P., & Lupi, A. 2019, MNRAS, 483, 3647

Genzel, R., Tacconi, L. J., Eisenhauer, F., et al. 2006, Nature, 442, 786

Genzel, R., Burkert, A., Bouché, N., et al. 2008, ApJ, 687, 59

Genzel, R., Tacconi, L. J., Gracia-Carpio, J., et al. 2010, MNRAS, 407, 2091

Genzel, R., Newman, S., Jones, T., et al. 2011, ApJ, 733, 101

Genzel, R., Tacconi, L. J., Kurk, J., et al. 2013, ApJ, 773, 68

Genzel, R., Förster Schreiber, N. M., Rosario, D., et al. 2014, ApJ, 796, 7

Genzel, R., Tacconi, L. J., Lutz, D., et al. 2015, ApJ, 800, 20

Genzel, R., Schreiber, N. M. F., Übler, H., et al. 2017, Nature, 543, 397

Girichidis, P., Naab, T., Hanasz, M., & Walch, S. 2018, MNRAS, 479, 3042

Gofford, J., Reeves, J. N., Tombesi, F., et al. 2013, MNRAS, 430, 60

Groves, B., Dopita, M. A., Sutherland, R. S., et al. 2008, ApJS, 176, 438

Gruppioni, C., Pozzi, F., Rodighiero, G., et al. 2013, MNRAS, 432, 23

Guillard, P., Boulanger, F., Pineau des Forêts, G., et al. 2012, ApJ, 749, 158

Guo, Y., Ferguson, H. C., Bell, E. F., et al. 2015, ApJ, 800, 39

Guo, Y., Rafelski, M., Bell, E. F., et al. 2018, ApJ, 853, 108

Gutiérrez, L., & Beckman, J. E. 2010, ApJ, 710, L44

Haffner, L. M., Reynolds, R. J., & Tufte, S. L. 1999, ApJ, 523, 223

Hainline, K. N., Shapley, A. E., Kornei, K. A., et al. 2009, ApJ, 701, 52

Harper-Clark, E., & Murray, N. 2009, ApJ, 693, 1696

Harrison, C. M., Alexander, D. M., Swinbank, A. M., et al. 2012, MNRAS, 426, 1073

Harrison, C. M., Alexander, D. M., Mullaney, J. R., et al. 2016, MNRAS, 456, 1195

Hayward, C. C., & Hopkins, P. F. 2017, MNRAS, 465, 1682

Heckman, T. M., Alexandroff, R. M., Borthakur, S., Overzier, R., & Leitherer, C. 2015, ApJ, 809, 147

Heckman, T. M., & Borthakur, S. 2016, ApJ, 822, 9

Heckman, T. M., Lehnert, M. D., Strickland, D. K., & Armus, L. 2000, ApJS, 129, 493

Heckman, T. M., & Thompson, T. A. 2017, ArXiv e-prints, arXiv:1701.09062

Hemmati, S., Mobasher, B., Darvish, B., et al. 2015, ApJ, 814, 46

Herrera-Camus, R., Bolatto, A., Smith, J. D., et al. 2016, ApJ, 826, 175

Herrera-Camus, R., Tacconi, L., Genzel, R., et al. 2019, ApJ, 871, 37

Herrera-Camus, R., Janssen, A., Sturm, E., et al. 2020, A&A, 635, A47

Hirschmann, M., Naab, T., Davé, R., et al. 2013, MNRAS, 436, 2929

Ho, I.-T., Kudritzki, R.-P., Kewley, L. J., et al. 2015, MNRAS, 448, 2030

Ho, I.-T., Kewley, L. J., Dopita, M. A., et al. 2014, MNRAS, 444, 3894

Hopkins, P. F., Hernquist, L., Cox, T. J., et al. 2006, ApJS, 163, 1

Hopkins, P. F., Hernquist, L., Cox, T. J., & Kereš, D. 2008, ApJS, 175, 356

Hopkins, P. F., Kereš, D., Murray, N., Quataert, E., & Hernquist, L. 2012a, MNRAS, 427, 968

Hopkins, P. F., & Quataert, E. 2010, MNRAS, 407, 1529

Hopkins, P. F., Quataert, E., & Murray, N. 2012b, MNRAS, 421, 3522

Hunt, L. K., & Hirashita, H. 2009, A&A, 507, 1327

Husemann, B., Scharwächter, J., Davis, T. A., et al. 2019, A&A, 627, A53

Ilbert, O., Capak, P., Salvato, M., et al. 2009, ApJ, 690, 1236

James, B. L., Auger, M., Pettini, M., et al. 2018, MNRAS, 476, 1726

Jiang, T., Malhotra, S., Yang, H., & Rhoads, J. E. 2019, ApJ, 872, 146

Johnson, H. L., Harrison, C. M., Swinbank, A. M., et al. 2018, MNRAS, 474, 5076

Jones, T., Martin, C., & Cooper, M. C. 2015, ApJ, 813, 126

Jullo, E., & Kneib, J.-P. 2009, MNRAS, 395, 1319

Jullo, E., Kneib, J.-P., Limousin, M., et al. 2007, New Journal of Physics, 9, 447

Kaasinen, M., Bian, F., Groves, B., Kewley, L. J., & Gupta, A. 2017, MNRAS, 465, 3220

Kaasinen, M., Kewley, L., Bian, F., et al. 2018, MNRAS, 477, 5568

Kakkad, D., Groves, B., Dopita, M., et al. 2018, A&A, 618, A6

Kashino, D., & Inoue, A. K. 2019, MNRAS, 486, 1053

Kashino, D., Silverman, J. D., Rodighiero, G., et al. 2013, ApJ, 777, L8

Kashino, D., Silverman, J. D., Sanders, D., et al. 2017, ApJ, 835, 88

Kauffmann, G., Heckman, T. M., Tremonti, C., et al. 2003, MNRAS, 346, 1055

Kelvin, L. S., Driver, S. P., Robotham, A. S. G., et al. 2012, MNRAS, 421, 1007

Kennicutt, R. C., J. 1984, ApJ, 287, 116

Kennicutt, Jr., R. C. 1998, ARA&A, 36, 189

Kewley, L. J., Dopita, M. A., Leitherer, C., et al. 2013, ApJ, 774, 100

Kewley, L. J., Dopita, M. A., Sutherland, R. S., Heisler, C. A., & Trevena, J. 2001, ApJ, 556, 121

Kewley, L. J., Nicholls, D. C., Sutherland, R., et al. 2019, ApJ, 880, 16

Kim, C.-G., & Ostriker, E. C. 2015, ApJ, 802, 99

—. 2018, ApJ, 853, 173

Kim, D.-C., Evans, A. S., Vavilkin, T., et al. 2013, ApJ, 768, 102

Kim, K.-T., & Koo, B.-C. 2001, ApJ, 549, 979

King, A. 2003, ApJ, 596, L27

King, A., & Pounds, K. 2015, ARA&A, 53, 115

King, A. R. 2010, MNRAS, 402, 1516

Kneib, J.-P., Ellis, R. S., Smail, I., Couch, W. J., & Sharples, R. M. 1996, ApJ, 471, 643

Kocevski, D. D., Barro, G., Faber, S. M., et al. 2017, ApJ, 846, 112

Kormendy, J., & Ho, L. C. 2013, ARA&A, 51, 511

Kornei, K. A., Shapley, A. E., Martin, C. L., et al. 2012, ApJ, 758, 135

Kreckel, K., Ho, I. T., Blanc, G. A., et al. 2019, ApJ, 887, 80

Kregel, M., van der Kruit, P. C., & de Grijs, R. 2002, MNRAS, 334, 646

Kriek, M., van Dokkum, P. G., Labbé, I., et al. 2009, ApJ, 700, 221

Kriek, M., van Dokkum, P. G., Franx, M., et al. 2007, ApJ, 669, 776

—. 2008, ApJ, 677, 219

Kruijssen, J. M. D., Schruba, A., Chevance, M., et al. 2019, Nature, 569, 519

Krumholz, M. R., & Burkhart, B. 2016, MNRAS, 458, 1671

Krumholz, M. R., Burkhart, B., Forbes, J. C., & Crocker, R. M. 2018, MNRAS, 477, 2716

Krumholz, M. R., & Matzner, C. D. 2009, ApJ, 703, 1352

Kurk, J., Cimatti, A., Daddi, E., et al. 2013, A&A, 549, A63

Lagos, C. d. P., Lacey, C. G., & Baugh, C. M. 2013, MNRAS, 436, 1787

Lang, P., Wuyts, S., Somerville, R. S., et al. 2014, ApJ, 788, 11

Lapi, A., Raimundo, S., Aversa, R., et al. 2014, ApJ, 782, 69

Larson, R. B. 1974, MNRAS, 169, 229

Law, D. R., Steidel, C. C., Erb, D. K., et al. 2009, ApJ, 697, 2057

Leclercq, F., Bacon, R., Verhamme, A., et al. 2020, A&A, 635, A82

Lenkić, L., Bolatto, A. D., Förster Schreiber, N. M., et al. 2020, AJ, 159, 190

Leroy, A. K., Walter, F., Brinks, E., et al. 2008, AJ, 136, 2782

Leroy, A. K., Bolatto, A. D., Ostriker, E. C., et al. 2015, ApJ, 801, 25

Leslie, S. K., Schinnerer, E., Liu, D., et al. 2020, ApJ, 899, 58

Leung, G. C. K., Coil, A. L., Azadi, M., et al. 2017, ApJ, 849, 48

Leung, G. C. K., Coil, A. L., Aird, J., et al. 2019, ApJ, 886, 11

Levy, R. C., Bolatto, A. D., Teuben, P., et al. 2018, ApJ, 860, 92

Levy, R. C., Bolatto, A. D., Sánchez, S. F., et al. 2019, ApJ, 882, 84

Li, C., & White, S. D. M. 2009, MNRAS, 398, 2177

Li, M., Bryan, G. L., & Ostriker, J. P. 2017, ApJ, 841, 101

Li, Z., Wang, Q. D., Irwin, J. A., & Chaves, T. 2006, MNRAS, 371, 147

Lilly, S. J., Carollo, C. M., Pipino, A., Renzini, A., & Peng, Y. 2013, ApJ, 772, 119

Limousin, M., Richard, J., Jullo, E., et al. 2007, ApJ, 668, 643

Liu, D., Schinnerer, E., Groves, B., et al. 2019, ApJ, 887, 235

Liu, F. S., Jiang, D., Faber, S. M., et al. 2017, ApJ, 844, L2

Liu, G., Zakamska, N. L., Greene, J. E., Nesvadba, N. P. H., & Liu, X. 2013, MNRAS, 436, 2576

Loiacono, F., Talia, M., Fraternali, F., et al. 2019, MNRAS, 489, 681

Lopez, L. A., Krumholz, M. R., Bolatto, A. D., et al. 2014, ApJ, 795, 121

Luo, B., Brandt, W. N., Xue, Y. Q., et al. 2017, ApJS, 228, 2

Lutz, D., Maiolino, R., Spoon, H. W. W., & Moorwood, A. F. M. 2004, A&A, 418, 465

Lutz, D., Sturm, E., Janssen, A., et al. 2020, A&A, 633, A134

Madau, P., & Dickinson, M. 2014, ARA&A, 52, 415

Madsen, G. J., Reynolds, R. J., & Haffner, L. M. 2006, ApJ, 652, 401

Magnelli, B., Popesso, P., Berta, S., et al. 2013, A&A, 553, A132

Magorrian, J., Tremaine, S., Richstone, D., et al. 1998, AJ, 115, 2285

Maiolino, R., Gallerani, S., Neri, R., et al. 2012, MNRAS, 425, L66

Maiolino, R., Russell, H. R., Fabian, A. C., et al. 2017, Nature, 544, 202

Mancini, C., Förster Schreiber, N. M., Renzini, A., et al. 2011, ApJ, 743, 86

Martig, M., Bournaud, F., Teyssier, R., & Dekel, A. 2009, ApJ, 707, 250

Martin, C. L. 1997, ApJ, 491, 561

—. 2005, ApJ, 621, 227

Martin, C. L., Shapley, A. E., Coil, A. L., et al. 2012, ApJ, 760, 127

Martin, D. C., O'Sullivan, D., Matuszewski, M., et al. 2019, Nature Astronomy, 3, 822

Martini, P. 2004, in Coevolution of Black Holes and Galaxies, ed. L. C. Ho, 169

Massey, R., Kitching, T., & Richard, J. 2010, Reports on Progress in Physics, 73, 086901

Masters, D., McCarthy, P., Siana, B., et al. 2014, ApJ, 785, 153

McConnell, N. J., & Ma, C.-P. 2013, ApJ, 764, 184

McCracken, H. J., Capak, P., Salvato, M., et al. 2010, ApJ, 708, 202

McElroy, R., Croom, S. M., Pracy, M., et al. 2015, MNRAS, 446, 2186

McKee, C. F., & Ostriker, J. P. 1977, ApJ, 218, 148

McKee, C. F., van Buren, D., & Lazareff, B. 1984, ApJ, 278, L115

McLeod, A. F., Dale, J. E., Evans, C. J., et al. 2019, MNRAS, 486, 5263

McLeod, A. F., Dale, J. E., Ginsburg, A., et al. 2015, MNRAS, 450, 1057

McLeod, A. F., Kruijssen, J. M. D., Weisz, D. R., et al. 2020, ApJ, 891, 25

Medling, A. M., Cortese, L., Croom, S. M., et al. 2018, MNRAS, 475, 5194

Merten, J., Meneghetti, M., Postman, M., et al. 2015, ApJ, 806, 4

Millard, J. S., Eales, S. A., Smith, M. W. L., et al. 2020, MNRAS, 494, 293

Miller, S. T., & Veilleux, S. 2003, ApJS, 148, 383

Mingozzi, M., Vallini, L., Pozzi, F., et al. 2018, MNRAS, 474, 3640

Mitchell, P. D., Schaye, J., Bower, R. G., & Crain, R. A. 2020, MNRAS, 494, 3971

Momcheva, I. G., Brammer, G. B., van Dokkum, P. G., et al. 2016, ApJS, 225, 27

Monreal-Ibero, A., Arribas, S., & Colina, L. 2006, ApJ, 637, 138

Moster, B. P., Naab, T., & White, S. D. M. 2013, MNRAS, 428, 3121

Moster, B. P., Naab, T., & White, S. D. M. 2018, MNRAS, 477, 1822

Moustakas, J., Kennicutt, Robert C., J., Tremonti, C. A., et al. 2010, ApJS, 190, 233

Moustakas, J., Coil, A. L., Aird, J., et al. 2013, ApJ, 767, 50

Muratov, A. L., Kereš, D., Faucher-Giguère, C.-A., et al. 2015, MNRAS, 454, 2691

Murray, N., Ménard, B., & Thompson, T. A. 2011, ApJ, 735, 66

Murray, N., Quataert, E., & Thompson, T. A. 2005, ApJ, 618, 569

—. 2010, ApJ, 709, 191

Mutch, S. J., Croton, D. J., & Poole, G. B. 2013, MNRAS, 435, 2445

Naab, T., & Ostriker, J. P. 2017, ARA&A, 55, 59

Nakajima, K., & Ouchi, M. 2014, MNRAS, 442, 900

Nath, B. B., Das, P., & Oey, M. S. 2020, MNRAS, 493, 1034

Nath, B. B., & Silk, J. 2009, MNRAS, 396, L90

Navarro, J. F., Frenk, C. S., & White, S. D. M. 1997, ApJ, 490, 493

Nelson, D., Pillepich, A., Springel, V., et al. 2018, MNRAS, 475, 624

—. 2019, MNRAS, 490, 3234

Nelson, E., van Dokkum, P., Franx, M., et al. 2014, Nature, 513, 394

Nelson, E. J., van Dokkum, P. G., Momcheva, I., et al. 2013, ApJ, 763, L16

Nelson, E. J., van Dokkum, P. G., Momcheva, I. G., et al. 2016a, ApJ, 817, L9

Nelson, E. J., van Dokkum, P. G., Förster Schreiber, N. M., et al. 2016b, ApJ, 828, 27

Nesvadba, N. P. H., Lehnert, M. D., De Breuck, C., Gilbert, A. M., & van Breugel, W. 2008, A&A, 491, 407

Nesvadba, N. P. H., Lehnert, M. D., Eisenhauer, F., et al. 2006, ApJ, 650, 693

Netzer, H. 2009, MNRAS, 399, 1907

Newman, S. F., Shapiro Griffin, K., Genzel, R., et al. 2012a, ApJ, 752, 111

Newman, S. F., Genzel, R., Förster-Schreiber, N. M., et al. 2012b, ApJ, 761, 43

Newman, S. F., Genzel, R., Förster Schreiber, N. M., et al. 2013, ApJ, 767, 104

Newman, S. F., Buschkamp, P., Genzel, R., et al. 2014, ApJ, 781, 21

Nielsen, N. M., Churchill, C. W., & Kacprzak, G. G. 2013, ApJ, 776, 115

Noeske, K. G., Weiner, B. J., Faber, S. M., et al. 2007, ApJ, 660, L43

Oey, M. S., & Clarke, C. J. 1997, MNRAS, 289, 570

Oey, M. S., & Clarke, C. J. 1998, in Magellanic Clouds and Other Dwarf Galaxies, 185–188

Oey, M. S., Meurer, G. R., Yelda, S., et al. 2007, ApJ, 661, 801

Okamoto, T., Eke, V. R., Frenk, C. S., & Jenkins, A. 2005, MNRAS, 363, 1299

Oppenheimer, B. D., & Davé, R. 2006, MNRAS, 373, 1265

Oppenheimer, B. D., Davé, R., Kereš, D., et al. 2010, MNRAS, 406, 2325

Oppenheimer, B. D., Davies, J. J., Crain, R. A., et al. 2020a, MNRAS, 491, 2939

Oppenheimer, B. D., Bogdán, Á., Crain, R. A., et al. 2020b, ApJ, 893, L24

Osterbrock, D., & Flather, E. 1959, ApJ, 129, 26

Osterbrock, D. E., & Ferland, G. J. 2006, Astrophysics of gaseous nebulae and active galactic nuclei (Sausalito, CA: University Science Books)

Ostriker, E. C., & Shetty, R. 2011, ApJ, 731, 41

Ostriker, J. P., Peebles, P. J. E., & Yahil, A. 1974, ApJ, 193, L1

Padovani, P., Alexander, D. M., Assef, R. J., et al. 2017, A&A Rev., 25, 2

Pearson, W. J., Wang, L., Hurley, P. D., et al. 2018, A&A, 615, A146

Peek, J. E. G., Ménard, B., & Corrales, L. 2015, ApJ, 813, 7

Peeples, M. S., Werk, J. K., Tumlinson, J., et al. 2014, ApJ, 786, 54

Pellegrini, E. W., Oey, M. S., Winkler, P. F., et al. 2012, ApJ, 755, 40

Peng, C. Y., Ho, L. C., Impey, C. D., & Rix, H.-W. 2002, AJ, 124, 266

—. 2010a, AJ, 139, 2097

Peng, Y.-j., Lilly, S. J., Kovač, K., et al. 2010b, ApJ, 721, 193

Penzias, A. A., & Wilson, R. W. 1965, ApJ, 142, 419

Perna, M., Lanzuisi, G., Brusa, M., Cresci, G., & Mignoli, M. 2017, A&A, 606, A96

Péroux, C., & Howk, J. C. 2020, ARA&A, 58, annurev

Pettini, M., & Pagel, B. E. J. 2004, MNRAS, 348, L59

Pety, J., Schinnerer, E., Leroy, A. K., et al. 2013, ApJ, 779, 43

Phillips, J. P. 2007, MNRAS, 380, 369

Pillepich, A., Springel, V., Nelson, D., et al. 2018, MNRAS, 473, 4077

Planck Collaboration, Aghanim, N., Akrami, Y., et al. 2018, arXiv e-prints, arXiv:1807.06209

Poetrodjojo, H., D'Agostino, J. J., Groves, B., et al. 2019, MNRAS, 487, 79

Poetrodjojo, H., Groves, B., Kewley, L. J., et al. 2018, MNRAS, 479, 5235

Popping, G., Decarli, R., Man, A. W. S., et al. 2017, A&A, 602, A11

Proxauf, B., Öttl, S., & Kimeswenger, S. 2014, A&A, 561, A10

Puchwein, E., & Springel, V. 2013, MNRAS, 428, 2966

Rabien, S., Angel, R., Barl, L., et al. 2019, A&A, 621, A4

Rahner, D., Pellegrini, E. W., Glover, S. C. O., & Klessen, R. S. 2017, MNRAS, 470, 4453

—. 2019, MNRAS, 483, 2547

Ramirez-Ballinas, I., & Hidalgo-Gámez, A. M. 2014, MNRAS, 442, 2282

Rand, R. J. 1998, ApJ, 501, 137

Reynolds, R. J. 1991, ApJ, 372, L17

Rhoads, J. E., Malhotra, S., Allam, S., et al. 2014, ApJ, 787, 8

Rich, J. A., Kewley, L. J., & Dopita, M. A. 2011, ApJ, 734, 87

—. 2015, ApJS, 221, 28

Richard, J., Bacon, R., Blaizot, J., et al. 2019, arXiv e-prints, arXiv:1906.01657

Riechers, D. A., Pavesi, R., Sharon, C. E., et al. 2019, ApJ, 872, 7

Roberts-Borsani, G. W. 2020, MNRAS, 494, 4266

Rodighiero, G., Daddi, E., Baronchelli, I., et al. 2011, ApJ, 739, L40

Rosario, D. J., Togi, A., Burtscher, L., et al. 2019, ApJ, 875, L8

Rosario, D. J., Santini, P., Lutz, D., et al. 2012, A&A, 545, A45

Rossa, J., & Dettmar, R. J. 2003, A&A, 406, 493

Rubin, K. H. R., Prochaska, J. X., Koo, D. C., et al. 2014, ApJ, 794, 156

Rubin, K. H. R., Weiner, B. J., Koo, D. C., et al. 2010, ApJ, 719, 1503

Rupke, D. S., Veilleux, S., & Sanders, D. B. 2005, ApJS, 160, 115

Rupke, D. S. N., Gültekin, K., & Veilleux, S. 2017, ApJ, 850, 40

Rupke, D. S. N., & Veilleux, S. 2013, ApJ, 768, 75

Ruszkowski, M., Yang, H.-Y. K., & Zweibel, E. 2017, ApJ, 834, 208

Saintonge, A., Lutz, D., Genzel, R., et al. 2013, ApJ, 778, 2

Sales, L. V., Navarro, J. F., Schaye, J., et al. 2010, MNRAS, 409, 1541

Sanders, R. L., Shapley, A. E., Zhang, K., & Yan, R. 2017, ApJ, 850, 136

Sanders, R. L., Shapley, A. E., Kriek, M., et al. 2016, ApJ, 816, 23

Sanders, R. L., Jones, T., Shapley, A. E., et al. 2020, ApJ, 888, L11

Sargent, M. T., Daddi, E., Béthermin, M., et al. 2014, ApJ, 793, 19

Scannapieco, C., Tissera, P. B., White, S. D. M., & Springel, V. 2006, MNRAS, 371, 1125

Scarrott, S. M., Eaton, N., & Axon, D. J. 1991, MNRAS, 252, 12P

Schaefer, A. L., Croom, S. M., Allen, J. T., et al. 2017, MNRAS, 464, 121

Schaye, J., Crain, R. A., Bower, R. G., et al. 2015, MNRAS, 446, 521

Schmidt, M. 1959, ApJ, 129, 243

Scholtz, J., Harrison, C. M., Rosario, D. J., et al. 2020, MNRAS, 492, 3194

Schreiber, C., Pannella, M., Elbaz, D., et al. 2015, A&A, 575, A74

Schruba, A., Bialy, S., & Sternberg, A. 2018, ApJ, 862, 110

Schruba, A., Leroy, A. K., Walter, F., et al. 2011, AJ, 142, 37

Scott, N., van de Sande, J., Croom, S. M., et al. 2018, MNRAS, 481, 2299

Scoville, N., Lee, N., Vanden Bout, P., et al. 2017, ApJ, 837, 150

Scoville, N. Z., Thakkar, D., Carlstrom, J. E., & Sargent, A. I. 1993, ApJ, 404, L59

Sedov, L. I. 1959, Similarity and Dimensional Methods in Mechanics

Shankar, F., Weinberg, D. H., & Miralda-Escudé, J. 2009, ApJ, 690, 20

Shapiro, K. L., Genzel, R., Quataert, E., et al. 2009, ApJ, 701, 955

Shapley, A. E., CoiSoto17l, A. L., Ma, C.-P., & Bundy, K. 2005, ApJ, 635, 1006

Shapley, A. E., Steidel, C. C., Pettini, M., & Adelberger, K. L. 2003, ApJ, 588, 65

Shapley, A. E., Reddy, N. A., Kriek, M., et al. 2015, ApJ, 801, 88

Shapley, A. E., Sanders, R. L., Shao, P., et al. 2019, ApJ, 881, L35

Sharma, M., & Nath, B. B. 2012, ApJ, 750, 55

Sharon, C. E., Tagore, A. S., Baker, A. J., et al. 2019, ApJ, 879, 52

Sharp, R. G., & Bland-Hawthorn, J. 2010, ApJ, 711, 818

Sharples, R., Bender, R., Agudo Berbel, A., et al. 2013, The Messenger, 151, 21

Sharples, R. M., Bender, R., Lehnert, M. D., et al. 2004, Society of Photo-Optical Instrumentation Engineers (SPIE) Conference Series, Vol. 5492, KMOS: an infrared multiple-object integral field spectrograph for the ESO VLT, ed. A. F. M. Moorwood & M. Iye, 1179–1186

Shen, S., Wadsley, J., & Stinson, G. 2010, MNRAS, 407, 1581

Shimakawa, R., Kodama, T., Steidel, C. C., et al. 2015, MNRAS, 451, 1284

Shimizu, T. T., Davies, R. I., Koss, M., et al. 2018, ApJ, 856, 154

Shimizu, T. T., Davies, R. I., Lutz, D., et al. 2019, MNRAS, 490, 5860

Shirazi, M., Vegetti, S., Nesvadba, N., et al. 2014, MNRAS, 440, 2201

Shopbell, P. L., & Bland-Hawthorn, J. 1998, ApJ, 493, 129

Sijacki, D., Springel, V., Di Matteo, T., & Hernquist, L. 2007, MNRAS, 380, 877

Silk, J., & Rees, M. J. 1998, A&A, 331, L1

Slavin, J. D., Shull, J. M., & Begelman, M. C. 1993, ApJ, 407, 83

Snijders, L., Kewley, L. J., & van der Werf, P. P. 2007, ApJ, 669, 269

Sobral, D., Best, P. N., Smail, I., et al. 2014, MNRAS, 437, 3516

Somerville, R. S., & Davé, R. 2015, ARA&A, 53, 51

Somerville, R. S., Hopkins, P. F., Cox, T. J., Robertson, B. E., & Hernquist, L. 2008, MNRAS, 391, 481

Soto, E., de Mello, D. F., Rafelski, M., et al. 2017, ApJ, 837, 6

Soto, K. T., Martin, C. L., Prescott, M. K. M., & Armus, L. 2012, ApJ, 757, 86

Speagle, J. S., Steinhardt, C. L., Capak, P. L., & Silverman, J. D. 2014, ApJS, 214, 15

Spilker, J. S., Bezanson, R., Marrone, D. P., et al. 2016, ApJ, 832, 19

Spitzer, L. 1978, Physical processes in the interstellar medium, doi:10.1002/9783527617722

Springel, V., & Hernquist, L. 2003, MNRAS, 339, 289

—. 2005, ApJ, 622, L9

Steidel, C. C., Erb, D. K., Shapley, A. E., et al. 2010, ApJ, 717, 289

Steidel, C. C., Strom, A. L., Pettini, M., et al. 2016, ApJ, 826, 159

Steidel, C. C., Rudie, G. C., Strom, A. L., et al. 2014, ApJ, 795, 165

Stott, J. P., Swinbank, A. M., Johnson, H. L., et al. 2016, MNRAS, 457, 1888

Strickland, D. K., Heckman, T. M., Colbert, E. J. M., Hoopes, C. G., & Weaver, K. A. 2004, ApJ, 606, 829

Strom, A. L., Steidel, C. C., Rudie, G. C., et al. 2017, ApJ, 836, 164

Sugahara, Y., Ouchi, M., Lin, L., et al. 2017, ApJ, 850, 51

Sun, J., Leroy, A. K., Ostriker, E. C., et al. 2020, ApJ, 892, 148

Suresh, J., Rubin, K. H. R., Kannan, R., et al. 2017, MNRAS, 465, 2966

Swinbank, A. M., Harrison, C. M., Tiley, A. L., et al. 2019, MNRAS, 487, 381

Tacchella, S., Dekel, A., Carollo, C. M., et al. 2016, MNRAS, 457, 2790

Tacchella, S., Lang, P., Carollo, C. M., et al. 2015a, ApJ, 802, 101

Tacchella, S., Carollo, C. M., Renzini, A., et al. 2015b, Science, 348, 314

Tacchella, S., Carollo, C. M., Förster Schreiber, N. M., et al. 2018, ApJ, 859, 56

Tacconi, L. J., Genzel, R., & Sternberg, A. 2020, arXiv e-prints, arXiv:2003.06245

Tacconi, L. J., Neri, R., Genzel, R., et al. 2013, ApJ, 768, 74

Tacconi, L. J., Genzel, R., Saintonge, A., et al. 2018, ApJ, 853, 179

Tadaki, K.-i., Kodama, T., Nelson, E. J., et al. 2017, ApJ, 841, L25

Tagore, A. S. 2014, PhD thesis, Rutgers The State University of New Jersey - New Brunswick

Talia, M., Mignoli, M., Cimatti, A., et al. 2012, A&A, 539, A61

Talia, M., Pozzi, F., Vallini, L., et al. 2018, MNRAS, 476, 3956

Taylor, G. 1950, Proceedings of the Royal Society of London Series A, 201, 159

Thilker, D. A., Walterbos, R. A. M., Braun, R., & Hoopes, C. G. 2002, AJ, 124, 3118

Thompson, T. A., Quataert, E., & Murray, N. 2005, ApJ, 630, 167

Tombesi, F., Cappi, M., Reeves, J. N., et al. 2011, ApJ, 742, 44

Tombesi, F., Meléndez, M., Veilleux, S., et al. 2015, Nature, 519, 436

Tombesi, F., Veilleux, S., Meléndez, M., et al. 2017, ApJ, 850, 151

Tomczak, A. R., Quadri, R. F., Tran, K.-V. H., et al. 2016, ApJ, 817, 118

Travascio, A., Zappacosta, L., Cantalupo, S., et al. 2020, A&A, 635, A157

Tremonti, C. A., Heckman, T. M., Kauffmann, G., et al. 2004, ApJ, 613, 898

Tumlinson, J., Peeples, M. S., & Werk, J. K. 2017, ARA&A, 55, 389

Tumlinson, J., Thom, C., Werk, J. K., et al. 2011, Science, 334, 948

Übler, H., Genzel, R., Tacconi, L. J., et al. 2018, ApJ, 854, L24

Übler, H., Genzel, R., Wisnioski, E., et al. 2019, ApJ, 880, 48

Umetsu, K., Zitrin, A., Gruen, D., et al. 2016, ApJ, 821, 116

van de Voort, F., & Schaye, J. 2012, MNRAS, 423, 2991

van der Kruit, P. C. 1988, A&A, 192, 117

van der Wel, A., Bell, E. F., Häussler, B., et al. 2012, ApJS, 203, 24

van der Wel, A., Franx, M., van Dokkum, P. G., et al. 2014, ApJ, 788, 28

van Dokkum, P. G., Kriek, M., Rodgers, B., Franx, M., & Puxley, P. 2005, ApJ, 622, L13

van Dokkum, P. G., Nelson, E. J., Franx, M., et al. 2015, ApJ, 813, 23

Varidel, M. R., Croom, S. M., Lewis, G. F., et al. 2020, MNRAS, 495, 2265

Vayner, A., Wright, S. A., Murray, N., et al. 2017, ApJ, 851, 126

Vazdekis, A., Sánchez-Blázquez, P., Falcón-Barroso, J., et al. 2010, MNRAS, 404, 1639

Veilleux, S., Cecil, G., & Bland-Hawthorn, J. 2005, ARA&A, 43, 769

Veilleux, S., & Rupke, D. S. 2002, ApJ, 565, L63

Veilleux, S., Meléndez, M., Sturm, E., et al. 2013, ApJ, 776, 27

Vogelsberger, M., Genel, S., Sijacki, D., et al. 2013, MNRAS, 436, 3031

Vogelsberger, M., Genel, S., Springel, V., et al. 2014, Nature, 509, 177

Walter, F., Weiss, A., & Scoville, N. 2002, ApJ, 580, L21

Wang, J., Koribalski, B. S., Serra, P., et al. 2016, MNRAS, 460, 2143

Weaver, R., McCray, R., Castor, J., Shapiro, P., & Moore, R. 1977, ApJ, 218, 377

Weinberger, R., Springel, V., Hernquist, L., et al. 2017, MNRAS, 465, 3291

Weiner, B. J., Coil, A. L., Prochaska, J. X., et al. 2009, ApJ, 692, 187

Werk, J. K., Prochaska, J. X., Thom, C., et al. 2013, ApJS, 204, 17

Westmoquette, M. S., Dale, J. E., Ercolano, B., & Smith, L. J. 2013, MNRAS, 435, 30

Westmoquette, M. S., Exter, K. M., Smith, L. J., & Gallagher, J. S. 2007, MNRAS, 381, 894

Westmoquette, M. S., Smith, L. J., & Gallagher, III, J. S. 2011, MNRAS, 414, 3719

Westmoquette, M. S., Smith, L. J., Gallagher, III, J. S., et al. 2009, ApJ, 696, 192

Whitaker, K. E., Franx, M., Leja, J., et al. 2014, ApJ, 795, 104

White, S. D. M., & Frenk, C. S. 1991, ApJ, 379, 52

Wielen, R. 1977, A&A, 60, 263

Williams, C. C., Giavalisco, M., Cassata, P., et al. 2014, ApJ, 780, 1

Wilman, D. J., Fossati, M., Mendel, J. T., et al. 2020, ApJ, 892, 1

Wisnioski, E., Glazebrook, K., Blake, C., et al. 2012, MNRAS, 422, 3339

Wisnioski, E., Förster Schreiber, N. M., Wuyts, S., et al. 2015, ApJ, 799, 209

Wisnioski, E., Mendel, J. T., Förster Schreiber, N. M., et al. 2018, ApJ, 855, 97

Wisnioski, E., Förster Schreiber, N. M., Fossati, M., et al. 2019, ApJ, 886, 124

Wisotzki, L., Bacon, R., Brinchmann, J., et al. 2018, Nature, 562, 229

Wood, C. M., Tremonti, C. A., Calzetti, D., et al. 2015, MNRAS, 452, 2712

Wuyts, S., Labbé, I., Förster Schreiber, N. M., et al. 2008, ApJ, 682, 985

Wuyts, S., Förster Schreiber, N. M., van der Wel, A., et al. 2011a, ApJ, 742, 96

Wuyts, S., Förster Schreiber, N. M., Lutz, D., et al. 2011b, ApJ, 738, 106

Wuyts, S., Förster Schreiber, N. M., Genzel, R., et al. 2012, ApJ, 753, 114

Wuyts, S., Förster Schreiber, N. M., Nelson, E. J., et al. 2013, ApJ, 779, 135

Wuyts, S., Förster Schreiber, N. M., Wisnioski, E., et al. 2016, ApJ, 831, 149

Yuan, T.-T., Kewley, L. J., Swinbank, A. M., & Richard, J. 2012, ApJ, 759, 66

Zahid, H. J., Torrey, P., Vogelsberger, M., et al. 2014, Ap&SS, 349, 873

Zakamska, N. L., Hamann, F., Pâris, I., et al. 2016, MNRAS, 459, 3144

Zaritsky, D., Kennicutt, Jr., R. C., & Huchra, J. P. 1994, ApJ, 420, 87

Zhang, K., Yan, R., Bundy, K., et al. 2017, MNRAS, 466, 3217

Zubovas, K., & King, A. 2012, ApJ, 745, L34